La borsa di dottorato è stata cofinanziata con risorse del
Programma Operativo Nazionale Ricerca e Innovazione 2014-202 (CCI 2014IT16M2OP005)
Fondo Sociale Europeo, Azione I.1 "Dottorati Innovativi con caratterizzazione Industriale"

UNIVERSITA' DELLA CALABRIA

Dipartimento di Fisica

Dottorato di Ricerca in

Scienze e Tecnologie Fisiche Chimiche e dei Materiali

CICLO

XXXIII

Self-assembled Materials for Anticounterfeiting Devices

Settore Scientifico Disciplinare FIS/07

Coordinatore: Ch.mo Prof. (Gabriella Cipparrone)

Firma oscurata in base alle linee guida del Garante della privacy

Firma

Supervisore/Tutor: Ch.mo Prof. (Maria Penelope De Santo)

Firma oscurata in base alle linee guida del Garante della privacy

Firma

Dottorando: Dott./ssa (Erica Fuoco)

Firma oscurata in base alle linee guida del Garante della privacy

Firma

Abstract

Negli ultimi anni il problema della contraffazione di prodotti ha assunto proporzioni allarmanti. Oltre ad essere un problema economico per aziende e governi, la contraffazione rappresenta un rischio notevole per la salute pubblica e per la sicurezza nazionale, questo soprattutto quando si ha a che fare con la contraffazione di medicinali o di componenti destinati ai comparti militari.

Le copie contraffatte sono sempre più spesso, in apparenza, talmente fedeli all'originale che gli stessi produttori incontrano difficoltà nel distinguere il prodotto originale da una sua copia non autorizzata. A causa di questo, i paesi sviluppati necessitano di soluzioni tecniche sempre più efficaci che forniscano un valido supporto per l'autenticazione, l'identificazione e la tracciabilità delle merci.

Le funzioni fisiche non clonabili (PUF) sono alla base dei sistemi di anticontraffazione più innovativi con elevati livelli di sicurezza. Una chiave PUF è una manifestazione fisica di una chiave crittografica, è impossibile da contraffare e si basa su una funzione fisica unica generata in maniera casuale.

La materia soffice, grazie alle sue peculiari proprietà, si presta alla creazione di chiavi PUF. Ad esempio, materiali quali i cristalli liquidi e la cellulosa, in grado di auto-assemblarsi in complesse strutture sopramolecolari, presentano particolari proprietà ottiche e fotoniche ed una alta responsività agli stimoli esterni. Nuovi materiali compositi, basati sull'unione con nanoparticelle organiche ed inorganiche, possono essere preparati tramite procedure che conferiscono loro una casualità intrinseca. In questo modo è possibile creare strutture complesse e impossibili da riprodurre che si riflettono in proprietà ottiche uniche. Tali materiali sono degli ottimi candidati per la realizzazione di chiavi PUF.

Il presente lavoro di dottorato si inquadra in questo filone di ricerca. In particolare sono presentati due esempi di chiavi PUF basate sull'utilizzo di emulsioni di cristallo liquido chirale. Confinando il materiale liquido cristallino, drogato con nanoparticelle metalliche, in microsfere e applicando un forte campo elettrico è possibile ottenere la creazione simultanea e casuale in ogni microsfera di diverse tessiture ottiche che mostrano le stesse caratteristiche delle impronte digitali umane. Tale sistema è proposto come generatore fisico di impronte digitali e viene mostrato un primo esempio di prototipo di etichetta anticontraffazione. Nel secondo caso l'emulsione di cristallo liquido, stavolta drogata con un colorante fluorescente e con dei nanocristalli di cellulosa, viene elettrofilata ottenendo un film sottile e flessibile che contiene al suo interno una disposizione casuale di microsfere fluorescenti. La mappa posizionale delle microsfere all'interno del filato costituisce una chiave PUF. Entrambi i risultati ottenuti sono originali e sono in fase avanzata di prototipazione.

Inoltre, in vista della creazione di dispositivi bio ed eco compatibili che possano essere usati nella tracciabilità di cibi e farmaci, vengono presentate due soluzioni basate sull'utilizzo di materiali quali

cellulosa e i suoi derivati (nanocristalli e idrossipropilcellulosa). Tali materiali, sintetizzati appositamente per questo lavoro di ricerca, sono utilizzati per la creazione di etichette autosupportate in grado di riflettere i colori in maniera selettiva, ma anche in grado di mostrare delle proprietà aggiuntive, quali la fluorescenza, se i nanocristalli di cellulosa sono funzionalizzati con un colorante. In questo caso, anche se i film utilizzati non presentano una casualità intrinseca, sono comunque strutture molto complesse di difficile riproduzione che possono essere arricchite da ulteriori proprietà ottiche. I film descritti si prestano a ulteriori miglioramenti, sia in termini della ottimizzazione delle procedure di sintesi dei materiali, sia in termini delle procedure di preparazione dei film.

Introduction

The cost of fraud and related corruption at the expense of the European Union economy is estimated to €120 billion per year, slightly lower than the annual budget of the EU itself.

The counterfeit market, according to European union office for individual property observatory (EUIPO) and the Organization for Economic Cooperation and Development (OECD) data, grows year by year, reaching 3.3% of world trade in 2016, compared to 2.5% in 2013. Italy, with “Made in Italy” products recognized all over the world as a synonym of quality and excellence, is the third country most affected by counterfeiting after USA and France.

In Italy, according to the General Directorate for the Protection of Industrial Property - Italian Patent and Trademark Office (DGTPI - UIBM) between 2008 and 2013 there were about 100 thousand seizures, for an amount of about 335 million pieces seized and a total economic value of 3.8 billion euros. Recently in 2020, DGTPI - UIBM and the Ministry of Economic Development (MISE), has prepared with the support of Invitalia the "Report on Anti-Counterfeiting Policies 2018-2019" which contains the results of the main initiatives implemented to prevent and effectively combat the fake goods market, also in collaboration with international and national partners [1].

According to the OECD, the value of world trade in fake products infringing Italian registered trademarks reached 31.7 billion euros in 2016, while the volume of lost sales by Italian manufacturing companies is approximately 24 billion euros due to the violations of its Industrial Property Rights (IPRs) in world trade.

The sectors in which Italian IPRs have been most counterfeited are: clothing, footwear and leather products (16.7%), followed by electronic products and electrical equipment (15.4%) and food products (13%).

In addition to outlining a picture on the impact of the phenomenon on a global level, the Report also illustrates the main anti-counterfeiting initiatives undertaken by the DGTPI-UIBM: the analysis of the territorial characteristics of the counterfeiting market to define targeted anti-counterfeiting policies; awareness and information actions aimed at institutions, law enforcement agencies, businesses and consumers; the activation of services to provide businesses and consumers with tools and information to protect themselves from violations; the management of databases for greater sharing of information with security operators and rights holders; territorial enforcement actions and initiatives carried out in collaboration with the members of the National Council for the Fight against Counterfeiting and Italian Sounding to combat crimes against Intellectual Property.

Beyond the actions undertaken by governments, great hopes in the fight against counterfeiting are placed in the development of increasingly efficient and connected devices for identifying, tracking and authenticating products and practices. Cyber physical security is the new frontier in this field,

promoting the use of sensors, processors and actuators, that sense and interact with the physical world and support real-time, guaranteed performance in safety-critical applications connecting them together by smart software grids.

I. Cyber Physical Security

The key technological innovations of the fourth industrial revolution are Cyber-physical systems (CPS). A cyber-physical system (CPS) integrates both physical and networked computing processes aimed at monitoring and controlling physical components and computational networks. This combination of machines, cyber intelligence and devices gives you all-round control. This means that physical security (which prevents an intruder from accessing a physical place) and logical security (which protects hardware systems and digital places) work together. CPS represent a set of different technologies that create an intercommunicating system, combining and integrating physical and IT factors to generate and acquire data, support decision-making and aggregate the data collected. The data is exchanged by the various communicating factors, at any time, creating systems that combine the physical aspect, that is the device itself, with the digital one. The cyber-physical security market is growing strongly and represents an area with significant opportunities.

The advent of the Internet of Things (IoT) has facilitated this growth, smart devices have become an inseparable part of our daily life and many physical devices and everyday objects are now connected. In fact, according to IHS Markit, there will be over 125 billion connected devices globally by 2030. The world is changing, and so are its infrastructures, products and services, all of which are now intelligent.

The main factors limiting the growth of the sector are different. First of all, the need for a qualified and updated workforce on CPS. Another limitation concerns security, since anyone who adopts CPS must adapt their security systems so that they guarantee both physical and IT coverage. Today, we must be concerned with protecting as well as innovating.

There have been many advances in technology in recent decades and today cyber-physical security is already of enormous importance. Just think that personal, professional and economic data already travels online, so the problem of security and the importance of prevention is evident, just think, for example, that even our money is virtually in motion.

Furthermore, many cyber-physical systems are the basis of critical infrastructures. US security agencies, including the FBI and Cybersecurity and Infrastructure Security Agency (CISA), have issued warnings of increased criminal activity in recent months. Cybercriminals are increasingly conducting malicious cyber activities against critical infrastructures by exploiting operational technology resources accessible from the Internet.

Gartner has predicted that the financial impact of CPS attacks with severe consequences will reach more than $ 50 billion by 2023. In addition to the financial implications, CSP attacks can also result in the loss of customers, theft of intellectual property, operational shutdowns or the damage of the performance and quality of the equipment.

a. CPS architecture

The CPS architecture is generally composed of two main levels connected to each other, the physical one that acquires the detected data and executes the commands of the other level which is the cybernetic one that analyses and processes the data from the other layer and releases the appropriate commands consequently[2]. There are different assumptions about the number of layers in the CPS architectures, [3] for example provides a subdivision with five levels which are business, application, processing, transmission and perception. But, as reported in other studies [4]–[7]. CPS basically operates at three levels as showed in figure i and they are called perception, transmission and application related to physical, network and cyber layer respectively.

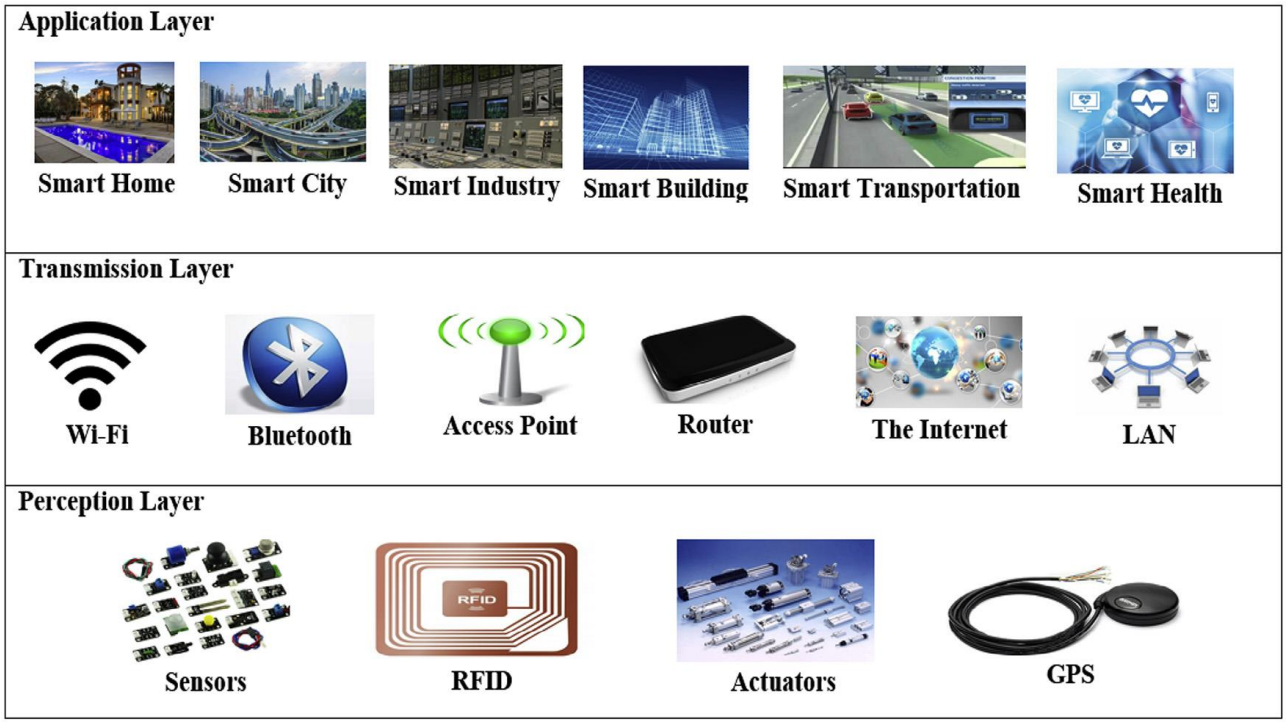

Figure i Cyber Physical Security architecture

The first layer is the perception layer (also called the recognition layer [8] or the sensor layer [5]. This layer is formed by physical devices such as sensors, cameras, global position systems (GPS), laser scanners, RFID tags, 2D barcode labels, others [2], [3], [9]. The devices have to collect data in real-

time, data such as sound, light, mechanics, chemistry, heat, electricity, biology or location [6], [7], then they have to interpret what they receive from the physical world and execute commands from the application layer.

The second level is the transmission layer (also known as the transport layer[2] or the network layer[10]. In this layer, the exchange of information and the processing of data between the perception and the application takes place through the use of the network or for example local networks, communication networks, Internet, Bluetooth, 4G and 5G, UMTS, Wi- Fi, infrared and more [10]. The most used network is the Internet for many reasons, including availability and cost effectiveness. Since large amounts of data are managed and processed, in this layer we can find the presence of protocols and added functions to guarantee everything in real time such as Internet Protocol version 6 (IPv6) [3].

The third is the application level and is the most interactive as it processes the information received from the second level and gives commands to be executed by the physical units of the first level [6]. This level receives and processes information from the first level and is based on complex decision algorithms and control commands, which generate correct decisions on the collected data [11]. The intelligent collection and processing of huge amounts of data is done with object control and management. System monitoring also takes place here. The objective of this level is to create an intelligent environment [5] and to combine CPS and professional applications of the sector.

b. CPS security

Given to the large amount of data exchanged, it is very important to apply mechanisms to protect the data. Security and the possibility of attacks affect every single level.

In general, CPS security can be divided into two macro areas, one concerning information (data) security and the other concerning control security. Data security includes information protection throughout the system from data aggregation, to large-scale processing and sharing over the network, such as using cryptography. Control security includes resolving any network control problem and mitigating the control system from any type of attack, it focuses primarily on the dynamics of control systems protection from cyber-attacks [6], [12].

Ensuring secure access for devices into the first level is one of the most important things. Indeed, if authentication is not or is poorly supported, unauthorized objects will have easy access and manipulate the system [13], so neither data reliability nor implementation in the second will be guaranteed. Data transmission security is also important in order to detect impostors and harmful activities in CPS communication networks and block unauthorized access. Protecting secret data stored on CPS devices is important.

c. Attacks on CPS

Attacks on the CPS could cause severe damage to the physical environment. Each level of CPS is susceptible to active or passive attacks and it is vulnerable to more attacks than traditional IT systems, since cyber-attacks on the network used are the most widespread and in CPS systems the network is used as a transmission layer. The first level consists of devices, such as RFID tags and sensors, which are limited by limited processing resources and memory capacity. In addition, these devices are mostly found in outdoor environments, resulting in possible physical attacks, such as tampering with device components or replacing the devices themselves. Hence, these end devices are the most susceptible to a variety of attacks[14]. Common attacks at the perception layer include equipment failures, line failures, electromagnetic interference, perceptual data corruption [6], information disclosure and tracking, tampering, information loss detection [4], physical destruction and energy depletion attacks[15]. Attacks in the second layer are in the form of data loss during the transmission of information. This occurs due to the openness of the means of transmission, especially in wireless communication. Such attacks, for example, capture a message transmitted via a radio interface, modify it and retransmit it, or exchange information between heterogeneous networks, thus impersonating the legitimate user. As a large amount of user information is collected in the third level, the attacks here result in data damage, loss of privacy such as users' health habits and conditions, and unauthorized access to devices [6]. Common application layer attacks include loss of user privacy, unauthorized access, malicious code, database forgery and control command attacks [2], [6].

II. Solutions for CPS security and attacks: PUFs

Encryption is the basis for solving many problems related to CPS security and CPS attacks. There are two basic encryption mechanisms used in CPS: hop-by-hop and end-to-end. In the hop-by-hop encryption mechanism, information is encrypted in the transmission process. With the end-to-end encryption mechanism, for example, only the sender and recipient can read the messages and no interceptor can access the cryptographic keys needed to decrypt the encrypted data.

Physical embodiment of cryptographic keys would be the ideal components to optimize the devices in the perception layer. TAGs are usually used as devices in the first layer of CPS. Anti-counterfeiting TAGs are distinctive signs of varying sizes and materials, which are used for traceability, authenticity and anti-tampering purposes and represent a tool for recognizing the authenticity of the goods on which it is applied. The recent techniques of identification and tracking of goods can be decisive in the implementation of effective anti-counterfeiting methods starting from TAGs. A TAG can be used in the production process for the purposes of authentication, anti-tampering / anti-alteration, identification / tracking.

TAGs can be divided into macro-categories based on the technologies used for their construction. For each macro-category there are many characteristics to consider, some of which will be briefly illustrated including the complexity of writing and reading the TAG, the information contained into the TAG and their security.

Macro categories and characteristics of TAGs:

- Electronic technologies are made up of integrated circuits with or without batteries, magnetic strips, radio components including for example RFID (passive, active) and NFC and they can have different dimensions and they are generally quite small. The readers needed to query NFCs and receive response information that are already available in almost all smartphones, so reading with the appropriate tools is instantaneous and costs are contained. The cost per item mainly depends on the functions required and therefore on the type of devices used. TAGs' security is related to the aspects of reproduction and tampering depending on the communication protocol and on the information stored in the Tag itself (for example code, password, etc.) and above all if such information is encrypted or not.

- Mechanical technologies are made up of watermarks, logos, inks, laser engravings, security seals such as labels. They usually are printed, the dimensions follow the shape or packaging of the product, the common material used is plastic or formed by ink. The cost per single solution is medium-low and in the specific case of labels the adoption times are very fast, since they do not require changes to the production process. They do not have methods for automatic reading (authentication takes place through visual inspection), with the exception of labels. Reproducibility and safety are linked to the difficulty of reproducing the design / effect as for example in holograms, watermarks and security threads.

- Marking technologies, which may be visible or not visible to the human eye, are the most widely used due to their variety, low costs and the simplicity of the reading procedures. Reading is immediate, the information can be read through the use of optical tools such as: visual inspection, barcode and QR readers, magnifying glasses, smartphones. They are imprinted on the product or on its packaging, they do not have depth, as they are varied and they are of different sizes but they always maintain small sizes. The most common are the optical solutions due to their variety and the simplicity of the verification procedures. The costs per item are low and in most of these solutions no changes to the production chain are required as they can be applied at a later time by means of labels or stickers on the product. If we want to integrate them into the product itself, appropriate changes in the production chain

will be necessary. In most of the marking solutions information are not contained into the TAG but only optical effects for authentication purposes, or links that recall information contained in third party servers such as in the case of two-dimensional and one-dimensional barcodes. In this case security is linked to the servers where the tag information is contained, if you do not have access to the servers, the TAG will not be readable.

- Chemical-physical technologies, which include types based on molecular particles, chemical coding, micro and nanotechnology tracers, glue coding, Surface Finger Print and Laser Surface Analysis – LSA and Physical Unclonable Function (PUF). These materials can be incorporated into the products or glued onto the products themselves, their size is variable. Authentication is generally carried out with specialized hardware or through the use of laboratory analyses. Automatic reading devices, if available, are expensive. The cost per item of these systems is generally low, while in the case of solutions based on molecular analysis for anti-counterfeiting currently available on the market they are covered by a patent and therefore the related costs are set by the patent holder. The security, reproducibility and tampering of chemical-physical solutions is generally based on the chemical-physical property of the materials that are used.

Based on these macro categories of TAG 'technologies, there is the possibility of combining two or more technologies and their characteristics to create a single better TAG and increase the complexity of the system.

Other features to be taken into consideration in TAGs are the possibility of cloning with the alteration of the information contained in the TAGs themselves and the way in which the TAGs can be read.

Taking into consideration the TAGs' clonability we can divide the TAGs as follows:

- *Clonable* TAGs: that are easily reproducible and alterable, such as two-dimensional barcodes, holograms, simple inks, simple labels, magnetic stripe.
- TAGs that are difficult to clone: that require more specific knowledge and machinery, such as RFID, NFC, inks sensitive to UV radiation, laser engravings.
- *Unclonable* TAGs: PUFs, chemical coding, Surface Fingerprint and Laser Surface Analysis.

Instead, considering the types of TAG' reading we have:

- "*Overt*" technologies immediately verifiable by the end user, even without the use of special tools or complex procedures (watermark, holograms, intaglio printing), these technologies are essentially for authentication purposes.

- "*Covert*" technologies require instrumentation (simple or complex) to be verified (inks sensitive to non-visible radiation, fluorescent fibrils, fluorescent inks, RFID, NFC, etc.) and these technologies have the purpose of authentication but also of tracing.
- Mixed technologies using a combination of "overt" and "covert" technologies (1D and 2D barcodes).

Table i TAGs classification

TAGs Macrocategories	Information contained	Information Security	Read / write complexity	Reproducibility	Type of recognition	Examples
Electronic technologies	Previously stored information about the product they are associated with	Communication protocol, information stored in the Tag, encryption	Reading: Low Writing: It depends on the type of device	Difficult to clone	Covert	RFID, NFC, electronic seals
Mechanical technologies	Images / logos, any type of text and identification codes	Difficulty in reproducing the design / effect	Reading: Medium-Low Writing: Easy	Difficult to clone	Mixed	Labels, laser engravings, seals, security threads
Marking technologies	Graphic motifs branded on the product, Barcodes	Optical effects for authentication purposes, links that recall information contained in third party servers	Reading: Low Writing: Low	Clonable	Overt	Holograms, machine-readable codes, inks, filigree designs
Chemical-physical technologies	Molecular, chemical-physical properties of the substance used, structures of matter	Physical and chemical property of the substance used	Reading: High Writing: depends on patent cost	Unclonable	Covert	Glues, Surface Fingerprint, chemical coding, PUF

In table i, we have tried to summarize all types of TAGs, now we focus our attention on PUF TAGs that could be one of the best possible solutions for CPS security.

A Physical Unclonable Functions (PUF) is a function that creates a unique value dependent on the physical structure of the hardware itself. On the other hand, many hardware devices are not provided with PUF implementation ability, hence not all devices can implement PUF technology. Although all the security objectives of the CPS are important, authenticity, validating claimed identity, should be ranked as the first objective of the security on which the other security classes are built. Authentication is the most important thing in addressing many security risks. A robust authentication mechanism will prevent unauthorized entities from joining the CPS environment and causing security issues. PUFs can be implemented in hardware, such as SRAM, and can be used to uniquely identify the device, this is due to the unique physical variations which occur naturally during semiconductor manufacturing. This technology could be used in CPS to ensure location-based access control and encryption, both of which would be desirable for CPS implementations. A common use of PUFs is for the secure storage of cryptographic keys. One problem with the approach of using PUFs for CPS is the current limited availability of the technology.

In 2002, Pappu[16] based on the idea that modern cryptography relies on algorithmic one-way functions, numerical functions which are easy to compute but very difficult to invert, in his works

introduces physical one-way functions and physical one-way hash functions as primitives for physical analogues of cryptosystems. His prototype uses a disordered three-dimensional microstructure as the underlying physical system and coherent radiation as the probe. It is shown that the output of the interaction between the physical system and the probe can be used to robustly derive a unique tamper resistant identifier at a very low cost per bit. The explicit use of three-dimensional structures marks a departure from prior efforts.

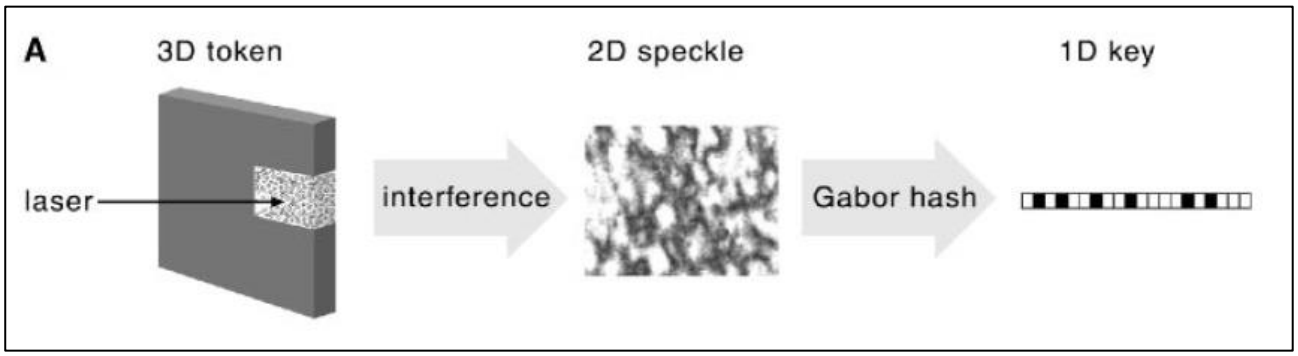

Figure ii A 3D inhomogeneous structure being optically hashed to produce a 2D image, which is in turn filtered by a multiscale Gabor transform to produce a 1D key. A 1-cm^3 cube has ~10^{12} 1-µm cubic blocks of wavelength size, corresponding to a terabit of structural information. The 320 by 240 pixels image shown contains on the order of a megabit of intensity information, and the Gabor transform reduces this to a 2400-bit key.

From Pappu's pioneering work, several PUF systems based on light scattering have been proposed in the years. An example is the so-called laser surface authentication, in which a laser light is scattered by the unique features of the surface topology of a piece of paper or plastic. The intrinsic randomness in the micro or nanostructure creates unique scattering patterns [17].

In more recent years several materials and processes have been investigated to create complex PUF keys. In this context, soft materials and, among them, liquid crystals (LCs) are very promising candidates for the creation of PUFs since they are excellent optical materials capable of self-assemble in complex photonic structures and self-repair. Among their most interesting optical properties are birefringence and Bragg-type reflection [[18]The polarization of the reflected light and the reflected colors can be controlled using external stimuli such as temperature, UV irradiation, application of electric fields. Also, cellulose-based materials are extremely promising for the creation of strong optical PUFs. Cellulose is formed by random oriented fibers, which can be easily imbibed with photo responsive molecules and can be patterned at microscale using low-cost methods. Thanks to the large flexibility, availability and biodegradability of paper, micro-nanostructured cellulose represents an ideal material to design molecular assemblies with random emitting properties.

This research work has been devoted to the creation of novel PUF keys with unprecedented coding capacities exploiting the optical properties of soft composite systems containing stimuli responsive materials confined in micron sized structures or in micro structured films.

This dissertation is divided in three parts. The first part is devoted to the description of a physical random generator of fingerprint-like textures based on chiral crystalline materials doped with metallic nanoparticles. Several microspheres containing the composite liquid crystalline material can be obtained preparing an emulsion of the liquid crystal in an immiscible matrix. Applying an electric field the director field reorients inside the microsphere generating a fingerprint like optical texture. The texture is random and different in each microsphere and this procedure can be used as an artificial fingerprints generator. Using a high resolution image of an artificial fingerprint, a prototype of an anti-counterfeiting tag is also presented.

In the second part we have focused on the development of novel anti-counterfeiting solutions starting from green and sustainable materials such as cellulose. With this purpose, a procedure to synthesize cellulose nanocrystals containing a fluorescent moiety has been developed. Two kinds of free standing films based on cellulose derivatives with peculiar optical properties are presented. Even if the films and their optical properties do not have an intrinsic random nature to be used as PUF keys, nevertheless, the presented materials are promising to develop anti-counterfeiting devices to be used in direct contact with food or drugs.

Finally, in the last part the possibility to create a flexible freestanding film containing a random optical pattern, combining the properties of liquid crystals with the ones of polymers and cellulose nanocrystals, is investigated. Using the electrospinning technique an emulsion containing liquid crystals, fluorescent dyes, cellulose nanocrystals and a polymer has been used to create thin films in which fluorescent microspheres are embedded. In this case, the random positional map of the microspheres can be used as a PUF key and the fluorescence helps in increasing the coding capacity of the tag.

References

[1] "Pubblicato il 'Rapporto sulle Politiche Anticontraffazione 2018-2019' - Invitalia." https://www.invitalia.it/chi-siamo/area-media/notizie-e-comunicati-stampa/pubblicato-il-rapporto-sulle-politiche-anticontraffazione-2018-2019.

[2] T. Lu, J. Lin, L. Zhao, Y. Li, and Y. Peng, "A Security Architecture in Cyber-Physical Systems: Security Theories, Analysis, Simulation and Application Fields," *International Journal of Security and Its Applications*, vol. 9, no. 7, pp. 1–16, 2015, doi: 10.14257/ijsia.2015.9.7.01.

[3] M. Wu, T. J. Lu, F. Y. Ling, J. Sun, and H. Y. Du, "Research on the architecture of Internet of Things," *undefined*, vol. 5, 2010, doi: 10.1109/ICACTE.2010.5579493.

[4] Q. Gou, L. Yan, Y. Liu, and Y. Li, "Construction and strategies in IoT security system," *Proceedings - 2013 IEEE International Conference on Green Computing and Communications and IEEE Internet of Things and IEEE Cyber, Physical and Social Computing, GreenCom-iThings-CPSCom 2013*, pp. 1129–1132, 2013, doi: 10.1109/GREENCOM-ITHINGS-CPSCOM.2013.195.

[5] R. Mahmoud, T. Yousuf, F. Aloul, and I. Zualkernan, "Internet of Things (IoT) Security: Current Status, Challenges and Prospective Measures" *2015 10th International Conference for Internet Technology and Secured Transactions (ICITST)*, 2015, pp. 336-341, doi: 10.1109/ICITST.2015.7412116.

[6] Y. Peng, T. Lu, J. Liu, Y. Gao, X. Guo, and F. Xie, "Cyber-physical System Risk Assessment," *2013 Ninth International Conference on Intelligent Information Hiding and Multimedia Signal Processing, 2013*, pp. 442-447, doi: 10.1109/IIH-MSP.2013.116.

[7] K. Zhao and L. Ge, "A Survey on the Internet of Things Security," *2013 Ninth International Conference on Computational Intelligence and Security*, pp. 663–667, 2013, doi: 10.1109/CIS.2013.145.

[8] J. S. Kumar and D. R. Patel, "A Survey on Internet of Things: Security and Privacy Issues," *International Journal of Computer Applications*, vol. 90, no. 11, pp. 975–8887, 2014.

[9] B. Zhang, X.-X. Ma, and Z.-G. Qin, "Security Architecture on the Trusting Internet of Things," *Journal of electronic science and technology*, vol. 9, no. 4, p. 364, 2011, doi: 10.3969/j.issn.1674-862X.2011.04.014.

[10] R. Zaheer and S. Khan, "Future Internet: The Internet of Things Architecture, Possible Applications and Key Challenges," pp. 257–260, 2012, doi: 10.1109/FIT.2012.53.

[11] C. Scheuer *et al.*, "Cyber security for cyber physical systems: A trust-based approach," *Journal of Theoretical and Applied Information Technology*, vol. 71, no. 2, pp. 144–152, Jan. 2015, doi: 10.2/JQUERY.MIN.JS.

[12] A. A. Cárdenas, S. Amin, Z.-S. Lin, Y.-L. Huang, C.-Y. Huang, and S. Sastry, "Attacks Against Process Control Systems: Risk Assessment, Detection, and Response General Terms Security".

[13] C. Konstantinou, M. Maniatakos, F. Saqib, S. Hu, J. Plusquellic, and Y. Jin, "Cyber-Physical Systems: A Security Perspective".

[14] Q. Shafi, “Cyber physical systems security: A brief survey,” *Proceedings - 12th International Conference on Computational Science and Its Applications, ICCSA 2012*, pp. 146–150, 2012, doi: 10.1109/ICCSA.2012.36.

[15] Bhattacharya, Rina, “A Comparative Study of Physical Attacks on Wireless Sensor Networks” *International Journal of Research in Engineering and Technology*, vol. 02, no. 01, pp. 72–74, 2013, doi:10.15623/ijret.2013.0201014.

[16] R. Pappu, B. Recht, J. Taylor, and N. Gershenfeld, “Physical one-way functions,” *Science (New York, N.Y.)*, vol. 297, no. 5589, pp. 2026–2030, Sep. 2002, doi: 10.1126/SCIENCE.1074376.

[17] R. Cowburn, “Laser surface authentication – reading Nature’s own security code,” *Contemporary Physics*, vol. 49, no. 5, pp. 331–342, Sep. 2008, doi: 10.1080/00107510802583948.

[18] P. G. de. Gennes and Jacques. Prost, “Liquid Crystals: Main Types and Properties,” *The physics of liquid crystals*, pp. 1–40, 1993.

1. Chapter 1: Liquid Crystals based Microfingerprints generator

Nowadays, our unique physical credentials like fingerprints, faces and retinas, are starting to be used as keys to unlock devices instead of passwords, as in the case of mobile telephones.

Unfortunately, biometrical information, stored in databases, can be hacked and data lost irreversibly. In 2019, fingerprint, facial recognition, username and password information for more than one million people were found on South Korean company Suprema's publicly viewable database, BioStar 2 [1]. Thankfully, electronic devices such as smartphones generally store fingerprint or facial data on a dedicated chip in the hardware itself and not in an online server. Nevertheless, even if remote, the possibility of hacking cannot be excluded.

In an antivirus firm, Kaspersky Lab, researchers have designed a ring to address this key vulnerability with biometric authentication that comes with a built-in synthetic fingerprint (Figure 1.1, a)[2]. Each ring comes with a unique fingerprint sourced to a software tool and the artificial prints are never stored to prevent leaks.

In general, fingerprint like patterns is generated by software but, in recent years, several methodologies have been developed that are able to produce artificial physical fingerprint-like structures. These structures are appealing since fingerprints are rich in minutiae, furrows and crests that bifurcate, curve, end abruptly or cross, then, they can be used to encode a high volume of information and be used as PUF keys. In 2014, J. Kim et al. obtained nanoscopic fingerprints using randomly distributed silver nanowires coated with fluorescent dyes embedded in a PET film [3] .

In 2015 Bae et al. obtained artificial micro fingerprints following the random drying procedure of a silicon film encapsulating discotic polymeric particles few hundreds of microns in size (Figure 1.1, d) [4].

From an encoding point of view, the fingerprint approach has a huge capacity that can be further increased if the pattern is enriched with other unique features. As an example, in 2016 Tian et al. obtained a fingerprint-like structure doping a random folded ultrathin gelatinous polymer with plasmonic nanostructures in the form of silver coated gold nanorods (figure 1.1, b) [5]. Then, in addition to the random pattern, the structure exhibited a unique surface enhanced Raman spectroscopy signal.

The possibility to superimpose random patterns of different nature (Raman and fluorescence emission, melting points and molecular masses) dramatically improves the encoding capacity of the PUF key. For this reason, materials that have the peculiarity to self-assemble or that can be easily

assembled in complex and/or random patterns that provides them with unique optical and electrical properties are extremely attractive for the creation of Physical Unclonable Functions keys.

Liquid crystals are suitable candidates for this purpose. In particular, chiral nematic LCs show peculiar optical properties being able to self-organize in periodic helical structures. CLCs possess several unique properties: 100% selective reflection of circularly polarized light and the ability to change their selective reflection wavelength changing external or internal factors (electric and electromagnetic fields, temperature, local order). Due to these properties chiral nematic LCs have been used in a plethora of applications in optics, photonics and, recently, in security. As an example, in 2012 Nakayama et al. have proposed the use of chiral LCs as materials for optical security devices, developing a way to prepare random patterns with a fingerprint like texture (figure 1.1, c) [6].

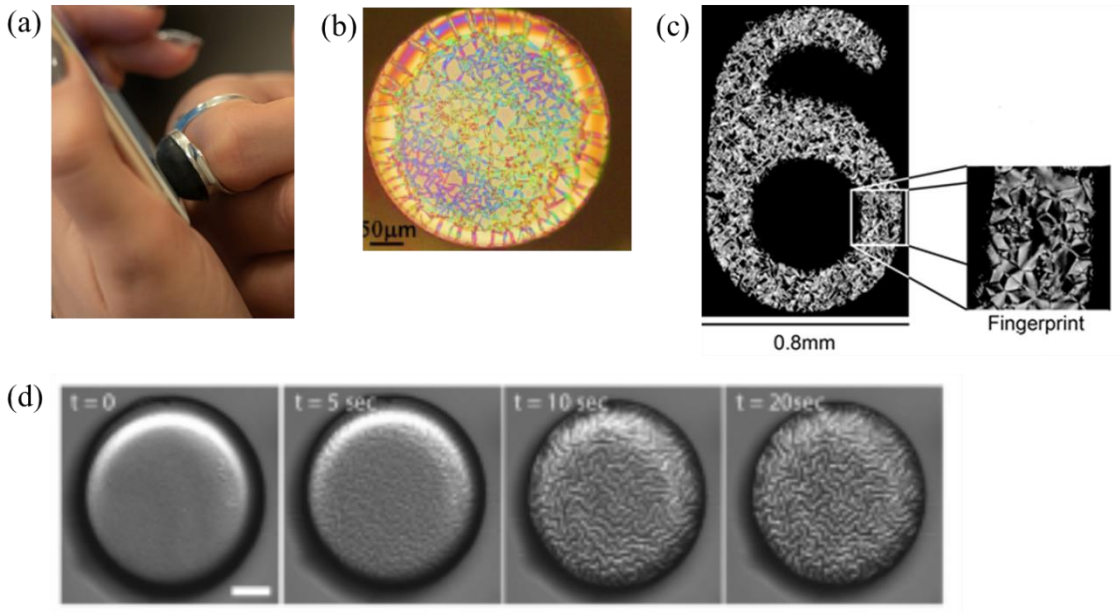

Figure 1. 1 (a) Kaspersky Lab ring [2], (b) Optical image of a multidimensional micro-taggant comprising folded plasmonic gel on a PDMS micro-disk [5] (c) A fingerprint pattern visible using an optical microscope between crossed polarizers [6] (d) Wrinkles forming on a disk during the drying procedure of the solution containing silicon and discotic polymeric particles (scale bar: 25 μm)[4] .

In the last decade, a lot of research has been carried out on the peculiar optical properties of LCs confined inside spheres, tens of microns in size[7] . The three-dimensional confinement of nematic and chiral LCs inside microdroplets has been investigated both theoretically and experimentally and a variety of topological structures have been studied and identified [8]–[10]. Further, topological transitions in chiral nematic microdroplets have been investigated as a function of external fields (temperature gradients, electric and electromagnetic fields) obtaining a plethora of complex free-standing metastable topological architectures at the micron scale[11], [12].

Our research group has demonstrated that chiral liquid crystals encapsulated in micrometric droplets and immersed in an isotropic fluid are able to produce, in a strong electric field, a texture that resembles a fingerprint-like one[13]. Each droplet immersed in the field shows a unique and randomly generated structure easily revealed through polarized light optical microscopy. In order to optimize the obtained texture and reduce the intensity of the electric field necessary to create it, chiral liquid crystals were doped with nanoparticles. The effects of the nanoparticles presence on the texture were extensively studied. The new protocol can be used as a physical fingerprint generator able to produce a considerable number of patterns at the same time. Finally, the possibility to create an anti-counterfeiting tag using the created patterns is demonstrated.

1.1. Liquid Crystals

1.1.1. Introduction

Materials in nature can be classified in different ways based on the property that is observed. Depending on the mobility of the individual atoms or molecules they are divided into different phases also called states of matter. We commonly have the solid, liquid and gaseous state, but there are some intermediate states. Materials that have both solid and fluid state characteristics, are called *liquid crystals (LCs)* (Fig.1.2).

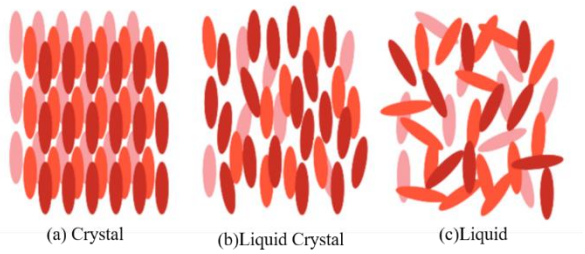

Figure 1. 2 (a) Crystal (b) Liquid Crystal (c) Liquid

The liquid crystalline phase shows anisotropy in its optical, mechanical, electrical and magnetic properties, like crystalline solids but at the same time possesses high fluidity, which is the property of liquids.

Phase transitions are the physical processes of transition between states in a medium, identified by some parameters where materials show different properties as a function of different physical and environmental parameters. Liquid crystals can be distinguished into different mesophases due to the fact that their internal order can be varied by acting on concentration or temperature, in this case we can classify liquid crystals into lyotropic and thermotropic LCs.

- *Lyotropic LCs* show a phase transition as a function of molecules' concentration in a solvent (typically water);

- *Thermotropic LCs* have a phase transition in the LC phase due to a change in temperature.

By Friedel's nomenclature, thermotropic liquid crystals are classified into three types: nematic, cholesteric and smectic.

- nematic phase exhibits a high degree of long range orientational order of the molecules, but no translational order [14];
- chiral phases or cholesteric phase is a nematic type of a liquid crystal except that it is composed of optically active molecules;
- smectic phase is composed of stratified structures and in each layer a variety of molecular arrangements are possible.

1.1.2. Nematic phase

The nematic mesophase is formed by molecules that have no positional order and are therefore free to rotate on themselves and slide over each other, the centres of mass are randomly arranged but they have an orientational order, whose direction is identified by a unit module vector, called director $\hat{n}$, (Fig. 1.3). Molecules will arrange themselves in space with the major axis predominantly oriented along the director to minimize the intermolecular interaction energy. Macroscopically there is a non-polar structure, due to the rotational symmetry ($\hat{n} = -\hat{n}$) around the axis of the director.

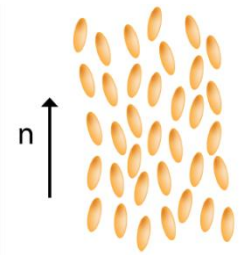

Figure 1. 3 Schematic representation of nematic liquid crystalline order

1.1.3. Chiral phases

In the chiral phase molecules are chiral, they have no specular symmetry and are optically active. The chiral structure can be imagined as a series of nematic planes. In each plane the director rotates with respect to the previous one. Then, the chiral structure has a nematic order in the planes and a helical superstructure in the volume this is why the cholesteric mesophase is also known as the chiral nematic mesophase[15] .

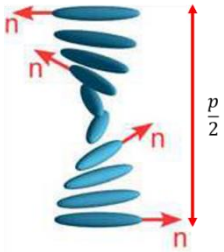

Figure 1. 4 Schematic representation of chiral order and pitch

A complete rotation of the director $\hat{n}$ is described by a parameter called *pitch* (p) (Fig. 1.4). The entire structure is symmetric ($\hat{n} = -\hat{n}$), if considered q_0 the initial phase equal to ± 2πp and ϕ the phase amplitude, the rotation of $\hat{n}$ around the helix axis (z axis), can be described as:

$$n_x = \cos(q_0 + \phi)$$
$$n_y = \text{sen}(q_0 + \phi)$$
$$n_z = 0 \qquad (1.\ 1)$$

the space period is equal to:

$$L = \frac{p}{2} = \frac{\pi}{|q_0|} \qquad (1.\ 2)$$

the amplitude determines the spatial periodicity and the sign of q_0 describes the direction of the helix, for $q_0 < 0$ is left-handed and for $q_0 > 0$ is right-handed.

The presence of a periodic structure gives a greater order to this mesophase with respect to the nematic one. The helix structure is responsible for most of the optical properties of this mesophase such as the selective reflection of circularly polarized light as will be shown later in this chapter (section 1.2.2).

The cholesteric phase appears naturally in organic compounds, such as cholesterol derivatives, usually these compounds have elongated molecules (nematogens) without mirror symmetry (chiral molecules). Chiral nematic liquid crystals, showing a cholesteric phase, may also occur in mixtures of achiral nematic doped with active optical moieties (induced cholesteric systems).

1.1.4. Smectic phase

The smectic mesophase has a higher degree of order with respect to the previous mesophases, since the molecules in this phase have both orientational and positional order of the centers of mass. The mesophase has a layered structure in which there is a spatial periodicity along the perpendicular axis to the layers and in which the molecules are arranged with the major axes parallel to each other. Molecules are free to move in the single layer but are not able to move between layers, in fact, the interlayer forces are weaker than the intralayer ones and as a consequence the layers are able to slide

easily over one another and smectic sub-phases can be defined. The sub-phases are many, all characterized by different types of positional and orientational order degrees, some are briefly described below:

- *Smectic A*, the intralayer molecules are oriented parallel to the nematic director, the long axis of the molecules is perpendicular to the layer and the thickness of each layer is of the order of molecules' length;
- *Smectic C*, inside the planes the molecules are slightly inclined and there is an angle θ between the normal to the layer and the molecules' orientation;
- *Chiral smectic C* the molecules in each layer rotate by a certain angle with respect to those of the next layer, generating a helical macroscopic structure.

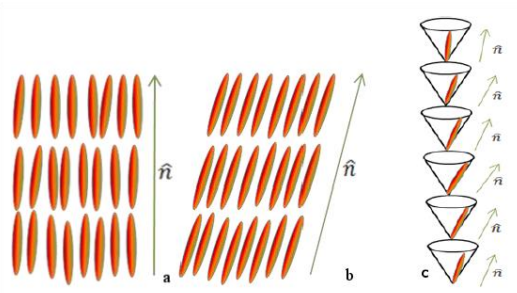

Figure 1. 5 Schematic representation of (a)Smectic A, (b) Smectic C, (c) Chiral Smectic C order

1.2.Properties of Liquid Crystals

1.2.1. The order parameter

In the study of LCs is the director $\hat{n}$ the key parameter that represents the average direction of the molecular axis (Fig. 1.6). The director is defined for a volume small enough to make meaningful talking about a molecular direction and large enough to contain a great number of molecules which make meaningful an average.

It is necessary to describe in a quantitative way this order parameter. The simplest type of objects that allows liquid crystal behaviour are rigid rods. We can describe the state of the rod's alignment with a distribution function, two assumptions are needed: the first is cylindrical symmetry (which means that there is a unique axis along which the properties of the phase display one set of values, and in all other directions perpendicular to this axis it exhibits another set of values) and the second one is to be non-polar ($\hat{n} = -\hat{n}$). The probability to find a molecule at a position r is described by the one-particle distribution function:

$$P\ (r, \Omega) \tag{1. 3}$$

where Ω is the solid angle that describes the orientation of the rod-like molecule using the three Eulerian angles shown in figure 1.6: the angle of rotation along the longitudinal molecular axis ψ, the angle of rotation in the azimuthal direction Φ, and the angle of the deviation of the longitudinal molecular axis from the director θ.

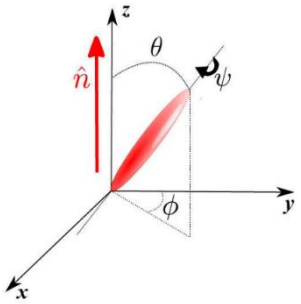

Figure 1. 6 Euler angles and alignment direction of an LC molecule

From the group theory the translational and orientational degrees of freedom can be treated separately, so the distribution function (equation 1.3) can be rewritten as,

$$P\ (r, \Omega)\ =\ P\ (r)\ x\ P\ (\Omega).$$

(1. 4)

For example, for the nematic phase where there isn't positional order, if ρ is the density, the distribution function can be written as

$$P\ (r, \Omega)\ =\ \rho\ P(\Omega)\ .$$

(1. 5)

Now consider the orientational distribution function f (Ω) and f (Ω) d Ω which gives the fraction of molecules with Euler angles φ and dφ, θ and dθ, ψ and dψ. In a uniaxial phase such as the nematic phase, since there is cylindrical symmetry, there is no order for the angles φ and ψ, so the only element with a degree of order is the angle θ. Then the orientational distribution function can be written as a f (θ) and, again for the symmetry we can write that f (θ) = f (π - θ). f (θ), as any symmetric axial function, can be expanded into a series of Legendre polynomials $P_i \cos\theta$:

$$f(\theta) = \left(\frac{1}{2}\right)[1 + a_1 P_1(\cos\theta) + a_2 P_2(\cos\theta) + a_3 P_3(\cos\theta) + a_4 P_4(\cos\theta) + \cdots]$$

(1. 6)

according to the following formula:

$$P(x) = \frac{1}{2^n n}\ \frac{d^n[(x^2-1)^n]}{dx^n}.$$

(1. 7)

To find the a_L coefficients into equation 1.6, it is necessary to multiply both sides by $P_L(\cos\theta)$ and integrate over θ, using the orthogonality, and finally it is possible to rewrite the orientational distribution function as

$$f(\theta) = \left(\frac{1}{2}\right)[1 + 3 < P_1(\cos\theta) > P_1(\cos\theta) + 5 < P_2(\cos\theta) > P_2(\cos\theta) + 7 < P_3(\cos\theta) > P_3(\cos\theta) + 9 < P_4(\cos\theta) > P_4(\cos\theta) + \ldots] .$$

(1. 8)

In the liquid crystal case, the polynomials depend on the angle θ, so x=cos θ, and cosθ is the projection of the molecular axis on the axis z.

In this way we have created a distribution function that contains all the information on the order status of a material, but instead of using a function it would be convenient to represent this order status as a number, an order parameter that assumed the value 0 for complete disorder, and 1 for perfect order.

Most LCs are uniaxial molecules with inversion centers where both directions of the director $\hat{n}$ (+ $\hat{n}$ and $-\hat{n}$) are equivalent, so we can avoid a description of a polar phase and only consider the even terms. The amplitude of each term of the series (1.8) can be considered as an order parameter, and it is possible to write:

$$f(\theta) = f(\cos\theta) = \sum_0^\infty \frac{1}{2}(4l+1) S_{2l} P_{2l}(cos\theta)$$

(1. 9)

and the coefficients

$$S_{2l} = < P_{2l}(cos\theta) > = \int_0^\pi P_{2l}(cos\theta)\, f(\theta)\, d(cos\theta)$$

(1. 10)

are the number we are looking for:

$S_0 \equiv 1$

$S_1 = < P_1(cos\,\theta) > \equiv < cos\,\theta >$

$S_2 = < P_2(cos\,\theta) > \equiv \frac{1}{2} < 3\cos^2\theta - 1 >$

. . .

(1. 11)

Among these coefficients in 1.11, we have to choose the one that best describes the liquid crystal structure, the first S_0 has a minor meaning because it is independent from the angle, the second S_1 is an odd function incompatible with the hypothesis of $\hat{n} = -\hat{n}$, so the next is the coefficient

$$S_2 = \frac{1}{2} < 3\cos^2\theta - 1 >$$

(1. 12)

which describe the quadrupolar order. This is the order parameter used to describe the order of the liquid crystalline phases.

1.2.2. Birefringence

The assumption of uniaxial symmetry for nematic LC, around the director leads to an anisotropy in many physical properties, which means that for example some properties such as viscosity, conductivity, refractive index, dielectric permittivity, magnetic susceptibility have a value in the parallel direction to the director while in all other perpendicular directions they exhibit another value. Anisotropy in the optical properties is particularly useful for applications.

When light passes through a nematic liquid crystal, it is divided into two components: one ray travels with the same velocity in every direction through the crystal, is termed ordinary ray (ordinary index n_o), the other ray travels with a velocity that is dependent upon the propagation direction within the crystal and is termed extraordinary ray (extraordinary index n_e). The phase separation between the ordinary and extraordinary ray increases with increasing the crystal thickness and it is related to its birefringence, a measure of the difference between the two indices:

$$B = \Delta n = |n_e - n_o| . \quad (1.13)$$

The refractive indices of a birefringent material can be represented using a mathematical tool the index ellipsoid (optical indicatrix) represented in figure 1.7.

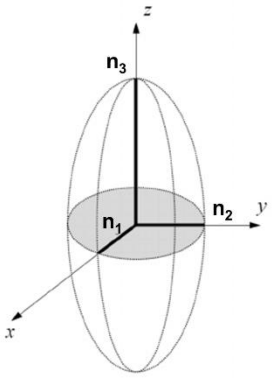

Figure 1. 7 Index ellipsoid

In Cartesian coordinates the index ellipsoid can be described by the following equation:

$$1 = \frac{x^2}{n_1^2} + \frac{y^2}{n_2^2} + \frac{z^2}{n_3^2} \quad (1.14)$$

where n_1, n_2, n_3 are the principal refractive index along the x, y, z axes respectively.

In uniaxial birefringent materials such as nematics, two of the three refractive indices are different from each other, $n_o = n_1 = n_2$ and $n_e = n_3$ where n_o and n_e are the ordinary and extraordinary indices respectively shown in the following figure.

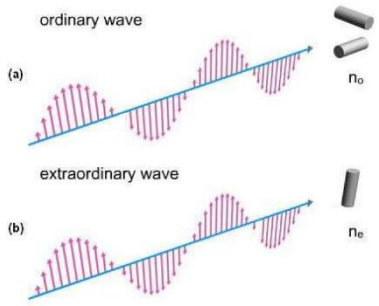

Figure 1. 8 Light propagation in liquid crystals along the normal to the optical axis (a) ordinary wave and along the optical axis (b) extraordinary wave

For nematic liquid crystals we can distinguish between materials with positive or negative birefringence. In particular, if $n_e > n_o$ the material has positive birefringence, otherwise the material has negative birefringence. The ellipsoid has a prolate shape if the birefringence is positive (Fig.1.9, a) and a oblate shape if it is negative (Fig.1.9, b).

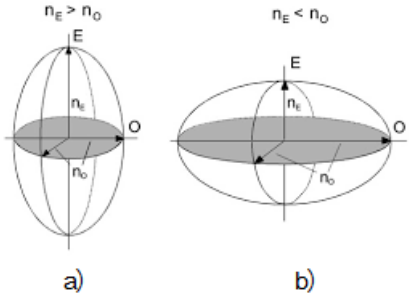

Figure 1. 9 Ellipsoid (a) elongated with positive birefringence, and (b) flattened with negative birefringence.

As previously described a cholesteric structure can be seen as composed by different planes where $\hat{n}$ rotates in the volume, we can define n_o and n_e as ordinary index and extraordinary index in each plane. In cholesteric liquid crystal optical anisotropy is negative, $n_{oh} > n_{eh}$ where $n_{eh} \equiv n \| h$ and $n_{oh} \equiv n \perp h$ (as shown in figure 1.10), the addition of the subscript h indicates that the macroscopic optical axis corresponds to the helix axis. The average refractive indices with respect to the helix axis can be written as:

$$n_{eh} = n_o$$

$$n_{oh} = \sqrt{n_e^2 + n_o^2} \quad . \tag{1. 15}$$

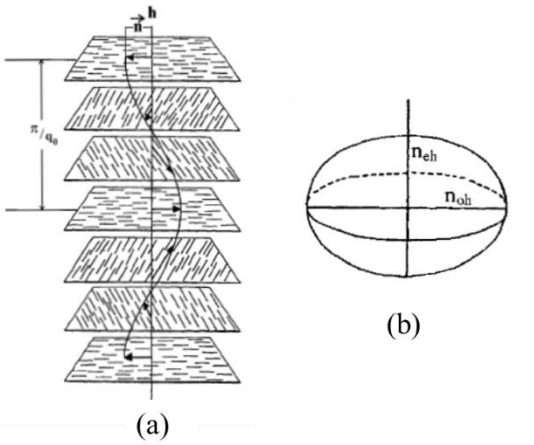

Figure 1. 10 The arrangement of (a) molecules and (b) the optical indicatrix in the cholesteric phase.[15]

To study the birefringence properties of liquid crystals, polarized light optical microscopy is used. In the following, we will examine how anisotropic crystals behave under polarized light. Figure 1.11 illustrates a sketch of a birefringent crystal placed between two crossed polarizers.

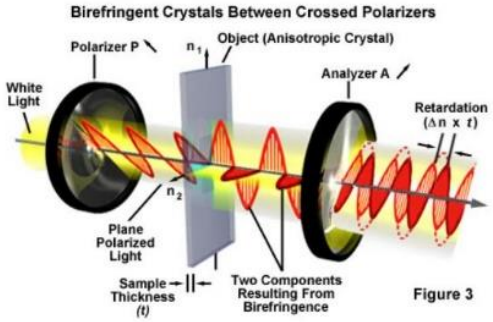

Figure 1. 11 Birefringent crystal between crossed polarizers[16]

White light entering the polarizer on the left is polarized with an orientation in the direction indicated by the arrow and is represented by a "red" sinusoidal light wave. Next, the polarized light enters the anisotropic crystal where it is refracted and divided into two separate components vibrating parallel to the crystallographic axes and perpendicular to each other. The polarized light waves then enter the analyzer which passes only those components of the light waves that are parallel to its polarization direction. When the ordinary and extraordinary rays emerge from the birefringent crystal, they are still vibrating at right angles with respect to one another. One wave is retarded with respect to the other, interference (either constructive or destructive) occurs between the two waves. The net result is that some birefringent samples acquire a spectrum of color when observed in white light through crossed polarizers. Color depends on phase shift, sample thickness and birefringence.

1.2.3. Anchoring

Liquid crystal molecules can take on different orientations if confined between two planar surfaces. The surface in contact with the liquid crystal at the microscale can be considered flat and $\hat{n}$ orientation close to it is determined by the polar (θ) and azimuth (Φ) angles. There are three main configurations for $\hat{n}$ nearby the substrate' surface:

- *planar alignment* where the polar angle is equal to 0°, $\hat{n}$ lies in the surface' plane. Here we can define two cases: one in which $\hat{n}$ is oriented uniformly on the surface and Φ remains fixed (*homogeneous planar orientation*) (Fig.1.12, a) and the other in which $\hat{n}$ is not oriented uniformly on the surface and Φ takes on different values in different points of the surface (*heterogeneous planar orientation*);
- *homeotropic alignment* where the polar angle is equal to 90° and $\hat{n}$ is orthogonal to the surface (Fig.1.12, b);
- *tilted* orientation where θ is fixed while Φ is arbitrary (Fig.1.12, c).

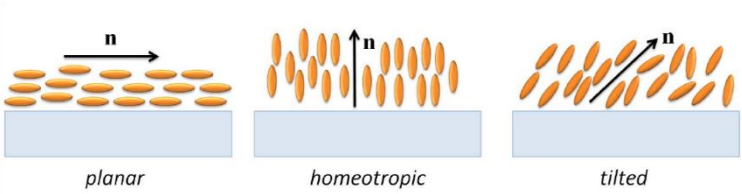

Figure 1. 12 Anchoring: (a) Planar, (b) Homeotropic, (c) Tilted

To align LCs, different techniques can be used as are the "rubbing" treatment and the chemical functionalization of the surface. In the first case a polymeric layer is deposited on the surface and a mechanical rubbing procedure is used to create microgrooves on the surface that are capable to align LC molecules.

1.2.4. The elastic free energy

A liquid crystal can be considered macroscopically as a continuous medium. and described as the sum of many small spatial regions characterized by a local director orientation. The free energy is then linked to the possible distortions of the director $\hat{n}$ in the volume: splay, twist and bend (Fig. 1.13).

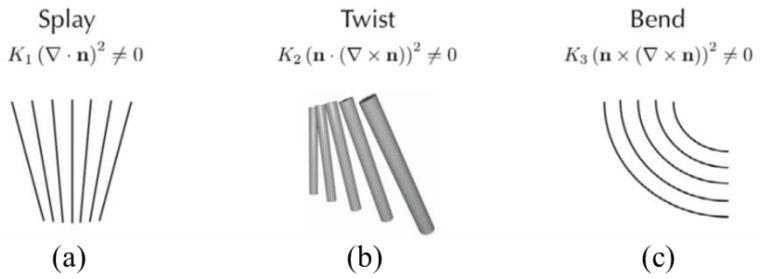

Figure 1. 13 (a)splay, (b) twist and (c) bend distorsions.

In splay and bend deformations, shown in figure 1.13 a, c, the director n̂ is always parallel to a given x-z plane and varies only as a function of z. In twist distortion, shown in Figure 1.13 b, the director $\hat{n}$ lies parallel to a given x-y plane, forming an angle ϕ (z) with the x axis which depends on the z coordinate only, this is also a one-dimensional deformation.

The free energy for a conventional nematic B (uniaxial non-polar) is

$$F_d = \frac{1}{2}\{K_1[\nabla \cdot \hat{n}]^2 + K_2[\hat{n} \cdot (\nabla \times \hat{n})]^2 + K_3[\hat{n} \times (\nabla \times \hat{n})]^2\} \quad (1.16)$$

where K_1 K_2 K_3 are the so-called Frank 'elastic constants and the elements of the sum are respectively associated with the three basic types of deformation:

$$K_1[\nabla \cdot \hat{n}]^2 \text{ conformations with } \nabla \cdot \hat{n} \neq 0 \text{ (splay)}$$
$$K_2[\hat{n} \cdot (\nabla \times \hat{n})]^2 \text{ conformations with } \hat{n} \cdot (\nabla \times \hat{n}) \neq 0 \text{ (twist)}$$
$$K_3[\hat{n} \times (\nabla \times \hat{n})]^2 \text{ conformations with } \hat{n} \times (\nabla \times \hat{n}) \neq 0 \text{ (bend)} \quad (1.17)$$

The equation assuming all three elastic constants equal $K_1 = K_2 = K_3$ =K can be simplified, and the free energy from equation 1.16 takes the form:

$$F_d = \frac{1}{2}K\{[\nabla \cdot \hat{n}]^2 + [(\nabla \times \hat{n})]^2\}. \quad (1.18)$$

For a cholesteric phase the free energy density expression must therefore be modified, extending the achiral twist term slightly to express the spontaneous twist:

$$F_{twist}^{Chol} = \frac{1}{2}K_2[\hat{n} \cdot (\nabla \times \hat{n}) + q_0]^2 \quad (1.19)$$

The added term $q_0 = \frac{2}{p_0}$ is the wave vector of the spontaneous cholesteric helix. If the tendency to twist is weak, q_0 is small and the term in equation 1.19 does not significantly affect the elastic energy density. For strong spontaneous twist, however, typically with the pitch on the same order as the wavelength of visible light or smaller, the added term in equation 1.19 can have a considerable impact.

1.3.Electric field effect

Many properties of liquid crystals can be influenced by the presence of external factors as electromagnetic and electric fields or temperature gradients. For practical applications, it is particularly interesting to study the behavior of liquid crystals in the presence of an electric field.

When an electric field $\bar{E}$ is applied to a liquid crystal, it becomes polarized by acquiring a dipole moment per unit of volume P (Polarization vector). The polarization is given by equation 1.20.

$$P_\alpha = \varepsilon_0 X_{\alpha\beta} E_\beta \tag{1. 20}$$

where $\varepsilon_0 = 8.854\ 10^{-12}$ F/m is the dielectric constant of vacuum, $X_{\alpha\beta}$ is the dimensionless tensor of dielectric susceptibility. Similarly, the electric induction vector D is:

$$D_\alpha = \varepsilon_{\alpha\beta}\varepsilon_0 E_\beta = \varepsilon_0\left(\delta_{\alpha\beta} + X_{\alpha\beta}\right) E_\beta \tag{1. 21}$$

$\varepsilon_{\alpha\beta}$ is the dielectric tensor (or relative dielectric constant).

If we choose an orthogonal Cartesian system with the z axis (α = 3) parallel to the director, the dielectric tensor in this system is diagonal and is schematically represented in the figure 1.14 and is given by the following equation

$$\overline{\overline{\varepsilon}} = \begin{vmatrix} \varepsilon_\perp & 0 & 0 \\ 0 & \varepsilon_\perp & 0 \\ 0 & 0 & \varepsilon_{//} \end{vmatrix} = \varepsilon_m \begin{vmatrix} 1 & 0 & 0 \\ 0 & 1 & 0 \\ 0 & 0 & 1 \end{vmatrix} + \frac{\Delta\varepsilon}{3} \begin{vmatrix} -1 & 0 & 0 \\ 0 & -1 & 0 \\ 0 & 0 & 2 \end{vmatrix} \tag{1. 22}$$

In equation 1.22, $\varepsilon_\perp$ and $\varepsilon_{||}$, respectively, indicate the dielectric constants measured perpendicularly and parallel to the director and represent the decomposition of the tensor in the isotropic and anisotropic part with zero trace where ε_m is the dielectric constant average equal to $\varepsilon_m = \frac{(\varepsilon_{//} + 2\varepsilon_\perp)}{3}$ and $\Delta\varepsilon$ is the dielectric anisotropy defined as $\Delta\varepsilon = \varepsilon_{//} - \varepsilon_\perp$. The dielectric anisotropy can have positive or negative values due to the values of $\varepsilon_{//}$, $\varepsilon_\perp$ and the dipole moment. The sign of $\Delta\varepsilon$ plays a fundamental role in the macroscopic behavior of LC.

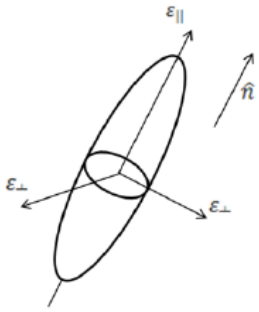

Figure 1. 14 Schematic representation of axes of the dielectric tensor in the nematic phase

The total polarization results from the sum of the deformation of the electronic clouds (*deformation polarization*) and the contribution due to the partial orientation of the permanent electric dipole moments in the direction of the electric field (*orientation polarization*). Deformation polarization is usually greater if the field is parallel to the long axis of the molecules and less in the opposite case. Therefore, the dielectric anisotropy due to deformation is $\Delta\varepsilon > 0$, for rod-shaped (calamitic) molecules while $\Delta\varepsilon < 0$ in the case of disk-shaped (discotic) molecules. The sign of the dielectric anisotropy due to the permanent dipoles orientation instead depends on the angle that the permanent dipole forms with the long axis of the molecule. Therefore, if the dipole is along the axis is positive while it is less than zero if the dipole is perpendicular or almost perpendicular to the axis[17] .

When an electric field applied to a liquid crystal if $\Delta\varepsilon$ is positive the dipole moment is aligned with the long axis of the molecule and the molecule will orient itself in the same direction as the electric field, if $\Delta\varepsilon$ is negative the dipole moment is perpendicular to the molecular axis and the molecules are aligned perpendicular to the applied field.

In a nematic liquid crystal with positive dielectric anisotropy in a cell with planar anchoring, if an orthogonal electric field is applied to the surfaces, the liquid crystal subjected to the electric field is distorted as shown in figure 1.15.

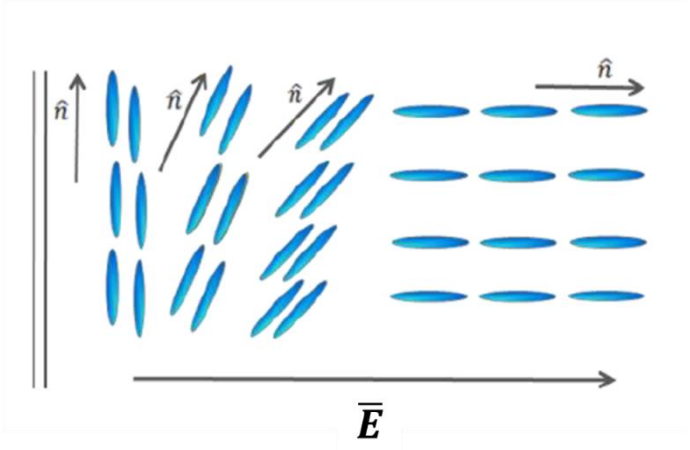

Figure 1. 15 Nematic director in an electric field

In the presence of the electric field there will be a contribution of the electric field to the free energy density of the liquid crystal which must be added to equation 1.16:

$$F_E = -\frac{\Delta\varepsilon}{8\pi}(\bar{E} \blacksquare \hat{n})^2 \qquad (1.\ 23)$$

1.3.1. Chiral liquid crystals in an electric field

In cholesteric liquid crystals, the effect of the electric field depends on several factors: the anchoring provided by the surfaces that confine the chiral mixture, the helix cholesteric pitch, the ratio between the sample thickness and the helix pitch, the frequency and intensity of the applied field. In CLCs when an electric field is applied, periodic structures arise due to counteraction between the electric field that tries to reorient the molecules and elastic forces of CLC that tends to maintain the original orientation[18], [19].

For example, let's consider a cholesteric mixture confined between two glasses covered with conductive material with the thickness of the cell larger than the helical pitch.

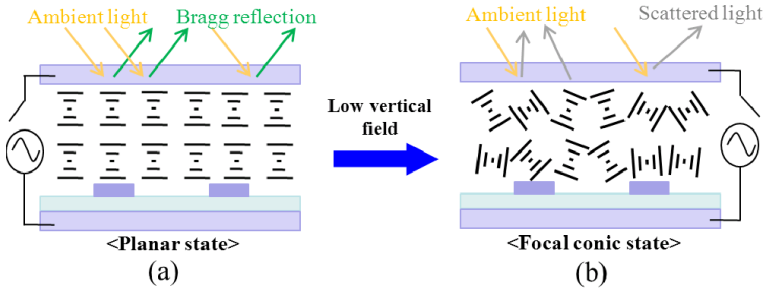

Figure 1. 16 CLC structure (a) without electric field and (b) with an electric field applied [20] .

Without an electric field there is a planar arrangement (Fig. 1.16 a), with the helices parallel to each other and arranged orthogonally to the surfaces. When the electric field is switched on the cholesteric helix pitch increases until the structure starts to deform and the cholesteric material is arranged in the so-called a focal conical texture (Fig.1.16 b). If the electric field is further increased, the cholesteric liquid crystal will orient homeotropically. When the electric field is switched off, the initial texture can be recovered from the focal conic texture but not from homeotropic one..

1.3.2. Low frequency phenomena

A liquid crystal immersed in an electric field can also be subject to other interactions in addition to purely dielectric one.

a) liquid crystals, even if pure, always have a certain amount of ionic impurities that causes it to behave like a weak electrolyte with electrical conductivities σ of the order of 10^{-10} $(\Omega\ cm)^{-1}$. Under a continuous electric field (dc), the charges can accumulate locally up to give rise to a local charge density ρ different from zero which interacts with the field giving rise to a force per unit volume equal to F =ρE which can originate complex hydrodynamic movements (*electrohydrodynamic effects*). These effects become negligible if the electric field is oscillating (ac) with a frequency higher than a few kilohertz. If the frequency of the field is

very large, the ionic charges do not have time to accumulate during a period of oscillation and the local charge is completely negligible;

b) if the orientation of the director in a nematic liquid crystal is not uniform in space, a polarization of the medium is created which depends on the spatial derivatives of the director even in the absence of an applied field (*flexoelectric polarization*)[21]. This effect also becomes negligible if the applied electric field is oscillating at a sufficiently high frequency (ν> 1 kHz).

Usually, effects a) and b) are present in nematic liquid crystals. In applications it is preferable to avoid such effects, for this reason ac field at sufficiently high frequencies (ν >> 1 kHz) are used. Under these conditions, the only important contribution remains the dielectric one. The oscillating term has no appreciable effect on the director's orientation and, from the dielectric point of view, the system behaves like a liquid crystal subjected to a constant electric field of intensity equal to the effective value $E_{ff} = \frac{E_0}{\sqrt{2}}$.

1.3.3. Textures and Topological defects in liquid crystals

The macroscopic texture of liquid crystals can be observed through polarized optical microscopy. As reported previously, depending on the confining surfaces liquid crystals orient differently and exhibit different optical textures according to the type of liquid crystal and the interactions with the surfaces.

1.3.3.1. Nematic Textures and defects

Nematic liquid crystals, when placed between two untreated surfaces, may have planar or planar degenerate anchoring.

In these cases, several textures have been observed and catalogued. *Schlieren texture* is observed when the molecules orientation is not homogeneous and the texture shows many colours. In figure 1.17, black lines corresponds to the points where the director is parallel to the analyzer or polarizer and converge into a singularity point which represents a topological defect in these textures.

Thread-like texture is also observed in liquid nematic crystals (Fig.1.17, b), defect lines, called *disclinations*, connect two defect points or form a closed line.

Marble texture is the most frequently observed texture in thin nematic liquid crystals samples, placed between two untreated surfaces (Fig1.17, c). The sample areas are very uniform, slight color changes are observed due to the variation of the director in the plane and out of the plane.

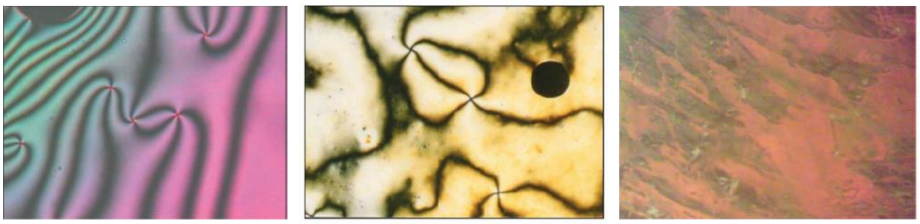

Figure 1. 17 a) Schlieren, b) Thread and c) Marble textures[22]

A force s is associated to singularities and it is equal to the number of lines(b) contained in a circumference drawn around the defect divided by 4:

$$s = \frac{b}{4} \tag{1. 24}$$

The s parameter can assume the following values s = ± 1/2 and s = ± 1. In a polarized light optical microscope, if the lines rotate in the same direction as the polarizer, s is positive, otherwise it is negative. The position of the singularity points is fixed while the black lines are in continuous motion, as there is a continuous local variation of the director. Singularities can be double or quadruple (Fig. 1.18 a, b).

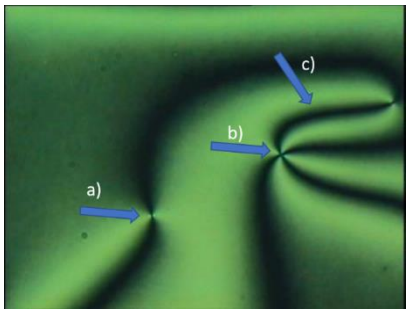

Figure 1. 18 Schlieren texture of the nematic phase, twofold and fourfold brushes are exhibited simultaneously within the same sample: a) double singularities, (b)quadruple and (c) defect lines.

In the close vicinity of a singularity the liquid crystalline order is reduced and the scalar order parameter decreases. The defects distribution is a dynamic characteristic. Defects of equal strength but opposite sign can cancel each other, leading to the formation of a uniform area without defects. Defects with different strength values, but of the same sign, can conjugate to form a new singularity whose strength is the sum of the forces of the individual defects.

1.3.3.2. Cholesteric Textures and defects

Cholesteric liquid crystal offer a variety of textures, some are shown in figure 1.19 where a, c, e and b, d, f are the director's orientation scheme and the polarized optical microscopy (POM) image

respectively. When a CLC is placed between two surfaces with the director anchored in planar condition and the cholesteric helix axis is oriented perpendicular to the glass plates the so-called *oily streaks* texture may be observed (figure 1.19 a, b). The structure can be seen as a network of defect lines dispersed in a uniform helical structure. The texture is influenced by the liquid crystal elasticity and by surface interactions.

Other types of textures observed in cholesterics are the *fan-like* texture observed in short-pitch cholesterics (p <1μm) and the *focal-conics* texture for a larger pitch (figure 1.19 c, d) with respect to the previous case.

Another type of texture is the *fan-shaped* one that has the helix axis inclined with respect to the substrate. If the helix pitch is increased, a *polygonal* texture appears (figure 1.19 e, f) the so-called fingerprint texture.

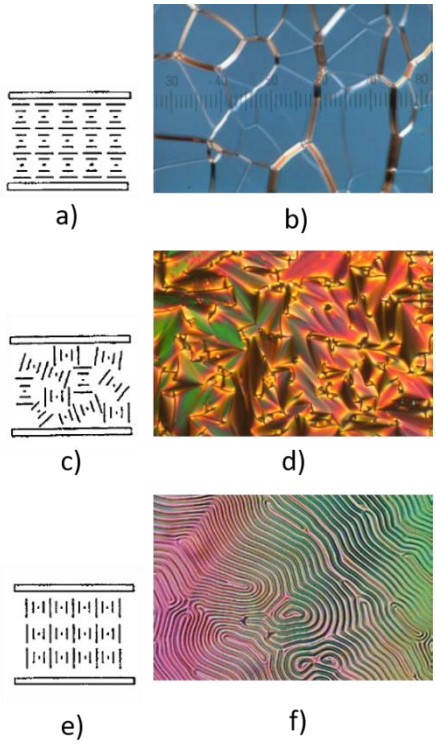

Figure 1. 19 Director's orientation scheme: (a) planar, (c) focal conic and fingerprint texture. POM images: (b) Oily streaks texture for a cholesteric liquid crystal sample under planar anchoring conditions with pitch P ≈ 2μm. (d) focal conic texture (f) Fingerprint texture of a cholesteric phase under homeotropic anchoring conditions, for the pitch P approaching the cell gap. [22]

In the fingerprint texture (figure 1.19 f), CLCs molecules are oriented perpendicular to the substrate plane and hence the axis of the helical superstructure lies in the substrate plane[23].

Also, in cholesteric texture defects may be observed including *dislocations* of the edges and "*pinches*" that are show in figure 1.20.

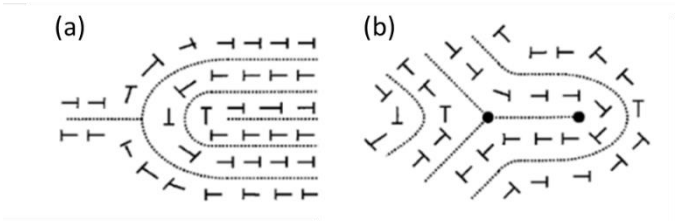

Figure 1. 20 Common defects that can be observed in cholesterics with polygonal texture: a) edge dislocation and b) pinches.

When a cholesteric liquid crystal is confined between two planar surfaces, with a suitable spacer, a uniform anchoring may be obtained. In this case the texture shows a uniform colour with all the cholesteric helices axes oriented perpendicular to the confinement surfaces, an example is shown in figure 1.21.

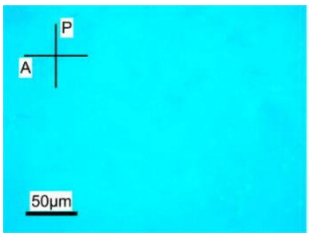

Figure 1. 21 CLC texture with uniform colour when the cholesteric helices axes are oriented perpendicular to the surface.

1.3.4. Confinement in curved geometries

Liquid crystals have different texture characteristics depending on the properties of the confinement surfaces. In section 1.1.4 we have presented the textures and defects obtained when the liquid crystal is confined between two planar surfaces. Here we describe what happens when liquid crystals are confined in a spherical geometry. This type of confinement is interesting because it is highly symmetrical. In this case textures and defects are influenced by various parameters i.e anchoring conditions, LC elastic properties, spheres dimensions and also external stimuli.

Liquid crystal microspheres can be easily obtained by dispersing the mesophase within an immiscible matrix [24]. Between the liquid crystal and the fluid matrix an interface is formed. To create the interface there is an energy cost and for this the liquid crystal phase tends to minimize the surface free energy by assuming a perfectly spherical shape. If the mixture is, then, vigorously shaken, a number of LC droplets is formed, obtaining a colloidal dispersion.

1.3.4.1. LC Colloidal Dispersions

As it is known colloidal dispersion is composed of solid, liquid or gas particles dispersed in a continuous phase (solid, liquid or gas). The term colloidal refers to particles with at least one

dimension ranging from 1nm to 1µm [25]. Among the colloidal dispersions we distinguish liquid-liquid dispersions, named *emulsions* and solid-liquid dispersions, named *suspensions*.

In dispersions particles interact with each other via attractive van der Waals forces that can destabilize the emulsion. Then, we can observe different phenomena: if the attractive interaction is not so intense particles will flocculate on the contrary for a strong interaction, particles might coalesce in big aggregates (Fig. 1.22, left). Depending on the particles density and dimensions they might migrate inside the emulsion (sedimentation or creaming) (Fig. 1.22, right). In order to stabilize dispersions electrolytes can be used to generate electrical double layer repulsive forces, or also polymers can be used to induce steric repulsion forces among particles. A fundamental role in the dispersion stability is also played by the viscosity of the fluid matrix which prevents coalescence.

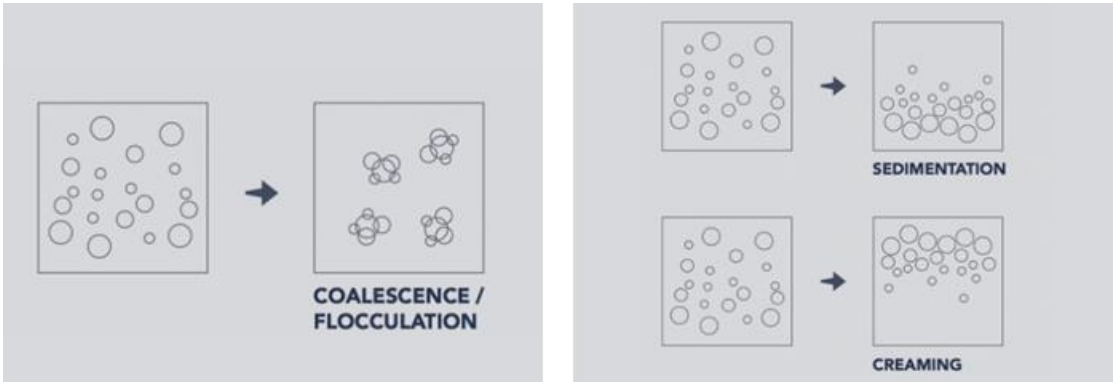

Figure 1. 22 Schematic representation of particles coalescence in big aggregates (left) and particles sedimentation and creaming on the right.[26]

The dispersion of liquid crystals microdroplets in a fluid matrix is an example of emulsion. An example of a colloidal suspension is represented by the dispersion of cellulose nanocrystals (CNCs) in water which will be discussed in detail in chapter 2.

1.3.4.2. Nematic liquid crystals microspheres

As mentioned at the beginning of this paragraph, several factors determine the type of textures observed in microspheres, among then, the anchoring conditions at the interface with the isotropic matrix and the microspheres' dimensions. In particular, the first one determines the boundary conditions of the director n̂ and fixes the topological constraints on the liquid crystal.

As in the case of LCs in cell even when the LCs is confined to a geometry there will be defects. In this case we must distinguish between *surface defects* [27] and *bulk defect* [28].

Bulk defects are called *hedgehogs* and carry an integer topological bulk charge of Q=±1 (figure 1.23).

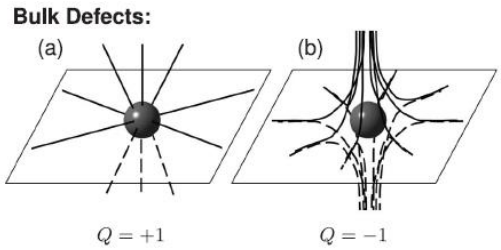

Figure 1. 23 Bulk defects (a) radial hedgehog defects with Q = +1 and (b) hyperbolic hedgehogs with Q = −1.[28]

Instead, surface defects are confined to interfaces and cannot exist freely in the bulk. They are characterized by a surface charge s, which is defined by the index of the director field projection onto the confining interface. In figure 1.24 some examples are shown:

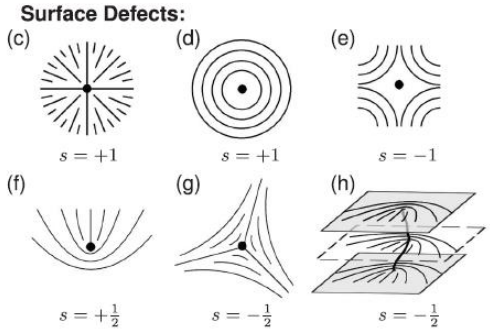

Figure 1. 24 Singular points confined to interfaces (c)–(g) and a disclination (h) in a nematic director field, with charge s which can be integer (c)–(e) or half integer(f)–(g). Half-integer surface defects induce defect lines(disclinations) in the bulk which connect two surface defects of similar sign (h).[27]

Surface defects with unity charge s=±1 are called *boojums* and they cannot move inside the nematic bulk and are restricted to the interface. Line' defect occur in the bulk and typically end at the surface and can be subdivided into wedge and twist types.

Recalling the free energy (equation 1.16) and the Frank' constants, K_1 K_2 and K_3, respectively associated with the three basic types of deformation splay, twist and bend, we can classify the different textures observed in microspheres as in the following.

- Nematic liquid crystals with planar anchoring conditions:
    - *bipolar* configuration (for $K_1 < K_3$). The microsphere has two defects point s = + 1 on the surface, which maximize their separation by aligning in the ends of the drop diameter. This configuration presents splay distortions near the defects and bend distortions in the rest of the drop. (Fig.1.25 a)

- *twisted bipolar* configuration (for $K_1 \geq K_2 + 0.431K_3$) is obtained by adding a twist to the bipolar drop described above. The structure has two boojums on the poles and the director's field on the surface creates an angle, α, relative to the axis that connect defects point (Fig.1.25 b).
- *concentric circles* configuration (if $K_1 < K_2 + 0.431\ K_3$, $K_1 > K_3$ and $K_2 < K_3$) with a defect line along the diameter of the drop. This structure is unstable.

- Nematic liquid crystals with homeotropic anchoring:
  - *radial drop* configuration is the most observed for splay-promoting nematics compared to bend distortion in which a pure splay is obtained with a hedgehog located in the center of the drop as shown in the figure 1.25 c.
  - *twisted radial drop* configuration is obtained by adding a twist to the radial drop described above (Fig.1.25 d)
  - In nematics that favour bend distortion with respect to splay distortion, the director organizes himself around a ring defect located on the surface of the drop along one of the two equatorial lines. In this case the director has cylindrical symmetry, and there is a defect line perpendicular to the director's privileged orientation (on the equator of the drop) (Fig.1.25, e).

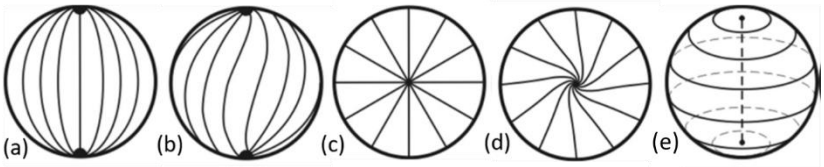

Figure 1. 25 Director configurations within nematic droplets, (a) bipolar, (b) twisted bipolar, (c) radial, (d) twisted radial and (f) toroidal structures.

As for planar geometries, applying an electric field to the microspheres it is possible to modify the director configuration. The configuration variation in a nematic microsphere depends also in this case on the dielectric anisotropy of the liquid crystal. For example if we consider a microsphere containing a nematic liquid crystal with positive dielectric anisotropy from a starting radial configuration (Fig.1.26 a) as the electric field increases, the director field progressively bends to orient parallel to the field as shown in (Fig.1.26 b), eventually leading to the formation of a defect in the plane perpendicular to the applied field, as shown in (Fig.1.26 c). If the electric field is further increased, the width of the defect decreases and eventually collapses into an equatorial disclination ring, as shown in (Fig.1.26 d) [27].

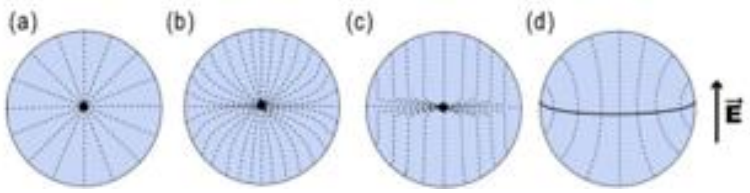

Figure 1. 26 Topological transformations induced by an electric field in a radial drop. When the dielectric anisotropy of the nematic is positive ($\Delta\varepsilon>0$), the radial drop, shown in a, undergoes the following transformations: as the electric field increases, the director field progressively bends to orientate parallel to the electric field, as shown in b, eventually leading to the formation of a defect in the plane perpendicular to the applied field, as shown in c. If the electric field is still increased, the width of the defect decreases and eventually collapses into an equatorial disclination ring, as shown in d , with perpendicular boundary conditions[27].

1.3.4.3. Cholesteric liquid crystals microsphere

More complex configurations arise when there are other liquid crystal phases involved (i.e cholesteric and smectic). In a cholesteric microsphere the director configuration is controlled by the anchoring conditions at the interface and by the twisting power *qR* (where R is the drop radius and *q* = 1/p), the possible configurations are the following:

- Cholesteric liquid crystals with planar anchoring[28]
    - bipolar twisted configuration observed with low twisting power (qR <1) (Fig. 1.27 a)
    - Frank-Pryce configuration observed with high twisting power (qR> 1), which shows a central hedgehog with a defect line s = + 2 of length R. In addition to radial defects, there are other defects such as disclinations or dislocations that are associated with the presence or absence of a chiral layer. These defects can be seen as a line that is the result of the concentric stacking of these nematic layers inside the drop, with each layer being slightly rotated relative to the other. The total topological charge must be +2 in each layer, so the defect line can be thought of as a linear stacking of defect points s = + 2 in each cholesteric layer. (Fig.1.27, d, e)

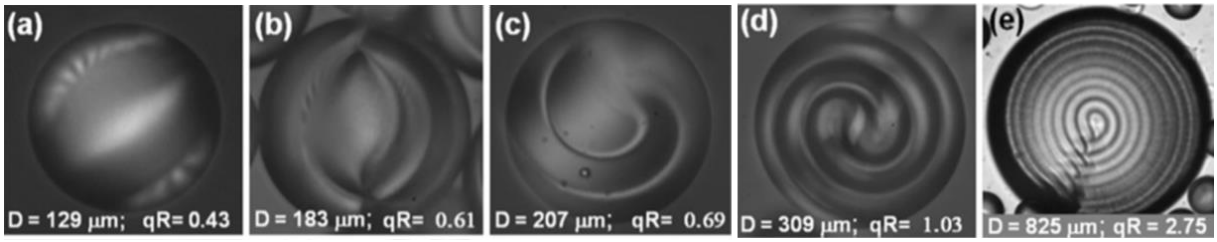

Figure 1. 27 Polarized light optical micrographs of cholesteric droplets with planar boundary conditions. The value of qR increases from (a)–(e). For low qR (a), a twisted bipolar texture is observed. As qR increases ((b)–(e)), the configuration evolves towards the Frank- Pryce structure (e).[28]

- For cholesteric droplets with homeotropic boundary conditions and high values of qR > 10, the conditions on the surface do not affect the packing of the helix. The textures in the droplets indicate that the Frank-Pryce structure prevails[27], [29] . For qR < 5 the appearance of an equatorial disclination ring is observed similar to the one presented in figure 1.27 d [29]. For smaller qR values, this ring relaxes to a surface point defect, which then for even smaller qR < 1 relocates to the center of the droplet, yielding to the radial structure frequently observed in nematic droplets [29] .

When a microsphere presenting a Frank-Pryce configuration is observed through a polarized light optical microscope the so-called *Maltese cross* is visible (Fig. 1.28) which is linked to the orientation of the liquid crystal molecules respect to the polarizer and the analyzer.

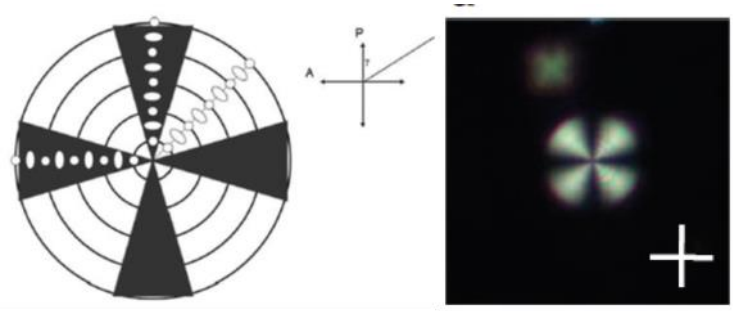

Figure 1. 28 Maltese cross between crossed polarizers, schematic representation (left) and observed under the optical microscope in polarized light (right).

The arms of the cross are visible as the light is not transmitted; in fact, along these two directions, the cholesteric liquid crystal molecules are perpendicular to the polarizer or to the analyzer. In all other directions, for the angles at which the molecules are not perpendicular to either the polarizer and the analyzer, the light is transmitted.

As for nematic microspheres an electric field is able to change the director configuration inside cholesteric microspheres. In the case of applied an electric field to cholesteric micro-drops the situation is more complex and nowadays there are few studies that are able to explain the existence of certain configurations. Orlova et al. in some works have shown that complex metastable topological structures may be obtained applying an electrical field on a CLC microdroplet. For example, if a 10-V_{rms} voltage at 2 kHz frequency is applied for a few minutes to a 250-μm-thick emulsion containing microspheres and, then the system is left to relax for 20 min, three different topological states are obtained (Fig. 1.29) [11].

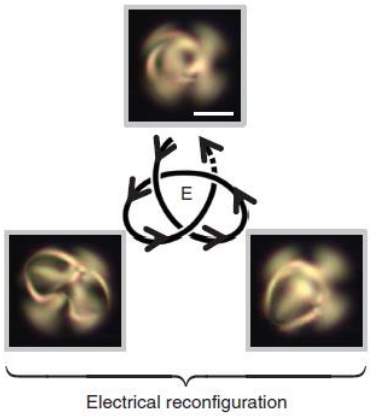

Figure 1. 29 Topological transformations under the application of electric fields for cholesteric droplets with perpendicular surface anchoring and pitch p=55 µm. All pictures correspond to XPOL imaging. droplet diameter d=67 µm, N=2.4. For each cycle, a 10-Vrms voltage at 2-kHz frequency is applied on the 250-µm-thick film in which the droplet is immersed, three distinct states are shown. Scale bars, 25 µm[11].

1.3.4.4. Texture variation and microsphere 'radius

When a liquid crystal is constrained by a spherical boundary, not only the anchoring conditions at the interface are fundamental to produce the configuration of the director but also the microsphere dimensions.

In an equilibrium condition, the total free energy of a microsphere can be separated into two contributions: a volume contribution (F_v) and a surface contribution (F_S), in a similar way to what is discussed in paragraph 1.1.2.4:

$$F = F_V + F_S = \int_V f\, dV + \int_S \sigma\, dS \qquad (1.\ 25)$$

In the first term, the integral is performed on the entire sphere volume and f is the free energy density of the liquid crystalline volume. In the second term S is the interface area and σ is the surface free energy per unit area. The description of the balance between volume and surface energies in a liquid crystal microsphere is complex, since the latter depends on the orientation of the director with respect to the surface. In this perspective, in a microsphere the director configuration is strongly influenced by its size (Fig. 1.30)[29]. There is a characteristic length called *extrapolation length (R_c)*, defined as the ratio between the elastic energy and the anchoring energy K/W [29]. The figure below shows nematic drops internal structure variation with an homeotropic and planar anchoring conditions vs microsphere's radius.

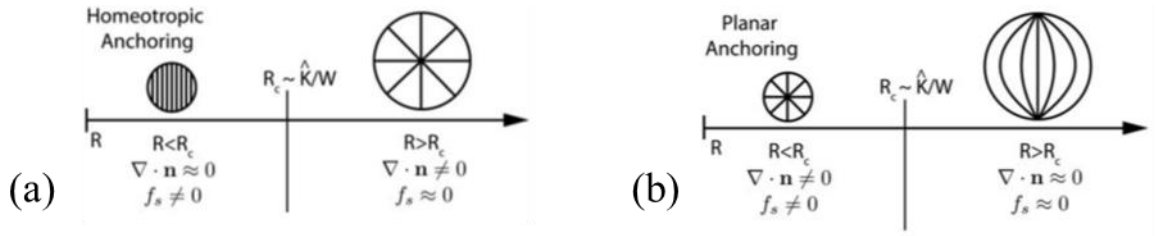

Figure 1. 30 Schematic representation of the director configuration in nematic droplets. For homeotropic boundary conditions (a), decreasing the drop radius R below a critical value Rc K/W induces a transition from a radial to a uniform director field for planar boundary conditions (b), a decrease of droplet size induces a transition from a bipolar configuration to a radial configuration [30].

If the microsphere 'radius is larger than R_c, in homeotropic boundary condition the drop will have a radial configuration with a defect in the center and with a splay-like distortion (Fig. 1.30 a, right). and for planar boundary conditions (Fig. 1.30 b, right) the drop will acquire a bipolar configuration. Instead, if the microsphere 'radius is smaller than R_c, in the homeotropic anchoring condition we will have a uniform director field (Fig. 1.30 a, left) and in planar anchoring conditions we will have a radial configuration (Fig. 1.30 b, left).

Decreasing the drop's radius, the anisotropic surface energy decreases more rapidly than the deformation energy and this implies that for the smallest drops it will be energetically favourable to modify the anchoring to the surface. In very small droplets, with radius of the order of tens microns [31] , there is a uniform orientation of the director as in figure 1.30 a, left, for such small droplet size, the energy cost for disregarding the anchoring conditions is smaller than the energy gain from decreasing the elastic energy density in the bulk.

Also, for cholesteric liquid crystals the director configuration depends on the size of the microspheres. By varying the droplets size versus the cholesteric pitch [9] for a cholesteric microsphere with planar anchoring conditions the configuration progressively changes from a twisted bipolar to a Frank-Pryce configuration, as shown in the following figure:

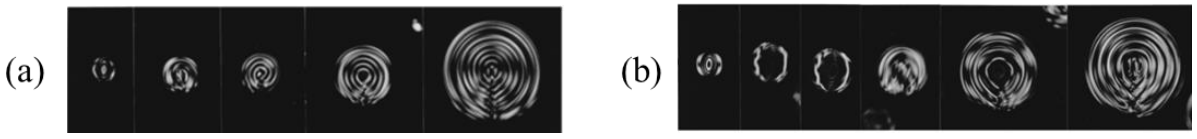

Figure 1. 31 Cholesteric drop with a pitch of (a) p=7,4µm and the radii vary from 8.2 to 31.4 µm (from left to right), and (b) p=17,7 µm and the radii of the droplets varies from 11.5 to 41.0 µm [9].

In figure 1.31, we can identify three regimes: the texture is twisted bipolar for p>R (low chirality); Frank-Pryce texture with a radial defect is observed for p<R (high chirality); and the third regime occurs when p<<R and the texture is still a Frank-Pryce one.

1.3.5. Nanoparticles doped liquid crystals

The possibility to disperse nanoparticles in liquid-crystalline matrices has generated a growing interest in the scientific community of condensed soft matter due to the many phenomena associated with the interaction between nanoparticles and soft matter. In particular, AuNPs are often cited as key materials and building blocks for the 21st century new materials in the context of emerging nanoscience and nanotechnologies. LCs are excellent candidates for matrix-guided self-assembly because the LC state combines order and mobility at the molecular (nanoscale) level and because the coupling of particles with the orientational order of the LC phase may give rise to hybrid materials with novel properties[32].

Metal NPs, especially gold nanoparticles (AuNPs) display unusual and unique size-dependent chemical and physical properties[33], their surface can be passivated in situ or via place-exchange reactions with a huge range of molecules. Spherical gold NPs have been widely used in association with LCs due to their well-controlled synthesis.[34].

In literature most of the studies deal with LC as templates for NP patterning, in some studies, the NPs are dispersed directly in a nematic phase, [35][36][37], in others the mesogens are directly grafted onto the NPs [38], [39] or the NPs have been synthesized in situ in the LC[40].

Investigations on self-assembly and self-organization in the chiral phases of LC are still rare and concern the study of interaction with metallic nanoparticles that can be organized in accordance with the helical structure of the CLC phase.

In their works Mitov and co-authors have shown that the NPs localized in regions that exhibited strong distortions in the molecular-director distribution [41], [42].and they self-assembled NPs into fingerprint patterns only close to the liquid crystal/air interface where the boundary conditions were homeotropic. Mitov et al. produced periodic ribbon-like assemblies of nanoparticles that could be fabricated by dispersing the particles in a cholesteric LC which presents a long-range helical structure (fig. 1.32) [41].

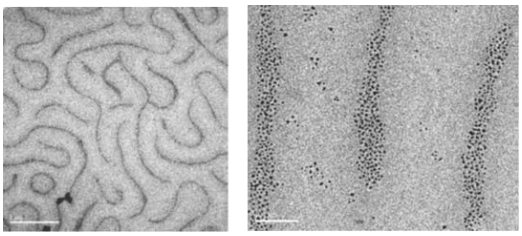

Figure 1. 32 TEM micrograph of cholesteric liquid crystal material doped with nanoparticles (1.5 wt.%). Particle assemblies are structured into ribbons which mimic the fingerprint texture, scale bar 1 μm (left). Nanoparticles inside ribbons are not aggregates. Scale bar: 100 nm (right) [41]

The causes of NP trapping in defects are complex and yet not well understood. On one hand, the formation of chains may be the result of a random process of diffusion and aggregation of NPs [43]. In nematics containing NPs, this process leads to the segregation of molecules into defects, but also leaves a significant fraction of molecules outside the defects in the form of aggregates[43] .In contrast, regions as wide as several micrometres between the defects appeared almost completely depleted of NPs, as if the NPs were attracted to the defects by a long-range interaction [44], [45].

Coursault et al. have demonstrated that defects can constitute efficient traps for NPs as small as 5 nm and in oily streaks, they can be precisely oriented along the directions of anisotropy imposed by the confining substrate[46].

Some studies show that the presence of nanoparticles and their aggregates has an effect on the electrical properties of the liquid crystal [47], [48]. Depending on the size of the nanoparticles and on the nature of the surface treatment, above a certain concentration NPs can introduce distortion in the alignment of the liquid crystals [35], [49]. The presence of nanoparticles and their aggregates plays an important role in the charge transport mechanisms in doped liquid crystal samples [50], [51]. Infusino et al. demonstrated that noble metal nanoparticles dispersed in chiral liquid crystal phases induce a modification of LC structural ordering accompanied by electric properties changes. They showed that cholesterol doped with NPs begins to feel the effect of the applied field at a much lower threshold value than pure cholesteric. Current measurements evidenced a threshold behavior: for low applied voltages nanoparticles inhibits impurities motion across the samples, while for higher voltages nanoparticles are able to participate to the charge motion mechanism [52] .

At present no studies on the effects of NPs presence inside microspheres when an electric field is applied are available.

1.4. Applications

Confining CLCs into unconventional geometries provides liquid crystals with peculiar properties that can be exploited to create new devices in the field of optics and photonics.

For example, Humar et al. demonstrated that CLC microdroplets could be used as tunable and omnidirectional microlaser [53]. The authors dispersed a dye doped CLC in a fluid matrix. The microdroplets exhibited omnidirectional lasing from the center of the drop when they were optically pumped, with the lasing wavelength depending upon the pitch of the CLC.

Gardiner et al. demonstrated that it is possible to create printable band edge lasers using dye-doped chiral nematic liquid crystals emulsified within a polymer matrix and deposited onto a rigid and flexible substrate[54]. When the aqueous film dried, the dispersed CLC droplets were observed to spontaneously align on the surface of the substrate without the help of any alignment layer and a laser emission occurred.

CLC droplets are used not only for laser application but also for sensing. Lee et al. demonstrated their use as biosensors [55]. Gia et al. showed the possibility to tune the laser emission from an emulsion of dye doped CLCs microdroplets dispersed in a glycerol matrix in presence of nitric acid molecules. Using a fluorescent dye with pH dependent optical properties (figure 1.33), the emitted laser wavelength could be tuned in a range of 60 nm as a function of the concentration of acid molecules inside the fluid matrix [56].

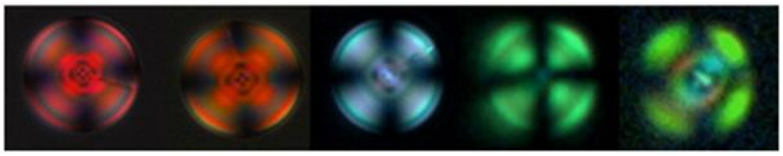

Figure 1. 33 Chiral microdroplets in presence of different nitric acid concentrations in a glycerol matrix. The concentration of acid molecules increases from left to right. [56]

1.5.Experimental part

1.5.1. Fingerprint like-textures

The first part of this section is devoted to the description of the experimental procedure developed to create a generator of random microfingerprints in the form of optical fingerprint-like textures obtained in chiral liquid crystal microspheres under the influence of a strong electric field. In the second part it is described the procedure developed to incorporate these micro textures in a macroscopic label that can be used as an anti-counterfeiting device.

1.5.1.1. Materials

Nematic liquid crystals HPC2170 (Δn =0.263, $\Delta\varepsilon > 0$) and HAE-625484 (Δn = 0.067, $\Delta\varepsilon > 0$) and chiral dopant S2011 (helical twisting power 10.3 μm^{-1}, figure 1.34, left) were purchased from HCCH, Jiansu HECCHNG Display Technology, China. Fluorescent dye Pyrromethene 650 was purchased from Exciton (figure 1.34, right).

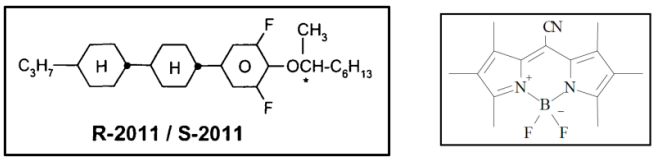

Figure 1. 34 Molecular structures: chiral dopant S2011 (left) and Pyrromethene 650 (right)

For the preparation of emulsions, as isotropic matrix Glycerol (Marco Viti, 85% w/w) was used. Gold nanoparticles (AuNPs) were prepared by dr. Rossella Grillo, Department of Physical Chemistry, University of Geneva. AuNPs were capped with dodecanethiol and dispersed in dichloromethane (DCM) suitable to be mixed in liquid crystals with a concentration of ~5.5E+13 particles/mL. AuNPs with a diameter of 5nm (AuNPs $_{d=5nm}$) were used. In figure 1.35 is reported the absorbance of a small amount of NPs before and after the capping procedure showing the absence of aggregates.

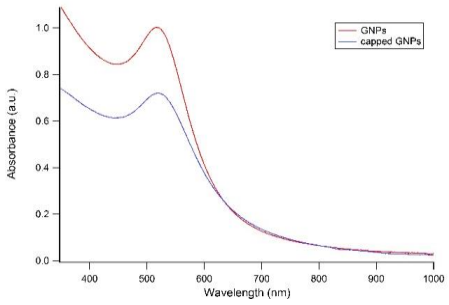

Figure 1. 35 UV-vis spectrum of gold nanoparticles with 5nm diameter before and after the capping procedure

1.5.1.2. Chiral Mixtures and emulsion preparation

A dye doped chiral liquid crystal (DD-CLC) mixture was prepared using the following concentrations in weight:

A. 99,6% (96% HPC2170 + 4% S2011) + 0,4% PM650 **mixture (A)**

The mixture was prepared first adding the chiral dopant to the nematic liquid crystal and stirring the blend in the isotropic phase at 90°C for 30 minutes, then the fluorescent dye was added and the blend mixed again. Nanoparticles were added to DD-CLC while in its isotropic phase stirring the blend at 90°C for 1 hour, then each mixture was sonicated for 10 minutes to avoid self-aggregation of nanoparticles. Several DD-CLC/NPs mixtures with different proportions in weight were studied in order to find the optimal concentration of NPs suitable for our goals. The best results were obtained with the following mixtures:

B. 100µl CLC **(A)** + 5 µl (DCM+ AuNPs $_{d=5nm}$) **mixture (B)**

C. 100µl CLC **(A)** + 10 µl (DCM+ AuNPs $_{d=5nm}$) **mixture (C)**

For the preparation of emulsions, a small amount (1%) of a DD-CLC/NPs mixture was added into a glass vial to a glycerol matrix at room temperature (Fig. 1.36, a). Then an emulsion was created, with a shaking process using a vortex mixer at 20Hz for 40s, at 40°C (Fig. 1.36, b). DD-CLC/NPs mixtures confined in an immiscible fluid matrix, will separate in form of droplets having spherical shape and diameters ranging from few to tens of microns [10 art FP]. To analyze the microdroplets' optical properties optical cells of appropriate thickness (usually 200µm) were prepared. The emulsion was filled by capillarity inside the cell and an electric field was applied using a high frequency alternating voltage generator (Agilent), coupled with an electric signal amplifier (Krohn-Hite 7500). Images of the microdroplets textures were acquired using a confocal laser scanning microscope (CLSM) TCS-SP8, Leica (Fig. 1.36, c, d). Data were analyzed using OriginPro 8 (OriginLab Corporation).

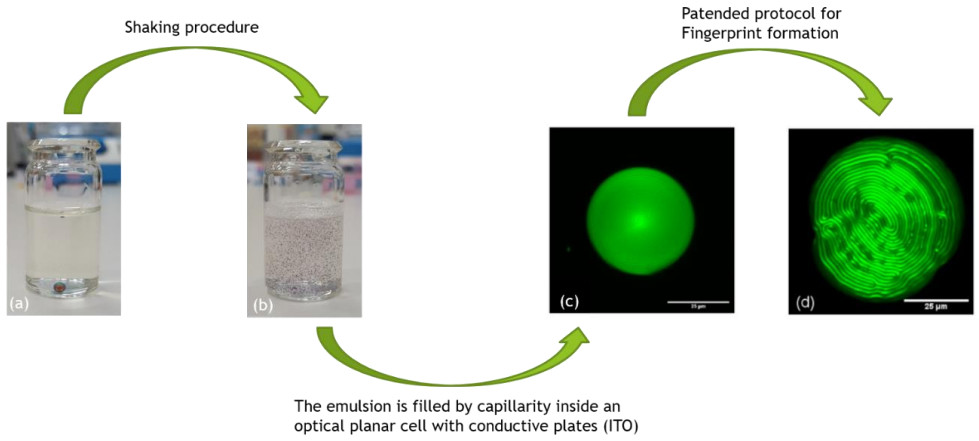

Figure 1. 36 (a) A millimetric drop of cholesteric liquid crystal in a glycerol matrix ; (b) Emulsion of micrometric cholesteric droplets obtained after a shaking procedure ; Confocal Laser Scanning

Microscope images of the same droplet (d≈50 μm) with no voltage applied (c) and with an applied voltage (d).

1.5.2. Experimental Results

The research group of Surfaces and Interfaces Laboratory at University of Calabria has patented a method to create spherical fingerprint-like textures using cholesteric liquid crystal microspheres doped with a fluorescent dye [57].. The peculiar optical texture is induced applying a high frequency voltage to the optical cell containing the micrometric objects able to distort the director molecular orientation. The obtained texture is transient and exists as long as the electric field is applied, nevertheless, it can be stabilized doping the chiral nematic liquid crystal with photosensitive materials. The most important aspect of this method is that each micro-object shows a unique fingerprint-like pattern that is fabricated in a completely random manner making this procedure suitable to generate physical unclonable functions keys to be used in high security anticounterfeiting devices. When the patented protocol is applied[57], it has been demonstrated that the texture starts to distort for an electric field at around 0.4V/μm and a frequency of 1MHz.

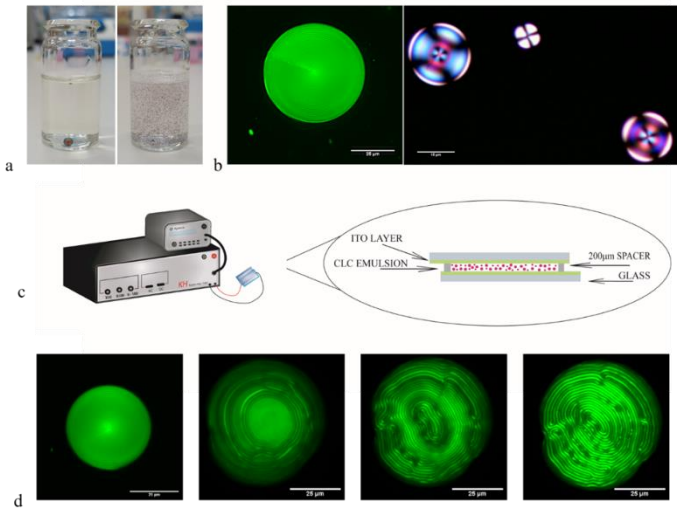

Figure 1. 37 Microfingerprint preparation. (a) Bottle containing a millimetric sphere of dye doped CLC immersed in a glycerol matrix and emulsion of micrometric chiral liquid crystal microdroplets obtained after a shaking procedure in a vortex mixer. (b) Single microsphere observed through CLSM and microspheres observed through a polarizing optical microscope between crossed polarizers. (c) Sketch of the experimental setup used to apply an oscillating electric field to the emulsion contained in an optical cell. (d) Fingerprint texture formation applying to the emulsion from left to right: 0V, 0.4 V/μm, 0.6 V/μm and 0.7 V/μm at 1MHz.

In figure 1.37,d is shown a CLSM image of a single droplet, with a radial texture when no voltage is applied to the cell. The texture starts to distort at around 0.4V/μm. Below this value of the applied voltage, the radial texture is completely recovered when the electric field is switched off. A

fingerprint-like texture appears at 0.6 V/µm applied to the cell and the texture stabilizes at 0.7V/µm. The fingerprint texture formation is not the only observable phenomenon, in fact, also a variation of the droplet shape is recorded. In general, for droplets with diameters between 40-70 µm, both distortion and fingerprint texture are observed at about the same voltages.

The fingerprint-like texture formation was studied varying the frequency and intensity of the applied voltage.

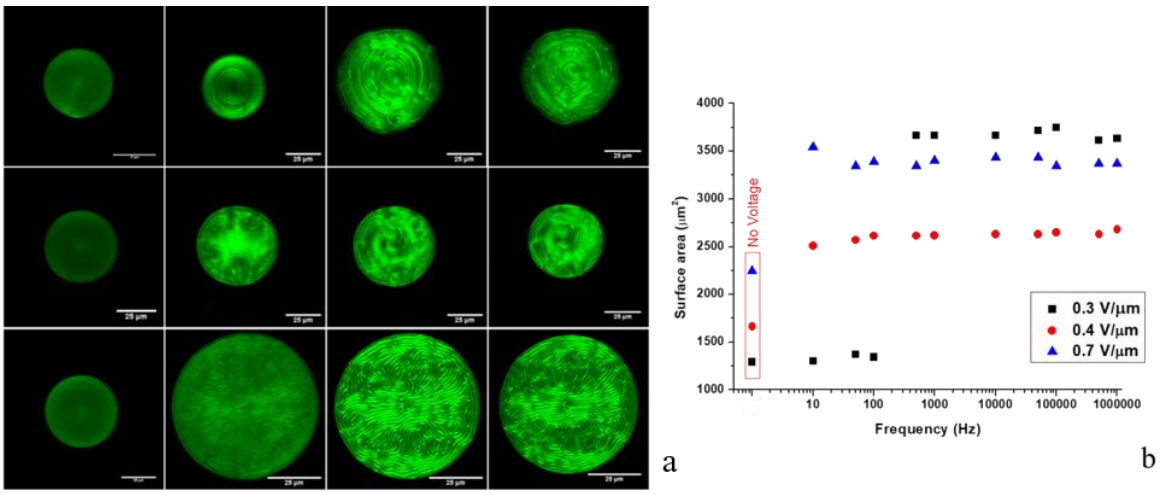

Figure 1. 38 Effects of the electric field intensity and frequency on the fingerprint texture. a) The first column refers to images acquired without applying an electric field to the droplets. Each row refers to a different intensity of the ac field: 0.3V/µm, 0.4V/µm and 0.7V/µm, showing the texture evolution observed increasing the frequency of the applied field: 50Hz, 100kHz and 1MHz. b) Imaged surface area as a function of the increasing frequency at three different applied voltages: 0.3V/µm (black squares), 0.4V/µm (red circles) and 0.7 V/µm (blue triangles).[71]

In Figure 1.38, a each row shows the deformation of a droplet when the field intensity is kept constant at 0.3V/µm (first row), 0.4V/µm (second row) and 0.7 V/µm (third row). The first column refers to the droplet when no field is applied to the cell, then, the frequency of the applied field is increased from 50Hz, to 100kHz and 1MHz that are the second, third and fourth column respectively. Applying a voltage of 0.3V/µm, the texture distortion is observed at 10Hz starting from the borders of the droplet while a structure that is in between the radial and the fingerprint one appears at 500Hz. At 0.4 V/µm, the texture is distorted at 10Hz, with the fingerprint structure appearing at the borders of the droplet and becoming more defined at 50Hz. The fingerprint covers the whole droplet area at 1kHz. At 0.7 V/µm, the texture is immediately distorted, with the fingerprint structure appearing well defined on the whole droplet area at 50kHz. Figure 1.38, b summarizes the above results reporting

the increase in the imaged surface area as a function of increasing frequencies for the three different voltages.

In order to reduce the intensity and frequency of the electric field applied to the optical cell necessary to obtain the fingerprint texture for application purposes and in an attempt to enrich the random optical texture obtained in microspheres, nanoparticles were added to the chiral mixtures. The same protocol described above was used, but using a liquid crystalline mixture doped with AuNPs.

In the following the experimental results obtained on the fingerprint texture formation in emulsions prepared using mixture B (Fig.1.39, top) and mixture C (Fig.1.39, bottom) are presented.

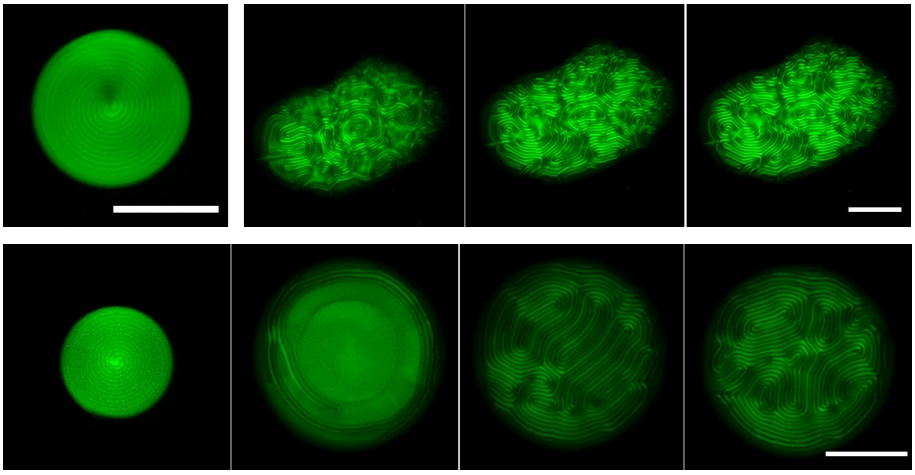

Figure 1. 39 Fingerprint texture formation applying to the emulsion containing: mixture B (from left to right) at 0V, 0.4 V/µm, 0.6 V/µm and 0.7 V/µm at 1MHz. scale bar 25µm (on top) and mixture C (from left to right) at 0V, 0.2 V/µm, 0.5 V/µm and 0.7 V/µm at 1MHz. scale bar 25µm.

Also, in this case a distortion and the fingerprint formation were recorded as expected and an increase in the droplets' size was observed, that leads to a reduction in its thickness.

In other words, since the droplet volume is fixed, an increase in the direction perpendicular to the electric field should lead to a shrinkage in the parallel direction. Then, the droplet is supposed to assume the form of an oblate spheroid. It is not trivial to understand this deformation. In 1971 Torza et al. developed a theory able to describe the deformation of a dielectric droplet immersed in a dielectric fluid under an alternating electric field.[18]. The author calculated the potentials inside and outside the as well as the electric stress at the interface. The electric stress generates a flow with associated hydrodynamic stresses. The sum of the electric and hydrodynamic stress determines the deformation of the drop: the total stress at the drop surface can be balanced by interfacial forces through a change in curvature of the interface. Then, the drop can assume an oblate or a prolate shape as a function of different parameters as dielectric constants, resistivities, viscosity and surface tension. In our case, both the presence of an anisotropic material inside droplets, that reorients due to the electric field, and the reduction in the drop thickness, that may reduce the volume contribution to the

total free energy, are able to destroy the Frank-Pryce texture and generate the fingerprint one. What was not observed in the case of emulsions not containing nanoparticles is that the droplet loses its circular shape and assumes also other forms as the “bean” one shown in figure 1.39 on top.

The size variation as a function of the applied voltage intensity was studied for emulsions containing mixture B and C and shown is in the following graph.

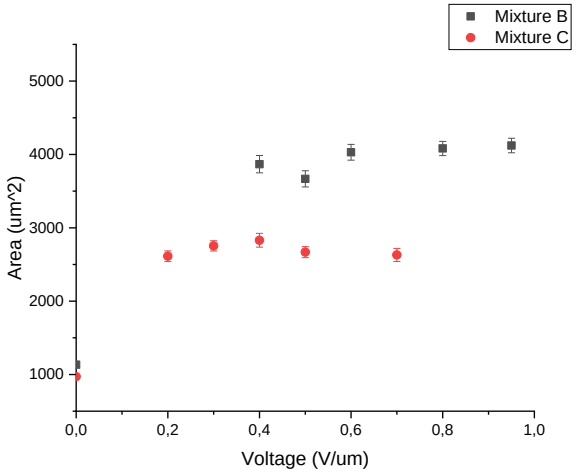

Figure 1. 40 Voltage vs droplet in-plane area for mixture B and mixture C

Measurements collected in figure 1.41 show that the droplets containing NPs in an electric field have a similar behaviour with respect to what is observed in mixtures not containing NPs, in terms of deformation and fingerprint texture formation. In this case, however, the presence of NPs affects the values of voltage intensity, about half the value recorded for mixtures not containing nanoparticles, for which both effects are observed. For microspheres containing mixture B no changes in the texture were visible for voltages lower than 0.2 V/μm, the fingerprint-like texture formation occurred at 0.4V/μm.

The addition of nanoparticles allows the formation of the fingerprint texture at lower voltages than the ones reported in the patented procedure. Repeated experiments have shown that the microspheres containing mixture B are the more stable and provide the most reproducible results. For this reason mixture B has been used for further measurements.

The size variation and fingerprint texture formation were studied varying frequency and intensity of the applied voltage using the emulsion containing mixture B. For frequency sweep measurement the voltage was fixed and the frequency increased slowly. Different droplets from the same emulsion were observed for each voltage. In figure 1.42 each column refers to a different intensity of the applied field and shows the deformation of a droplet when the field intensity is kept constant at 0.2V/μm (first column), 0.3V/μm (second column), 0.35 V/μm (third column) and 0.4 V/μm (fourth column) the

texture evolution is observed increasing the frequency of the applied field: 0Hz, 10Hz, 100Hz, 1kHz, 10kHz, 100kHz, 1MHz from top to bottom. The first row shows the textures of the droplets when no electric field is applied.

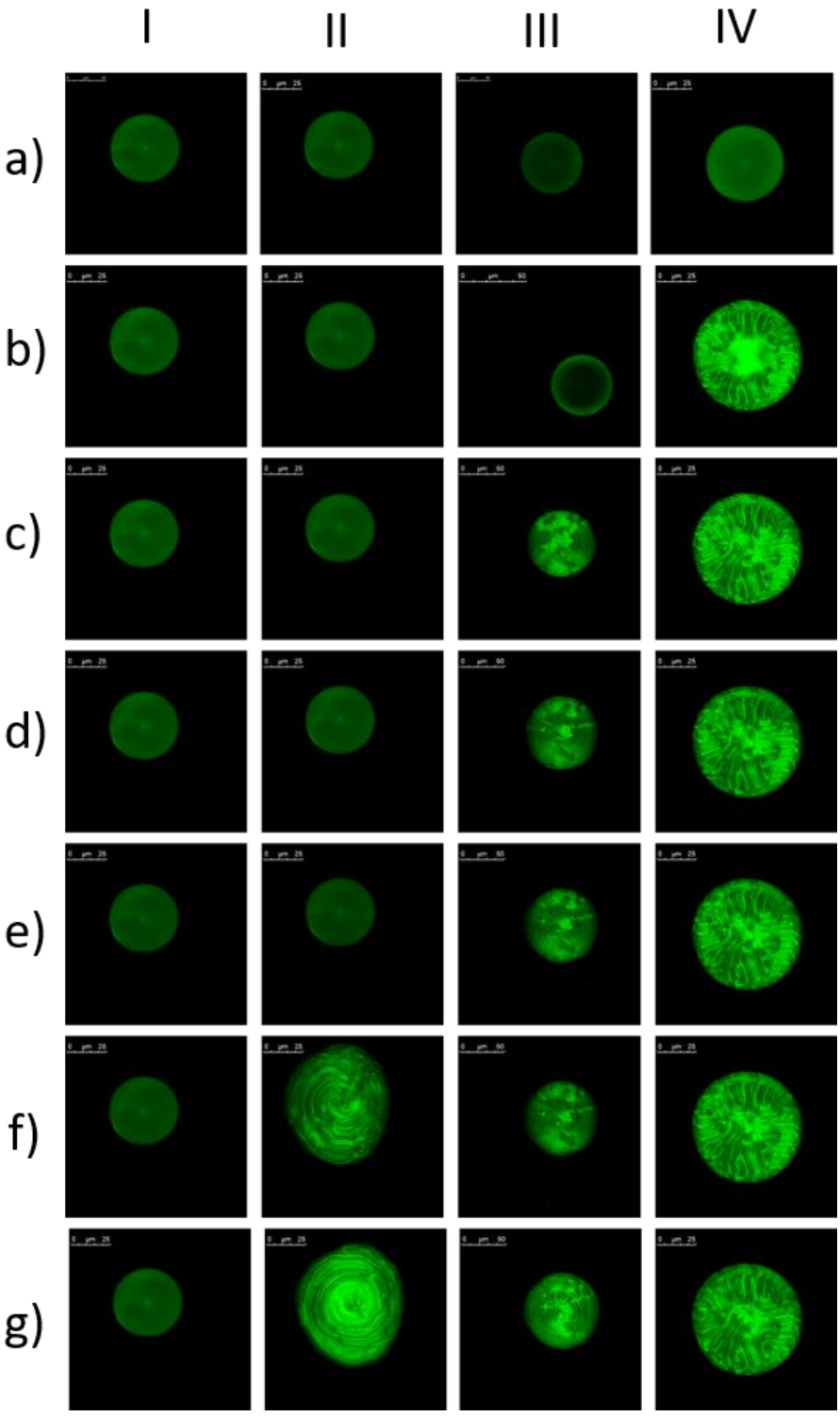

Figure 1. 41 Frequency sweep: each column refers to a different intensity of the ac field applied : 0.2V/um, 0,3 , 0,35, 0,4 are respectively I,II,III, IV , showing the texture evolution observed increasing the frequency of the applied field: 0Hz, 10Hz, 100Hz, 1kHz,10kHz, 100kHz, 1MHz from a to g.

As reported in figure 1.42, the presence of an electric field of 0.2 V/µm is not sufficient to induce the droplet deformation and, consequently, the fingerprint texture formation while for increasing frequencies both are triggered for intensity of the voltage larger than 0.3 V/µm. Also, in this case low intensity electric fields need higher frequencies to induce the fingerprint texture, that better develops when the droplet dimension increases dramatically.

In figure 1.43 is reported a graph of the drop imaged area as a function of the voltage frequency, it can be noted that at the frequency of 100kHz for voltage intensities larger of 0.3 V/µm the droplet deformation occurs and, then, fingerprint texture. It can also be observed that the increase of the droplet area could be dependent on precise values of frequency and intensity of the applied voltage but this aspect needs further investigations.

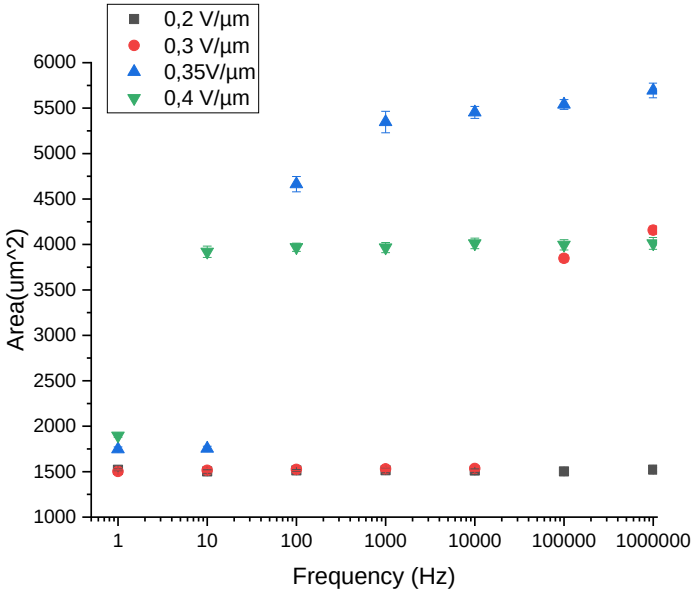

Figure 1. 42 Surface area as a function of the increasing frequency at four different applied voltages: 0.2V/µm (black squares), 0.3V/µm (red circles) ,0.35 V/µm (blue triangles) and 0.4 V/µm (green triangles).

In order to precisely fix the lowest values at which the fingerprint texture appears, frequency was fixed at 100kHz and the voltage was slowly increased from 0 to 0.4 V/µm with step of 0.01 V/µm. Figure 1.44 shows that the droplet deformation starts at 0.28V/µm and the fingerprint texture fully develops at 0.3V/µm confirming what we had already observed from the frequency sweep shown in figure 1.42.

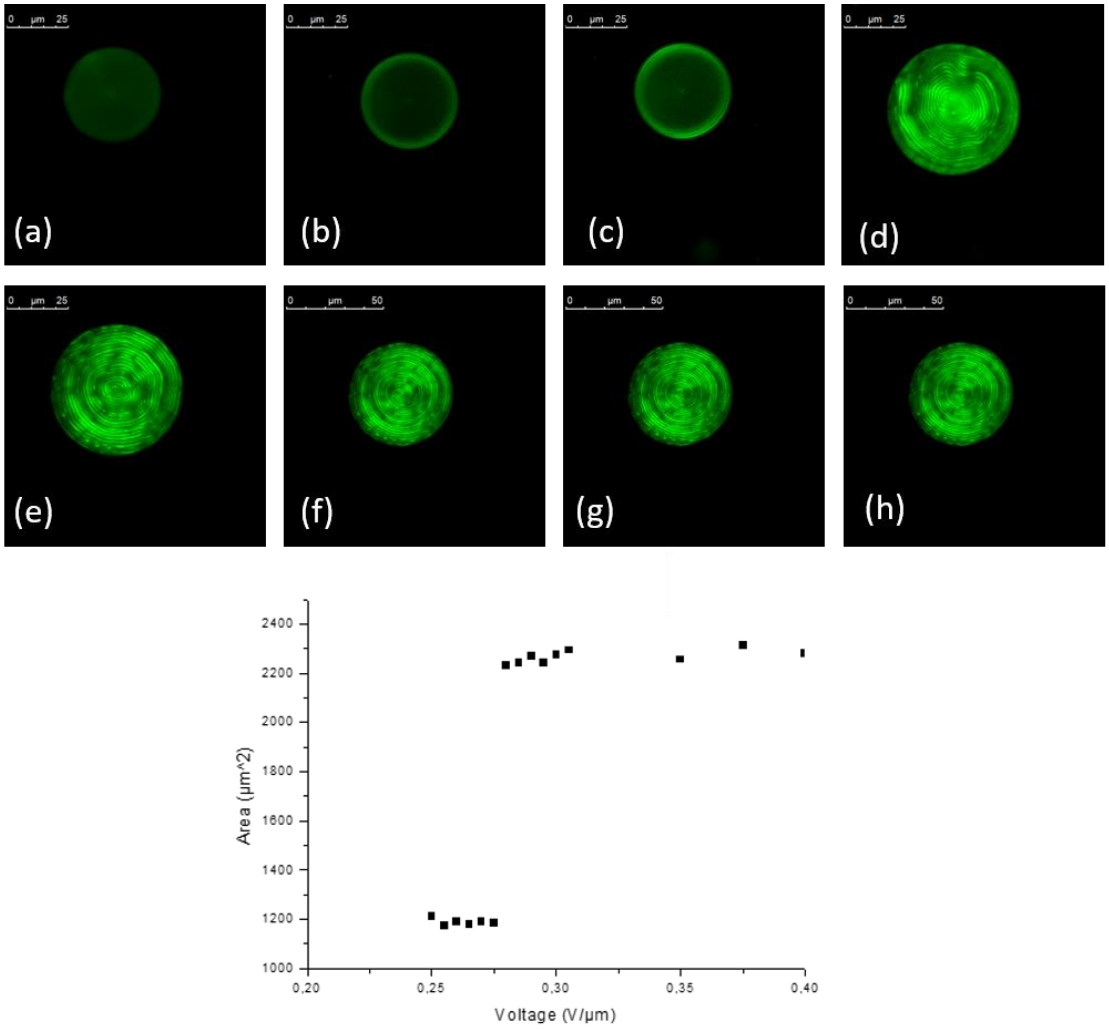

Figure 1. 43 From a to h 0- 0.25 - 0.275 – 0.28 – 0.3 – 0.35 – 0.375 – 0.4 V/um respectively(top). Surface area vs applied voltage at the fixed frequency of 100Hz(bottom).

In order to compare the results obtained on microdroplets containing mixture B with the starting mixture containing only liquid crystal the results are collected in tables 1.1 and 1.2.

Table 1. 1 Deformation and fingerprint formation voltage in a LC mixture vs a doped LC mixture with gold nanoparticles.

	Mixture LC	Mixture with $NPs_{d=5nm}$
Deformation	0.4 V/µm	(0.25-0.3) V/µm
Fingerprint Formation	(0.6-0.7) V/µm	(0.4-0.5) V/µm

Table 1. 2 Frequency sweep at fixed voltage in a liquid crystals mixture and a liquid crystals mixture doped with gold nanoparticles.

	Mixture LC	Mixture with $NPs_{d=5nm}$
0.2 V/µm	Data not available	Frank-Pryce texture
0.3 V/µm	Droplet deformation at 10Hz and fingerprint texture starts to form at 500Hz	Droplet deformation and fingerprint texture starts to form at 100kHz Fully developed fingeprint texture at 1MHz
0.4 V/µm	Droplet deformation at 10Hz fingerprint texture starts to form at 50Hz. Fully developed fingerprint texture at kMHz	Droplet deformation and fingerprint formation at 10Hz
0.7 V/µm	Droplet deformation and fingerprint texture starts to form at 10Hz. At 50kHz fingerprint complete	Data not available

As can be seen from table 1.1, there is a noticeable decrease in the voltage values at which deformation and fingerprint formation are observed in mixtures doped with NP compared to those containing only liquid crystals. From table 1.2 it can also be noticed that even at fixed voltages there is a decrease in the values of the frequency at which the fingerprint is formed.

This observation seems to confirm what reported in section 1.1.6. The presence of nanoparticles and eventually of aggregates may have an effect on the LC structural ordering and may cause a change in the electric properties of the system.

In this sense, it would be of fundamental importance to understand where the NPs position themselves inside the microdroplet before and during the application of the electric field and if aggregates are present. This question is partially answered and the preliminary results are shown in the following paragraph.

1.5.2.1. NPs position inside microdroplets

As we have already discussed in section 1.1.6 from the work carried out with NPs doped CLC in planar cells, it is evident that gold nanoparticles rearrange in cholesteric structures, especially along defects. It should be borne in mind that the causes of the entrapment of NPs in defects are complex and the texture decoration process is not well understood. We can hypothesize that similar processes occur also when the chiral liquid crystals is confined in a microsphere.

In order to visualize the areas in which gold nanoparticles position themselves within the CLC spheres, experiments were carried out using a SNOM microscope (Alpha 300S by WITec). The

design of the experimental procedure was not simple because the microscope had a short working distance that make the use of the standard optical cell impossible. Further, to localize NPs inside a microsphere they have to be labeled with a fluorescent marker. For this purpose, fluorescein coated gold NPs were specially synthesized by the group of Prof. Massimo La Deda at the Department of Chemistry of University of Calabria. As preliminary test an emulsion containing a cholesteric liquid crystal doped with these NPs was prepared and filled into an optical cell created using a common laboratory glass slide and a coverslip. The microscope used a wavelength of 500nm to excite the fluorescein contained in the sample. Both a scattering image (figure 1.45, left) and a fluorescence image (figure 1.45, right) of the same droplet were simultaneously acquired. In the scattering image, an aggregate of oval shape is visible at the centre of the droplet, while from the fluorescence image a maximum of signal is recorded at the centre of the microsphere. This allows us to infer that nanoparticle in a Frank-Pryce texture tend to aggregate and position themselves mainly at the centre of the droplet, where a defect is present.

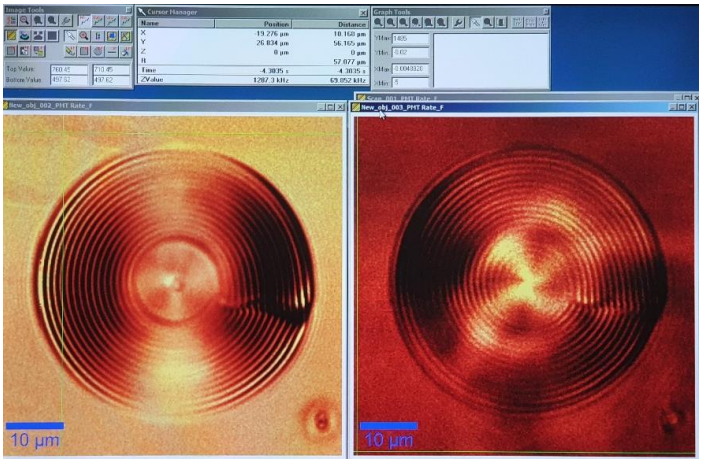

Figure 1. 44 Images were captured with a 100X objective. On the left the image acquired in scattering mode, on the right the image acquired in fluorescence mode.

Further, in the fluorescence image it is possible to distinguish the typical concentric circles structure of the Frank-Pryce texture, while in the scattering image they are not visible at the centre of the microsphere. This points to the fact that the amount of nanoparticles used is sufficient not to cause a loss of the cholesteric order inside the whole sphere but a reduction of the order may be possible at the center of the microsphere.

To investigate the effect due to an applied electric field a cell was prepared using an ITO covered glass coverslip. One electrode was soldered to the coverslip and the cell was filled with the emulsion. Unfortunately, due to the application of the electric field the optical cell heated around the point where the wire was attached causing the burning of the emulsion. An alternative way to prepare the optical cell is under investigation.

From the point of view of applications, the fluorescein signal is weak and further work must be done in order to find suitable nanomaterials able to provide a stronger signal that may enhance the visibility of the texture.

1.5.3. Anti-counterfeiting tags

1.5.3.1. Fingerprints generator

An optical cell may contain hundreds of microspheres, each one possessing its own unique fingerprint texture, created in a random way and impossible to reproduce. The use of nanoparticles allows to reduce the intensity and frequency of the electric field necessary to create the texture and has added also the possibility to create not circular microdroplets with a random shape. The whole procedure, then, can be seen as a way to produce random microscopic fingerprints, the embodiment of a PUF key. For a practical use of this fingerprint generator in an anticounterfeiting device, these random textures must be rescaled in a such way that they can be read and authenticated using state of the art technologies. For this purpose, each texture can be imaged with high resolution using a confocal microscope allowing to obtain a database of randomly generated fingerprints. Then, these pictures can be used to create macroscopic labels that can be printed with different techniques to create anticounterfeiting labels to be used to protect goods.

It is interesting to present at this point a quick survey of the fingerprint generators present on the market, most of them are algorithms able to provide a picture that mimic the characteristic of a human fingerprint.

Human fingerprints have a peculiar shape and are unique. A fingerprint is essentially composed of a set of wrinkles or groove lines (ridge lines), which flow mainly parallel to each other, creating a pattern (ridge pattern). Sometimes the ridge lines produce local macro-singularities, called whorls (or vortices, in which the lines form circularly around a central point of the finger), loops (the lines enter from one side of the finger, form a curve and exit the finger- side) and arch (lines enter from one side of the finger, form a curve, and exit from the other side of the finger).

Figure 1. 45 Fingerprint images where characteristic points called minutiae are highlighted[58]

Referring to figure 1.46, a series of micro-characteristics can be identified in fingerprints called minutiae, or Galton features and consist of singularities of the ridge lines.
The most common minutiae are described as follows:
- termination, the abrupt interruption of a ridge line;
- bifurcation, a single ridge line divides into two ridge lines (or even trifurcations if the division is into three ridge lines);
- lake, a single ridge line forks and the two ridge lines soon converge again in a single ridge line, forming a small ellipse;
- independent ridge, a ridge line showing a beginning and an end, usually short;
- island, a small ridge line that is not connected to other ridge lines;
- spur, a bifurcation leading to a short and a long ridge line;
- crossing or bridge, a small ridge line that joins two parallel ridge lines;
- delta: point where the ridge lines assume a triangular shape;
- core: it is the center of the fingerprint, where there may be an elbow curve or the end of a ridge.
Forensic science uses these minutiae to recognize an individual without ambiguity, through image processing software [57].

Nowadays, fingerprint is the biometric authentication parameter most used and widespread. Many studies have focused on their synthetic production and on new databases creation. In particular it has been shown that biometric authentication systems have significant drawbacks. The key shortcomings of biometric authentication technologies have to do with information security issues. In recent years it has been discovered that biometric data can be stored in a format that is easily accessible to attackers and due to the fragility of the databases that contain the information, it is very important to have more fingerprints available.
This is why several studies have been dedicated to the creation of synthetic fingerprint generators, from which to create a database that can be continuously implemented and always have new fingerprints available.
Previous work on the generation of synthetic fingerprints can be classified into two large groups: the first is based on the formulation of mathematical models to generate artificial fingerprints, one example is the Synthetic Fingerprint Generator (SFinGe) [59], while the second exploits various classes of deep learning models and an example is Synthetic Fingerprint Generation (SynFi)[60].
In general, the generation of a synthetic fingerprint four are main steps (fig. 1.47):

(i) fingerprint shape generation (where a fingerprint shape is randomly generated via specific geometric models defining the global shape of the fingerprint itself);

(ii) directional map generation produced through a ridge-flow mathematical model starting from the positions of cores and deltas;

(iii) density map is generation (creates a density map on the basis of some heuristic criteria inferred by the visual inspection of several real fingerprints);

(iv) ridge pattern generation where the first three maps are combined using a ridge-flow model and ridge-line pattern and minutiae are created through linear space-varying filtering;

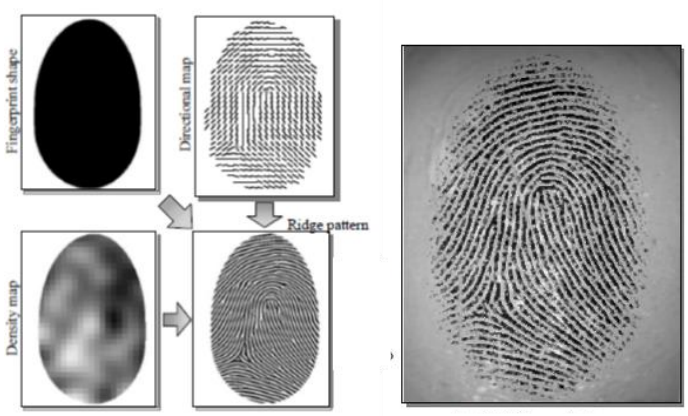

Figure 1. 46 Schematic representation of the four steps to create a synthetic fingerprint[61] (left) and a synthetic fingerprint image created with SFinGe approach (right).

In the systems based on mathematical models after the four-steps, noise is added to make the generated image more realistic but unfortunately, solutions based on this model suffer from the low level of entropy due to the rigorous structure of the generation process.

In contrast, the system that uses various classes of deep learning models like SynFi generates each fingerprint starting from a completely random noise.

SynFi fingerprint generation data flow involves two phases: the first based on a generative adversarial network [60]and the second based on super-resolution (SR) methodologies. In the first phase GANs method is used to estimate the probability distribution of real fingerprints and create a low-quality image out of a randomly generated texture. In the second phase, it uses a Super-Resolution (SR) model the low-quality image is transformed into a realistic high-resolution image with a more detailed texture (ridge endings, bifurcations).

SynFi is the newest approach to automatically generate high-fidelity synthetic fingerprints. It was demonstrated that this the methodology is the first to generate fingerprints that are computationally indistinguishable from real ones (Fig.1.48) unlike the previously proposed methodologies.

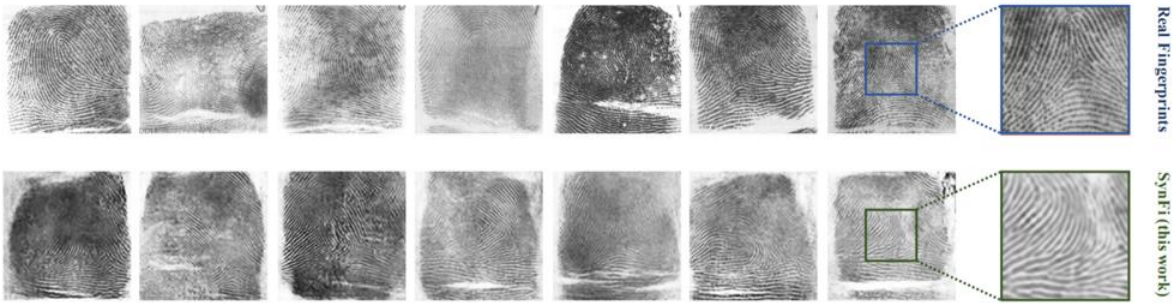

Figure 1. 47 Quality comparison between real and synthetic fingerprint samples. Top row: NIST dataset real fingerprint samples. Bottom row: Synthetic fingerprints generated by SYNFI.[60]

With respect to the synthetic fingerprints generated using algorithms, we propose optical artificial fingerprints created using a physical method.

The unique patterns are characterized, like human fingerprints, by numerous lines that run parallel to each other, creating local macro-singularities, in particular loops. Furthermore, they also show the characteristic singularities of core and delta and they also present a minutia: the bifurcation.

Due to these similarities can be authenticate using the same methods of recognition as real fingerprints.

In general, authentication methods involve the use of algorithms to improve the visualization of the fingerprint pattern, that is, to identify the ridges and grooves that characterize it. From the crests, for example, two types of minutiae can be extracted: the end points of the single ridge and the position and angular orientation of the bifurcation points. The detected minutiae are transformed into a binary matrix and compared with those contained in the database through cross-correlations. Although fingerprint detection technologies are reliable in 80% of cases, the strength of fingerprint weaving is its impressive encoding capacity.

Using our procedure to create fingerprints, the complexity of the pattern can be further enriched increasing the microspheres' diameter as well as reducing the spacing between the lines varying the chiral dopant concentration in the cholesteric liquid crystal mixture (Fig. 1.49). A collection of other fingerprints images is shown in Appendix A.

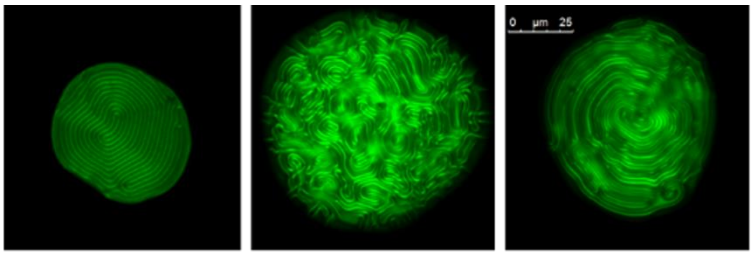

Figure 1. 48 Some fingerprints image produced with our methodology

Using Open Access programs and algorithms based on the extraction of minutiae for the recognition of fingerprints already available online, the image recognition process is easy to be implemented for our fingerprints. An example is shown below, where a CLSM image acquired of the artificial fingerprint was processed (fig. 1.50, a). First, image is converted into grey scale, binarized and segmented (skeletonized) in order to make the characteristics of the pattern immediately recognizable (fig. 1.50, b and c), then, minutiae can be extracted (fig. 1.50, c zoom).

Figure 1. 49 a) starting image acquired by confocal microscopy; b) binarized image; c) skeletonized image (where red points are the FP minutiae useful for the recognition)

At this point, a method to create labels incorporating the fingerprint image that could be easily read using a common device as, for example, a smartphone, is necessary. With this purpose, different techniques were used under the guidance of the engineers of BioAge company. The idea is to transpose the fingerprint image on an active label that could be switched on and off to maximize the brightness of the image to favour image recognition using electroluminescent inks. BioAge is a leading company in printed electronics, in the years it has produced software tools to establish the shape of resistors and capacitors to be printed on paper, plastic and textile. The company has developed an approach to design very large and complex printed electronic circuits, allowing the possibility to define several different layers, each of them linked to a particular electronic ink (for example: conductive ink, resistive ink, insulator ink, electrolyte ink).

BioAge has developed the technology to print RF antennas on textile substrates using only textile-like materials such as conductive fabrics and conductive threads. These antennas are one of the most important solutions for "energy harvesting", to capture and store energy coming from renewable energy sources and use it in low-power electronic devices (figure 1.51).

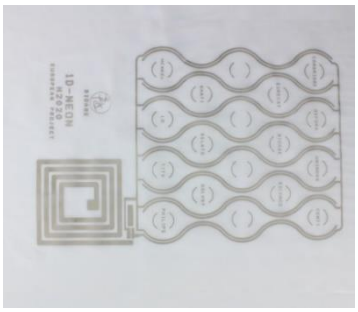

Figure 1. 50 RF Powered bright smart curtain developed by BioAge

They have also recently developed a prototype (designed by RFE) made on a PET substrate on which silver electrodes, used for the realization of electroluminescent displays and piezoresistive buttons, have been printed (figure 1.52).

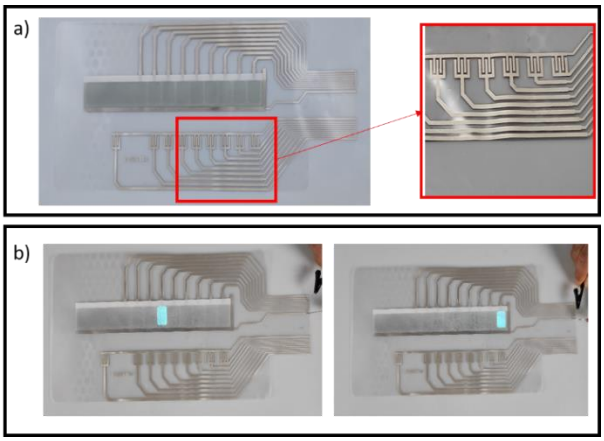

Figure 1. 51 a) Piezoelectric prototype (BioAge) with electroluminescent ink (left), a particular of the printed electrodes (right); b) pictures of the prototype during a functioning cycle.

The processes developed by BioAge were revisited in order to reproduce fingerprints on a flexible substrate using electroluminescent ink to enhance the visibility of the pattern.

In this type of device, a layer of electroluminescent material is sandwiched between two conductive layers. When current flows, the layer of electroluminescent material emits light. Several tests were carried out to identify the protocol to create the device.

The procedure that the company usually uses for the realization of electroluminescent displays, is based on the subsequent deposition of different layers: first, electrodes are printed, then the dielectric layer, the electroluminescent layer and finally the conductive ink. This procedure is not suitable for our labels since the goal is to have the fingerprint pattern image integrated in the label itself. The order of the deposited layers had to be reversed, starting from a substrate where the conductive layer was printed first, then the electroluminescent layer, the dielectric one and finally electrodes. In the normal procedure, inks are printed on the substrate and the last one is at the interface with air, in our case the fingerprint image is printed on a photographic film, in the following we will refer to it as

“fingerprint layer”, and used as substrate for the subsequent layer’s deposition. In the final device the fingerprint layer will be the top one. The techniques used for inks deposition are described in the following paragraph.

1.5.3.2. Printing techniques

Two techniques were considered as conductive ink printing techniques: Spray-coating and Screen Printing.

Spray coating is a well-known deposition technique widely used in graphic art and industrial coating [62] applications, allowing fast deposition of functional inks over both rigid and flexible large-area substrates (several cm) [63]. Spray-coating technique is very versatile and it consists in forcing a printing dispersion through an airbrush with a nozzle which spray paints of various types by nebulizing them with compressed air schematically represented in figure 1.53. The one used in this work (Iwata Hi-Line HP-TH) is equipped with a 0.50 mm nozzle with increased thread and a double action airbrush. This device has a unique control that allows to independently adjust the air flow and the amount of colour released, allowing great versatility to the operator. In this technique coating uniformity is due to different parameters, the most important are the inks’ viscosity and the distance between the nozzle and the substrate as short distances form thick and irregular films while too long distances will result in large materials waste.

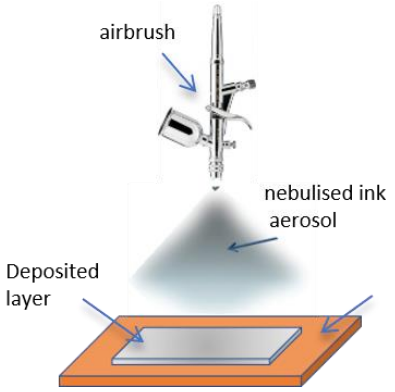

Figure 1. 52 Spray coating schematic representation: airbrush sprays the ink by nebulising it, ink is deposited in the form of a layer on the substrate.

.

The spray coating’ inks used were: Backplane (BP-B311), Dielectric (DE-B311), Lumigreen (LC-B311-GR), Conductive top coat (CTC-B311) purchased from LumiLor (figure 1.54).

Figure 1. 53 LumiLor inks: Conductive top coat, Lumigreen, Dielectric, Backplane (from left to right).

Screen printing or serigraphy is a mass-printing technology widely used for electronics[64], displays[65], and automotives [66]. It is a permeo-graphic printing technique that uses as a matrix a polyester fabric, a steel fabric or a nylon fabric, stretched on an aluminum, painted metal or wood panel defined as "screen printing framework". There are different types of "screen printing tissues" which are characterized not only by the material kind, but by its texture, by the thickness of the polyester threads and, moreover, by the number of threads per cm that characterizes the frame itself. The key advantages of screen printing over other printing technologies reliy on the compatibility with a wide variety of functional inks and substrates [67], [68] and on uniformity and thickness of the layers. Screen printing process is shown in figure 5, an image is printed on a substrate starting from one created on a screen using a photo emulsion, appropriately photopolymerized. A squeegee is used to move the ink through the screen, it gives a shear stress to the ink to reduce viscosity allowing it to flow through the screen so it will be deposited onto the substrate and the image from the screen will be printed on the substrate itself (fig. 1.55).

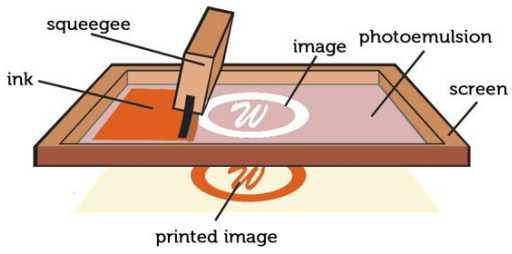

Figure 1. 54 Schematic representation of the screen-printing process.

Comparing the two techniques, screen printing has a significant advantage over spray coating due to the known thickness of the ink deposited. Indeed, the theoretical deposited ink thickness can be calculated, it is an approximate value used to help select the most appropriate mesh count for the printing application.

As previously seen in the figure 1.55 the ink is forced through the screen that is wire cloth, whose volume is determined by the mesh aperture (w) and the cloth thickness (D). Since stainless steel wire

cloth can be made with extremely thin wire diameters, it can deposit ink cubes with very small gaps between them. Therefore, the ink cubes have only a small distance to flow and form a uniform ink deposition as we can see in the centre part. In addition to the wire cloth, other factors as ink viscosity and surface characteristics influence the ultimate ink deposit. The theoretical deposit (V_{th}) can be calculated in cm^3 per m^2 of wire cloth using the following formula:

$$V_{th} = [W]^2 * D \quad (1.\ 26)$$

where W = w + d and w = mesh aperture (opening/microns), d = wire diameter (microns), D = cloth thickness (microns).

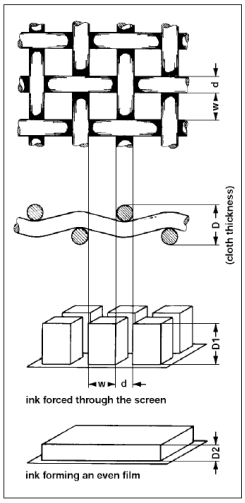

Figure 1. 55 Schematic representation of the wire cloth when mesh aperture (w), wire diameter (d), cloth thickness (D) are showed in the top part and related to the final ink volume deposition, with D2 height shown in the bottom picture.

Screen-printing inks used were: Conductive EL 7080, Ciano fluo dye EL 7002AC, Dielectric EL 7030D, Silver ink CP 6662 were purchased from Bectron®, which description, curing procedure and benefits are summarized in Table 1.3.

Table 1. 3 Screen printing inks characteristics

Product	Description	Curing	Benefit
Bectron ® EL 7080 TC	Transparent conductive ink	5min at 100°C	Paper and various films like PET and PC
Bectron ® EL 7002 AC	Active phosphor cyan ink	5m/min at >600mJ/cm² UVA	PEDOT, paper and various films like PET or PC
Bectron ® EL 7030 D	Dielectric ink	5m/min at >600mJ/cm² UVA	PEDOT, paper and various films like PET or PC
Bectron ® CP 6662	Conductive silver ink	10 min at 120°	Optimized for fine printing, very flexible, long screen open time, good adhesion to untreated and treated PET films, <0,010 Ω/sq/mil

For the curing process a UVA lamp was used, a Elmi B2-UV professional bromograph with 12 lamps of 20W each and an emission wavelength of 350nm.

A Maishi Monofilament Polyester Printing Mesh (Bolting Cloth) was used, mesh specifications are grouped in Table 1.4.

Table 1. 4 Mesh specification

Model	Mesh count (mesh/inch)	Aperture (micron)	Thread Diameter (micron)	Opening (%)	Thickness (micron)	Ink through volume theoretically (cm^3/ m^2)
77-55	190	81	55	30	88-97	26.6

1.5.3.3. Electroluminescent label

As underlined previously, the active label uses as substrate the "fingerprint layer". It was prepared using a confocal microscope image (figure 1.57, left), optimizing it for the printing procedure. The image was pixelated and processed using Photoshop applying the "Pixelate" filter and the "Error diffusion" filter. It was, then, converted into grayscale, and reconstructed with white and black dots depending on the grayscale as shown in figure 1.57, right. This procedure was necessary for the printing process.

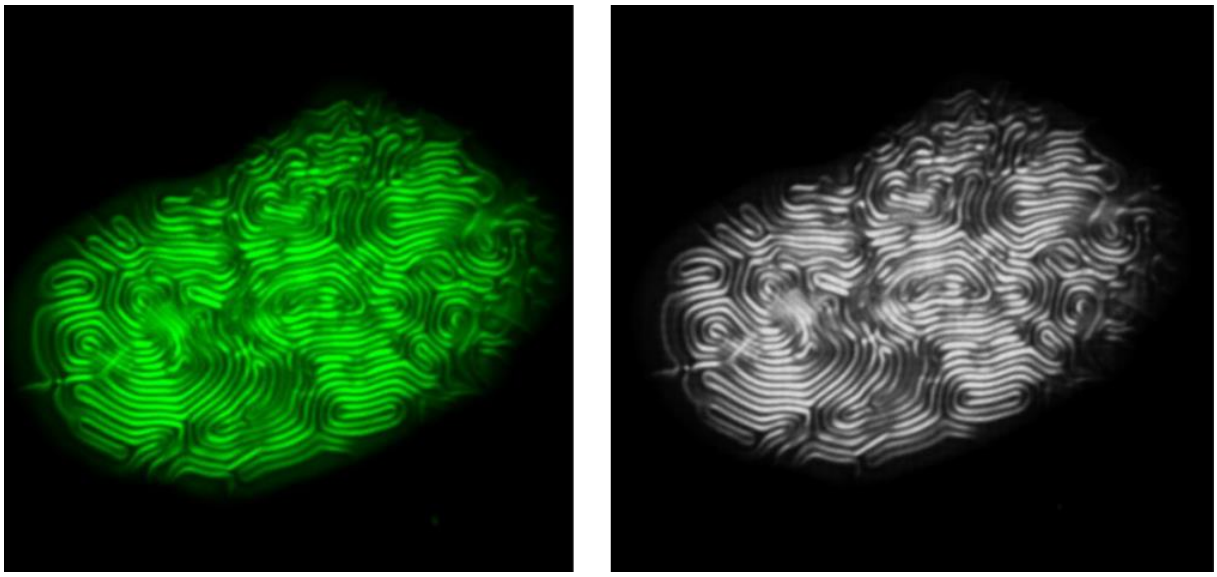

Figure 1. 56 Image acquired using a confocal microscope (left) and processed image (right)

The image was also resized (7cm x 7cm) and its resolution was increased to 1016 dpi. The final image was printed using a photoplotter (FP-8000/8000 XL) which impresses it on a film by means of a laser diode light. A photographic film DigiDot far red film (Alliance DigiDot HND) with a spectral sensitivity in the wavelength range of a HeNe laser and a red laserdiode (630-670nm) and emulsion coated on a 0.10 mm antistatic polyester base were used in this work.

During the substrate preparation procedure, a piece of the photosensitive film was placed into the photoplotter and the image shown in figure 6 was sent to print. There was also the possibility to print the negative image (with black and white values reversed) or the mirror image (i.e. the specular image). Once the image was printed, the image development was carried out using a developing liquid (G101c), a Graphic Black and White Rapid Access Developer for Graphic Art applications based on Hydrochinon and Phenidone developing agents in an alkaline environment. Finally, a fixing liquid (G333c), a Graphic Rapid Solid Fixer based on Ammonium Thiosulfate in an Acid solution was used to fix the image. For the photographic processing two containers with two mixtures were prepared: one with the developing liquid and water and the other with the fixing liquid and water, with volume ratio of 1: 2 and 1: 4 respectively. The film was taken from the photoplotter and immersed for 60 seconds in the developer container and immediately thereafter for 120 seconds in the container for the fixing. Then, the film was rinsed under a stream of water and left to dry. The final result is shown in figure 1.58.

Figure 1. 57 Fingerprint image printed on a photosensitive film

Once the “fingerprint layer” was ready, the different inks were deposed.

A schematic representation of the ink layers deposition is shown in figure 1.59. The same deposition order was used for both layer deposition techniques (spray-coating and screen-printing).

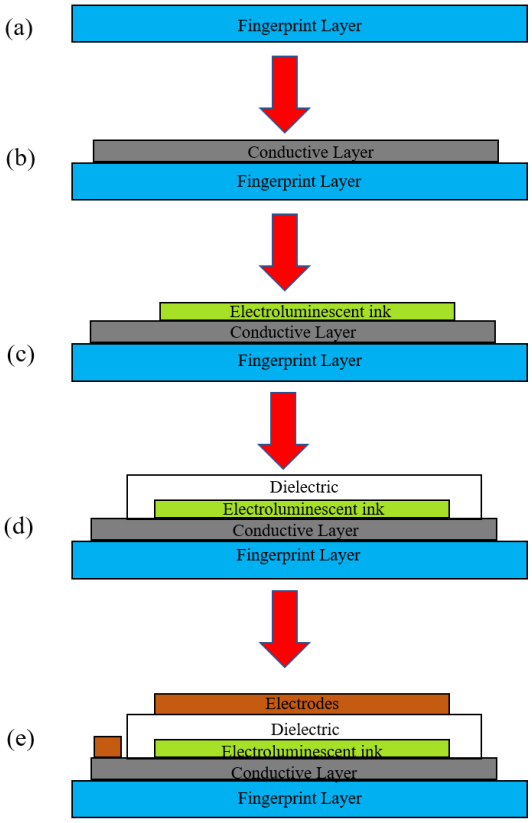

Figure 1. 58 Schematic representation of the layer by layer deposition.

- Spray coating

The layers of different materials were deposited by spray coating technique using an airbrush, at a pressure between 20-30psi, and a filter to avoid condensation coming from the compressor, in order avoid the presence of water droplets during the deposition. The construction steps are schematized and shown in figure 1.60. The first layer (Fig.1.60, a) of conductive material was deposited in subsequent steps moving the airbrush horizontally and vertically for 9 times, after each step the deposited material was left to dry. The second layer (Fig. 1.60 , b) was prepared using the electroluminescent ink in two steps, we checked qualitatively the deposition thickness using a UV lamp (Fig. 1.60, c). The third layer (Fig. 1.60, d) was made using dielectric material. Finally, the fourth layer (Fig. 1.60, e), the electrode, was prepared using the backplane material. Each layer was exposed to a flow of hot air at a temperature of 100 °C to be sure that the deposited layers were completely dry before proceeding with the subsequent depositions. In each step, masks were created to deposit the various materials in the appropriate areas (the masks were made using paper tape but for a large-scale reproducibility of the labels the creation of masks starting from CAD drawings would be the best choice).

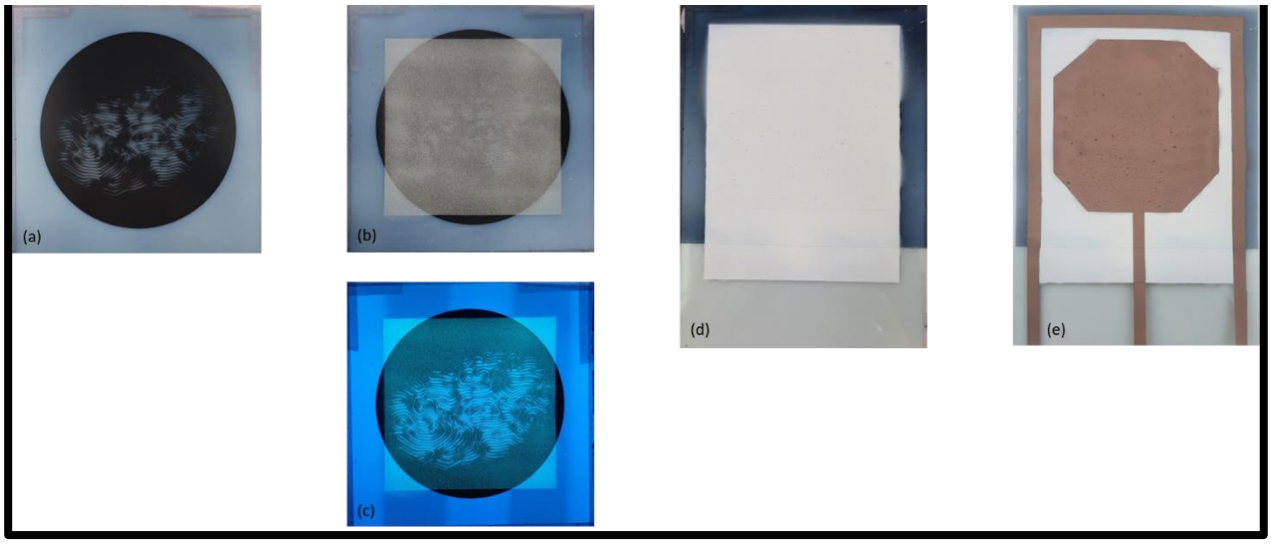

Figure 1. 59 Layer deposition with spray coating technique: conductive layer (a), layer with electroluminescent dye under normal light (b) and under UV light (c), (d) dielectric layer and (e) electrodes.

- Screen printing

Using the screen-printing technique each layer was deposited in a single step, followed by a curing process (Table 1.3). Since there was no image to print on the screen, it was sufficient to create a specific mask using paper tape on the screen (Fig.1.61) for each layer to be deposited to obtain the desired geometry.

Figure 1. 60 Masks on the screen

The first conductive layer (fig. 1.62,a) was deposited and then baked in the oven for 10 minutes at 100 ° C, before depositing the second layer. A test was made to ensure that the layer has a good conductivity. The second layer (fig. 1.62, b) was deposited and placed under a UV lamp to polymerize (two cycles of 999 seconds). The third layer (figure 1.62, c) was prepared using the dielectric material that was cured under a UV lamp, (5 cycles of 999 seconds) plus 10 minutes in an oven at 110 ° C.

The last layer (Fig. 1.62, d) was deposited and subsequently dried in the oven (2 cycles of 10 minutes at 110 ° C).

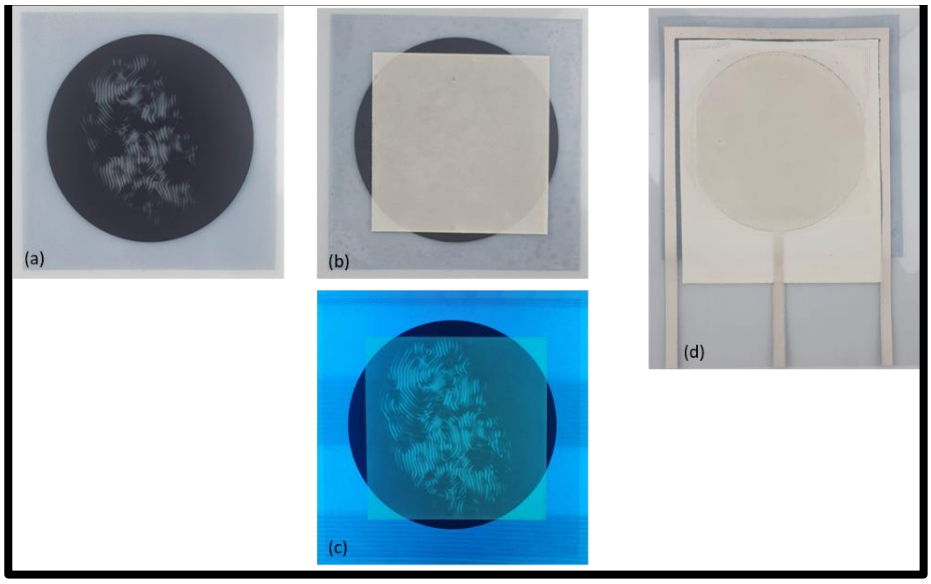

Figure 1. 61 Layer deposition with the screen-printing technique: conductive layer(a), layer with electroluminescent dye under normal light (b) and under UV light (c), dielectric layer and electrodes (d)

The layers obtained using both techniques were characterized in terms of thickness and homogeneity. Unfortunately, in both cases not all the layers were accessible for measurements due to the structure of the final device. Results related to thickness are reported in Table 1.5.

Table 1. 5 Layer's thickness

	Spray-coating	Screen-printing
Layer 1	2 µm	3 µm
Layer 3	17 µm	3 µm
Layer 4	3 µm	3 µm

As expected, the screen-printing technique provides a more homogeneous layer thicknesses since spray-coating depends much more on the operator skills compared to the screen-printing technique where the layer thickness depends on the frame used.

On a large-scale reproducibility both techniques are suitable but to have similar thickness for all the layers, screen-printing techniques must be used.

Using polarized light optical microscopy, the layers homogeneity was investigated (fig.1.63).

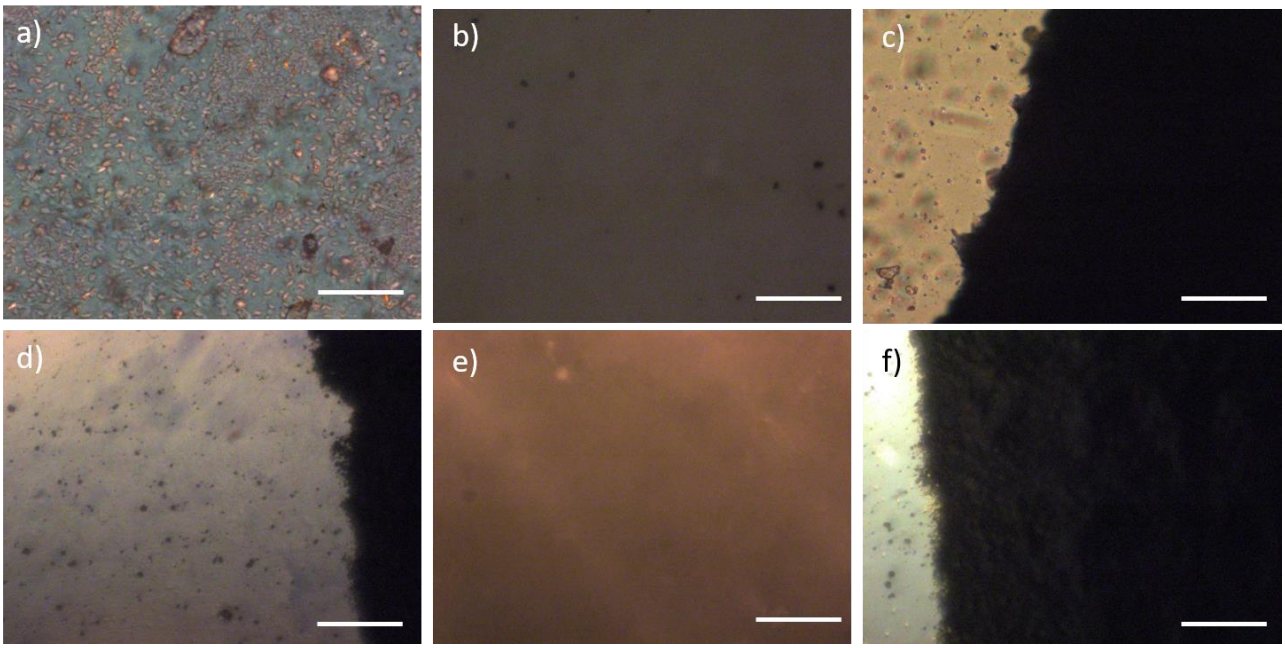

Figure 1. 62 Polarized light optical images of the layers. In the top row spray-coated inks layers and in the bottom row screen-printed layers: a) and d) conductive ink layer ; b) and e) dielectric ink layer; c) and f) blackplane ink layer (scale bar 100µm)

From optical images obtained with both techniques, the conductive layers are not uniform, on the contrary the dielectric and backplane layers are more homogeneous. This is not unexpected since the first inks are emulsions while the others are isotropic liquids.

Once the label is ready, it can be connected to a proper circuit (figure 1.64). The pattern is visualized with the "fingerprint layer" face up.

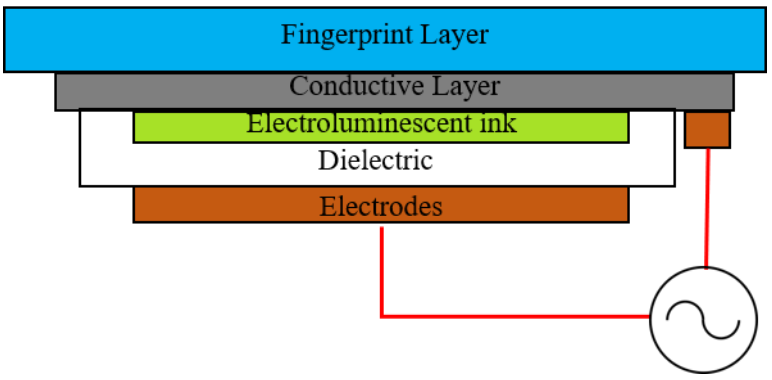

Figure 1. 63 Schematic representation of the electroluminescent label connected to a voltage generator.

To check the functioning of the electroluminescent label, an AC generator (Inverter - KPTA-0144-18) was connected to our system (V_{pp} = 400-600 V, f = 2-4 kHz). The results are shown in the

following images with the displays created with both techniques, photography is acquired with light switched on and off and with the AC generator switched off and on that will represent the OFF and ON state in the proposed device.

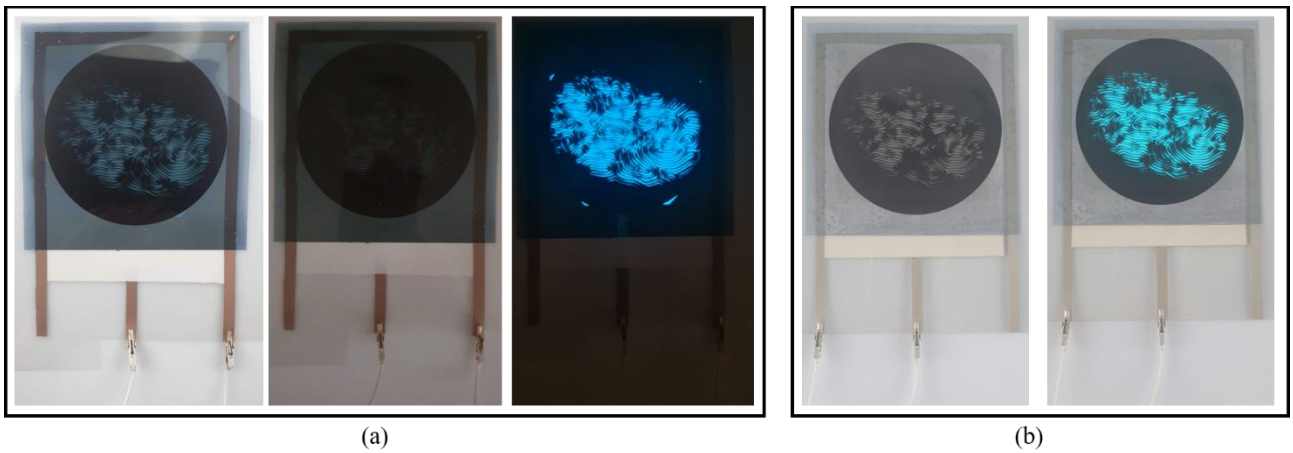

Figure 1. 64 (a) Label created with the spray coating technique (left), with light switched off (centre) and with the AC generator switched on (right). (b) Label created with the screen-printing technique (left), with light switched off (centre) and with the AC generator switched on (right)

From a visual investigation both the labels have excellent qualities of visibility and flexibility. In terms of reproducibility the screen-printing technique offers a better control on the deposition parameters.

1.5.3.4. Authentication System

As final step a preliminary test was performed on the labels using a fingerprint authentication system. The authentication part, which include image recognition and features matching was carried out in collaboration with Dr. A. Forestiero and Eng. G. Papuzzo of the CNR – ICAR (High Performance Computing and Networking Institute) by means of a software application based on the Scale Invariant Feature Transform (SIFT) algorithm. This algorithm is used for pattern recognition in 2D-images invariants to rotation, brightness changing and scale zooming[69].

Basically, the recognition software works following fundamental steps: (i) construction of a scale space, to ensure that the points forming the image are independent of the scale; (ii) localization of the key points of the image that will be related to the minutiae of the fingerprint; (iii) assigning the orientation to each key point found, to guarantee invariant key points to rotation and create the so-called Keypoint Descriptor, to assign unique information to each key point [70].The correspondence among feature points in the original image and feature points in a second image can be evaluated, identifying, for each feature point, the nearest neighbor in feature vectors of the input image. A software library implementing the SIFT algorithm written in C++, available on https://opencv.org/ ,

was employed to design a Java tool for analyzing and comparing the acquired images, allowing to obtain the results reported in following part.

The fingerprint recognition was tested acquiring images of the same label at different angles using a mobile camera and comparing them through the software in order to test if they are recognizable as similar (fig. 1.66).

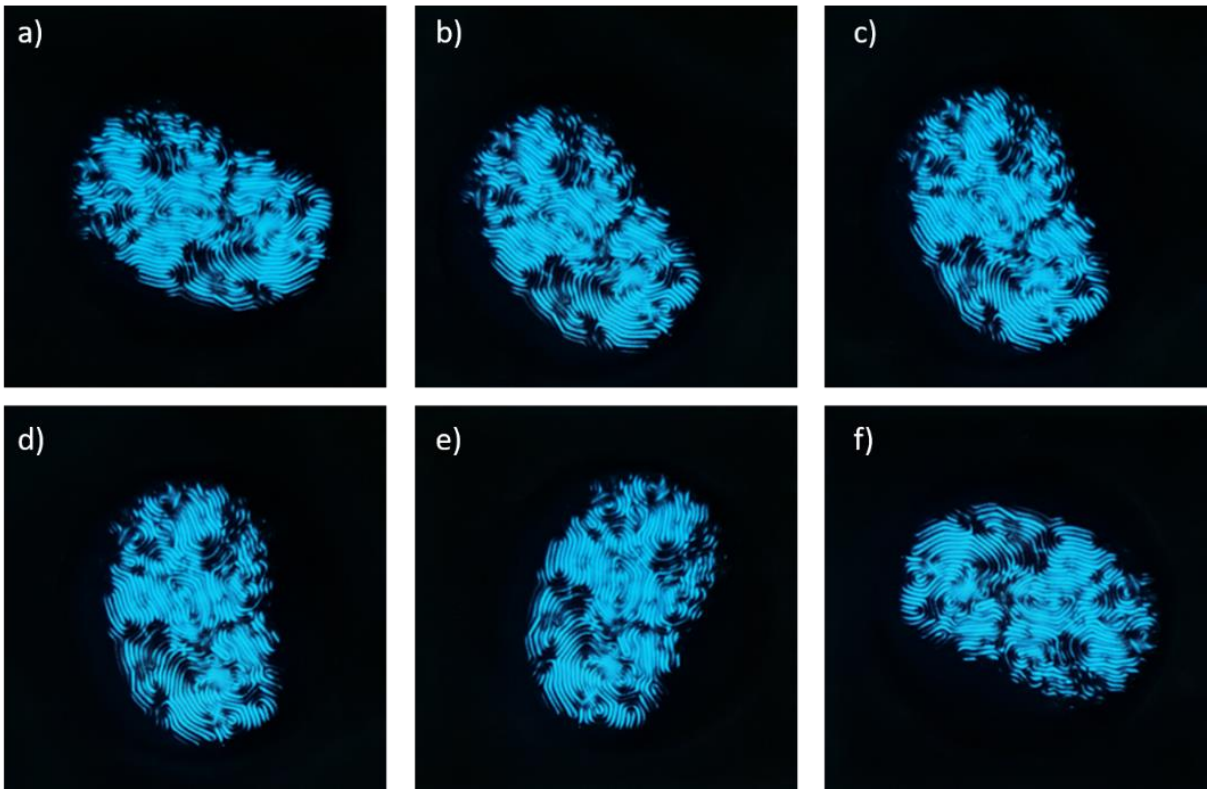

Figure 1. 65 Photographic fingerprint images with different rotation: 0°- 30° - 45°- 60° - 90° - 180° from a to f acquired with phone camera.

Given two images of the same label at different rotation angles, the software recognizes and associates the characteristic-key points connecting them with a coloured line (fig. 1.67). The more lines there are, the more characteristic points are associated, the greater the certainty that it is the same image. Different images usually have no more than 3 - 4 associated key-points. The presence of many lines corresponds to many characteristic points recognized in the images and causes the result to be positive, the matching is to be considered good.

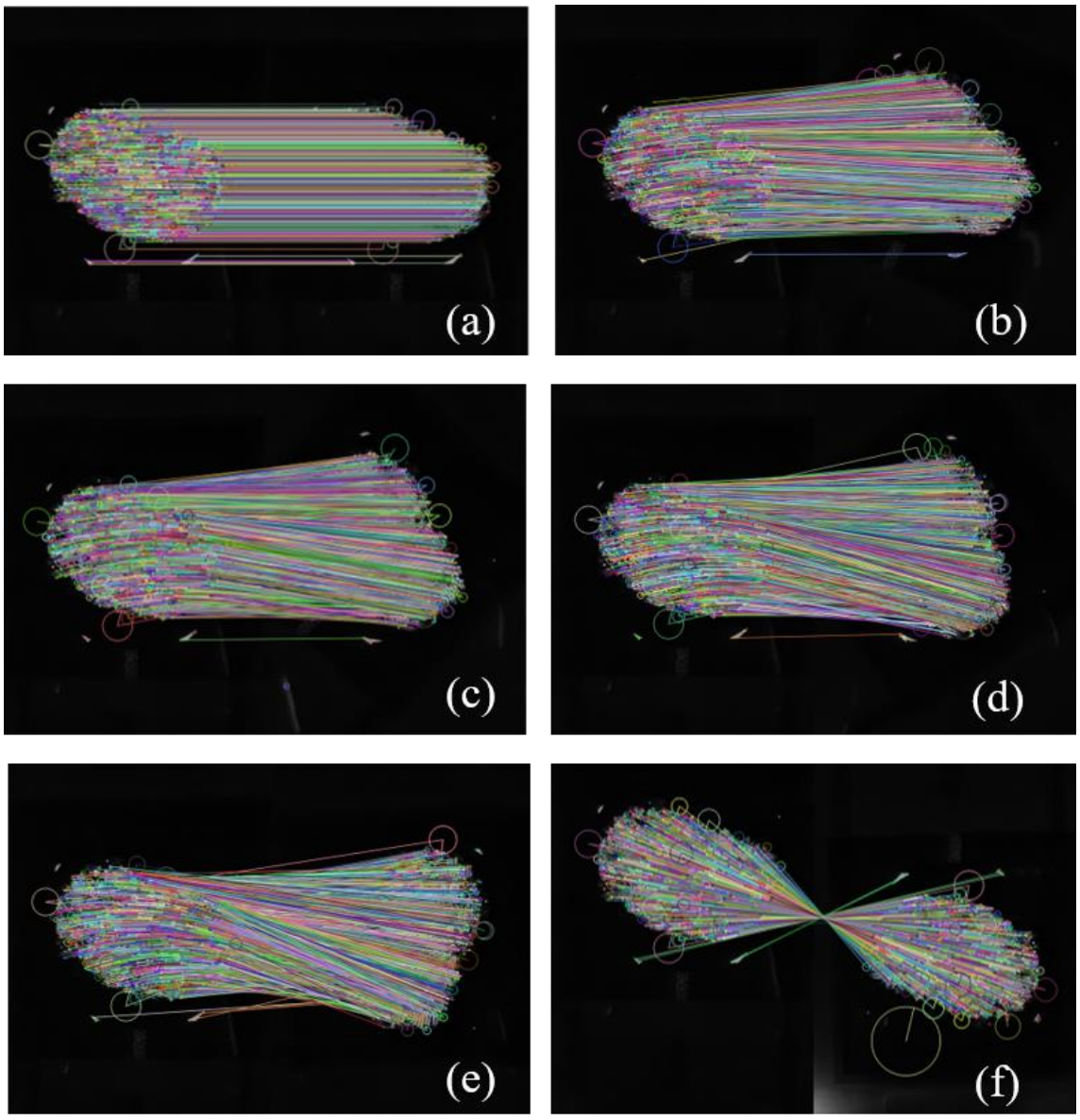

Figure 1. 66 Software recognition procedure: comparing couples of images shown in figure 36: (a) a-a ; (b) a-b ; (c)a-c ; (d)a-d ; (e)a-e ;(f)a-f

The recognition software was applied to images of the labels produced with the two different techniques, comparing their functionality, we named the images of the label created using spray coating as “1” and as “2” the ones of the label produced by screen printing. Percentage of recognized while rotating the sample in all the positions is shown in figure 1.68. At first, we compare the starting image acquired at 0° with all the images acquired at different rotation angles with the same technique, for both techniques. Then, comparison was performed using as starting image the one acquired with no rotation and created with one technique and comparing it with the rotated images of the label created with the other technique. From each comparison the algorithm gave as an output a matrix from which the graphs shown in figure 1.68 were extrapolated.

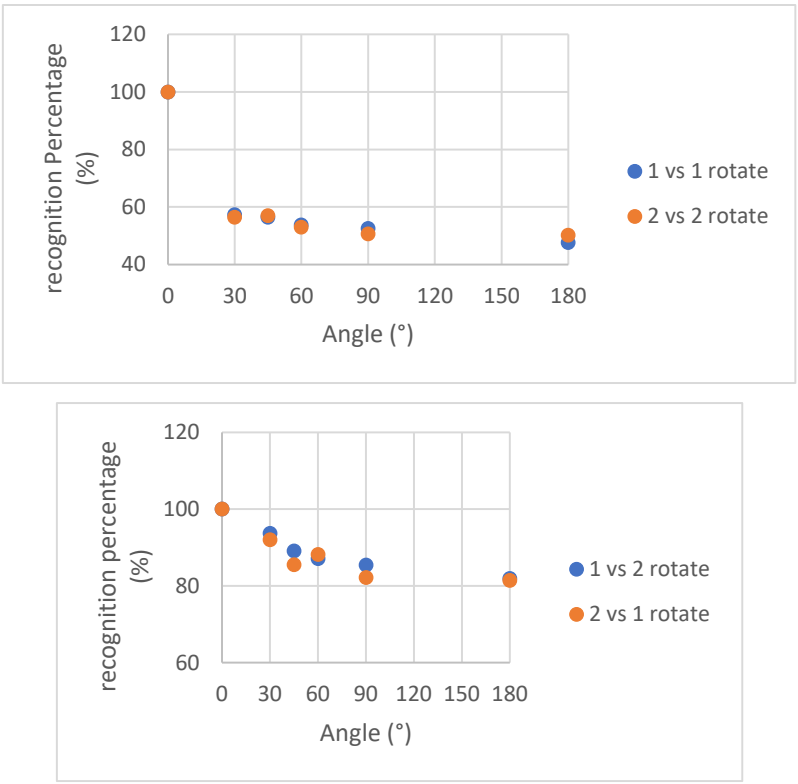

Figure 1. 67 Percentage of features recognized while rotating the sample in all the fifth possibilities: Image at 0° compared with all the images acquired at different rotation angles from the same technique (top); Image at 0° from one technique compared with all the images acquired at different rotation angles from the other technique (bottom)

As shown in the graphs, for both techniques the recognition percentage is similar and very good for each different rotation angle. When the image is compared with itself, or the images acquired on labels created with the two different techniques, and no rotation is applied to the images, are compared, the recognition is total. When images acquired from the same label but rotated were compared, recognition percentage is never lower than 50% and this can be considered as a successful recognition. Also good recognition percentages are obtained when images acquired on labels obtained with the two different techniques and rotated are compared. Since the recognition percentage is very high in both analyzed cases, we can assume that the two images, and therefore the two production methods are equivalent in terms of the recognition algorithm.

1.6. Conclusions

Fingerprint like PUF keys have impressive encoding capacities and several chemical and physical methods have proposed in the last years to provide randomly generated textures that can be used as fingerprint textures. As discussed at the beginning of chapter 1, artificial fingerprint-like textures can be obtained using liquid crystals or relying on the random wrinkling of polymeric films. In 2018 our

research group has patented a method that uses a high voltage and frequency electric field to generate inside chiral liquid crystals confined in microspheres a fingerprint-like optical texture. On these textures some of the characteristic minutiae of a human fingerprint can be observed. The research work reported in this chapter can be considered the natural prosecution of this investigation in an attempt to optimize the experimental procedure and to obtain more complex textures with respect to what is described in the patent. With this purpose in mind, the use of Gold Nanoparticles has shown its efficacy in improving the fingerprint-like texture production parameters. In fact, the use of small nanoparticles has allowed to obtain a reduction of the electric field values necessary to create the desired textures. The mechanisms by which this is possible is not clearly understood but, as reported in several papers (1.1.6) it may be due to the tendency of NPs to interfere with the local order of the liquid crystal, maybe also due to NPs aggregation phenomena, and changing its electric properties. This could facilitate the transition in a distorted configuration of the director, as the fingerprint-like one, when the electric field is applied.

Further, the presence of NPs causes microspheres deformation that may assume different random shapes, some similar to human finger and this increases the encoding capability of the object.

The optimized procedure allows to create simultaneously different micrometric fingerprints and it can be considered by all means as a physical generator of fingerprints that can be used to create anti-counterfeiting tags.

But, since the objects are small and the tags must be easy to read, the idea is to image microspheres with a high resolution microscope and to create an image database. Images can, then, be printed on a suitable support and used as tag to be attached to the goods that need to be traced and authenticated.

With this purpose in mind an electroluminescent tag that uses one of the microfingerprints images has been created using screen printing and spray coating techniques. In normal light conditions the tag is not well visible and it could be easily concealed, when the tag is connected to a power supply it becomes well visible and can be easily imaged using a mobile telephone camera. The authentication of the image has been performed using a modified biometric software that has proven to be suitable for the proposed tags.

1.7.Appendix A

Collection of FP images

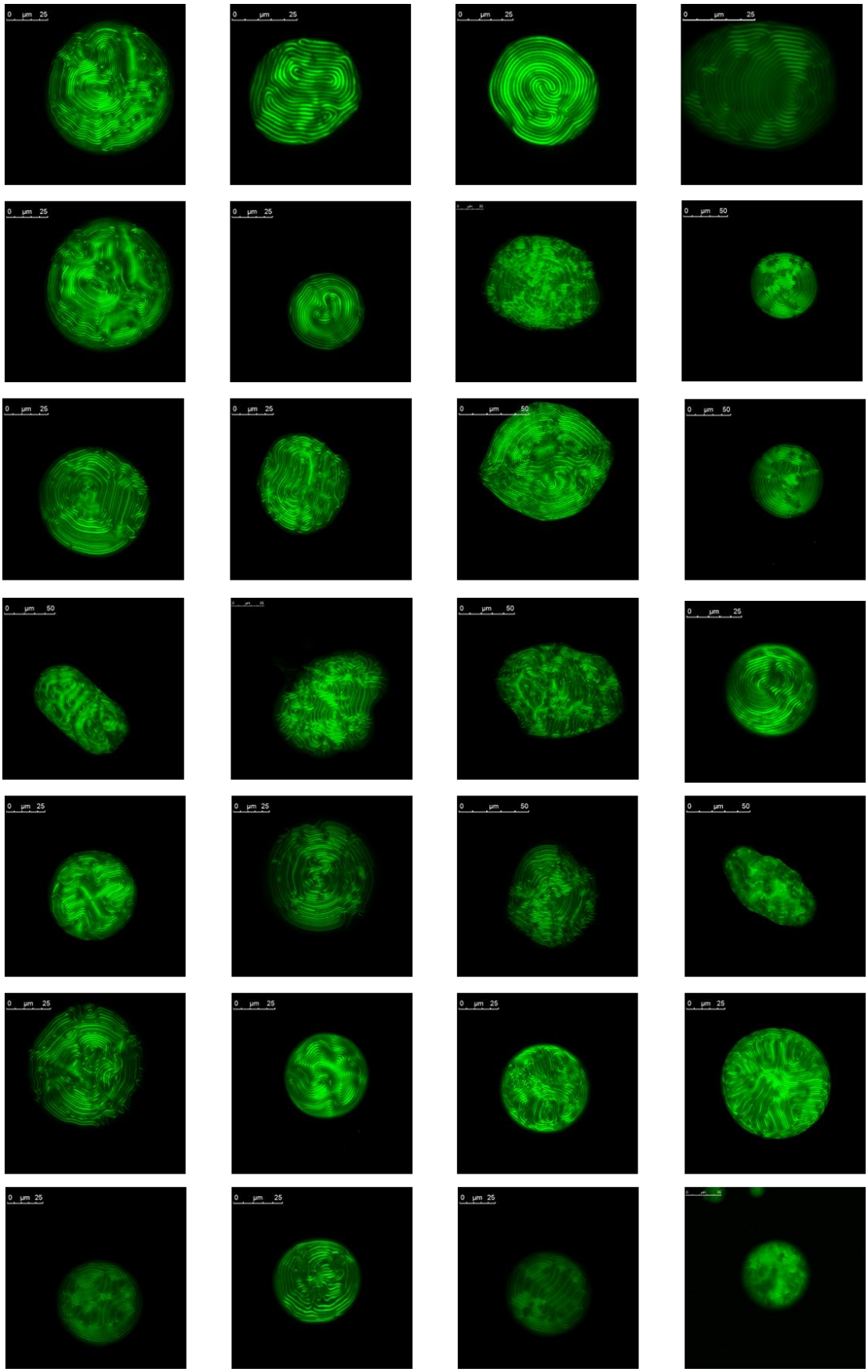

1.8. References

[1] "Major breach found in biometrics system used by banks, UK police and defence firms | Data and computer security | The Guardian." https://www.theguardian.com/technology/2019/aug/14/major-breach-found-in-biometrics-system-used-by-banks-uk-police-and-defence-firms (accessed Dec. 29, 2021).

[2] "Own Your Digital Identity | Kaspersky official blog." https://www.kaspersky.com/blog/future-of-biometrics/ (accessed Mar. 23, 2022).

[3] J. Kim, J. M. Yun, J. Jung, H. Song, J. B. Kim, and H. Ihee, "Anti-counterfeit nanoscale fingerprints based on randomly distributed nanowires," *Nanotechnology*, vol. 25, no. 15, Apr. 2014, doi: 10.1088/0957-4484/25/15/155303.

[4] H. J. Bae *et al.*, "Biomimetic Microfingerprints for Anti-Counterfeiting Strategies," *Advanced Materials*, vol. 27, no. 12, pp. 2083–2089, Mar. 2015, doi: 10.1002/ADMA.201405483.

[5] L. Tian *et al.*, "Plasmonic Nanogels for Unclonable Optical Tagging," *ACS Applied Materials and Interfaces*, vol. 8, no. 6, pp. 4031–4041, Feb. 2016.

[6] K. Nakayama, "Optical security device providing fingerprint and designed pattern indicator using fingerprint texture in liquid crystal," *Optical Engineering*, vol. 51, no. 4, p. 040506, Apr. 2012, doi: 10.1117/1.OE.51.4.040506.

[7] Y. Geng, J. Noh, I. Drevensek-Olenik, R. Rupp, G. Lenzini, and J. P. F. Lagerwall, "High-fidelity spherical cholesteric liquid crystal Bragg reflectors generating unclonable patterns for secure authentication," *Scientific Reports 2016 6:1*, vol. 6, no. 1, pp. 1–9, May 2016, doi: 10.1038/srep26840.

[8] J. Bezić and S. Žumer, "Structures of the cholesteric liquid crystal droplets with parallel surface anchoring ", *Liquid Crystals*, vol. 11, no. 4, pp. 593–619, 2006, doi: 10.1080/02678299208029013.

[9] F. Xu and P. P. Crooker, "Chiral nematic droplets with parallel surface anchoring," *Physical Review*, vol. 56, no. 6, p. 6853, Dec. 1997, doi: 10.1103/PhysRevE.56.6853.

[10] D. Seč, S. Čopar, and S. Žumer, "Topological zoo of free-standing knots in confined chiral nematic fluids," *Nature Communications 2014 5:1*, vol. 5, no. 1, pp. 1–7, Jan. 2014, doi: 10.1038/ncomms4057.

[11] T. Orlova, S. J. Aßhoff, T. Yamaguchi, N. Katsonis, and E. Brasselet, "Creation and manipulation of topological states in chiral nematic microspheres," *Nature Communications*, vol. 6, Jul. 2015, doi: 10.1038/NCOMMS8603.

[12] F. Fadda, G. Gonnella, D. Marenduzzo, E. Orlandini, and A. Tiribocchi, "Switching dynamics in cholesteric liquid crystal emulsions," *The Journal of Chemical Physics*, vol. 147, no. 6, p. 064903, Aug. 2017, doi: 10.1063/1.4997637.

[13] M. D. L. Bruno, M. P. De Santo , R. Barberi, G. Petriashvili, "Photonic micro-fingerprints as anti-counterfeiting device," 102018000009886.

[14] P. G. de Gennes, J. Prost, and R. Pelcovits, "The Physics of Liquid Crystals," *Physics Today*, vol. 48, no. 5, pp. 70–71, May 1995, doi: 10.1063/1.2808028.

[15] H. S. Kitzerow, C. Bahr, *Chirality in Liquid Crystals*, 2001, doi: 10.1007/B97374.

[16] "Molecular Expressions: Science, Optics, and You: Light and Color - Optical Birefringence." https://micro.magnet.fsu.edu/optics/lightandcolor/birefringence.html.

[17] E. B. Priestley, P. J. Wojtowicz, and P. Sheng, *Introduction to liquid crystals*. Springer, 1975.

[18] C. J. Gerritsma and P. van Zanten, "Periodic perturbations in the cholesteric plane texture," *Physics Letters A*, vol. 37, no. 1, pp. 47–48, Oct. 1971, doi: 10.1016/0375-9601(71)90325-2.

[19] T. J. Scheffer, "Electric and magnetic field investigations of the periodic gridlike deformation of a cholesteric liquid crystal," *Physical Review Letters*, vol. 28, no. 10, pp. 593–596, 1972, doi: 10.1103/PHYSREVLETT.28.593.

[20]. L.-C Chien *et al.*, "Dual mode switching of cholesteric liquid crystal device with three-terminal electrode structure," *Optics Express*, vol. 20, no. 22, pp. 24376–24381, Oct. 2012, doi: 10.1364/OE.20.024376.

[21] J. S. Patel and R. B. Meyer, "Flexoelectric electro-optics of a cholesteric liquid crystal," *Phys Rev Lett*, vol. 58, no. 15, pp. 1538–1540, 1987, doi: 10.1103/PHYSREVLETT.58.1538.

[22] I. Dierking, *Textures of Liquid Crystals*, May 2003, doi: 10.1002/3527602054.

[23] "Handbook of Liquid Crystals, 8 Volume Set, 2nd Edition | Wiley." https://www.wiley.com/en-sg/Handbook+of+Liquid+Crystals,+8+Volume+Set,+2nd+Edition-p-9783527327737.

[24] C. Provenzano *et al.*, "Self-organized internal architectures of chiral micro-particles," *APL Materials*, vol. 2, no. 2, p. 022103, Feb. 2014, doi: 10.1063/1.4863837.

[25] R. G. Jones *et al.*, "Compendium of Polymer Terminology and Nomenclature IUPAC Recommendations 2008 With advice from : Compendium of Polymer Terminology and Nomenclature IUPAC Recommendations 2008".

[26] "What is a colloidal dispersion and how to measure its stability?" https://www.formulaction.com/en/about-us/news/blog/what-is-a-colloidal-dispersion-and-how-to-measure-its-stability.

[27] T. Lopez-Leon and A. Fernandez-Nieves, "Drops and shells of liquid crystal", *Colloid Polym Sci* (2011) 289:345–359, doi: 10.1007/s00396-010-2367-7.

[28] M. Urbanski *et al.*, "Liquid crystals in micron-scale droplets, shells and fibers," *J Phys Condens Matter*, vol. 29, no. 13, Feb. 2017, doi: 10.1088/1361-648X/AA5706.

[29] M. v. Kurik and O. D. Lavrentovich, "Negative-positive monopole transitions in cholesteric liquid crystals," *ZhPmR Pisma Redaktsiiu*, vol. 35, p. 362, 1982.

[30] V. Tomar, S. I. Hernández, N. L. Abbott, J. P. Hernández-Ortiz, and J. J. de Pablo, "Morphological transitions in liquid crystal nanodroplets," *Soft Matter*, vol. 8, no. 33, pp. 8679–8689, Aug. 2012, doi: 10.1039/C2SM25383F.

[31] I. Muševič, "Liquid Crystal Colloids," 2017, doi: 10.1007/978-3-319-54916-3.

[32] R. Bitar, G. Agez, and M. Mitov, “Cholesteric liquid crystal self-organization of gold nanoparticles,” *Soft Matter*, vol. 7, no. 18, pp. 8198–8206, Sep. 2011, doi: 10.1039/C1SM05628J.

[33] S. Lal, S. Link, and N. J. Halas, “Nano-optics from sensing to waveguiding,” *Nature Photonics*, vol. 1, no. 11, pp. 641–648, Nov. 2007, doi: 10.1038/NPHOTON.2007.223.

[34] H. Ayeb *et al.*, “Gold nanoparticles in a cholesteric liquid crystal matrix: self-organization and localized surface plasmon properties,” *Journal of Materials Chemistry*, vol. 22, no. 16, pp. 7856–7862, Mar. 2012, doi: 10.1039/C2JM30622K.

[35] H. Qi and T. Hegmann, “Formation of periodic stripe patterns in nematic liquid crystals doped with functionalized gold nanoparticles,” *Journal of Materials Chemistry*, vol. 16, no. 43, pp. 4197–4205, Nov. 2006, doi: 10.1039/B611501B/.

[36] H. Qi, B. Kinkead, V. M. Marx, H. R. Zhang, and T. Hegmann, “Miscibility and alignment effects of mixed monolayer cyanobiphenyl liquid-crystal-capped gold nanoparticles in nematic cyanobiphenyl liquid crystal hosts,” *ChemPhysChem*, vol. 10, no. 8, pp. 1211–1218, Jun. 2009, doi: 10.1002/CPHC.200800765.

[37] T. Hegmann, H. Qi, and V. M. Marx, “Nanoparticles in liquid crystals: Synthesis, self-assembly, defect formation and potential applications,” *Journal of Inorganic and Organometallic Polymers and Materials*, vol. 17, no. 3, pp. 483–508, Sep. 2007, doi: 10.1007/S10904-007-9140-5.

[38] L. Cseh and G. H. Mehl, “The design and investigation of room temperature thermotropic nematic gold nanoparticles,” *J Am Chem Soc*, vol. 128, no. 41, pp. 13376–13377, Oct. 2006, doi: 10.1021/JA066099C/SUPPL_FILE/JA066099CSI20060918_014027.PDF.

[39] X. Zeng *et al.*, “3D Ordered Gold Strings by Coating Nanoparticles with Mesogens,” *Advanced Materials*, vol. 21, no. 17, pp. 1746–1750, May 2009, doi: 10.1002/ADMA.200803403.

[40] V. A. Mallia, P. K. Vemula, G. John, A. Kumar, and P. M. Ajayan, “In situ synthesis and assembly of gold nanoparticles embedded in glass-forming liquid crystals,” *Angew Chem Int Ed Engl*, vol. 46, no. 18, pp. 3269–3274, 2007, doi: 10.1002/ANIE.200604218.

[41] M. Mitov, C. Bourgerette, and F. de Guerville, “Self-assembly of metallic nanoparticles in a cholesteric liquid crystal,” *Nanofabrication Technologies*, vol. 5220, p. 20, Oct. 2003, doi: 10.1117/12.503558.

[42] M. Mitov, C. Portet, C. Bourgerette, E. Snoeck, and M. Verelst, “Long-range structuring of nanoparticles by mimicry of a cholesteric liquid crystal,” *Nature Materials 2002 1:4*, vol. 1, no. 4, pp. 229–231, Nov. 2002, doi: 10.1038/nmat772.

[43] D. Voloschenko, O. P. Pishnyak, S. v. Shiyanovskii, and O. D. Lavrentovich, “Effect of director distortions on morphologies of phase separation in liquid crystals,” *Physical Review E*, vol. 65, no. 6, p. 060701, Jun. 2002, doi: 10.1103/PhysRevE.65.060701.

[44] J. B. Fleury, D. Pires, and Y. Galerne, “Self-Connected 3D architecture of microwires,” *Physical Review Letters*, vol. 103, no. 26, p. 267801, Dec. 2009, doi: 10.1103/PHYSREVLETT.103.267801/FIGURES/3/MEDIUM.

[45] D. Pires, J. B. Fleury, and Y. Galerne, “Colloid particles in the interaction field of a disclination line in a nematic phase,” *Physical Review Letters*, vol. 98, no. 24, p. 247801, Jun. 2007, doi: 10.1103/PHYSREVLETT.98.247801/FIGURES/3/MEDIUM.

[46] D. Coursault *et al.*, “Linear Self-Assembly of Nanoparticles Within Liquid Crystal Defect Arrays,” *Advanced Materials*, vol. 24, no. 11, pp. 1461–1465, Mar. 2012, doi: 10.1002/ADMA.201103791.

[47] N. Podoliak *et al.*, “Macroscopic optical effects in low concentration ferronematics,” *Soft Matter*, vol. 7, no. 10, pp. 4742–4749, May 2011, doi: 10.1039/C1SM05051F.

[48] C. da Cruz, O. Sandre, and V. Cabuil, “Phase behavior of nanoparticles in a thermotropic liquid crystal,” *Journal of Physical Chemistry B*, vol. 109, no. 30, pp. 14292–14299, Aug. 2005,

[49] M. Gupta, I. Satpathy, A. Roy, and R. Pratibha, “Nanoparticle induced director distortion and disorder in liquid crystal-nanoparticle dispersions,” *J Colloid Interface Sci*, vol. 352, no. 2, pp. 292–298, Dec. 2010, doi: 10.1016/J.JCIS.2010.08.027.

[50] P. S. Chen, C. C. Huang, Y. W. Liu, and C. Y. Chao, “Effect of insulating-nanoparticles addition on ion current and voltage-holding ratio in nematic liquid crystal cells,” *Applied Physics Letters*, vol. 90, no. 21, p. 211111, May 2007, doi: 10.1063/1.2740581.

[51] D. Sikharulidze, “Nanoparticles: An approach to controlling an electro-optical behavior of nematic liquid crystals,” *Applied Physics Letters*, vol. 86, no. 3, p. 033507, Jan. 2005, doi: 10.1063/1.1855416.

[52] M. Infusino, A. de Luca, F. Ciuchi, A. Ionescu, N. Scaramuzza, and G. Strangi, “Effects of Gold Nanoparticle Dispersion in a Chiral Liquid Crystal Matrix” , vol. 572, no. 1, pp. 59–65, Mar. 2013, doi: 10.1080/15421406.2012.763211.

[53] M. Humar, I. Muševič, K. G. Sullivan, and D. G. Hall, “3D microlasers from self-assembled cholesteric liquid-crystal microdroplets,” *Optics Express, Vol. 18, Issue 26, pp. 26995-27003*, vol. 18, no. 26, pp. 26995–27003, Dec. 2010, doi: 10.1364/OE.18.026995.

[54] C. Mowatt *et al.*, “Paintable band-edge liquid crystal lasers,” *Optics Express, Vol. 19, Issue 3, pp. 2432-2439*, vol. 19, no. 3, pp. 2432–2439, Jan. 2011, doi: 10.1364/OE.19.002432.

[55] H. G. Lee, S. Munir, and S. Y. Park, “Cholesteric Liquid Crystal Droplets for Biosensors,” *ACS Applied Materials and Interfaces*, vol. 8, no. 39, pp. 26407–26417, Oct. 2016.

[56] G. Petriashvili, M. D. L. Bruno, M. P. de Santo, E. Fuoco, and R. Barberi, “Acid mediated tunability of stimulated laser emission from dye doped chiral microdroplets,” *Molecular Crystals and Liquid Crystals*, vol. 684, no. 1, pp. 82–88, May 2019, doi: 10.1080/15421406.2019.1581712.

[57] G. Petriashvili, M. D. L. Bruno, M. P. de Santo, and Barberi Riccardo, “Photonic micro-fingerprints as anti-counterfeiting device”, WIPO Patent Application WO/2021/111349.

[58] C. Kant and R. Nath ,“ Reducing Process-Time for Fingerprint Identification System.” *International Journal of Biometric and Bioinformatics 3, 2009.*

[59] R. Cappelli, “SFinGe: an Approach to Synthetic Fingerprint Generation.” *Computer Science,* 2004.

[60] M. S. Riazi, S. M. Chavoshian, and F. Koushanfar, “SYNFI: Automatic Synthetic Fingerprint Generation.” *arXiv* 2002.08900.

[61] “Biometric System Laboratory.” http://biolab.csr.unibo.it/research.asp?organize=Activities&select=&selObj=12&pathSubj=111%7C%7C12&.

[62] A. Moridi, S. M. Hassani-Gangaraj, M. Guagliano, and M. Dao, “Cold spray coating: review of material systems and future perspectives”, *Surface Engineering*, vol. 30, no. 6, pp. 369–395, 2014, doi: 10.1179/1743294414Y.0000000270.

[63] Y. Zheng, S. Li, W. Shi, and J. Yu, “Spray-coated nanoscale conductive patterns based on in situ sintered silver nanoparticle inks,” *Nanoscale Research Letters*, vol. 9, no. 1, pp. 1–7, Dec. 2014, doi: 10.1186/1556-276X-9-145/TABLES/2.

[64] Z. Bao, J. A. Rogers, and H. E. Katz, “Printable organic and polymeric semiconducting materials and devices,” *Journal of Materials Chemistry*, vol. 9, no. 9, pp. 1895–1904, Jan. 1999, doi: 10.1039/A902652E.

[65] D. A. Pardo, G. E. Jabbour, N. Peyghambarian ,“Application of Screen Printing in the Fabrication of Organic Light-Emitting Devices” *Adv. Mater.*, 12: 1249-1252. https://doi.org/10.1002/1521-4095(200009)12:17<1249::AID-ADMA1249>3.0.CO;2-Y.

[66] M. Sauer, S. Meilchen, A. Kalleder, M. Mennig, and H. Schmidt, “Screen Printing,” *Sol-Gel Technologies for Glass Producers and Users*, pp. 117–122, 2004, doi: 10.1007/978-0-387-88953-5_14.

[67] T. M. Lee, J. H. Noh, I. Kim, D. S. Kim, and S. Chun, “Reliability of gravure offset printing under various printing conditions,” *Journal of Applied Physics*, vol. 108, no. 10, p. 102802, Nov. 2010, doi: 10.1063/1.3510466.

[68] M. Zirkl *et al.*, “An All-Printed Ferroelectric Active Matrix Sensor Network Based on Only Five Functional Materials Forming a Touchless Control Interface,” *Advanced Materials*, vol. 23, no. 18, pp. 2069–2074, May 2011, doi: 10.1002/ADMA.201100054.

[69] D. G. Lowe, “Object recognition from local scale-invariant features,” *Proceedings of the IEEE International Conference on Computer Vision*, vol. 2, pp. 1150–1157, 1999, doi: 10.1109/ICCV.1999.790410.

[70] D. G. Lowe, “Distinctive Image Features from Scale-Invariant Keypoints,” *International Journal of Computer Vision 2004 60:2*, vol. 60, no. 2, pp. 91–110, Nov. 2004, doi: 10.1023/B:VISI.0000029664.99615.94.

[71] Unclonable Patterns by Soft Matter Textures, Bruno M.D.L, Doctoral Thesis 2022 (submission).

2. Chapter 2: Cellulose based systems for security devices

2.1. Introduction (Bioinspiration and Sustainability)

The protection of consumers from trade in counterfeit products and the disposal of seized products in an environmentally responsible manner are part of the problems that arise from anti-counterfeiting. Since in addition to the problem that the counterfeiting of goods imparts in society, the money lost due to this field of crime, there is also the problem of the disposal of counterfeit goods.

On the one hand, we must consider the possibility of creating sustainable and eco-friendly anti-counterfeiting solutions. But, on the other hand, we must take into account the environmental consequences that this sector can have. It is sufficient to think, for example, of the way in which seized counterfeit goods are disposed of, usually incinerated or landfilled, with potentially harmful environmental consequences. To solve this part, we have to think about the landfills for recycling where things are processed, dismantled, and made available for recycling.

In the first case, it is enough to propose "Green" solutions. But it is evident that modern society is in desperate need of renewable resources that can be implemented in every field, all in order to become more sustainable. If we think of renewable energies and resources, in this context, cellulose is the main component of plant biomass and is the most abundant, renewable and biodegradable natural polymer. Cellulose is insoluble in most solvents, resistant and cheap. All of these characteristics make it one of the most studied materials for the replication of natural biomimetism and to develop sustainable materials[1]. As a renewable material, it is used in numerous applications. Industrial common applications include paper, pulps, packaging but other applications are in the medicine field (pharmaceutical, biomedicine). New advanced technological applications concern the use of cellulose for paints, food, glues, thermoplastic polymers

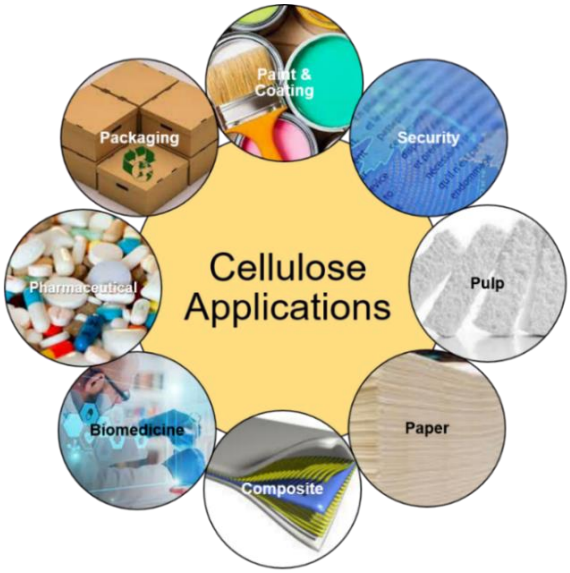

Figure 2. 1 Some of the most common applications fields of cellulose.

Inspiration to develop complex systems can arise from nature. The idea is to develop biomimetic materials replicating the structural colour of plants or animals [3], using cellulose and especially cellulose nanocrystals for new security device (s), with the advantages of being more accessible, environmentally friendly than the materials that are currently present [4], [5].

In many applications, cellulose has been used as a passive constituent such as a filler or substrate. But in modern applications, the main objective is to transform cellulose into an active constituent in order to reduce our carbon footprint is crucial for future generations and to become more sustainable.

The first part of the chapter describes cellulose and its properties. We focused on its derivatives: cellulose nanocrystals (CNCs), their synthesis and properties and hydroxypropyl cellulose (HPC). CNCs-based nanocomposite materials have been introduced and a list of applications using them will be presented.

Part of this work is based on the application of cellulose as an active part in anti-counterfeiting devices. We develop optical responsive all-cellulosic composite films with structural colouration that can be used as an anticounterfeiting device. To improve the mechanical properties and the brittleness, hydroxypropyl cellulose will be introduce into the CNCs films. And to introduce new properties, such as fluorescence, films of CNCs doped with a CNCs-dye were made.

2.1.1. The chemistry of cellulose: Molecular Structure

Payen coined for the first time in 1838 the word “cellulose” derived from Latin that means rich in small cells. He deduced the molecular formula by elemental analysis and observed the isomerism with starch[6], [8]. After that, almost 100 years were necessary to the scientific community to accept the macromolecular nature of this substance, with the work of Staudinger[7].

As a raw source for industrial processing, 93% of cellulosic fibres are obtained from either hardwood (angiosperms) or softwood (gymnosperms), while the rest comes from other sources, including bagasse, algae, straw, bacteria or seeds [8]–[10] as we see grouped in the figure 2.2.

Figure 2. 2 Some common cellulose sources.

In nature, cellulose is produced through the condensation and polymerization of glucose, which is a product of plant photosynthesis, but also bacteria, slime moulds and a group of marine animals (tunicates) have the ability to synthesize cellulose. Plant cells have a wall that acts like a box, which surrounds the cell, as we can see in figure 2.3. The thickness of the cell walls of plants is generally between 0.1 and 0.3 mm but sometimes can exceed 1 mm. The walls form a continuous network along the entire plant. The wall is made up of sequentially deposited layers of different thicknesses, chemical compositions and structural organizations. There are two types of walls: primary and secondary, which differ in function and composition. The primary wall is the first layer to be deposited after cell division and its formation coincides with cell growth. It is a fibrous composite (‘fibreglass’) with an ordered array of stiff cellulose microfibrils embedded in a less rigid matrix of polysaccharides and glycoproteins (hemicellulose, pectin and other macromolecules). The secondary wall is the central layer, comprising about 80–90% of the entire cell wall volume. The layers of the secondary wall are much thicker and stronger than the primary wall; they contain lignin. The secondary walls are not found in all cell types.

Cellulose microfibrils (Fig.2.3) are composed of approximately 36 hydrogen-bonded chains and each chain contains 500–14000 glucose units. Microfibrils may self-assemble in the cell wall with different kinds of organisations: axial (nematic-like), transverse, crisscrossed, so-called helical, and helicoidal (cholesteric-like) [11].The cholesteric organisation can be found both in the primary and secondary walls.

The morphological structure of cellulose describes the organization of crystals into microfibrils, cell walls, fibres, tissues and other cellulosic arrangements. Nature cellulose generally occurs as fibres while regenerated cellulose can be transformed into different materials as fibres, films or other products with morphology largely different from that of native cellulose.

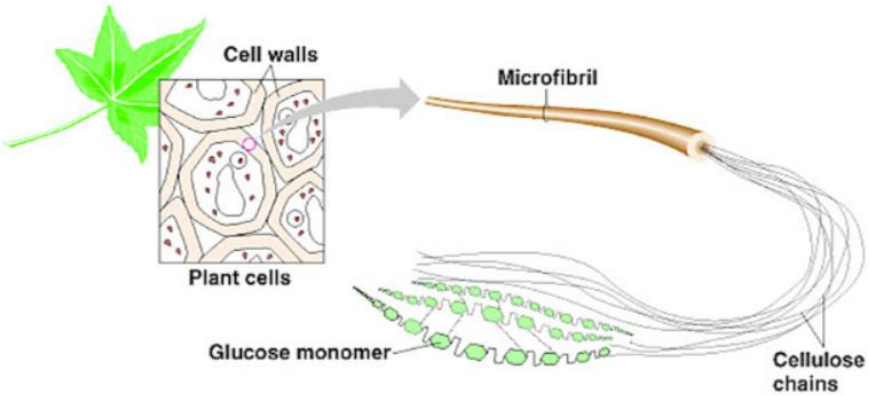

Figure 2. 3 Scheme of the cellulose cell wall and micro fibril organization.

The cellulose nature microfibril is assumed to be the basic structural component of cellulose, formed during the biosynthesis. Cellulose or poly(anhydro-β-1,4-glucopyranose), is a polysaccharide, whose chemical formula is $[C_6H_{10}O_5]_n$, where n=10,000–15,000 depending on the source material and exists in nature as a polydisperse, linear, crystalline macromolecule of high molecular weight and degree of polymerization [10]. Cellulose is a linear chain with hundreds to thousands repeating chain units called *cellobiose* $[C_{12}H_{22}O_{11}]$, with a ß-1,4-glicosidic bond generated between two glucose units that rotate of 180° releasing a water molecular (Fig. 2.4) in the polycondensation reaction.

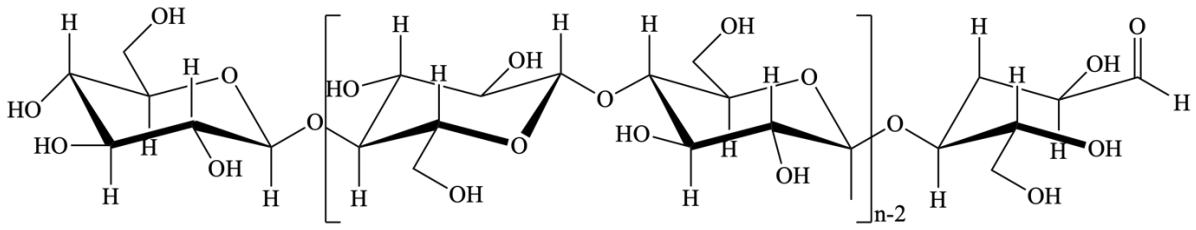

Figure 2. 4 Basic chemical structure of cellulose showing the cellobiose repeat unit

The numbering of the carbon and oxygen atoms in one of the cellobiose rings is shown in figure 2.5.

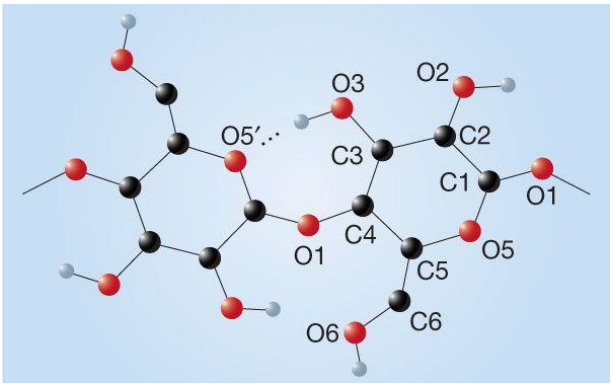

Figure 2. 5 Numbering system for carbon and oxygen atoms in two consecutive glucosyl units of cellulose[12].

As we can see in the ring, the carbon atoms: C1 is linked to two oxygen atoms (O1 and O5), to C2 that is linked to a hydroxyl substituent O2; C3 is linked to a hydroxyl substituent O3 and to C4 also linked to an oxygen atom O1 into the glycosidic bond and to C5 linked to a hydroxymethyl group (C6 and O6). The number of oxygen atoms in the ring are 5, where O6 is in the primary alcohol, O2 and O3 are the secondary alcohols. C1 is the acetal centre that exists along the entire polymeric structure except at one end of the macromolecule where it is a reducing hemiacetal centre (figure 2.4)[13].

2.1.2. The Physics of Cellulose: Supramolecular Structure

Cellulose due to different unit cell parameters can form different kinds of polymorphs crystalline structure denoted as cellulose I, II, IIII, $IIII_I$, IV_I and IV_{II} defined by different unit cell parameters and that can be inter-converted depending on the chemical treatment and source[14], [15].

The two main polymorphs of cellulose are Cellulose I and II. Nature cellulose consists of cellulose I and is present in the α and β forms, the ratio between the two species depends on the source. For instance, bacteria and algae produced cellulose enriched in Iα, while plants have predominately beta and tunicates have almost pure beta. Current knowledge on cellulose suggests that the cellulose structure consists into chains organized in sheets packed in a parallel structure, linked by intra and inter-hydrogen bonds. Adjacent chains are linked by a *zig-zag*, repeating O–H···O–H···. For example, in I_β type crystal, the structure consists of two parallel chains having slightly different conformations and organized in sheets packed in a "parallel-up" fashion, with all hydroxymethyl groups adopting the trans-gauche (*tg)* conformation (Fig.2.6, a).

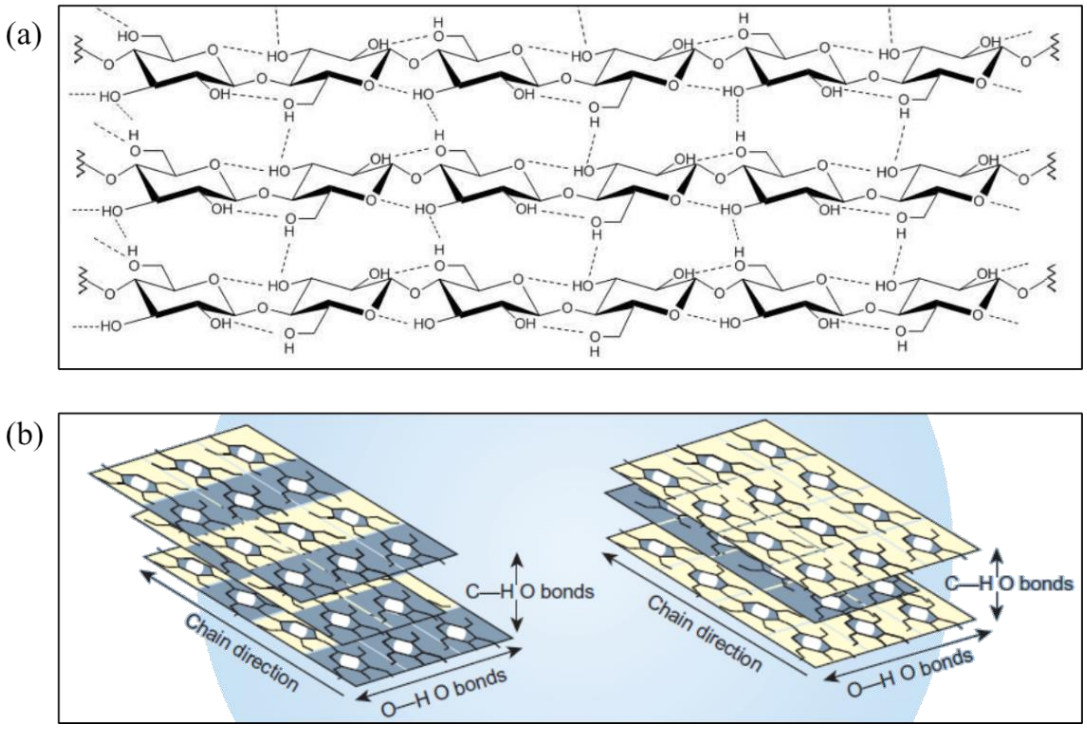

Figure 2. 6 a) Schematic drawing of the intra- and intermolecular hydrogen bonding network in cellulose I. b) Symmetry and directions of hydrogen bonding in cellulose and the sheet arrangement, Cellulose Iα, in which all chains are crystallographically identical but alternating glucose units in each chain, shaded grey and yellow, differ slightly in conformation (on the left). Cellulose Iβ, in which chains of two distinct kinds are arranged in alternating sheets (on the right). Chains passing through the origin and centre of the unit cell are shaded respectively yellow and grey[13].

As represented in figure 2.6, b the cellulose molecule has the shape of a flat ribbon with hydroxyl groups laterally along the extended chain, these hydroxyl groups are readily available for hydrogen

bonding, either within the same cellulose chain (intramolecular) or between different chains (intermolecular).

The presence of intramolecular hydrogen bonds is the most important feature regarding the single-chain conformation of cellulose, since they make the chain rigid as they hinder the free rotation of the rings along their glycosidic bonds. On the other hand, the intermolecular hydrogen bonds are considered to be the major responsible of the supramolecular structure, the state of aggregation and the interchain cohesion[16]–[19]. Therefore, this very complex and strong network of hydrogen bonds present in cellulose is extremely important for the particular characteristics of cellulose as we will see in detail in the next paragraph.

Nishiyama et al. [20], [21] determined the crystal and molecular structure together with the hydrogen-bonding system in cellulose using synchrotron and neutron diffraction data. Due to the flat ribbon-like shape of the cellulose molecule and the positioning of its hydroxyl groups and hydrogen atoms in the pyranose ring (in the molecule the OH groups are equatorial, while the H atoms are axially oriented to the plane of the ring) different polarity sites are present. In fact, within the same cellobiose unit we find hydrophilic sites parallel to the plane of the ring (Fig. 2.7, a) and hydrophobic sites perpendicular to the ring (Fig. 2.7, b) [13], [22]–[24].

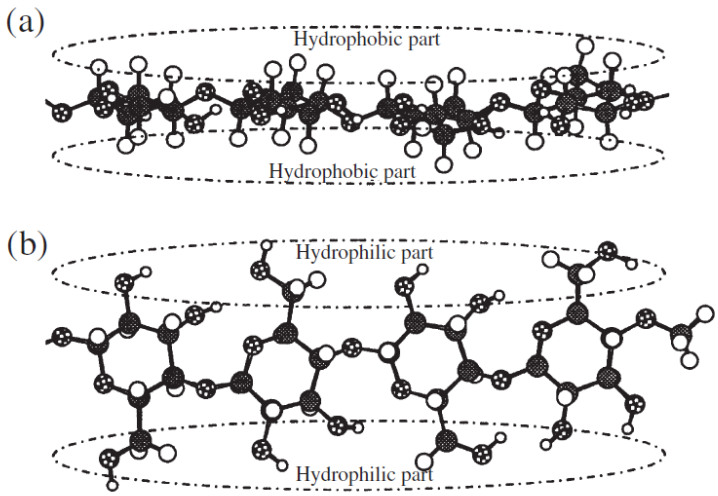

Figure 2. 7 Hydrophilic and hydrophobic parts of cellulose molecule. (a) Hydrophobic sites of cellulose macromolecule in side view of glucopyranose ring plane showing the hydrogen atoms of C–H bonds on the axial positions of the rings, (b) hydrophilic sites of cellulose molecule in top view of glucopyranose ring plane showing the hydroxyl groups located on the equatorial positions of the rings[24].

For instance, the chemical structure affects:

(i) the reactivity of the hydroxyl groups (responsible for a wide range of derivatives and possible functionalization);

(ii) the solubility (cellulose is insoluble in water and in most conventional solvents and, since the intermolecular forces of attraction that hold the cellulose molecules together are very strong and in order to solubilized it the solvent-solute attraction force must be greater than them);

(iii) the thermal stability (the total bond strength between cellulose molecules is stronger than their covalent intramolecular bonds and high energy in the form of heat is required to overcome this force);

(iv) mechanical properties (a relatively high axial stiffness and good strength due to the intra- and inter-chain hydrogen bond).

So, the structure influences both the microscopic (e.g., interactions) and macroscopic properties (e.g., solubility) of cellulose.

2.2. Cellulose Properties

Due to its particular structure, cellulose exhibits unusual physical and chemical properties. The most important and relevant are listed below:

- Highly hydrophilic nature (however, it is insoluble in water and in most organic solvents but this does not mean that cellulose interact poorly with water in this sense, the hydrophilic cellulose surface means that despite being insoluble it can absorb water) [25];
- Good thermal stability, but it is a non-thermoplastic material;
- Resistant to chemicals attack (cellulose is relatively resistant to chemical derivatization, and added groups are seldom evenly distributed)
- Good mechanical properties (cellulose forms fibres with high tensile strength and stiffness, that usually are used as reinforcing element in composites);
- Low density and thermal conductivity.

Mechanical, biological and physiological properties of cellulose are most influenced by the size of the cellulose molecule, which is usually indicated by the degree of polymerization (DP) or by the average molecular weight ($\overline{M_w}$). In this sense it is believed that a glucan bound to β with DP around 20-30 can offer all the properties of cellulose [17], [26]. In literature one can encounter DP values ranging from hundreds to several tens of thousands and that DP is dependent on the source of the original cellulose and less dependent on isolation and purification methods. For example, [17]–[19] and others suggest that the molecular mass distribution must be homogeneous for cellulose of a given

source and the molecular mass and the DP of cellulose can be considered as average values. In other word the high DP in cellulose structure can be seen in the fibrils' length that are quite long.
But among the most important properties we must not look only at cellulose as it is but also at the properties of its derivatives, which retain many of the properties of cellulose while adding other very interesting ones. One of the main properties of cellulose derivatives is the fact that they can originate, under suitable conditions, liquid crystalline phases (that will be discussed in detail in section 2.5.3)

2.2.1. Cellulose synthesis

As we have already seen before in nature, cellulose is not present as an isolated molecule, but is found as assemblies of single chains that form a fibre-like structure, whose biosynthesis can be described as a complex multistep sequential phenomenon that includes coupled processes of enzymatic polymerization of single glucose monomers and the assembly of these glucan chains to form fibrillar supramolecular structures [17].

2.2.2. Bragg reflection and structural colour

Since, as we have already mentioned, the most important feature is the formation of a liquid crystalline phase, so in addition to everything that has been described in chapter 2 regarding liquid crystals and crystalline phases, before to describe in detail cellulose and its derivatives liquid crystalline phases, we need to add some details about the birefringence and specifically about Bragg reflection. Bragg 's law is known to be equal to $n\lambda = 2d\ sin\theta$ where θ is the angle that the outgoing beam forms with the crystalline plane, λ is the wavelength of the radiation, d is the distance between two adjacent floors and n is a positive integer as we can see in figure 2.8, a.
The cholesteric phase is characterized by the pitch (p) which corresponds to a complete turn 360 ° of the director $\hat{n}$. De Vries [27] proposed a model to determine the birefringence of a cholesteric material, that represents the easy way to measure birefringence. The model is based on the reflection of one circularly polarized component of the light when a planar cholesteric is illuminated with white light normally to the plane. Reflection will have a wavelength range that has the maximum wavelength (λ_0) given by the expression:

$$\lambda_0 = n\,p \tag{2. 1}$$

where n is the average refractive index of the cholesteric phase and p is the value of the helical pitch. In a generic form, if the light reaches the cholesteric with an angle that is not normal to the cholesteric planes the wavelength of the reflected light will be dependent on the incidence angle and the observed colour of the cholesteric will change with the angle of incidence [28] eq.2.1 can be rewritten as:

$$\lambda_0 = n\, p\, cos\theta$$

(2. 2)

where θ is the angle between the helix axis and the incident light and it is schematically represented in figure 2.8.

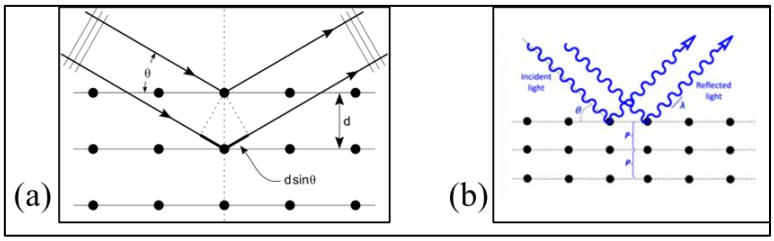

Figure 2. 8 (a) Bragg' Law schematic representation (b) the reflected light with helical pitch P and incident light angle θ.

The cholesteric phase will have bright colours if the wavelength will be in the visible range of the electromagnetic spectrum of light and we will have iridescence phenomenon.

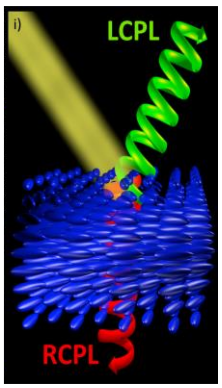

Figure 2. 9 Schematic representation of circular polarized light (CPL) selectivity through a CNCs film (reflected and transmitted colours are for better visualization and do not represent any physical properties).

In other words, into cholesteric structures, the incident polarized light with the same handedness as the cholesteric structure is totally reflected, while opposite handedness is transmitted (figure 2.9). Meaning, right circularly polarized (RCP) light will be selectively reflected by cholesteric materials with a right-handed helix, such as HPC aqueous solutions, while left circularly polarized (LCP) light will be reflected by cholesteric materials with a left-handed helix, as is the case of the aqueous CNCs LC phase [29].

2.3.Derivates

The hydroxyl (-OH) groups in cellulose are all accessible sites for chemical reactions, where the hydrogen atom of each hydroxyl group can be substituted, which explains the wide variety of

cellulose derivatives commercially available with different properties[28]. Depending on the type of substitutes added to lateral chain and on the degree of substitution we will have many different cellulose derivatives with different properties [30].

For example, by substituting the hydroxyl groups of the C2, C3 and C6 carbons with hydroxypropyl groups a highly substituted ether cellulose derivative is obtained which takes the name of hydroxypropyl cellulose (HPC) (Fig.2.10).

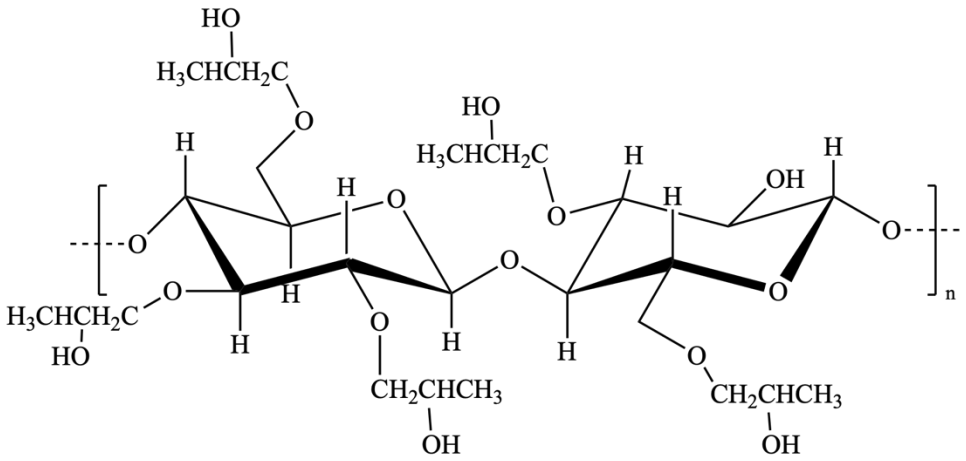

Figure 2. 10 Schematic of a idealized structure of HPC where the degree of substitution is 2.0.

The presence in the structure of both hydrophobic and hydrophilic groups, causes HPC to have a lower critical solution temperature (LCST), below 45 ºC [31]. HPC is water and polar organic solvents soluble. The polymer is biodegradable, biocompatible, electroneutral, widely used in pharmaceutical and food products mainly has emulsifiers and encapsulators [30], [31].

Instead, if ones use acid hydrolysis it is possible to remove the amorphous parts of cellulose fibrils and obtain cellulose nanocrystals (CNCs). These nanoparticles are spindle-like nanometre-scale materials with unique properties such as high strength [33], [34] high specific surface area[35] , high thermal stability [36], optical transparency [37], [38] ,biodegradability [39], biocompatibility, and present self-assembly capability [26], [40]. CNCs will be discussed in detail in the following section.

2.4. Cellulose Nanocrystals

Bulk cellulose consists of ordered crystalline regions and some disordered (amorphous) areas, depending on its source [41]. The most used synthesis technique is the acid hydrolysis, which by raising the temperature above room temperature and adding sources of hydrogen, through an acid that can be sulfuric (H_2SO_4) or hydrochloric (HCl), it is possible to remove the amorphous areas of the microfibrils and release the crystalline ones obtaining CNCs from cellulose.

The resulting nanoparticles show unique and better properties than the starting cellulose such as high specific strength, high Young's modulus, high surface area and well-defined liquid crystalline

properties in water [41] and this was also shown in other organic solvents. CNCs suspension (CNCs dispersed in water) self-assemble into a cholesteric phase forming the liquid crystalline phases at relatively low concentrations (between 3 w/w% and 7 w/w%). This particularity can be exploited to produce systems with structural colouring without the need to use a dye [10].

Another important feature is that solid films of CNCs prepared by solvent casting technique (evaporation) of aqueous suspensions of cellulose nanocrystals retain the lyotropic structure and show extraordinary optical properties such as iridescence, selective reflection of left circularly polarized light and transmission of circularly right polarized light [42]. These films' production process is designated as EISA (evaporation induced self-assembly).

2.4.1. CNCs Properties

CNCs suspensions and CNCs films with all their properties, above all thanks to their optical properties, resistance, biocompatibility biodegradability and nontoxicity are excellent candidates with a huge potential for a large scale of applications. Here we resumed CNCs most important features.

- Aspect ratio (L/D)

Rod-like shape is the most common shape for CNCs. The average length is generally, of the order of a few hundred nanometres, while the width is of the order of a few nanometres. CNCs are often described in terms of its aspect ratio. This morphological feature depends on the origin of the cellulose substrate and on the extraction method. However, it is accepted that the raw starting material is the most important factor [17], [43], [44]. In literature several aspect ratio values are reported, one example for leaves of cotton and Posidonia oceanica, vary approximately between 10 and 75, respectively [45]. Another example is reported by Saraiva et al. for CNCs derived from 50 μm cotton microcrystals where the length and the width values are 153 ± 34 nm and 6± 2 nm respectively and an aspect ratio of 26 were obtained [46].

The aspect ratio has a close relationship with the mechanical properties of the CNCs when it is incorporated into a polymer matrix, in fact there is a direct proportionality between the aspect ratio and the reinforcement effect.

- Specific Surface Area

An intrinsic feature of CNCs' dimensions at the nanoscale is the large specific surface area. The reported CNCs specific surface is estimated to be greater than 100 $m^2 \cdot g^{-1}$ but can reach values up to several hundred $m^2 \cdot g^{-1}$. Assuming a rod-like geometry and a density of 1.5 or 1.6 $g \cdot cm^{-3}$ for crystalline cellulose the specific surface area of the CNCs can be estimated from the average

geometric dimensions of the nanoparticles. It can be fully assumed generic that the specific surface area is directly proportional to the aspect ratio and inversely to the CNCs' diameter.

- Excellent mechanical properties

There is limited understanding of the intrinsic mechanical properties of the individual CNCs, as there are several factors that can influence them such as crystal structure (polymorphism), crystallinity, anisotropy, sample preparation etc. Therefore, it is important to take all these factors into consideration when comparing the mechanical property values reported for the CNCs [35], [47].

For native cellulose (mixture of cellulose Iα and Iβ) the average value of the longitudinal elastic modulus is estimated to be around 137* GPa when considering intramolecular hydrogen bonding, and 92** GPa without intramolecular hydrogen bonding. For cellulose II, the average value of the longitudinal elastic modulus is around 113* GPa (where *meaning considering theoretical and experimental data and ** only theoretical data) [48].

These extraordinary mechanical properties, the high stiffness and strength associated with its renewable nature and low density, make the CNCs an ideal candidate as a reinforcing nano-elements for machining reinforced polymer nanocomposites with better mechanical performance.

- Crystallinity

CNCs can be considered as crystals with no apparent or containing a small number of defects, so its degree of crystallinity should be very high. The crystallinity values reported in the literature range from 46 to 96% and depend significantly on the measurement method and the data analysis method applied [17], [49]. The degree of crystallinity is also strongly dependent on the original cellulose source and isolation process. A higher crystallinity value will give a high CNCs modulus that will approach the theoretical modulus of a perfect crystal.

- Toxicology assessment and biodegradability

Among the most important properties of CNCs we have low toxicity (i.e., are practically non-toxic) and biodegradability. The biodegradability of CNCs in aqueous environment has been investigated according to OECD (Organisation of Economic Cooperation and Development) standards and it was found that unlike common nanostructures used such as fullerenes and carbon nanotubes that do not biodegrade, CNCs degrade faster than its macroscopic counterpart.

2.4.2. CNCs synthesis

The isolation of CNCs from cellulose materials depends on what type of sources of cellulose fibrils are used. Common the process occurs in two stages:

I. pre-treatment of the source material; useful to make the cellulose macromolecules more accessible and make them react better in the next step, removing impurities and non-cellulosic constituents from the cellulose molecules but leaving cellulose moieties intact, i.e. avoiding the breakdown of cellulose chains [35], [50], [51]. Based on cellulose source there are different types of pre-treatments, but usually it is always performed as a chemical treatment in two steps:
    a. alkali delignification performed with a 2% aqueous solution of NaOH at 80 o 100 °C and it is used to degrade and solubilize the non-cellulosic constituents;
    b. bleaching using oxidizing agents such as hydrogen peroxide (H_2O_2), ozone (O_3) or sodium hypochlorite ($NaClO_2$) that serves to remove residual phenolic molecules.

II. well-controlled and chemically induced treatment, generally it is a strong chemical hydrolysis reaction [52] which will be seen in detail in section 2.5.2.1. In this step a "complete" regioselective degradation of the less organized and more accessible fraction of the cellulosic material takes place, so releasing the crystalline domains from the "purified" material. In other words, the amorphous domains surrounded and incorporated in the cellulose microfibrils are hydrolysed and the result will be well defined nanocrystals.

If we start from microcrystalline cellulose or kraft pulp as source material, we will not have to do the first treatment and we can do directly the chemical treatment.

The structure and most of the properties, especially the morphological features (shape and size) of the CNCs, depend on the source of the original cellulose, which is linked to the biosynthesis of cellulose microfibrils, and on the isolation process of the CNCs from the cellulose microfibrils, including any pre-treatment or deconstruction processes [35], [53].

2.4.2.1. Acid hydrolysis

Rånby (1951) was the first to produce cellulose fibres by controlled hydrolysis of sulfuric acid giving rise from colloidal suspensions of cellulose crystals. His method is based on controlled sulfuric acid hydrolysis for CNCs isolation probably due to the resulting suspension stability and the possible application simplicity at laboratory scale. During the acid hydrolysis process illustrated in figure 2.11, hydronium ions ($H3O^+$) penetrate the amorphous domains of the cellulose chains, promoting the

hydrolytic cleavage of glycosidic bonds and releasing the individual crystallites. All the currently used procedures reported in the literature consist of the following four steps:

I. Strong acid hydrolysis of pure cellulosic material under controlled conditions of temperature, time, stirring but also by controlling the nature and concentration of the acid and the acid/cellulose ratio;

II. Dilution with water to stop the hydrolysis reaction and repeated washing cycles by centrifugation to eliminate excess acid and soluble saccharides.

III. Extensive dialysis in distilled water to completely remove free acid molecules and any soluble sugars present;

IV. Mechanical treatment, usually sonication, to disperse the nanocrystals as a more or less uniform stable suspension.

Additional post-treatment steps have also been reported to obtain particles with reduced polydispersion in size and / or effectively disperse and homogenize the CNCs suspension such as filtration, differential centrifugation, ultracentrifugation or high-pressure homogenization [17], [18], [51].

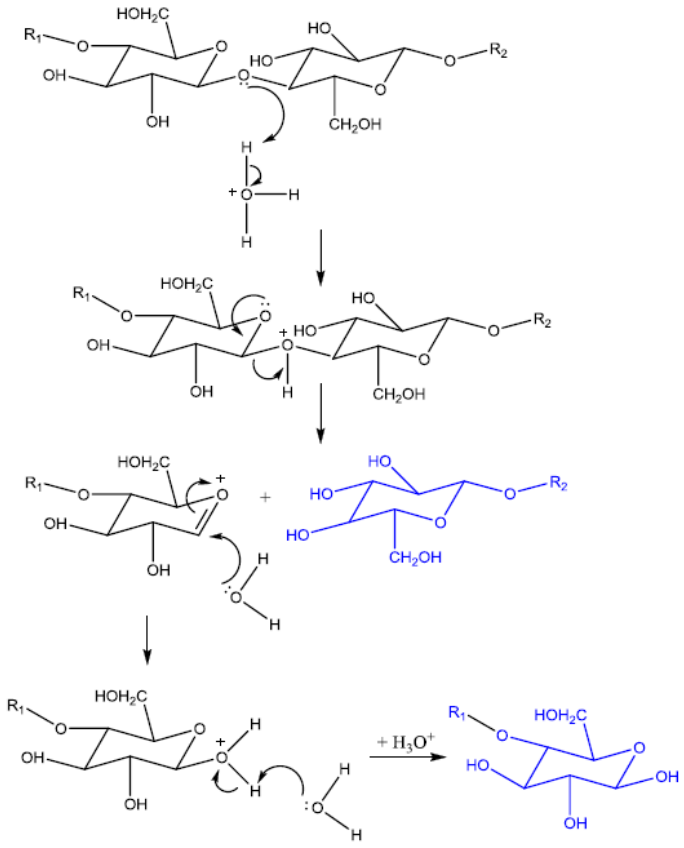

Figure 2. 11 Acid Hydrolysis mechanism

In acid hydrolysis the important parameters that influence the morphology, polymorphism and final properties of the resulting CNCs are the temperature and the reaction time, the acid nature, the acid concentration and the acid/cellulose ratio that are reported in step I and influenced the total reaction [54], [55].

The production of nanocrystals is based on the hydrolysis with sulfuric acid. In this case the sulfuric acid reacts with the surface hydroxyl groups of the cellulose to give surface sulfate ester groups (-OSO^{3-}) leading to the formation of a product with a negative electrostatic layer that covers the nanocrystals and favours their dispersion in water by repelling forces between the individual nanoparticles (Fig.2.12)

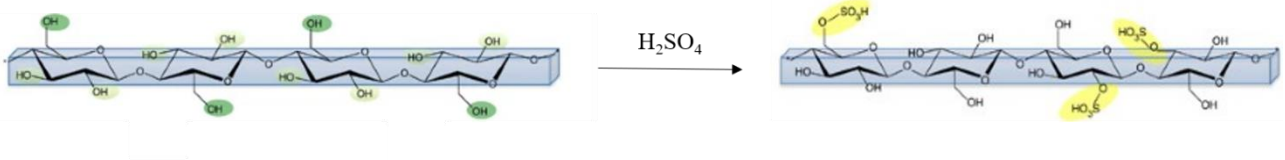

Figure 2. 12 Schematic representation of the reaction hydrolysis CNCs with sulfuric acid where some esterification of OH groups with sulfate groups are visible.

However, the thermostability of the nanocrystals is compromised by the presence of the charged sulfate groups, which can be easily neutralized by using a strong base, usually sodium hydroxide (NaOH) to improve its stability[18], [56]. This is one of the reasons why sulfuric acid is the most used to obtain stable aqueous CNCs suspensions. Typically, in hydrolysis catalysed by sulfuric acid, the concentration of sulfuric acid has a value of around 65% by weight, the temperature varies from room temperature up to 70 ° C, the hydrolysis time used typically ranges from 30 to 60 minutes but can go from 30 min to overnight, and the acid/raw material ratio values range from 8.3 to 35 mL · g-1 [17], [57]. In our case the preparation of CNCs was based on the experimental method used by Hamad et al. [58] with adaptations from Fernandes et al [59]. As the hydrolysis proceeds, the degree of polymerization (DP) of the cellulose the molecules should decrease and for example Battista et al. reported a good correlation between DP and nanocrystals' length measured through microscopic analysis[60].

2.4.2.1.1.Effects of internal factors during preparation CNCs

According to the Bragg diffraction equation, during the self-assembly of CNCs into a structural cholesteric coloured film, the main factor controlling the colour change of the film is the chiral nematic pitch which is influenced by many internal parameters such as the size, the size distribution, the surface charge density (i.e the sulfuric content) and the ionic strength [61]. If the molecules are

charged, they exhibit electrostatic interactions related to free energy in the system, which makes the formation of a chiral nematic phase of the charged particles more complex.

The most important relationship is the proportionality between the average length of the CNCs and the pitch (i.e. the greater the average length of the CNCs rod, the greater the pitch). The dried film shows an uneven rainbow colour or even the disappearance of the structural colour. Controlling the CNCs particle size is very important for achieving self-assembled monochromatic layers. With a decrease in the particle size, the prepared CNCs rainbow film could reflect natural light with a wavelength ranging from 360 to 695 nm, showing blue to orange structural colour.

The force between the particles is affected by the size of the particles themselves, and the most direct method of rigorously controlling electrostatic repulsion between CNCs is to change the surface charge density of the CNCs to vary the pitch-value in a controlled manner. For example, by increasing the hydrolysis time in the synthesis process, the particle size of the CNCs decreased and the sulfate content of the CNCs product increased. In this sense there will be an increase in the surface charge density, an increase in the electrostatic repulsion force, which will lead to an increase in the reflection peak of the main wavelength of the dry CNCs film from 271 ± 10nm to 517 ± 8nm. By adding an electrolyte that is capable of partially shielding the negative charge of the sulphate group, a decrease in the electrostatic repulsion between the particles occurs (and the particles move closer to each other) and therefore a decrease in the pitch of the cholesteric liquid crystals will be obtained resulting in a shift of the reflection band towards the blue end of the spectrum.

2.4.2.1.2. Effects of external factors in the preparation process

Since cellulose nanocrystals are small in size and have many hydroxyls active sites [62], their self-assembly is easily influenced by the environment. Physical methods are applied to prepare structural colour films of CNCs and by controlling the starting suspension properties the desired film colour can be obtained. The most commonly used method for the preparation of CNCs film is the EISA - evaporation induced self-assembly, method, that entails in solvent evaporations and self-assembly of CNCs into the LC phase.

The main external factors influencing the preparation process are here described: temperature, humidity, magnetic and electric field, ultrasonic treatments and different substrates.

Liu et al. [63]found that slow drying at a low temperature helps CNCs organize themselves into a perfect cholesterol-like structure, while at high temperatures the process becomes quick-drying and there is the formation of defects in the intermediate stage. Specifically, the authors show that at a temperature of 45 ° C, the nanocrystals were slowly desulfurized and at 70 ° C, severe damage to the helical cholesteric nature of the CNCs was observed due to deep desulfurization. By increasing the

treatment temperature, the liquid crystal structure of the CNCs suspension showed a change from the cholesteric phase to the nematic phase until no cholesteric phase remained.

Tran et al. [64] use the addition of masks in the process to produce CNCs patterned films. Through the use of masks, it is possible to locally control the evaporation of water and by monitoring it the self-assembly process of photonic structures made with CNCs is controlled. Furthermore, by controlling the humidity of the environment during evaporation, it is possible to prepare a series of films with different colours using the same suspension.

Frka-Petesic et al. [65]used an external magnetic field to control the orientation of the cholesteric phase. They found improved pitch uniformity and cholesteric phase orientation as well as improved optical contrast and unique angular response of the prepared thin films. In fact, the organization of the cholesteric suspension in a magnetic field was due to the intrinsic anisotropic diamagnetism of a single CNCs (as in the case of liquid crystals itself). Frka-Petesic et al. [66] also tried to use electric fields to control the orientation of the cholesteric phase in the suspensions. Through this method it is possible not only to precisely adjust the pitch, but also to guarantee the uniformity of the sample on a macroscale.

Another parameter taking into account into the CNCs' preparation process is the ultrasonic treatment that typically is used to obtain well dispersed CNCs suspensions. Ultrasonic treatment is used because it is able to destroy the hydrogen bond in the molecules of CNCs, thus preventing cellulose aggregation, providing fine and small CNCs particles and a stable colloidal suspension [63], [67]. Beck et al.[68] found that the ultrasonic energy given to the CNCs suspension prior to casting the film increased the distance between the chiral nematic phase and led to a redshift of the reflected light from the solid-state iridescent film. If the CNCs cholesteric liquid crystal suspension is subjected to high-power or long-term ultrasonic treatment, the energy provided by the ultrasound could release the charged ions bound to the bilayer on the surfaces of the CNCs. Consequently, the electrical conductivity of the system and the electrostatic repulsion between the CNCs will be increased, and there will be an increase in the pitch of the CNC's cholesteric liquid crystal.

Liu et al.[69] proposed a different explanation for ultrasonic treatments 'effects. In fact, the authors argue that through mechanical ultrasound the CNCs are broken into smaller nanocrystals, thus increasing the total number of particles and the specific surface. Therefore, under the action of low-energy incoming sound waves, it leads to a decrease in the torsion angle θ as the repulsive force between the particles and the internal axial force at a constant distance between the axes decreases.

Furthermore, Nguyen et al. [70] studied the effects of different supporting substrates on the formation of CNCs films. CNCs dispersions tend to minimize contact with highly hydrophobic substrates (e.g., polytetrafluorethylene, paraffin, and polyethylene), which is conducive to the formation of opaque

thick films such as mother-of-pearl. On highly hydrophilic surfaces (e.g., aluminium and alloy steel) CNCs dispersions can disperse and adhere to the substrate to form a blue film. Different rainbow-coloured films can be produced by drying the CNCs dispersion on different surfaces. In fact, the substrate' type could influence film 'thickness, and this determines a significant change in the pitch and consequently in the observed colour.

In summary, we learned that by imposing different physical restrictions under different conditions, CNCs assembly could be effectively controlled while preparing CNCs-based structural-colour films. We can say that: temperature changes will affect the desulfurization of the crystals' surface and the transformation of the liquid crystal; controlling the evaporation time will affect the cholesteric pitch; the CNCs suspension can be cholesterically oriented by applying a magnetic or electric field.

2.4.3. Liquid Crystal Phase

The structure of cellulose was assumed to be chiral when it self-assembly into a LC phase with a helical modulation. The first observation of LC phase in any cellulosic was with CNCs do by Marchessault et al. in 1957 [71]. In 1976 the LC was observed for HPC/H_2O mixture, HPC forms lyotropic cholesteric crystalline liquid phase according to its concentration in water. In 1980s Chanzy et al.[72] reported the cellulose' liquid crystalline phase and Navard [73] and Patel [74] observed the cellulose-based liquid crystalline phases. The liquid crystalline phases of most cellulose derivatives form chiral nematic structures as a result of the chirality of the cellulose backbone. The helical pitch and twist sense are the main parameters of a cholesteric phase, and we found them also in the liquid crystalline phases of cellulose.

2.4.3.1. Liquid Crystal HPC

Gray et al. [75] in 1976 observed HPC cellulosic liquid crystalline phase. They report that a drop of a concentrated aqueous solutions of hydroxypropyl cellulose placed between two glass plates and after the water was allowed to evaporate from the edges to centre, could generate lyotropic mesophases, which displayed a range of iridescent colours where the pitch in the visible range depending on water content [76] as we can see from figure 2.13, b. The authors attributed to the water molecules that occupy positions between the polymer chains, increasing the mobility of the polymer backbone and allowing the polymeric chains to align spontaneously parallel to each other to form a lyotropic mesophase.

The crystalline liquid phase formation is influenced by pressure, temperature, molar mass of the polymer, degree of substitution and solvents. When dissolved in water, the chiral nematic phase will

appear at 50–75 w/w% of HPC, when dissolved in water [8], [42] and at higher concentration if it dissolved in methanol and ethanol. It is capable of forming both thermotropic and lyotropic liquid crystalline phases [77]. It is well known that HPC-water solutions exhibit a complex phase diagram (Fig.2.13, c) including at room temperature an isotropic phase at HPC concentrations below 40 wt. % followed by a biphasic region and a cholesteric phase at higher concentrations.

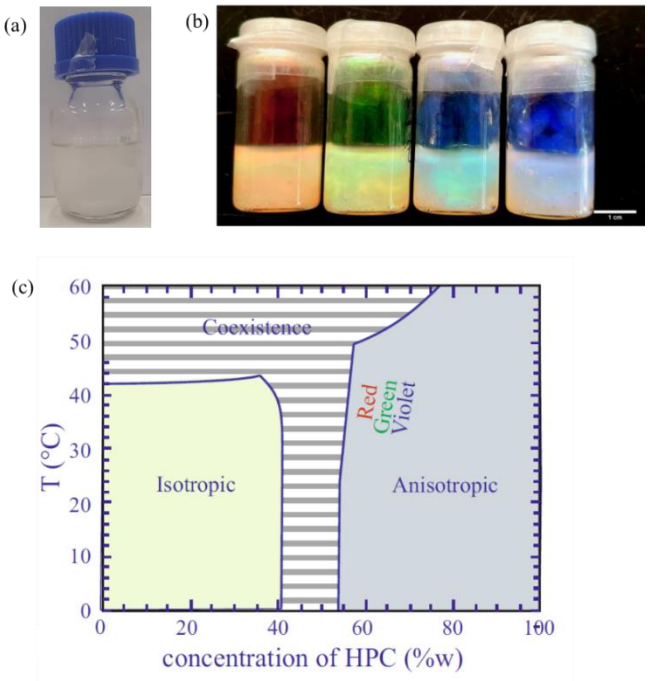

Figure 2. 13 (a) Optical aspect of isotropic sample of HPC/water mixtures with a concentration of 20%ww. (b) Visible colours from HPC/H2O anisotropic solution that reflected structural colour in the visible range where red, green, blue and violet correspond to 60, 62, 64.5 and 66% w/w. (c) Phase diagrams of the HPC/water binary system adapted from R. Werbowyj and D.G. Gray [76].

Textures observed through polarized optical microscopy (POM) samples with concentrations of water in the range of 45-65% are shown in figure 2.14. Transmission images show planar and focal conic textures for 45% and 65% HPC (Fig.2.14, a-d), only focal conic texture for 55% HPC (Fig.2.14, b) and oily streak texture for 55% HPC (Fig.2.14, c). The colours in figure 2.14 of the planar regions correspond to the reflection of structural colours from the samples.

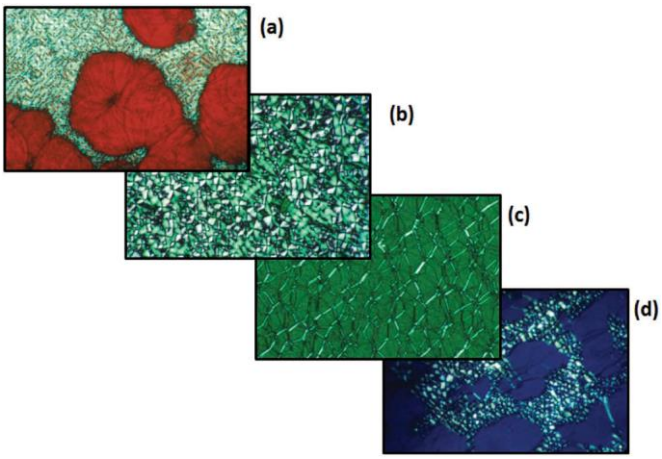

Figure 2. 14 HPC/water polarised light microscope, crossed polars, transmission images (a) ~45% HPC, planar and focal conic textures; (b) 55% HPC, focal conic texture; (c) 55% HPC, oily streak texture; (d) ~65% HPC, planar and focal conic textures.[78]

HPC and its derivatives generally form right-handed chiral nematic mesophases, with a pitch that increases with increasing temperature and decreasing polymer concentration. The pitch and chiral nematic twist sense of mesophases of cellulose derivatives are strongly influenced by the nature of the side-group substitution and the solvent.

2.4.3.2. CNCs suspensions Liquid Crystalline Phase and Properties

Marchessault [71], [79], was the first to observed birefringence in an aqueous suspension of CNCs, Revol et al. found that aqueous suspensions of CNCs can self-assembly into a chiral nematic phase[Revol 1982]. At very low concentrations, CNCs randomly suspend in water and form an isotropic phase. A nematic or cholesteric organisation of CNCs above a critical concentration is the result of favourable excluded volume interactions leading to higher packing entropy than in the isotropic phase [80]. Both left-handed (LH) and right-handed (RH), [81] structures have been observed in the past mean in other cellulosic derivatives but to date only CLC LH have been observed for CNCs suspensions. The CLC phase formation in CNCs suspensions can be explained by the phase equilibrium theories related to colloidal LCs such as the Onsager theory [80] or its extended version the Stroobants, Lekkerkerker, and Odijk (SLO) theory [82].

The phase diagram of CNCs/water system present three distinct regions [83] figure 2.15: an isotropic region in which the suspension does not appear to self-organize, a biphasic region in which the isotropic and the chiral nematic phases are in equilibrium and there is a critical value, C_a, that is the concentration where the chiral nematic phase starts to form [84]. Once the CNCs aqueous suspension concentration passes C_i starts the third region and CNCs will only show cholesteric LC phase [85] [35] where the chiral nematic pitch decreased with increasing CNCs content.

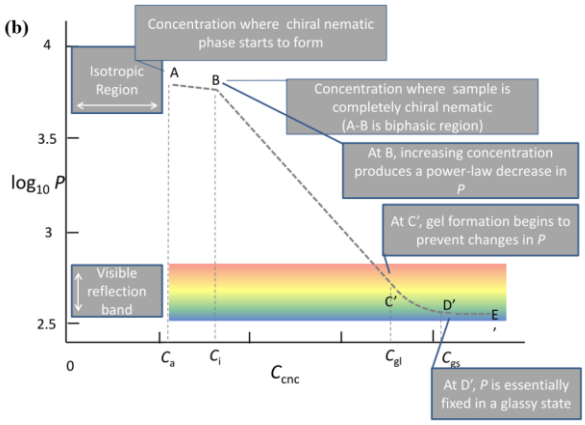

Figure 2. 15 Phase diagram of CNCs/water system.[83]

The three regions can be also observed with POM and the result will be for the first region a black image (Fig. 2.16, a), for the second region partial colour image (Fig.2.16, b) and a colourful image for the third region (Fig.2.16, c).

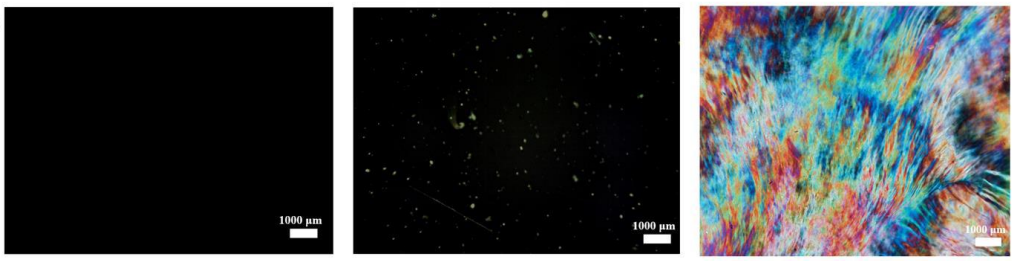

Figure 2. 16 POM images from the three regions of the diagram, from isotropic phase to crystalline phase [86].

POM images of a CNCs/H_2O aqueous suspension, placed in a rectangular capillary glass tube vertically, are shown in figure 2.17 where we can see the difference between the isotropic and anisotropic (~10% of volume fraction) regions. In the first region (left image) the typical tactoids with different sizes can be seen. As the concentration of CNCs increase the tactoid coalescence and bigger anisotropic domains can be seen (middle image). In the right image the formation of a polygonal texture is observed and as expected and a drastically reduction of isotropic region occurs.

Figure 2. 17 POM images CNCs of an aqueous suspension of CNCs at low concentration (~3% wt.) taken in transmission mode with cross-polarisers on three regions (from left to right): isotropic, border between isotropic-anisotropic phases and anisotropic region. Scale bar 100 µm.

2.4.4. Photonic CNCs-based nanocomposite

In this section it will be highlighted the structural colour in cellulose nanocomposite to see the possible applications considering what is already present in nature, as scarabee, beetles exoskeleton, flower petals and fruits [87] and future possibilities of application.

Structural colour is a type of gloss caused by the action of light waves and is widely observed in nature.

Structural colour, also known as physical colour, is the colour produced by a pure physical structure without any pigment [88]. They are produced by periodic and ordered structures via light scattering, diffraction, and interference [72]–[74].

A composite is any multiphase material that demonstrates a significant proportionality of the intrinsic properties of both its constituent phases, usually the constituent phases must have different physical and chemical properties and must be separated by a distinct interface. Many composite materials are composed of only two phases from a dispersed phase which is surrounded by the other phase which takes the name of matrix. Due for example to the dimension of the phases, if one or both phases have a dimension of less than 100 nm, the composite exhibits many unique and superior properties compared to conventional composite and are called *nanocomposites*. The most significant changes in the physicochemical properties of nanocomposites are due to the nanometer size of the particles translated in a high surface area which favour a greater interfacial interaction between filler and matrix. Hence the nanometric dimensions of CNCs make them an excellent candidate for the development of fully-biobased and biodegradable nanocomposites systems with enhanced technical performance.

Photonic nanocomposite materials are generally constructed by embedding an optically functional nanosized guest material (e.g. nanoparticles, nanocrystals and molecules) into an optically transparent host matrix such as organics (e.g. (photo)polymers, polymer blends, liquid crystals) or inorganic solids (e.g. glasses and ceramics). The addition of the guest material to the host matrix can yield significant improvement and modification in their mechanical, thermal, transport and optical properties over bulk materials [75].

As we seen in previous section the cholesteric phase of CNCs suspensions occurs at low critical concentrations of nanoparticles, between 3 w/w% and 7 w/w%. An important work was reported by Gray and co-workers [76] in 1990s with respect to the development of photonic materials based on CNCs.

We have already mentioned that the nematic chiral structure from the organization of the CNCs was preserved by the slow evaporation of water, after air drying, resulting in iridescent films [75]. The final structure depends on the drying conditions [57], [64], [78]. The pitch decreases with an

increasing cellulose concentration, and it increases with an increasing rod length. So, we can manipulate the structural coloration changing the helical pitch of the cholesteric structure.

It should therefore be kept in mind that CNCs films carry chirality on three different scales: at the molecular level due to the asymmetric carbon atoms of each D-glucose unit; on a nanometric scale for the screw morphology of the single crystals; and on a mesoscopic scale with the LH CLC structure. As we already seen structural colour and results can be affected by internal or external factors. In this sense a lot of applications in different fields are present in the literature.

2.4.5. Application

Due to the parameter, we take into consideration, which we can vary as presented above, a different response is obtained in the CNCs film colour that can be exploited in different fields of application. Researchers have studied the potential applications of CNCs in sensors [79] as for example humidity sensors based [80], tissue engineering[81], reinforced plastics and optical devices [82], [83].

Nowadays, cellulose-based products are widespread, but are still mainly used for low-tech applications such as banknotes, information storage and packaging [84]. But if we look at the excellent attractive optical properties of cholesteric solid films, this makes them promising candidates for new applications such as in anti-counterfeiting components in security papers (banknotes, passports, and certificates), polarizing mirrors, mirrorless lasing lasers, intelligent packaging materials, printed paper electronic devices, additives for paints, inks and cosmetic products and optical encryption. [51], [84]–[87].

During the last two decades many studies have been published where the authors introduce photonic structures from CNCs or CNCs nanocomposites. Is this revision some examples in different fields are illustrated below that intends to show the amplitude of applications explored so far.

Cao et al. (2018) [105] added hundreds of sub-micrometer micelles of anionic surfactant in aqueous CNCs suspension to prepare CNCs-based LC films. In this way the authors were able to widen the left circular polarized reflection band of the film. This can be exploited for the creation of optical composite devices.

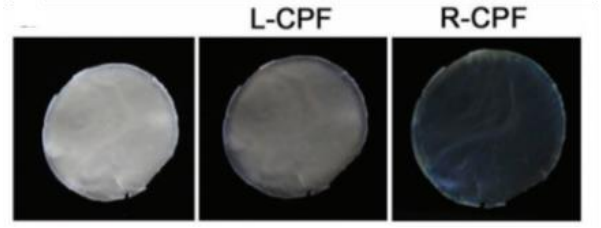

Figure 2. 18 Photographs of the broadband cellulose film viewed with natural light, left and right circular polarizing filter.[105]

Zhao et al. (2019) [106] developed a scalable printing method to produce arrays of structurally coloured CNCs microfilms from spatially-defined nanoliter sessile droplets. They fabricated responsive microfilms with high reflectivity, where the colour is deterministically controlled by the CNC ink formulation.

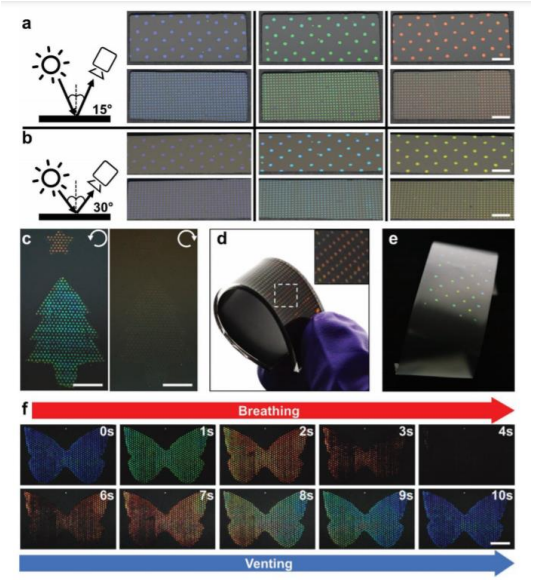

Figure 2. 19 a,b) Photographs of uniform red, green, and blue arrays of CNCs microfilms deposited onto a patterned glass substrate, with individual microfilm diameters of 1000 µm (top) and 600 µm (bottom). As the viewing angle is increased from (a) 15° (relative to the normal) to (b) 30° the arrays are observed to iridescently blue-shift, characteristic of a well-ordered 1D photonic structure. c) A "Christmas tree" dot matrix image consisting of both red and green arrays of 600 µm CNCs microfilms is clearly visible when imaged through a left-handed circular polarizer, but not visible through a right-handed circular polarizer. d) A CNCs microfilm array prepared on a flexible PDMS substrate. e) An array of CNCs microfilms was transferred onto adhesive tape. f) A blue "butterfly" dot matrix image rapidly and reversibly changed colour in response to the moisture in an exhaled breath. All scale bars correspond to 5 mm[106]

Fernandes et al. [59] reported a cellulose-based photonic structure that reflected both RCP and LCP light, that can be tuned by temperature variation and the application of an external electric field (Fig. 2.20, a), in this case CNCs were doped with active optically response element (5CB).

CNCs doped with passive elements was proposed by Wu et al. [107] that developed a cellulose nanocrystal-based film with left-handed cholesteric photonic (Fig.2.20, b).

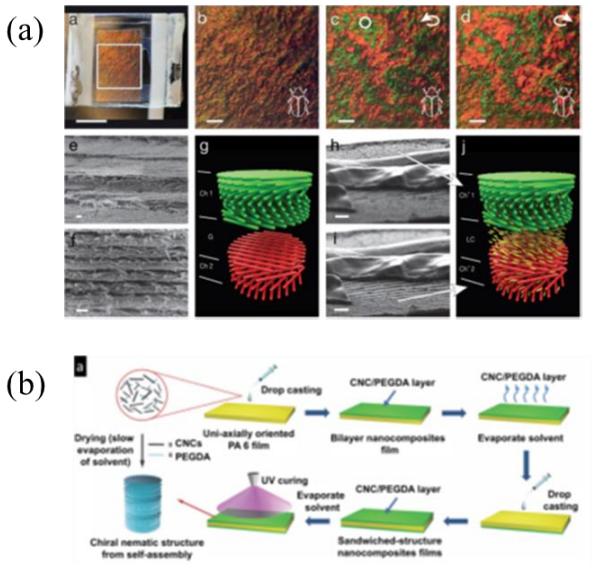

Figure 2. 20 (a) Photographs of CNC and 5CB composite film observed through unpolarized white light (a, b) and circularly polarized light showing different colour reflection in LCP (c) and RCP (d). Details of a CNC chiral nematic film SEM image cross-section showing cholesteric regions separated by gaps(e) SEM pictures, taken at room temperature, of the CNC film with the gap filled with an anisotropic liquid crystal (5CB), which is solid at room temperature, and infiltrated in (h,i). (j) Scheme showing the gap filled with the anisotropic layer sandwiched between the two left cholesteric domains [59]. (b) Schematic diagram of fabrication of biomimetic hyper-reflective CNCs-based nanocomposite film with a sandwiched structure [107].

Grey et al. [108] reported the integration of bioinspired photonic films based on cellulose nanocrystals into transistor devices capable of sensing distinct polarization states of CPL (fig. 2.21, bottom part). They produced the final devices, using an ion infiltration method necessary to enrich the photonic CNCs films with sodium ions from a sodium hydroxide solution. The infiltrated films are integrated as gate dielectrics in a staggered bottom-gate transistor architecture with amorphous IGZO as the semiconductor.

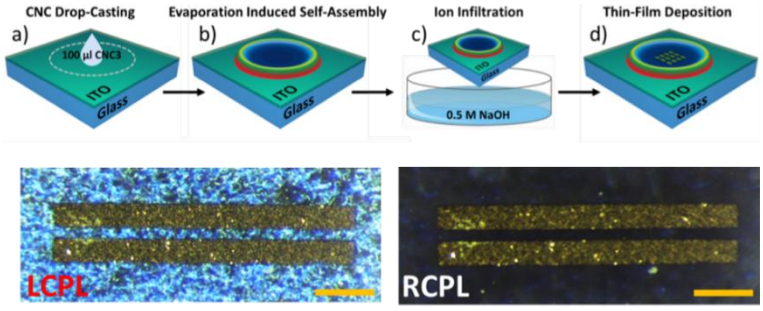

Figure 2. 21 Schematic representation of device fabrication, on top. The a-IGZO transistors under LCPL and RCPL illumination in reflection mode, respectively. Scale bars indicate 500 µm. [108]

Yao et al. [109] produced large, flexible, and flat photonic composite films with uniform structured colours from blue to red by assembling poly (ethylene glycol) (PEG) and CNCs creating a colourimetric sensor (Fig.2.22, left). In particular CNCs/PEG (80/20) composite film demonstrated a

structural colour change between green and transparent according to an increase and decrease of relative humidity (fig.2.22, right).

Wang and co-workers in 2018 [110] produced highly flexible CNCs films by adding glycerol with humidity and pressure-responsive chromism. With the additive, an improvement in the mechanical resistance of the CNCs has been achieved, allowing to obtain independent iridescent CNCs films with adjustable structural colours.

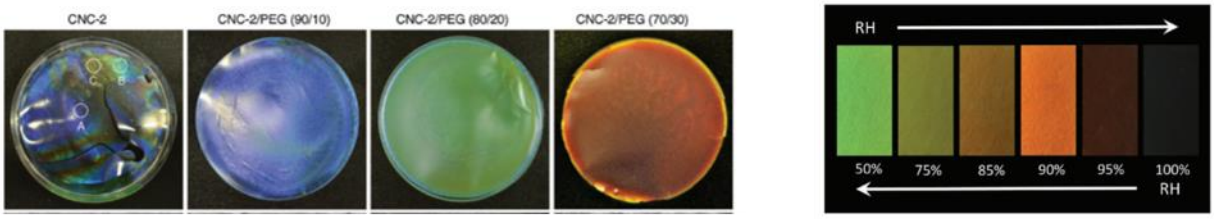

Figure 2. 22 Photographs of neat CNC and the CNC/PEG composite films showing various structural colours under white light illumination (left); Reversible structural colour change of the CNC/PEG(80/20) film under different RH (right).[110]

The iridescent characteristics of the CNCs film change according to the method of observation of the film itself (the irradiation of an ultraviolet light source, circular polarizer, naked eye or chiral spectrometer), the films have a good potential for application in the anti-counterfeiting field.

Chen et al. [111] a self-healing and responsive chiral photonic film (SCPF) based on the co-assembly of boronic ester crosslinked poly(vinyl alcohol)-polyacrylamide with CNCs. A QR code was printed on paper and covered by a thin film of the reported CNCs/polymer composite. It was proven that the QR code was exclusively encoded by a cell phone, when right-handed circular polarized light was used (Fig.2.23).

Zhang et al. (2012) [92] presented an iridescent fluorescent CNCs film with multiple potential security features: overt security (iridescence) and covert security (selective circular reflection and fluorescence). They also found that the addition of a fluorescent whitening agent (FWA or OBA) can increase the spacing of CNCs-based linear LC structures and at the same time, the iridescent properties will not be affected. The structural colours were preserved in fragment film, which made them show strong iridescent colour, thus realizing an anti-counterfeiting function. (Fig.2.24)

Gan et al. recentely (2019) [113] created a vertical assembled device, where one of the layers is a CNCs film and in this way they are able to hide its information in natural light and show the information hidden under UV radiation. (Fig.2.25)

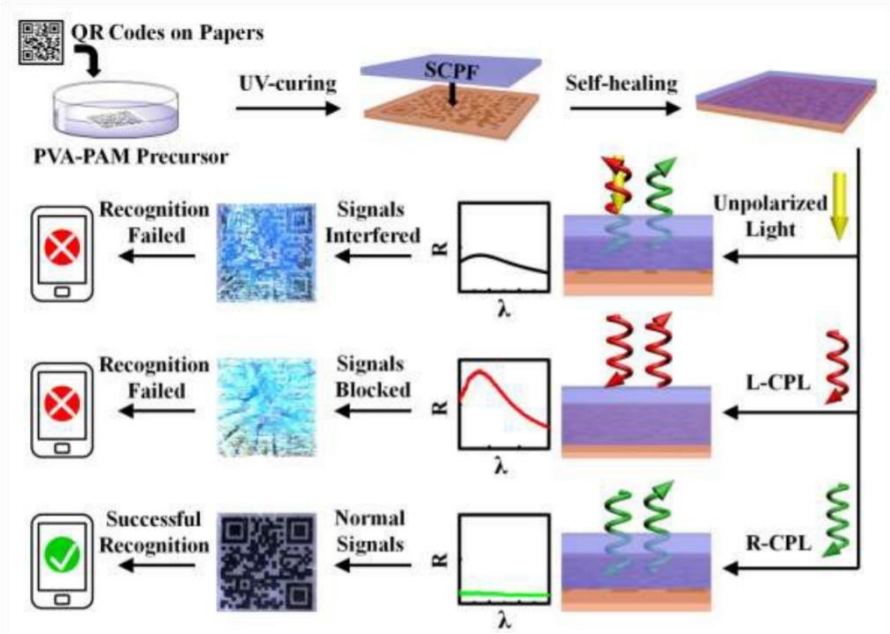

Figure 2. 23 Schematic illustrations showing encryption and recognition of the paper printed QR codes encoded by SCPFs. [111]

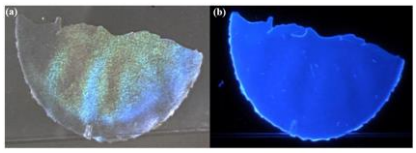

Figure 2. 24 Iridescent CNCs-based LC film doped with 50 ppm TINOPAL OBA (a, under conventional illumination) and excited with UV light (b).

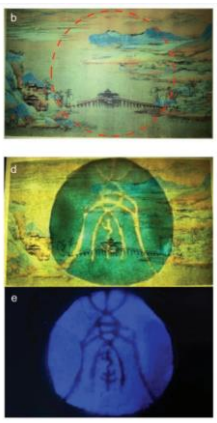

Figure 2. 25 b) A copy of Chinese painting “The Vast Land (author: Wang Ximeng)” under natural light with a patterned vertical-assembly film (in red break circle) of SCNCs in its back. d) with natural light, and e) without natural light.[113]

2.5.Experimental Part

Recently, much interest has been given by the scientific community to cellulose nanocrystals (CNCs)-based materials, since these nanoparticles present a set of advantages that are built on the ones derived from their precursor, the biopolymer cellulose. Based on several research studies, it can be found that the addition of small molecules or polymers to an unmodified CNCs colloidal suspension allows it to retain the chiral nematic arrangement; this addition does not inhibit the LC formation. Starting from this, with this work, we focused on the production of iridescence and flexible CNCs composite films. Firstly, the synthesis of CNCs from cellulose microcrystalline (Avicel®), the influence of the nanoparticles counter-ion CNCs-H and CNCs-K on the structural colour, and some characterisation as FTIR and EA will be presented. Mixtures are obtained starting from the same CNCs lyotropic suspension in which we add first hydroxypropyl cellulose in different ratio, and second CNCs functionalised with a dye. Films in all cases obtained from solvent evaporation, are intended to display selectively reflection of left circularly polarised (LCP) light, within the visible range, and responsiveness to external stimuli were produced.

We report the addition of hydroxypropyl cellulose into a LC CNCs colloidal suspension and study the effect of the presence of this non-ionic water-soluble polymer in the chiral nematic organisation of the lyotropic suspension and produced films. The CNCs-K/HPC films produced by solvent evaporation were photographed, its thickness measured, characterised using POM, Vis spectrometry, FTIR, XRD, DSC-TG, SEM and photos.

On the other hand, based on the idea that Rhodamine B is an important Laser dye with excellent photophysical properties, such as a long wavelength absorption and emission, high fluorescence quantum yield, large extinction coefficient and high stability against light [114], the introduction of such compound in our systems will increment the advantages of CNCs iridescent films. Use of Rhodamine B it is particularly interesting to obtain fluorescent chemosensors since the dye framework offers selectivity based on its particular structural property [114]. With the goal to develop a cellulose derivative with a fluorescent response that could be used as an anti-counterfeiting device, synthesised functionalisation of CNCs with rhodamine B ester [ref], that sequentially were added it to the CNCs lyotropic suspension previously prepared. CNCs/CNCs_RhodB film are obtained with EISA and characterised using POM, Vis spectrometry, FTIR, CD, SEM and photos.

2.5.1. Flexible CNC-K/HPC nanocomposite films

CNCs/HPC nanocomposite films aimed to be prepared with the idea to tune iridescent structural coloured films that reflect wavelengths in the visible range of the electromagnetic spectrum. As previously mentioned CNCs, films tend to be brittle, so it is important to add a plasticizer to diminish

their strength and induce flexibility, which lead to a change in their mechanical properties. For instance, the addition of the HPC reported by Gouveia[115] to CNCs suspension allows increases the pitch values of the films while raise flexibility, which extends its range of applications, especially where flexibility is necessary.

The work of Gouveia [115], soon after published by Saraiva et al. ref, showed that as the content of HPC, $\overline{M_w} = 86000$, in the CNC-H suspension increases a shift of the reflected wavelength on the films to the Near-Infrared region occurs. This work also showed that the flexibility of the films was increased. The presented results were in line to what Yao et al. [89]stated about the use of CMC PH-101 (50 μm size particle) in composite systems. The authors refer that starting with CNCs from CMC PH101 would not lead to composite films (CNCs/PEG) with reflected colouration in the visible range of the electromagnetic spectrum and showed that the use of longer CMC particles (PH-200). Yao et al. also showed that the reflected wavelength of a CNCs-H film is 623 ± 17, in line to what Saraiva et al. shows (670 nm). Although this comment, films with a covert reflection were obtained and are valuable for anti-counterfeiting systems.

In this work, it was expected to improve flexibility in the composite films and maintained the structural colouration in the visible region by rising the average molecular weight of HPC (from 86 000 to 300 000). This study also allowed us to attest if these larger polymeric chains of this derivative did not hinder the liquid crystalline phase of the aqueous suspensions. However, having in mind that CNCs-H already shows an orange like structural colour and CMC PH200 is not easy to acquire a solution was sought.

Dong et al. [93]were able to demonstrate that the presence of inorganic counterions affect the critical concentration of LC formation in charged CNCs with the of order $H^+ < Na^+ < K^+ < Cs^+$; this is the presence of counterions will not hinder the LC formation but shift it to higher values for the phase transition of isotropic-anisotropic. The ionic strength of these suspensions is altered by the different counterions and induces changes in the electrostatic repulsions and subsequently on the forces between particles. However, the authors emphasized that this type of forces is also dependent in steric and hydration forces, hydrophobic interactions, and hydrogen bonding. The counterions used present different properties as size, hydration number and hydrated ion size, with both last two properties decreasing with higher atomic number. The binding of these ions to the CNCs with a negative charge will induce hydration forces between the nanoparticles. Since this type of force is repulsive for CNCs, it is expected to be higher for small counterions. So, these ions will affect the hydrodynamic volume of the CNCs that decreases from H^+ to Cs^+. So, adding the bigger counterions will favour the formation of LC suspensions with higher pitch values. Having in mind this work, a change of the CNCs' counterions seemed to be the best route to continuing using CMC-PH101. In our case, we

decide to exchange our counterion (H+) for potassium (K+). First, CNCs-H aqueous suspension were prepared, followed ion exchange and its characterization and succeeded by the addition of different contents of HPC with an average molecular weight of 300 000.

2.5.1.1. Isolation of CNCs from microcellulose fibers

Cellulose nanocrystals from microcrystalline cellulose (Avicel® PH-101, 50~ μm particle size, lot #BCBJ0229V) (CNCs) were produced based on the experimental method used by Saraiva et al. [X] [46]with adaptations from Fernandes et al [35B], with a reaction scheme represented in figure 2.26.

The cellulose was hydrolysed in sulfuric acid (95-98% purity, Sigma-Aldrich) diluted at a concentration of 64% w/w, with an acid/solid ratio of 8:1, at 45 ºC, for 45 minutes while under continuous mechanical stirring.

The cellulose was added to the sulfuric acid and hydrolysed at a medium speed (300 rpm) which was increased as the viscosity of the reactional mixture decrease. The resulting suspension was washed with ultrapure water type II (~10 times the volume of the acid solution used) to stop the hydrolysis and allowed to settle overnight. The process was repeated until a pH in the 0.7-0.9 range were reached. The white remaining layer was submitted to subsequent wash by centrifugation cycles (at 12 000 rpm for 20 minutes, using a Thermo Scientific Heraeus Multifuge X1R Centrifuge Series).

The CNCs suspends when the pH is between 1.9-3.9 and the supernatant was collected. This suspension was placed into cellulose films (Spectrum Spectra/Por® 4 dialysis films) and then dialyzed with ultrapure water for a minimum of one month, with daily water changes until the pH remained constant, to ensure the elimination of the remaining sulfuric acid and other sub-products of the reaction.

A CNCs suspension with 3.81 ± 0.08% w/w. concentration was obtained.

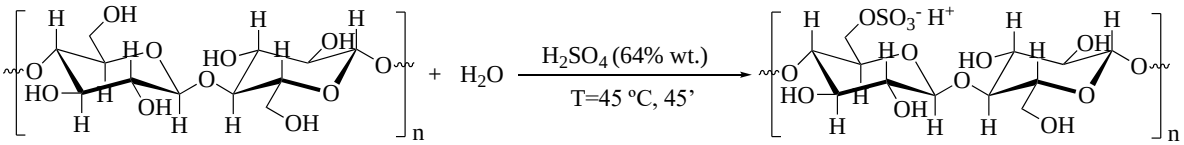

Figure 2. 26 Schematic representation of the acid catalysed hydrolysis and esterification reaction of cellulose using sulfuric acid to produce cellulose nanocrystals. As the reaction occurs the protons (H+) from the acid attack the β-(1,4) glycosidic bonds in the amorphous regions leading to a decrease of the degree of polymerisation of the cellulose. The process proceeds to the esterification reaction introducing sulphate groups of the nanoparticles.

1.1.1.1. Ion Exchange

Based on article by Dong and Gray [42], where ion-exchange resin was used to replace the protons from the surface of the CNCs to other ions, H^+ ions of CNCs nanoparticles (CNCs-H) were replaced

by potassium ions (CNCs-K). In figure 2.27 is shown a schematic representation of the ion-exchange effect on the surface charge of the cellobiose unit.

Starting from a sodium ion exchange resin (Amberlite® IR120 Na^+ form, Sigma-Aldrich), the ions Na^+ in the resin, were replaced by K^+ ions using a 20% w/w aqueous potassium chloride solution. Several washing/filtration cycles were done with water until the conductivity of the water removed was equal to the one added. After that, CNCs was added to this new ion-exchange phase and the mixture was gently stirred to induce replacement of the ions as presented, until a constant pH was reached (~5).

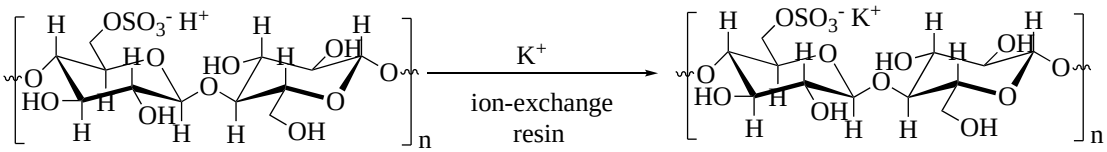

Figure 2. 27 Schematic representation of the ion-exchange effect on the surface charge of the cellobiose unit.

2.5.1.2. CNCs Characterisations

Once CNCs were produced it was necessary to perform some chemical and physical characterization if order to confirm that the extraction of nanoparticles was done. First a chemical analysis was performed by Attenuated Total Reflectance Fourier Transform Infrared spectroscopy, since is an effective tool to allow the qualitative composition of a compound. The obtained spectra are presented below (Figure 2.28) where the black correspond to the CMC, to be able to compare with the one of CNCs-CMC (red line).

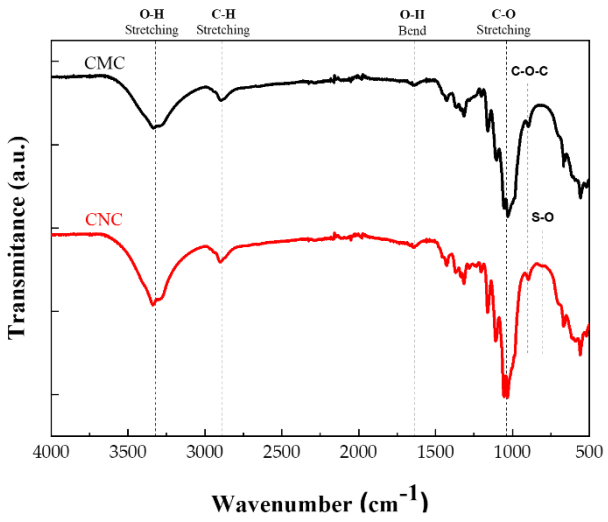

Figure 2. 28 ATR-FTIR spectra of CMC (black line) and CNCs (red line). Each vertical dotted line corresponds to the absorption's bands characteristic of the macromolecule of cellulose and nanocellulose.

Several absorption bands associated with molecular vibrations of cellulose bonds can be observed. The coincident bands of both CMC and CNCs are 3338 cm^{-1} (O-H stretching), 2900 cm^{-1}(C-H stretching) and 1060 cm^{-1} (C-O stretching) [117]. The absorption band at 1638 cm^{-1} and at 890 cm^{-1} are associated with the vibration of the O-H bond of water absorption in the cellulose and with a C-O-C stretching effect on the β-(1,4) glycosidic bonds (assigned to the amorphous region), respectively [118], [119]. The similarities observed between the two spectrum allows to conclude that the hydrolyses process does not affect the molecular structure of our polymer. However, CNCs spectrum shows a band at approximately 817 cm^{-1}, that is non-existent in the CMC sample, and is attributed to stretching of the S-O bond. This allows to infer that the esterification reaction occurs, and deprotonated half-ester sulphate groups are introduced on the surface of CNCs [120].

The amount of sulphate groups attached to the cellulose nanocrystals surface can be verified by elemental analysis presented in Table 1, where the content of each element within the samples is detailed. It was also included the predicted values for pure cellulose[121]. Samples from the raw microcrystalline cellulose lack the sulphur element as it has not undergone acid hydrolysis. The degree of substitution (DS) considering the empirical formula $C_6H_{10}O_5$—(SO_3) was estimated with the equation[58] $S(\%) = \frac{100n \times S}{6C+10H+(5+3n)O+nS}$, resulting in 4.92 half-ester sulphate groups per 100 anydroglucose unit. The slightly higher value of DS, when compared with the one reported by Saraiva et al. [46] might be related to the longer reaction time use here.

Table 2. 1 C, H, S and estimated Oxygen elements content of the sample CMC and CNCs-CMC, as well as the predicted values for pure cellulose.

Samples	Carbon (w/w%)	Hydrogen (w/w%)	Sulphur (w/w%)	Oxygen* (w/w%)	-OSO_3H/ 100
Pure cellulose predicted values	44.44	6.18	-	49.38	-
CMC	43.51	6.42	-	50.09	-
CNCs	41.03	6.04	0.95	51.98	4.92

To guarantee that the hydrolyses of cellulose was efficient the size of our nanoparticles were determined. Images of AFM images (see an image example in figure 1B in appendix B) obtained in tapping mode. Using Gwyddion software and the methodology described by Hornatos-Rios et al. [94]it was possible to determined that our nanoparticles have an average length and diameter are 153 ± 34 nm and 6 ± 1 nm, respectively, with n=135 (particles measured).

Further characterisation was exploited, but it will be presented as comparison with the nanocomposite films. Instruments and sample preparation are presented in appendix B.

To corroborate that a blue shift of the reflected wavelength was obtained, films from CNCs-H and CNCs-K suspension were produced by solvent evaporation of 2 ml of 3 wt% nanoparticles suspension and with a controlled temperature and relative humidity. In figure 2.29, it can be seen that the intended shift to shorter wavelengths was observed by changing the counterion from H^+ (a) to K^+ (b). The CNC-H originated a film with an orange-ref structural colouration, while with CNC-K a film with a light blue film when illuminated with an uncollimated light. Since this structural colouration derived from retaining the cholesteric arrangement in the solid film verification of selected reflection of left-handed circular polarised light was achieved. As expected, the reflection of left-handed circular polarise light is observed for both films, and the transmission of right-handed circular polarise light is observed.

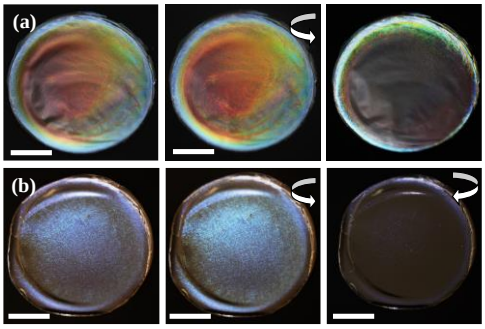

Figure 2. 29 Photographic images of CNCs-H (a), CNCs-K (b), respectively. They photographs were obtained under unilluminated visible light (first column), with a left circular polarizer (second column) and aright circular polarizer (third column). The scale bar corresponds to 1cm.

2.5.2. CNCs-K/HPC film

2.5.2.1. CNCs-K/HPC film production

In order to prepare the CNCs-K/HPC films, HPC (Sigma Aldrich, $\overline{M_w} = 300000$) was added to a ~3wt.% CNCs aqueous suspension in different ratios. The prepared suspensions will give rise to films with CNCs-K/HPC ratio of 90/10, 80/20, 70/30, 60/40, 50/50, and the sample identifier is the CNC/HPC ratio.

CNCs-K/HPC films were produced by the solvent evaporation technique. A certain amount, corresponding to 0%, 10%, 20%, 30% (e), 40% (f) and 50% (g) wt% of HPC was added to CNC-K aqueous suspension, the resulting mixture were homogenised by means of magnetic stirring until complete HPC dissolution and allowed to set until the presence of the anisotropic phase was observed. 2 ml of each obtained composite suspensions were deposited into polystyrene Petri dishes, with 35 mm diameter, under controlled environment, until all the solvent evaporated. Evaporation took place at ~ 4 ° C and 60-70% of RH and it took about three weeks for it to be complete and the iridescent films to form.

2.5.2.2. CNCs-K/HPC film's Characterisations

The first part of the characterisation was based on macroscopic observation. The films were observed and photographed under uncollimated visible light, left column of figure 2.30. The observation of the reflection selectivity with circular polarisers was achieved and photographs, using a left circular polariser (LCP) and a right circular polariser (RCP) of the CNCs-K/HPC's composite films, with a diameter of 3.5 cm, with 10% (b), 20% (c), 30% (d), 40% (e) and 50% (f) w/w of HPC were obtained. It is important to notice that while doing this work the group of Professor Mark MacLachlan published an article with a similar work [123]. Nevertheless, the authors present a series of composite films where HPC of 80 and 370 kDa was used.

From the photographic collection (Fig. 2.30), we can see that all the films exhibited iridescence, selective left-handed circularly polarised light reflection, with the observation of a strong bright colouration and right-handed circularly polarised light transmission, where the films became almost colourless. As we can see a uniform colouration throughout the entire films were not achieved and, in all films, a small blue outer ring, probably induced by the geometry of the container during the evaporation rate process was presented. The film with 30% w/w HPC exhibited a brightness decrease and the films with 40% w/w of HPC and upwards presented a matte finish. CNCs-K film (Figure 2.30, a) is blue and is the only one with a slightly uniform colouration considering the film's diameter. Looking to CNCs-K/HPC films: the 10% w/w HPC (Figure 2.30, b) film shown a predominant green iridescent colouration while the 20% w/w HPC (Figure 2.30, c) a reddish colour. Films with 30%, 40% and 50% w/w HPC, in figure 2.30 d, e, f respectively, have a colour variation in three distinct areas, the red centre, which tends to gradually become wider as HPC percentages increase, a blue periphery and a green area in between.

Figure 2.30 on the right column shows SEM images acquire in a cross-section region of the films. All the films exhibit nanostructures derived from the left-handed cholesteric arrangement of the LC of the suspensions of the nanocomposites. These results showed that the HPC used in this study did not disturb the cholesteric arrangement of the CNCs-K in aqueous suspension. Moreover, the experimental conditions used to prepare this series, as long settle times after adding HPC to the CNCs' suspension and long solvent evaporation rates, gave rise to structures that show a similar arrangement of the one observed for the brittle films even with 50 % w/w of HPC in the system. This result was not observed by Saraiva et al.[46], where the SEM images of the films with 50% w/w of HPC present products with not so well organised structures with higher contents of HPC.

The thickness of the films was measured with a micrometer from Mitutoyo (Appendix B) and the composite systems with 10 and 20% w/w of HPC present similar values (181 and 186 μm, respectively) than the one returned for pristine CNCs-K film (178 μm). As the content of HPC

increases the thickness of the films decrease reaching 70 for the nanocomposite with 50% w/w of HPC. No evidence of polymer segregation was observed macro- or microscopically in the free-standing films. If one compares these values with the ones obtained by Saraiva et al.[46], it seems that the increase on the HPC molecular weight and its increase of content in the composites leads to a decrease in films' thickness, whereas the authors did not encounter considerable difference on the film's thickness. One might attribute this result to the non-entangled/entanglement state of the macromolecules within the materials, as reported by Bercea and Navard [124]for HPC solutions with different molecular weights.

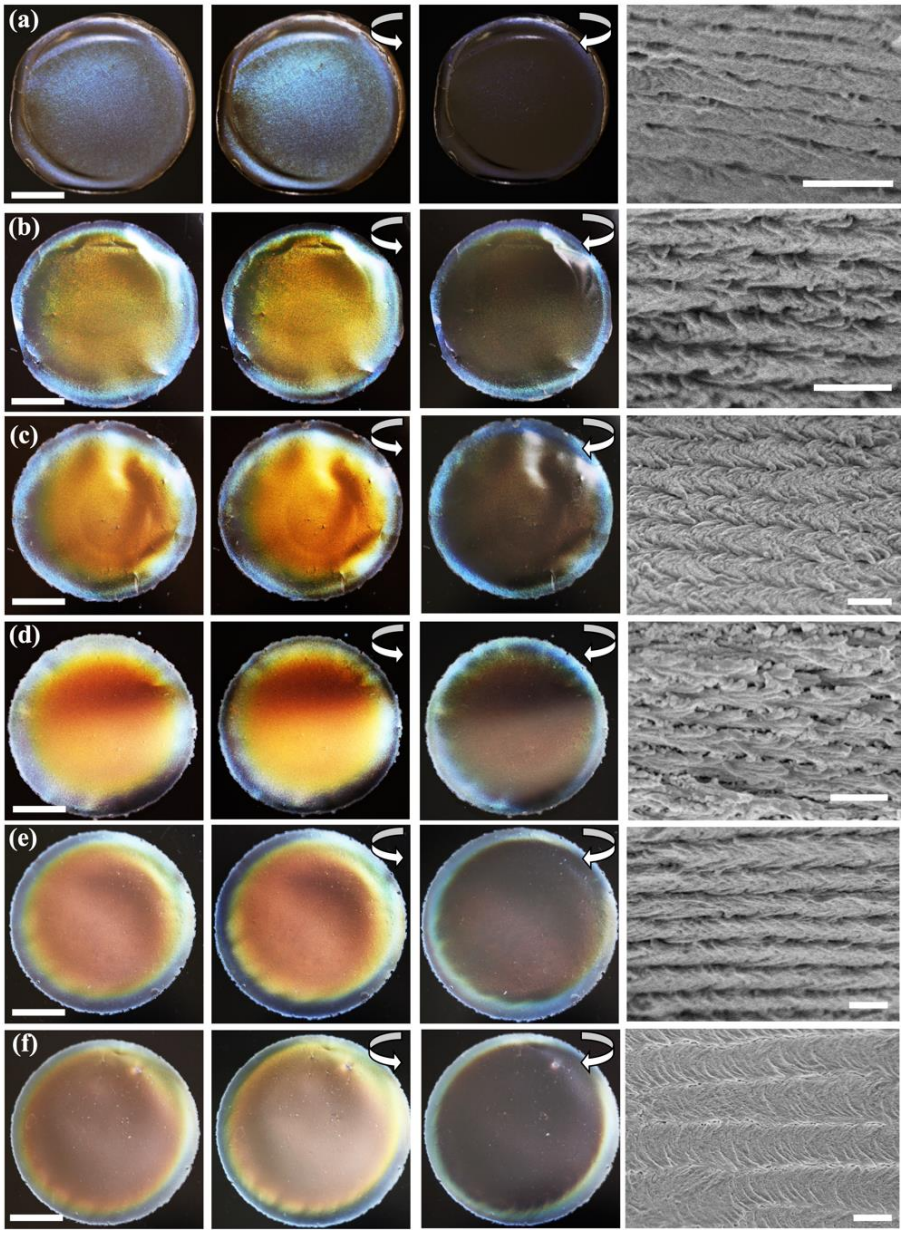

Figure 2. 30 Photographic images and cross-section SEM images of, CNCs-K (a), 10% (b), 20%c), 30%(d), 40% (e) and 50% (f) w/w of HPC films, respectively. They were observed under visible light (first row), using left circular polarizer (second row) and using right circular polarizer (third row). The scale bar in macro photographs corresponds to 1cm, in SEM images a-e 500 nm and f 1 μm.

The structural colouration of the centre of the films was confirmed using POM reflection images. POM analyses were performed, also in this case under visible light, left-handed circular polarisation, right-handed circular polarisation and its characteristic wavelengths determined by spectroscopy (figure 2.31). The LCP spectra were used to determinate the maximum wavelength peak, the wavelength variation (by the FWHM value) and the estimated pitch value, using the Vries equation (equation 2.1), for each film, which are reported in table 2.3.

Table 2. 2 Maximum wavelength peak determined from spectra maximum reflectivity value, the cholesteric pitch value using the de Vries expression and Δλ wavelength variation (FWHM values, related to the spectral width) determined from each spectrum, of CNCs-K/HPC composite films (CNCs-H , CNCs-K, and different percentages of 10% (c),20%(d), 30%(e), 40% (f) and 50% (g) w/w of HPC). Data acquired from Figure 2.31.

Samples	λ_{max} (nm)	Estimated pitch value (nm)	Δλ (FWHM)
CNCs-H	665	426	230
CNCs-K	426	273	116
10% w/w HPC	544	349	172
20% w/w HPC	554	355	168
30% w/w HPC	621	398	179
40% w/w HPC	686	440	194
50% w/w HPC	742	476	234

Based on Figure 2.31, its noticeable that all CNCs-K/HPC composite films present structural colouration within the visible range of the electromagnetic spectrum and that the maximum wavelength tends to increase with the addition of HPC, also reported in Table 2.3. CNCs-H film presents a higher number of multi-coloured domains and the highest value of wavelength variation of 230 nm, twice the value of CNCs-K and reflects a strong colouration in the red wavelength, with 665 nm, while CNCs-K has a well-defined peak, with 116 nm of Δλ and a maximum wavelength in the blue visible range, with 426 nm.

Based on the POM and Vis-spectroscopy results and CNCs-K/HPC films photographs, it was found that it would be possible to produce films with structural colouration with maximum wavelength reflection within the visible range of the electromagnetic spectrum, between blue and red. The introduction of 10 % w/w of HPC rise the maximum wavelength reflection of 118 nm since the composite system presents a value of 544 nm, and a green-orange colouration is observed. If the amount of HPC is double the maximum wavelength reflected is redshift by 10 nm, so no major macroscopic or microscopic structural colouration reflection is observed between these two samples. The subsequent increase in the HPC content seems to lead to a stead increment in the maximum

wavelength reflected by the structures of around 60 nm between samples. This result is in line to what was observed by Walter et al.[123] for HPC with 370 kDa, excluding the sample with 50% w/w, and Saraiva et al. [46]for the composite system with HPC with molecular weight of 80 kDa.

From the observation of figure 2.31 one can also see that the composites films have multi-coloured domains which translate in a width reflection of wavelengths. From table 2.3 it is noted that the films with only CNCs-K have the smallest variation of reflected wavelength, as stated before. The addition of 10% w/w HPC lead to a variation of reflected wavelengths of 172 nm, 56 nm wider than the CNCs-K's film. Subsequent increase in the HPC content up to 40% w/w, only lightly leads to a higher wavelength variation. If 50 % w/w of HPC is used the $\Delta\lambda$ is similar to what is observed by the CNCs-H films. These results seem to show that not only the molecular weight of the added polymer HPC governed the variation of the pitch and consequently the reflected wavelength but also the initial CNCs suspension used, and the experimental conditions imposed during films formation.

To obtain more information regarding the composite systems FTIR spectra and XRD diffractograms of CNCs, CNCs-K, HPC and CNCs-K/HPC films were performed and shown in figure 6. From FTIR spectra (figure 2.32, a) is evident that the CNCs and CNCs-K are identical which indicates that the ion exchange does not interfere with the absorbance of the characteristic bonds of cellulose. Also, the difference between the CNCs and the HPC spectra are not significant since HPC is derived from cellulose with addition of 2-hydroxypropyl groups [125], therefore, it has similar characteristics chemical bonds. In both cases common bands such as O-H, C-H and C-O at around, 3330 cm^{-1}, 2900 cm^{-1} and 1069 cm^{-1}, respectively are observed [126]. In the HPC sample (brown line in figure 6a), the characteristic bands at 2876 and 2900 cm^{-1} correspond to the C-H vibration due to the aliphatic chain within the hydroxypropyl moiety and the sharp band at 1455 cm^{-1} to the deformation vibration of the -CH2 group. The films with 20% and 50% w/w of HPC (orange and red line in figure 2.32, a) are very similar as well, the band in the 2876 to 2900 cm^{-1} region become more pronounced with the increased of HPC percentages.

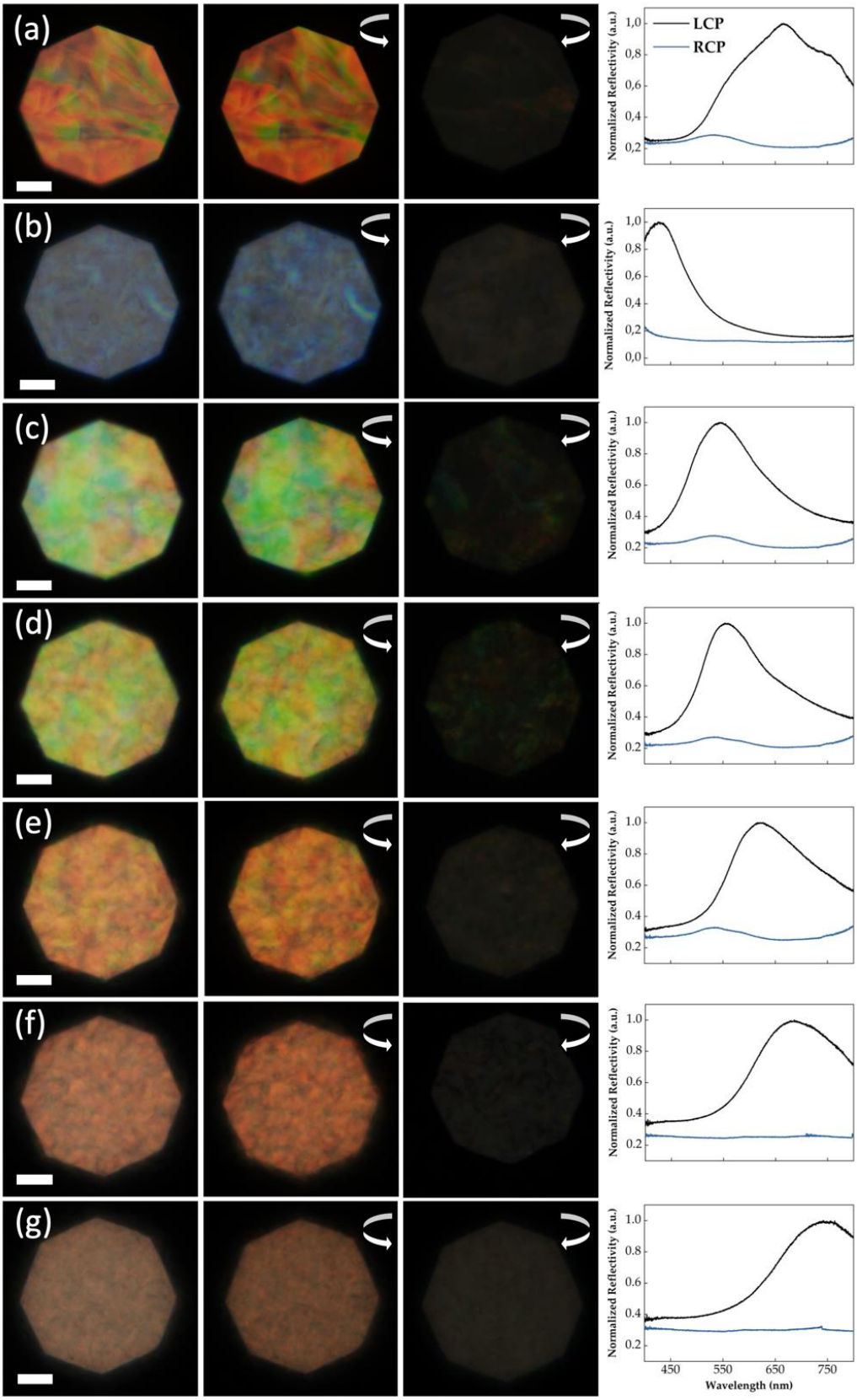

Figure 2. 31 POM images, obtained in reflection mode of CNCs-H (a), CNCs-K (b), and different percentages of 10% (c),20%(d), 30%(e), 40% (f) and 50% (g) w/w of HPC, respectively. They were observed with visible light (first column), left circular polarization (second row) and right circular polarization (third row). The spectra were acquired with LCP and RCP and scale bar corresponds to 50μm.

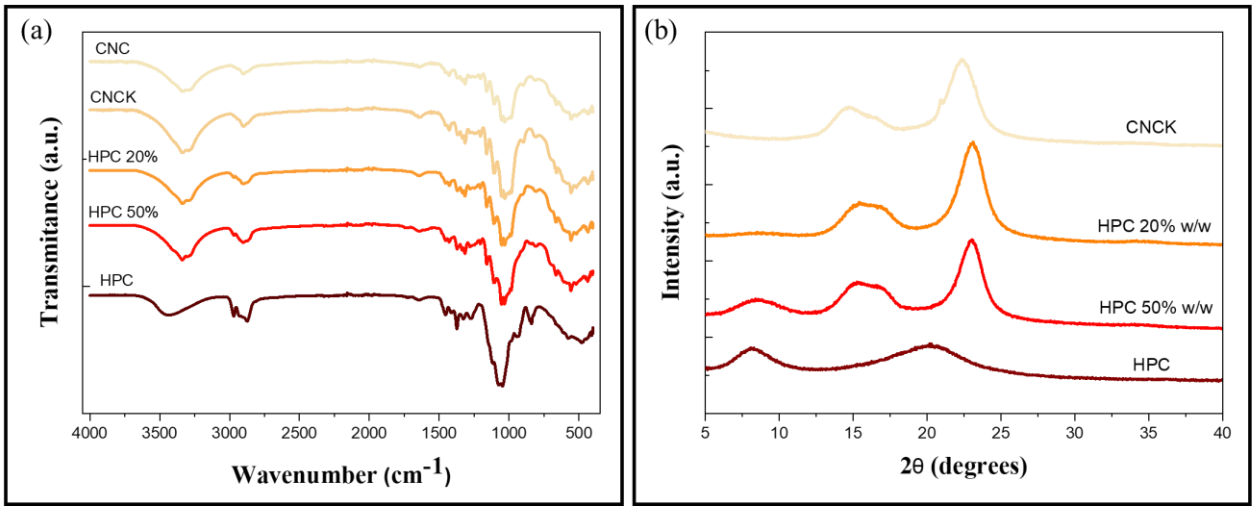

Figure 2. 32 (a) FTIR spectra and (b) XRD diffractograms of CNCs-K/HPC ($M\bar{\bar{w}}$= 300 000) films of CNCs, CNCs-K, 20%, 50% and 100% w/w of HPC, respectively.

XRD diffractograms of CNCs-K and 20%, 50% and 100% w/w of HPC with 300 000 molecular weights are presented in figure 2.32, b. XRD diffractogram of CNCs-K (yellow line in Figure 2.32, b) display the characteristic peak of cellulose nanocrystals, peaks at 2θ= 15.0°, 16.3° and 22.7° gives to the crystallographic planes of 101, $10\bar{1}$ and 002, where the latter is the main peak and characteristic of crystalline region of cellulose[127]. The diffractogram of HPC film (brown line in Figure 2.32, b) exhibits a peak at 2θ= 7.5° attributed to the HPC crystallographic plane (100), and the presence of a broad peak centred at 2θ=20.3° is ascribed to the amorphous region [128].

As expected, the presence of the HPC as a reinforcement in the CNCs-K/HPC composite films does not affect the supramolecular arrangement of cellulose, this is proven by the appearance of these characteristics' peaks in the 20% and 50% w/w HPC, where the 100 plane is most evident for the higher concentration and all the characteristic lattices of cellulose are present (red and orange lines in Figure 2.32, b). Nevertheless, the crystallographic plane of HPC centred at 2θ = 7.5° is more evident in the samples with a higher content of HPC.

As thermal stability is important for optical materials, as oxidation will affect intrinsic colours and water absorbency [109], to understand the influence of the HPC on thermal properties of the CNCs/HPC films thermogravimetric analysis was performed. TGA of CNCs, 50% and 100% w/w HPC were accomplished to verify the stability acquired by the composite films when HPC is used as reinforcement of the CNCs-K matrix and the thermogravimetric curves show that the CNCs thermal behaviour dictates the thermal behaviour of the composites CNC/HPC, since the curves resemble what is obtained for the neat CNCs (Figure 2.33).

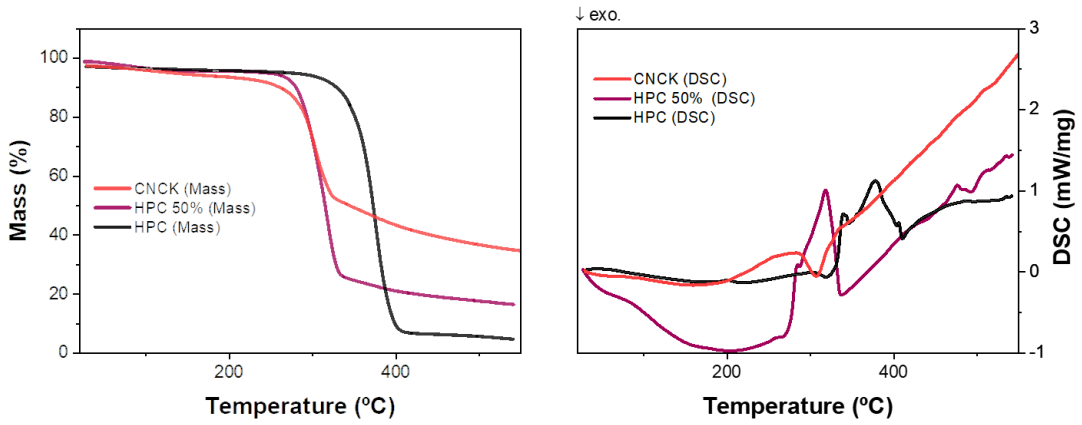

Figure 2. 33 DSC-TGA analysis of CNCs-K, 50% and 100% w/w of HPC films (red, purple, and black lines respectively).

Known that the ion exchange of the protonated CNCs from H+ to K+ leads to a first order reaction, the degradation process of the CNCs-K, Figure 2.33 red line, displays a mass change of 45.95% between 270 ºC to 320 ºC. In the HPC film (fig. 2.33 black line), the degradation process occurs also in one single stage and starts at a higher temperature, at 300 ºC, with a mass drop of 92.69%. It appears to have an endothermic peak at 378 ºC. The film with 50% w/w of HPC, represented by the purple line, is a first order degradation reaction where only one massive drop appears, between the ones registered for CNCs-K and HPC diffractogram, this is between 290 ºC and 335 ºC, with an 82.46% mass variation. Meaning that the introduction of HPC in the composite system causes an improvement in the mass degradation making the CNCs-K/HPC composite films more thermally stable[32].

2.5.3. CNCs/CNCs_RhB films

2.5.3.1. CNCs rhodamine B ester: synthesis

To obtain CNCs derivative with fluorescent properties, CNCs rhodamine ester was produced by covalently bond to the dye. Rhodamine B (RhB) is known to be water-soluble and fluorescent when excited, showing a maximum emission at 580 nm[101]. The synthesis took place in 2 different steps: first, rhodamine B acyl chloride was prepared, which was one of the reactants; second, the CNCs functionalisation with rhodamine B, by esterification reaction, occurs at the surface of the nanoparticles. Toluene and DMF were used as a coupling agent allow CNCs rhodamine B ester production [95].

2.5.3.1.1. Preparation of rhodamine B acyl chloride

The acyl chloride of rhodamine B was produced based on a protocol described in the literature with some modifications [96]. Briefly, 1 equivalent of rhodamine B was suspended in 10 ml of dry toluene with 50 µl of dry DMF (used as a catalyst). Then 5 equivalents of thionyl chloride were added dropwise under stirring. Next, the mixture was placed under reflux for 2 hours at a controlled temperature of 100°C until the mixture became homogeneous. After this time, the product was solubilised in toluene, and the temperature was removed to stop the reaction. As the last step, the product was dried in a rotary evaporator, so toluene, unreacted thionyl chloride and hydrochloric acid were removed. Thus, the rhodamine B acyl chloride is obtained without further purification.

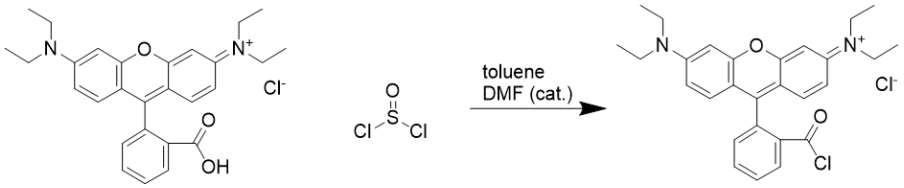

Figure 2. 34 Reaction scheme for the synthesis of rhodamine B acyl chloride

2.5.3.1.2. Preparation of CNCs rhodamine B ester

Preparation of CNC rhodamine B ester was performed in heterogeneous conditions using DMF as the reaction solvent. A first attempt where triethylamine and 4-dimethylamino pyridine was used, although complete purification was not achieved, as can be seen in Appendix B.

CNCs (1 equivalent) were dispersed in 8 mL of dry DMF using ultrasounds. To this suspension, pyridine (20 equivalents) was added, and rhodamine B acyl chloride (0.5 equivalents) dissolved in 2 mL of dry DMF was added dropwise. The solution was maintained at 50^{o} C for 48 hours under an N_2 atmosphere. After this time, the precipitate is filtered in a sintered glass filter and washed in glacial acetic acid and isopropanol to remove unreacted rhodamine acyl chloride and pyridine hydrochloride. The product was further washed with acetone (200 mL) for 24 hours with vigorous agitation and filtered to isolate the product, and then it was dried under vacuum at room temperature. Sample prepared with this approach will be called sample 2.

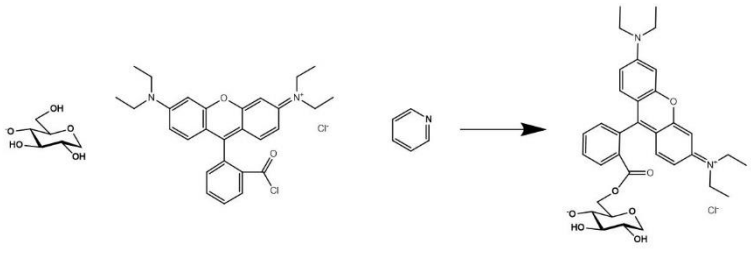

Figure 2. 35 Reaction scheme of the CNCs rhodamine B ester synthesised with the second approach.

Following, synthesis of the CNCs rhodamine ester, the product was further washed with an excess of acetone and methanol to remove residual rhodamine B from the product powder before it could be used. The resulting product showed a pink colour, characteristic of rhodamine B. Nevertheless, oppositely to pure rhodamine B, the obtained product is insoluble in water, THF, methanol and acetone, as verified with CNCs. After confirming by FTIR that our product was pure, a scale-up reaction was followed, starting from 3 equivalents of CNCs, which in terms of mass are equal to 600 mg, and we obtained 603 mg of final mass of the final product after the purification process. Sample prepared with scale-up reaction will be called sample 3.

2.5.3.2. CNC rhodamine B ester Characterisation

FTIR analysis, spectra in figure 5, identify the characteristic cellulose backbone modes of vibration with the appearance of several bands between 800 and 1500 cm^{-1} in the reaction product. The main indication of derivatisation is based on the appearance of a new band at 1737 cm^{-1}, assigned to the carbonyl group of the ester bond that does not exists in native CNCs as seen in figure 2.36. The ester group of Rhodamine normally appears around 1705 cm^{-1} [96] in free rhodamine. New bands appear between 1660 and 1200 cm^{-1} that can be ascribed to the stretching vibrations of C=C, C=N, C-N bonds from or linked to the aromatic rings. Therefore, the FTIR spectrum was used as preliminary proof of the CNC's successful esterification.

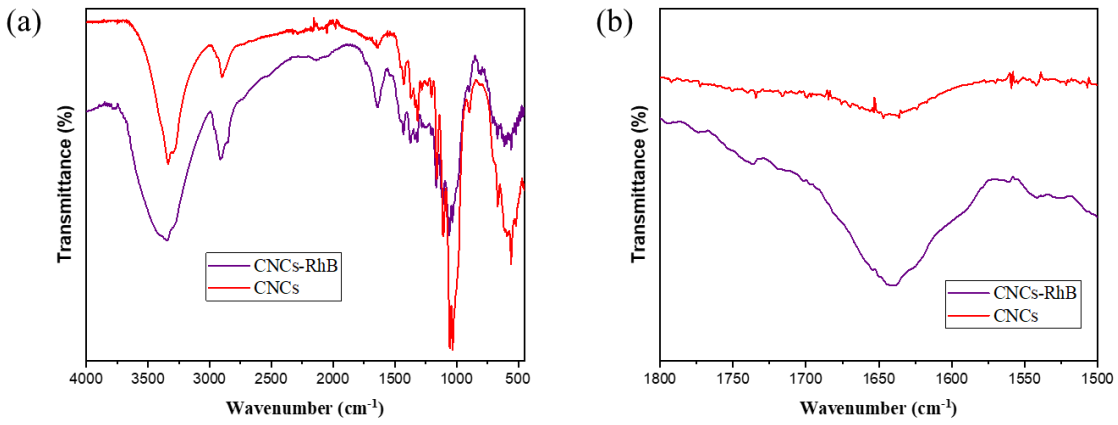

Figure 2. 36 FTIR spectra of CNCs rhodamine B and CNCs ester in KBr (a)full spectra and (b) zooming in the region between 1800 and 1500.

The amount of RhB groups attached to the cellulose nanocrystals surface can be verified by elemental analysis presented in Table 2.4, where the content of C, N, H, S in CNCs_RhB samples is detailed.

Compared with CNCs elemental analysis, it is evident the presence of N in both samples, that came from the rhodamine B attached to the CNCs, also confirming the functionalization of the surface of CNCs with the fluorescent dye, giving rise to cationic CNCs_RhB. A slight decrease in the sulphur content, from 0.95 to 0.74 w/w %, was observe from CNCs to CNCs_RhB, which is indicative of some superficial desulfation of the nanocrystals during funcionalisation. The scale-up did not affect the nitrogen or sulphur content.

Table 2. 3 C, N, H, S elemental data of the CNCs_RhB of samples 2 and 3.

Samples	Carbon (w/w%)	Nitrogen (w/w%)	Hydrogen (w/w%)	Sulphur (w/w%)
2	39.82	0.28	5.80	0.74
3	40.74	0.32	5.44	0.70

2.5.3.3. CNCs/CNCs_RhB films

CNCs_RhB [132] was dispersed in an organic solvent, isopropanol, using a vortex mixer, and a final concentration of 1,4 wt.%, determined through gravimetry, was obtained. Fluorescence of CNCs_RhB powder and suspension was tested, using UV light as shown in figure 2.37, b and c. Photographs of the solid and suspension were taken under visible light (figure 2.37, a), with a longwave with 365 nm (figure 2.37, b) and shortwave with 254nm (figure 2.37, c) UV light irradiation. Some aggregation was observed in this suspension. However, one can see the difference between Vis and UV irradiations.

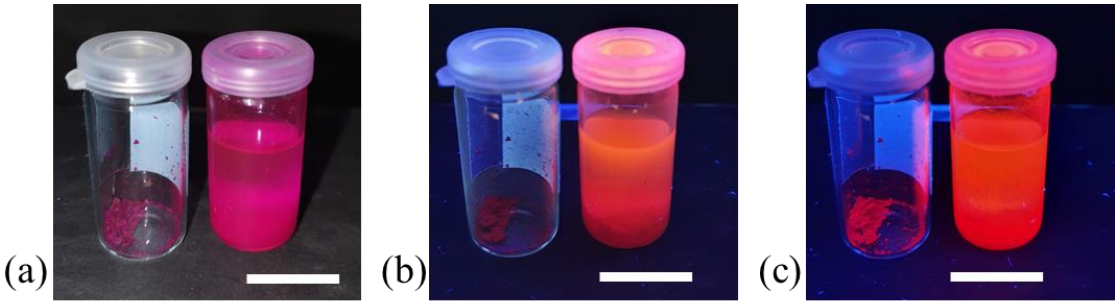

Figure 2. 37 Photographic images of CNCs_RhB powder (in the left vial) and CNCs_RhB/isopropanol suspension (in the right vial), observed under visible light (a), with UV light λ_1=365 nm (b) and λ_2=254 nm (c). Scale bar 1 cm.

Under visible light, both powder and suspension show a pink colouration. However, an orange colouration is observed when the suspensions are irradiated with UV light. This behaviour is equal for both shortwave and longwave UV light. Nevertheless, the orange colouration is more intense with

a shortwave irradiation of 254 nm. The powders show a different behaviour, as with UV light of 365 nm, a slight variation from pink to dark red occurs. It is important to notice that this change in colouration is obtained immediately after exposer to UV light. Once the UV light is removed, the compound and suspension return to the same state observed under visible light.

2.5.3.3.1. CNCs/CNCs_RhB Sample preparation

Isopropanol/ CNCs_RhB suspension (concentration ~1.4 wt.%) was added to 1ml of ~3 wt.% CNCs aqueous suspension in different ratios, to give rise to films with CNC/ CNCs_RhB ratios of 100/0, 99.4/0.6, 99.1/0.9, 98.9/1.1, 98.7/1.3, 98.5/1.5, 98.3/1.7 and 98.1/1.9, referenced as sample 0, 1, 2, 3, 4, 5, 6, 7, respectively. Mixtures were prepared using a vortex mixer and allowed to settle, when no phase separation appeared the mixtures were transferred into a 24 well culture plate (TC Plate 24 Well, Suspension, F- SARSTEDT), with a hydrophobic surface to remove films easily. These types of plates allow the preparation of small films, although the depth of the wells leads to longer evaporation times. The solvent is composed of a mixture of water and isopropanol, but this last one is present in a low percentage, so it does not seem to influence the evaporation rate. Solvent evaporation occurs at 30°C for ten days to allow slow evaporation and LC mesophase re-organisation, plus five days at 45°C, to promote a total solvent's evaporation. The obtained free-standing films were removed and characterised.

2.5.3.3.2. Characterisations

The first stage consisted of preliminary characterisation through photographs of the film acquired first with white uncollimated light and with right-handed (RCP) and left-handed (LCP) circular polarizers (Figure 2.38). Next, these structures were analysed with a POM microscope, using transmission mode with cross-polarisers and reflection mode with LCP and RCP light. Reflection spectra were obtained at the same spot of the samples with both circular polarisers. Subsequently, photographic images under a UV lamp, using 2 different wavelengths (λ_1=365nm and λ_2=254nm), at 30° angle perpendicular to the substrate, were also acquired (Figure 2.41, b and c). This angle was chosen since the UV light is on top of the samples.

From the photographic images for all nanocomposite films, in the first column of figure 2.38, obtained under visible light, a blue-pink colouration, which is stronger as the amount of rhodamine B increases, is observed. In contrast with the first image of the film composed only of CNCs, which reflects a pale blue-like colouration at this angle of observation. The observation of these images leads to considering that macroscopically the fluorescent nanoparticles are evenly distributed within the films since the compatibility between host and additive is a key to preparing nanocomposites with the

aspired structure. When a left-handed circularly polariser is used (Figure 2.38, third column left to right), sample 0 presents the normal selective response of CNCs films that arise from the LC phase, and a more vibrant colouration is observed. With samples 1, 2, 3, the blueish colouration is still visible but is reduced as the amount of CNCs_RhB increases in the composite. For higher concentrations of fluorescent nanoparticles, the pink colours have now a higher contribution and pink films, although not so pink as the images observed with no polariser. With a right-handed circularly polarizer (Figure 2.38, second column), sample 0 shows extinction of colouration in most of the film's area since this light is transmitted by the left-handed CNCs film's structure. The presence of CNCs_RhB does not seem to affect this behaviour in all range of concentrations. The pink colouration became more evident as the content of CNCs_RhB rose (samples 4 to 7), but the films still transmitted RCP light. The results presented here are in good agreement with what was observed by He et al. by co-assembling CNCs, from the LC phase, with Rhodamine B (not covalently linked to the nanoparticles). In this work, the authors confirmed that even the presence of loose dye did not affect the selective reflection of the films when observed with LCP and RCP light.[97] POM images in Figure 2.37 on the left obtained in transmission mode with the cross-polarizers show, for all the samples, a fingerprint-like texture and birefringence, typically observed for CNCs's [46].

In the figure 2.39 are shown the POM images in reflection mode and spectra recorded on the centre of each film. The spectra were obtained with left-handed and right-handed circular polarized light, corresponding to the black and red lines, respectively. The xx's axis scale starts at 400 nm since the circular polarized filters (Edmund Optics) cut wavelengths lower than this value. From LCP's spectra observation, in figure 2.39 (third column), and considering the minimum value of wavelength available by this equipment set, the maximum wavelength reflections ($\lambda_{max,1}$) is around 450 nm for all samples as we can see from $\lambda_{max,1}$values in table 2.4.

Table 2. 4 Maximum reflection wavelength values obtained from LCP spectra.

Samples	LCP $\lambda_{max\ 1}$(nm)	LCP $\lambda_{?}$(nm)
0	456	-
1	452	607
2	430	610
3	449	610
4	453	621
5	451	620
6	453	620
7	437	620

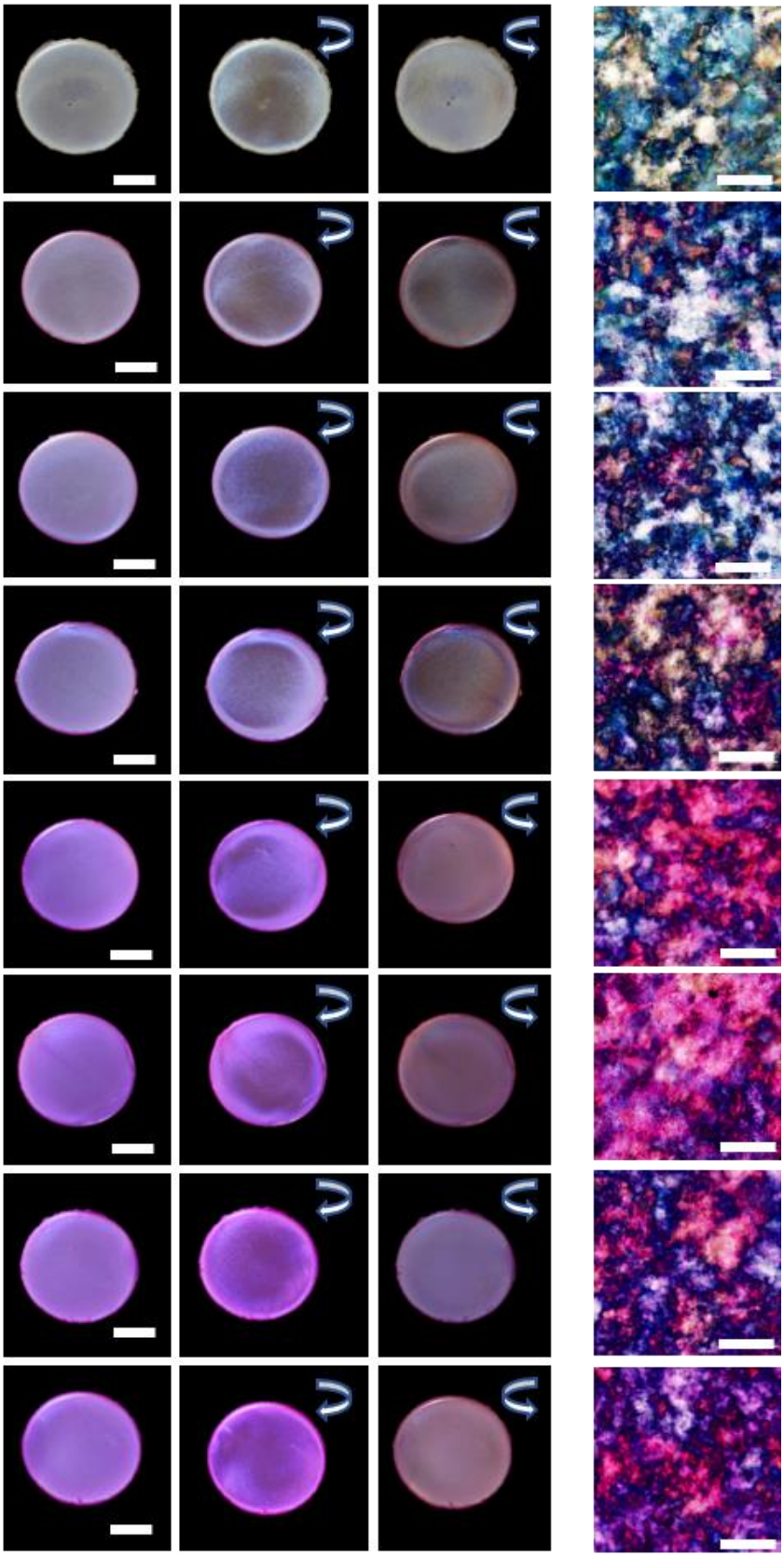

Figure 2. 38 Images of CNCs/CNCs_RhB films referenced as 0, 1, 2, 3, 4, 5, 6, 7 from top to bottom. On the left part: photos were taken under visible unpolarized light, using the right- and left-handed circular polarizers (as indicated by the arrows) and the scale bar is 0,5cm. On the right part POM images obtained in transmission mode with cross polarizers are presented for each film, scale bar 100µm.

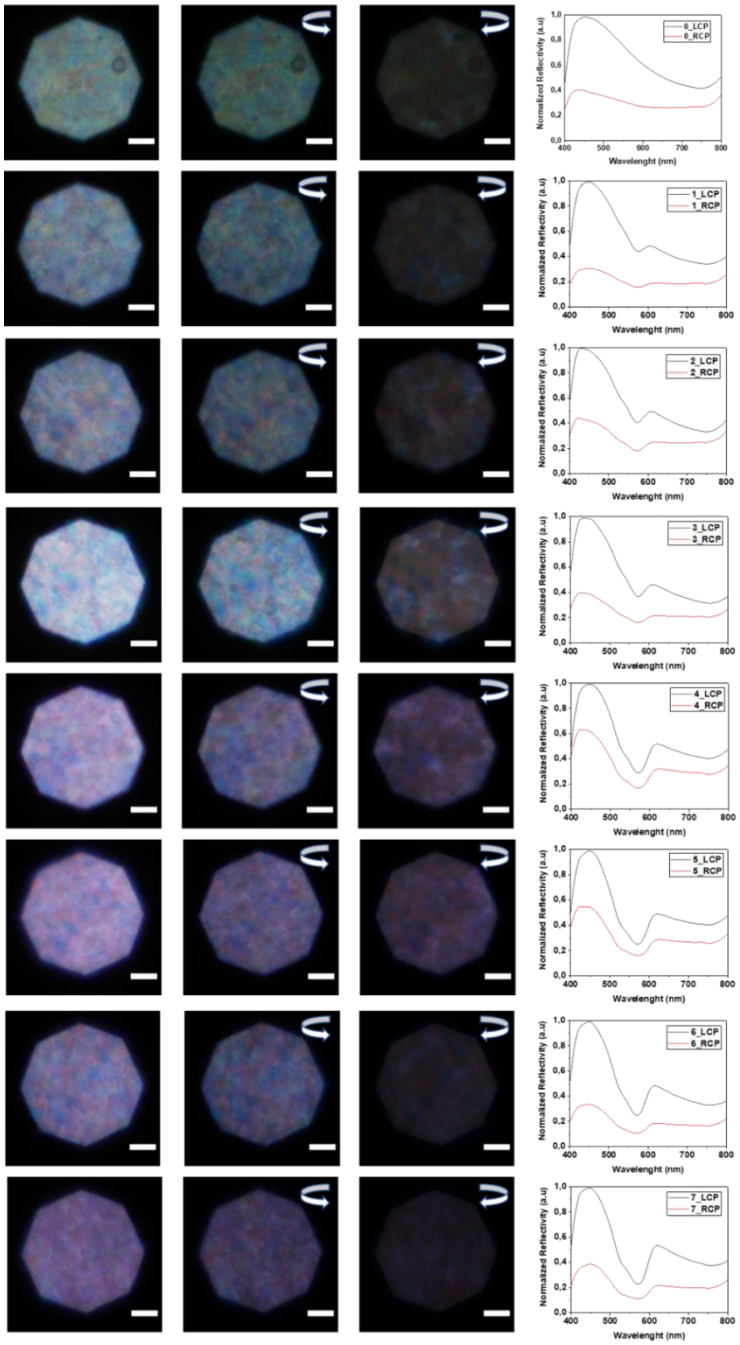

Figure 2. 39 POM images, obtained in reflection mode of CNCs/CNCs_RhB films, observed with visible light (first column), left circular (second column) and right circular polarizer (third column). In the right part, spectra were acquired with LCP and RCP light. From top to bottom the images and spectra correspond to samples 0 to 7 (as can be seen in the Vis spectra) The scale bar corresponds to 50 μm.

The difference between the CNCs and CNCs/CNCs_RhB samples in the LCP spectra is the appearance of a second peak which is not present in the sample of CNCs only and appears when CNCs-rhodamine is present. The maximum lambda values of this peak are shown in table 2.5 (λ_2) and the signal is not equal in all the samples, in fact samples 1,2,3 have a wavelength of about 610nm

while from sample 4 onwards lambda is equal to 620nm. This change in wavelength represents a red-shift due to the increase of the content of fluorescent CNCs. Instead, due to the same values of $\lambda_{max,1}$ we can assume that CNCs_RhB did not affect the sample reflection, as we have a good LCP light response given from the chirality organisation of the CNCs and transmission of the RCP light. We can also assume that within the range of concentration of CNCs_RhB used, and considering the de Vries equation, these functionalised nanoparticles co not greatly affect the structure pitch value.

To obtain more information about CNCs/CNCs_RhB films, FTIR, CD, SEM analyses were performed and are shown below.

FTIR analysis were performed in all the films prepared and compared with CNCs spectrum (showed in Appendix B). Since the CNCs-RhB are present in the nanocomposite system in a low quantity the carbonyl group of the ester bond is not visible. However, one can still see the vibration band at around 1580 cm-1 for samples 3 onwards assigned to the double bonds of the aromatic rings or C=N.

To further examined the chiral nematic structure of the films, the cross-section of some films of the series was examined by SEM and images are presented in figure 2.40 (films 0, 1, 2, 3, 4, 5, 6, 7 are respectively from a to h). As observed on the sample without dye functionalised CNCs, the images of the composite films showed that the cholesteric structure was retained after solvent evaporation. The same can be observed from the circular dichroism spectra, where one can see that all the samples present a broad positive ellipsity, which indicates that all the structures present a left-handed chiral nematic arrangement. The maximum wavelength values obtained from CD spectra were collected in table 2.5, where $\lambda_{1,\,max}$ is the maximum wavelength values from the principal peak of the spectra, instead λ_2 is the maximum wavelength values from the second peak in the range 500-600nm and it is not present in all samples.

With this study it is possible to establish that the maximum wavelength of CNCs' pure film presents a photonic bandgap in the blue/UV region of the spectrum at ~350nm, and not 450 nm as showed by the spectrum in figure 2.39. This difference can be explained by the circular polarizer filters and spectrometer used that only allow measurements in the 400-750 nm wavelength range. If we look to the maximum wavelength return from CD spectra (table 2.5) we cannot see a linear correlation between samples and the CNCs_RhB content, since the values either increase or decrease between 331 and 428 nm. The difference observed here, and not in figure 2.39, might be attributed to the fact that we have multi-coloured domain, or digital coloured, films and the analysis might occur at different points with a high contribution of nanostructured material with a specific pitch value. In some nanocomposite samples (4,5,6,7) a new positive peak between ~570-580 nm is observed. This new CD signal, around the absorption wavelength of RhB, can be attributed to the transfer of the chiral nematic arrangement of aqueous suspensions of CNCs to the CNCs_RhB. This phenomenon

is normally called induced circular dichroism and appears due to the interactions, as non-covalent bonds, H-bond or electrostatic forces, between the guest and the mesogen unit of the host. Indeed, in recent years authors have showed that this effect is observed in CNCs composite films with polymers as polyaniline [98]or even RhB added directly to CNCs suspensions [97]. The absorbance spectra of all the composite films (figure 2.40, j) show a strong absorption peak at 555 nm ascribed to the π-π* transition of RhB [97]. The peak is stronger as the content of CNCs-RhB increases in the system. From these spectra we can see that there is no shift in the absorption wavelength of the RhB when is covalently linked to the CNCs. As expected, the CNCs films do not show significative absorbance signal, except in the region between 200-300 nm.

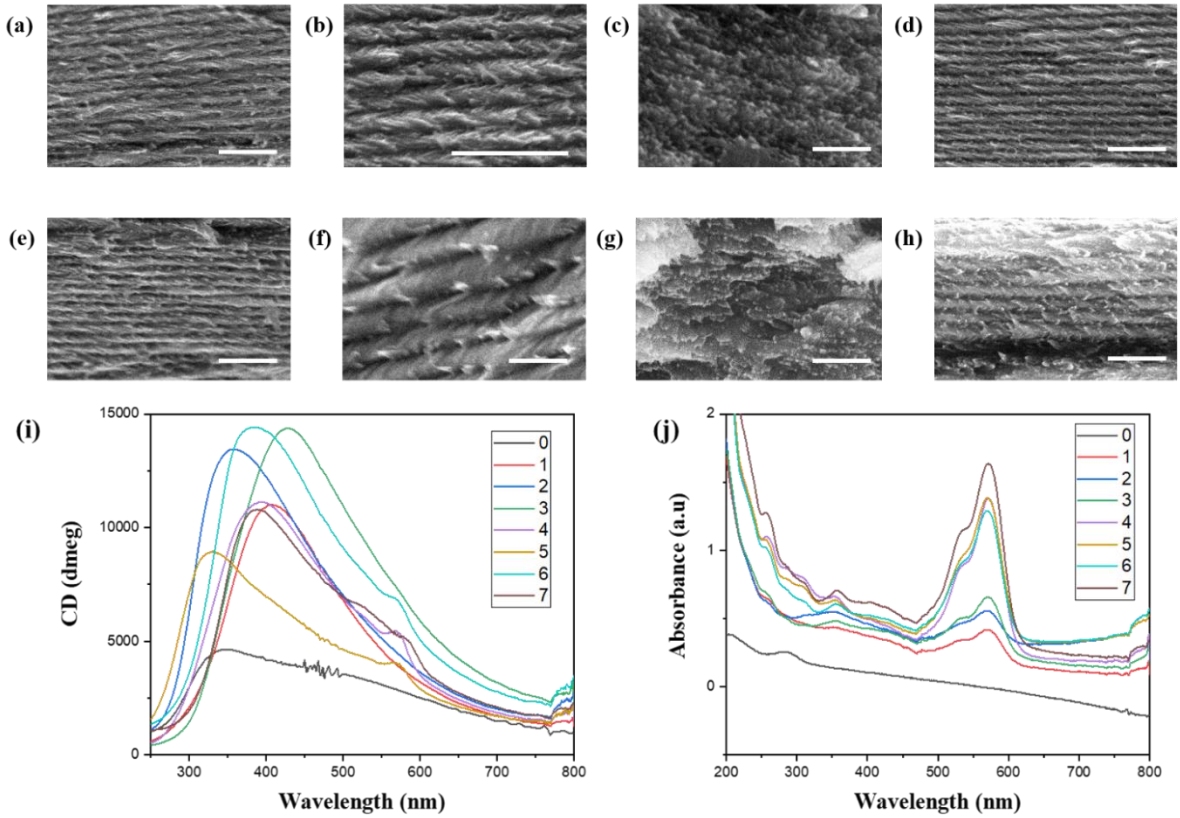

Figure 2. 40 From a to h SEM images of the central region of the cross section of the CNCs/CNCs_RhB films 0, 1, 2, 3, 4, 5, 6, 7, where the chiral nematic arrangement can be observed, scale bar 1 µm; (i) circular dichroism spectra of CNCs/CNCs_RhB films; (j) Absorbance spectra of CNCs/CNCs_RhB films.

Table 2. 5 Maximum wavelength values obtained from CD spectra.

Samples	0	1	2	3	4	5	6	7
λ_{1max}(nm)	349	405	357	428	393	331	386	387
λ_2 (nm)	-	-	-	-	568	564	574	582

Qualitative fluorescence analyses were collected through photographic images acquired with the samples in the same position with an angular inclination of the camera of 30 °. Images were acquired under visible light (figure 2.41 b) and under two different UV light wavelength (λ_1 and λ_2, 361 and 254 nm, respectively). Fluorescence seems to increase when we look at the naked eye when the UV wavelength changes, as it shown in figure 2.41 b and c. This is confirmed by fluorescence spectra presented in figure 2.41 d where the ratios between the fluorescence intensity for composites (F) *and CNCs (F0), showed a linear increase with fluorescent nanoparticles content figure 2.41 e. The images obtained when irradiated with UV light with 254 nm are intense in orange colouration that the ones irradiated with 361 nm. The CNCs films is also optical active under both UV light irradiation and a strong blue colouration is observed, that can be attributed to the absorbance at ~280 nm seen in the absorbance spectra in figure 2.40 j.

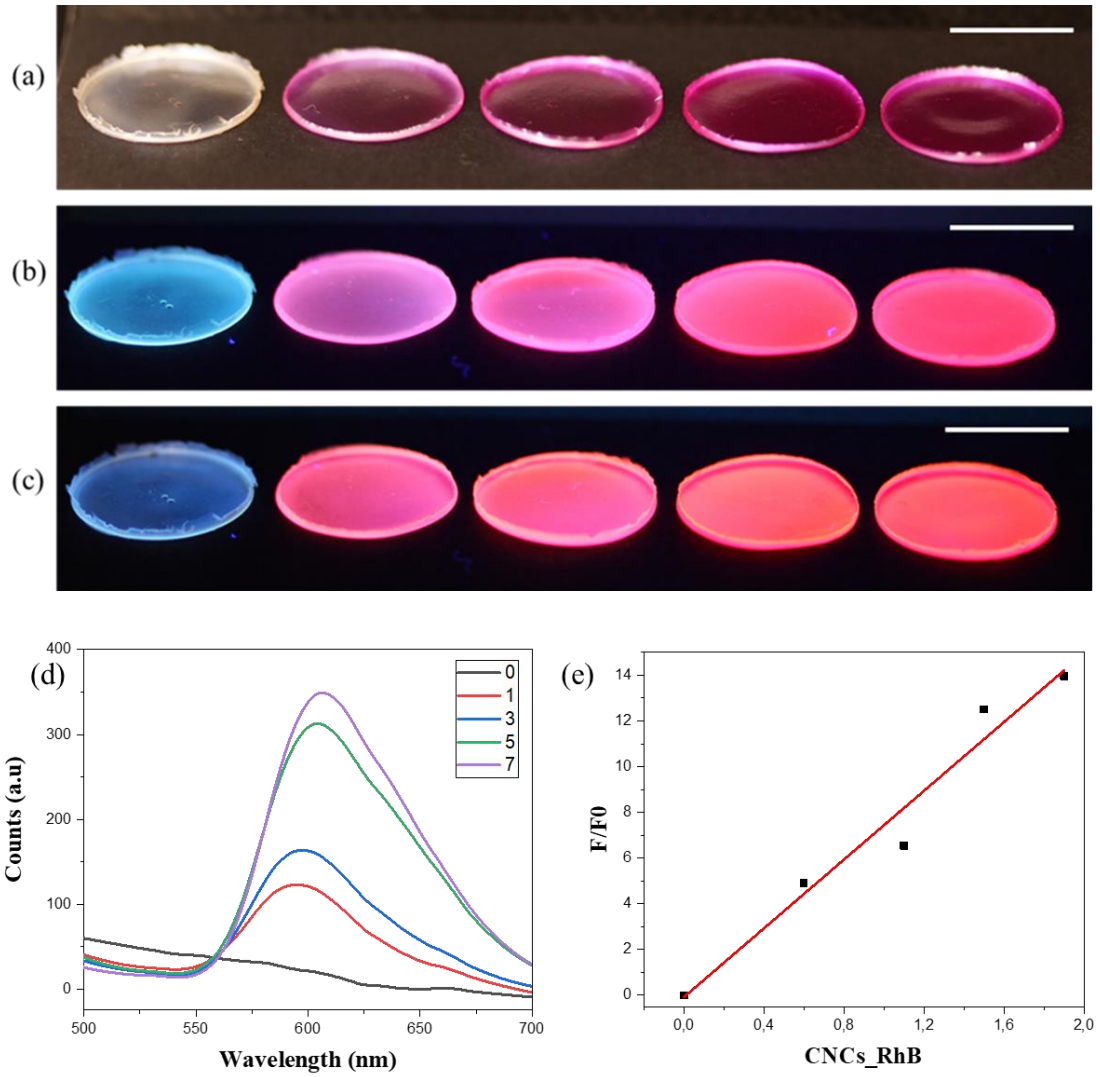

Figure 2. 41 Photographic images acquired under visible light (a), under UV light λ1 (b) and λ2 (c) of 0,1,3,5,7 films from left to right respectively. Scale bar 1 cm. (d) Fluorescence spectra of CNCs/CNCs_RhB films; (e) Dependence of F/F0 on the concentration of RhB. F0 was fluorescence

intensity of CNCs without RhB. F was fluorescence intensity of CNCs with different concentrations of RhB, respectively.

2.6. Conclusions

In the first part of the work, we were able to demonstrate that the addition of HPC, with a molecular weight of 300 000 kDa, to a suspension of CNCs, with a small fraction of CNCs (of 3 wt.%, in the isotropic-anisotropic biphase regime), in the range of 10 to 50 wt.% leads to the retention of the chiral nematic arrangement. If the solvent is slowly evaporated from these LC suspensions, the helicoidal structure is still obtained and an increase in the reflected wavelength of the nanocomposite films is observed. A concentration equal or higher than 20 wt.% of HPC in the suspension still gives rise to a structurally coloured composite CNCs/HPC film, predominantly yellowish green, while further HPC increase leads to a red-shift of the reflected wavelength. We were able to obtain films that present iridescence or a matte finish, demonstrating the high versatility of this system. The exchange of the CNCs's counter-ion from proton to K^+ allow, and to the best of our knowledge for the first time, to use cellulose microcrystalline PH-101 (easy commercially available product) to produce CNCs. If these nanoparticles are use in a composite system, the addition of the cellulosic derivative hydroxypropyl cellulose did lead to the production of films with visible structural colouration. The exchange of the counter-ion also allows increasing the thermostability of the CNCs films, that rose with the content of HPC.

In the second part of this work a UV-responsive system composed of CNCs and rhodamine B-functionalised CNCs was obtained. First, the functionalization with the fluorescent moiety was successfully done, with the Rh B presence confirmed by means of FTIR and Elemental Analysis, that evidences the esterification reaction with the cellulosic nanoparticles by the appearance of a new carbonyl vibration band and the presence of nitrogen in the samples.

We have therefore shown that we were capable of producing films from rhodamine-functionalized CNC and CNC blends. From macro images it was shown that the films present structural colouration and selective reflect left-handed circular polarise light. In the range of concentrations of CNCs-RhB used a pink colouration is always observed being the dominant observation colour as the content of the fluorescent nanoparticles increase. POM analysis, in transmission and reflection modes, allow confirmation that the retention of the liquid crystalline phase from the CNCs occurred, since the typical textures are observed and selective circularly light reflection. A new peak is observed at around 605 nm, which is also observed in the CD spectra, by a positive peak at ~575 nm, at around

the emission wavelength of rhodamine B. This new left-handed circularly reflection can be attributed to induced circular dichroism, derived from the chiral nematic arrangement of CNCs transferred to the CNCs-RhB. The films present a pink-to-orange strong colouration under UV light, dependent on the amount of CNCs-RhB used and the UV wavelength. Films of CNC-K also show an strong blue colouration under UV light, for both UV wavelengths used.

From a fluorescent point of view, the strong colouration due to the fluorescence can be as authentication property in an anticounterfeiting device.

All films presented are examples of low-cost all-cellulose based photonic materials that can be used in commercial applications such as circularly polarised light sensors, decorative coatings, active inks and optically variable devices as security features.

2.7. Appendix B.

Characterizations Techniques and sample preparation

Photographs of CNCs films and CNCs/HPC composite films were obtained with a Canon EOS 550D coupled with an EF-S 60 mm Canon macro-lens (Tokyo, Japan), at an 8° angle perpendicularly to the substrate, under uncollimated unpolarised white light illumination.

Thermogravimetric analyses (TGA/DSC) were performed using a Netzsch 449 F3 Jupiter® simultaneous thermal analyser (Selb, Germany). Each sample was heated from 25 to 550 C, at a heating rate of 10° C/min under nitrogen.

Circular dichroism (CD) experiments were performed using an Applied Photophysics Chirascan CD spectrometer (Surrey, UK). The scanned wavelengths ranged from 200 and 800 nm, with a bandwidth of 1 nm and a scanning rate of 200 nm/s. Spectrophotometric analysis in UV/VIS/NIR (PerkinElmer Lambda 950, Waltham, WA, USA) was performed in reflective mode with an integrating sphere, with measured wavelength data ranging from 200 to 2500 nm.

The structural assembly of CNCs and CNCs/HPC composite films was observed by SEM (Scanning Electron Microscope) using a Carl Zeiss AURIGA CrossBeam SEMWorkstation, Oberkochen, Germany equipped with an Oxford energy-dispersive X-ray spectrometer. The in-lens mode was used with an accelerating voltage of 2 kV and a 20 µm aperture size. As preparation for SEM observation of the films, its cross-sections where obtained from hit the film until fractured, mounted onto aluminium stubs and coated with a thin carbon layer using a Q150T ES pumped coater from Quorum (Washington D.C.,WA, USA).

Elemental analysis and AFM were used to attest the composition and dimensions of the CNCs. CHS elemental determination was obtained using the Thermo Finnigan-CE Instruments Flash EA 1112 CHNS series analyzer.

AFM analysis of CNCs

Employing an Atomic Force Microscopy (AFM- Asylum Re-search MFP-3D), a standalone system in tapping mode, with commercially available silicon AFM probes with a scanning frequency of 300 kHz and k = 26 N/m), top view images were collected. Preparation of CNCs samples involves preparing films from the drop-casting technique of a suspension with CNCs content of 0.01 wt.% onto a clean mica substrate (Muscovite Mica, V-5 from Electronic Microscopy Sciences). Immediately before deposition, the aqueous CNCs suspension was sonicated to allow higher dispersion of CNCs.

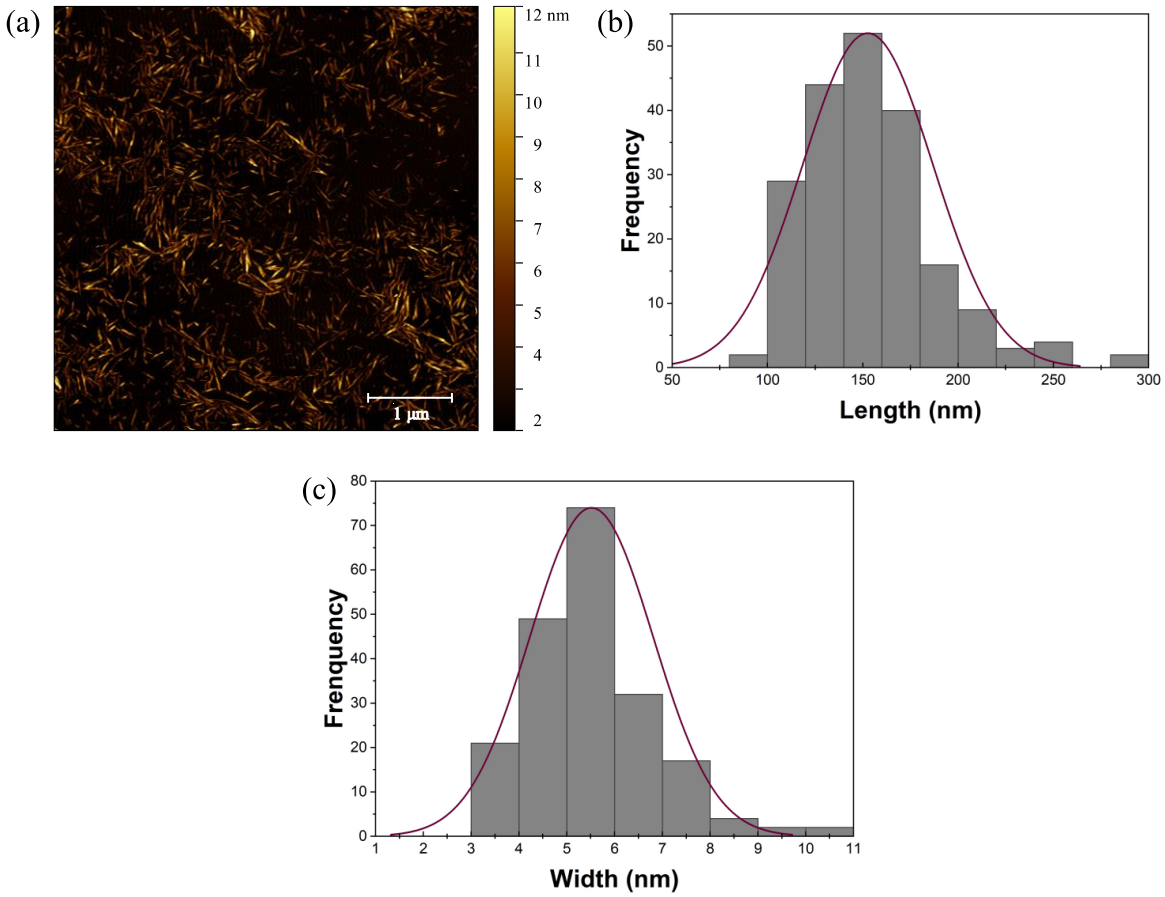

Figure 1B (a) Example of AFM image (5x5 µm) of CNCs-CMC used for particle determination. (b) and (C) present the length and width histograms, respectively, and its normal distribution curves (n=135).

Table 2B Thickness determination of the CNC-K films with different content of HPC.

HPC content in CNC-K/ HPC	0%	10%	20%	30%	40%	50%
Thickness	165	168	151	67	99	67
	178	198	204	71	101	65
	181	159	197	82	92	60
	199	178	193	73	94	81
	163	190	211	76	86	59
	210	176	180	75	97	76
	176	185	215	84	85	78
	155	182	106	57	95	74
	167	161	199	84	61	68
	189	209	202	72	76	75
Average	**178**	**181**	**186**	**74**	**89**	**70**
Standard Deviation	**16**	**15**	**32**	**8**	**12**	**7**

Preparation of CNCs rhodamine B ester (approach 1)

In the first approach, CNC (1 equivalent) was dispersed in 5 mL of dry DMF using ultrasounds. Subsequently, triethylamine (15.5 equivalents) and 4-dimethylamino pyridine (0.2 equivalents) were added. Then, 0.5 equivalents of rhodamine B acyl chloride prepared in the first step were dissolved in 5 mL of dry DMF and added dropwise. The solution was maintained at 80º C for 24 hours. The product was further washed with acetone (200 mL) for 24 hours with vigorous agitation and filtered to isolate the product and then it was dried under vacuum at room temperature Sample prepared with this approach will be called sample 1.

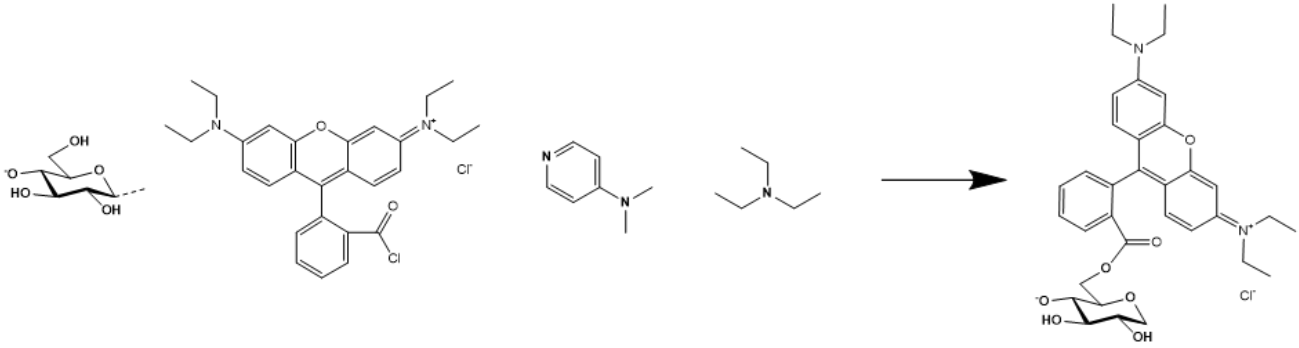

Figure 2B Reaction scheme of the CNC rhodamine B ester synthesised with the first approach

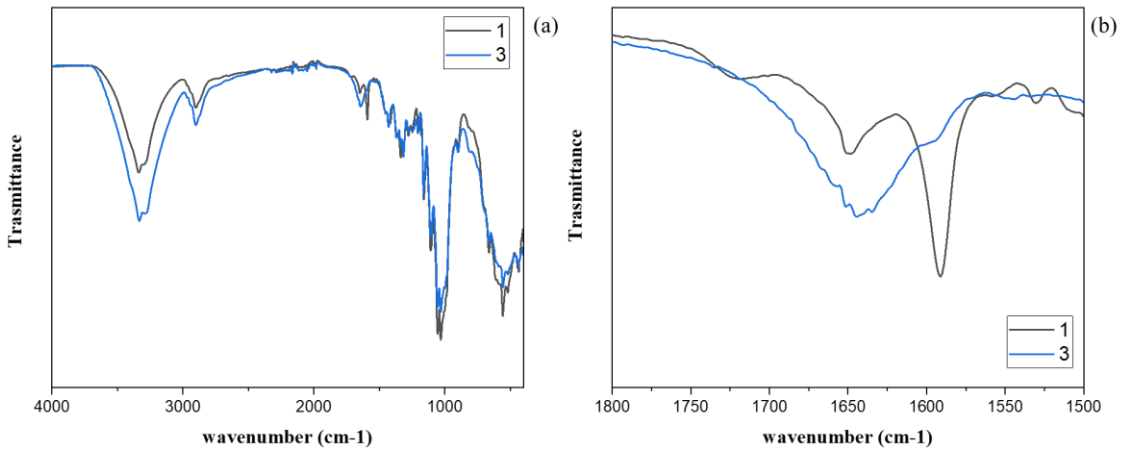

Figure 2B FTIR spectra of CNC rhodamine B ester in KBr, where 1 is the ester produced with the first approach and 3 is the product of scale up reaction , (a) full spectra and (b) zooming in the region between 1800 and 1500 to highlight pitch at 1600 and 1740.

FTIR CNCs/CNCs_RhB Samples

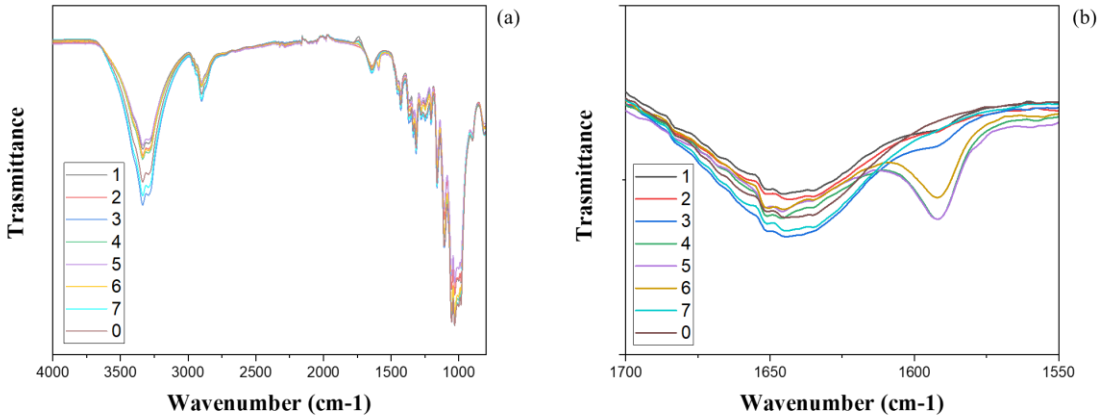

Figure 4B FTIR spectra of all films.

2.8. References

[1] J. George and S. N. Sabapathi, "Cellulose nanocrystals: synthesis, functional properties, and applications," *Nanotechnology, Science and Applications*, vol. 8, p. 45, Nov. 2015, doi: 10.2147/NSA.S64386.

[2] S. Vignolini and N. Bruns, "Bioinspiration Across All Length Scales of Materials," *Advanced Materials*, vol. 30, no. 19, May 2018, doi: 10.1002/ADMA.201801687.

[3] C. Chindawong, "Drying-Induced Structure Formation in Polymer Films", Si Sa Ket Thailand, Faculty of Natural and Materials Science Clausthal University of Technology, 2015.

[4] T. D. Nguyen, E. Sierra, H. Eguiraun, and E. Lizundia, "Iridescent cellulose nanocrystal films: The link between structural colour and Bragg's law," *European Journal of Physics*, vol. 39, no. 4, Apr. 2018, doi: 10.1088/1361-6404/AAB598.

[5] D. Klemm, B. Heublein, H. P. Fink, and A. Bohn, "Cellulose: Fascinating Biopolymer and Sustainable Raw Material," *Angewandte Chemie International Edition*, vol. 44, no. 22, pp. 3358–3393, May 2005, doi: 10.1002/ANIE.200460587.

[6] S. Pérez and K. Mazeau, "Conformations, Structures, and Morphologies of Celluloses," *Polysaccharides*, Nov. 2004, doi: 10.1201/9781420030822.CH2.

[7] R. Mülhaupt, "Hermann Staudinger and the Origin of Macromolecular Chemistry," *Angewandte Chemie International Edition*, vol. 43, no. 9, pp. 1054–1063, Feb. 2004, doi: 10.1002/ANIE.200330070.

[8] J. A. Kelly, M. Giese, K. E. Shopsowitz, W. Y. Hamad, and M. J. MacLachlan, "The Development of Chiral Nematic Mesoporous Materials," *Accounts of Chemical Research*, vol. 47, no. 4, pp. 1088–1096, Apr. 2014, doi: 10.1021/AR400243M.

[9] M. K. Khan, M. Giese, M. Yu, J. A. Kelly, W. Y. Hamad, and M. J. Maclachlan, "Flexible Mesoporous Photonic Resins with Tunable Chiral Nematic Structures," *Angewandte Chemie International Edition*, vol. 52, no. 34, pp. 8921–8924, Aug. 2013, doi: 10.1002/ANIE.201303829.

[10] W. Y. Hamad, "Cellulose Nanocrystals : Properties, Production and Applications.," p. 332, Wiley, 2017.

[11] A. M. C. Emons and B. M. Mulder, "How the deposition of cellulose microfibrils builds cell wall architecture," *Trends in Plant Science*, vol. 5, no. 1, pp. 35–40, Jan. 2000, doi: 10.1016/S1360-1385(99)01507-1.

[12] R. H. Atalla, "The Structures of Cellulose," *MRS Online Proceedings Library* vol. 15, p. 36, 2022.

[13] M. Jarvis, "Cellulose stacks up," *Nature 2003 426:6967*, vol. 426, no. 6967, pp. 611–612, Dec. 2003, doi: 10.1038/426611a.

[14] P. Zugenmaier, "Crystalline Cellulose and Derivatives," *Springer Series in Wood Science*. Springer, Berlin, Heidelberg. https://doi.org/10.1007/978-3-540-73934-0_5 2008

[15] J. J. Hermans, “Encyclopedia of polymer science and technology”, *Journal of Polymer Science Part A: General Papers*, vol. 3, no. 3, pp. 1245–1246, Mar. 1965, doi: 10.1002/POL.1965.100030330.

[16] C. Djahedi, M. Bergenstråhle-Wohlert, L. A. Berglund, and J. Wohlert, “Role of hydrogen bonding in cellulose deformation: the leverage effect analyzed by molecular modeling,” *Cellulose*, vol. 23, no. 4, pp. 2315–2323, Aug. 2016, doi: 10.1007/S10570-016-0968-0.

[17] A. Dufresne, “Nanocellulose,” *Nanocellulose*, Nov. 2012, doi: 10.1515/9783110254600.

[18] Y. Habibi, L. A. Lucia, and O. J. Rojas, “Cellulose Nanocrystals: Chemistry, Self-Assembly, and Applications,” *Chemical Reviews*, vol. 110, no. 6, pp. 3479–3500, Jun. 2010, doi: 10.1021/CR900339W.

[19] V. K. Varshney and S. Naithani, “Chemical Functionalization of Cellulose Derived from Nonconventional Sources,” *I. (eds) Cellulose Fibers: Bio- and Nano-Polymer Composites*. Springer, pp. 43–60, 2011, doi: 10.1007/978-3-642-17370-7_2.

[20] Y. Nishiyama, P. Langan, and H. Chanzy, “Crystal structure and hydrogen-bonding system in cellulose Iβ from synchrotron X-ray and neutron fiber diffraction,” *J Am Chem Soc*, vol. 124, no. 31, pp. 9074–9082, Aug. 2002, doi: 10.1021/JA0257319/SUPPL_FILE/JA0257319_S1.CIF.

[21] Y. Nishiyama, J. Sugiyama, H. Chanzy, and P. Langan, “Crystal Structure and Hydrogen Bonding System in Cellulose Iα from Synchrotron X-ray and Neutron Fiber Diffraction,” *J Am Chem Soc*, vol. 125, no. 47, pp. 14300–14306, Nov. 2003, doi: 10.1021/JA037055W/SUPPL_FILE/JA037055WSI20030711_112804.CIF.

[22] Q. Li and S. Renneckar, “Supramolecular structure characterization of molecularly thin cellulose I nanoparticles,” *Biomacromolecules*, vol. 12, no. 3, pp. 650–659, Mar. 2011, doi: 10.1021/BM101315Y.

[23] B. Medronho and B. Lindman, “Brief overview on cellulose dissolution/regeneration interactions and mechanisms,” *Adv Colloid Interface Sci*, vol. 222, pp. 502–508, Aug. 2015, doi: 10.1016/J.CIS.2014.05.004.

[24] C. Yamane, T. Aoyagi, M. Ago, K. Sato, K. Okajima, and T. Takahashi, “Two Different Surface Properties of Regenerated Cellulose due to Structural Anisotropy,” *Polymer Journal 2006 38:8*, vol. 38, no. 8, pp. 819–826, Jul. 2006, doi: 10.1295/polymj.pj2005187.

[25] R. C. Monica and R. Cremonini, “Nanoparticles and higher plants,” *Firenze University Press*, vol. 62, no. 2, pp. 161–165, Jan. 2014, doi: 10.1080/00087114.2004.10589681.

[26] D. Klemm, B. Heublein, H. P. Fink, and A. Bohn, “Cellulose: Fascinating Biopolymer and Sustainable Raw Material,” *Angewandte Chemie International Edition*, vol. 44, no. 22, pp. 3358–3393, May 2005, doi: 10.1002/ANIE.200460587.

[27] S. Tongye, P. Langan, A. D. French, G. P. Johnson, and S. Gnanakaran, “Conformational Flexibility of Soluble Cellulose Oligomers: Chain Length and Temperature Dependence,” *J Am Chem Soc*, vol. 131, no. 41, pp. 14786–14794, Oct. 2009, doi: 10.1021/JA9034158.

[28] J. P. Borges, J. P. Canejo, S. N. Fernandes, P. Brogueira, and M. H. Godinho, “Cellulose-Based Liquid Crystalline Composite Systems,” *Nanocellulose Polymer Nanocomposites:*

Fundamentals and Applications, vol. 9781118871904, pp. 215–235, Dec. 2014, doi: 10.1002/9781118872246.CH8.

[29] A. P. C. Almeida, J. P. Canejo, S. N. Fernandes, C. Echeverria, P. L. Almeida, and M. H. Godinho, "Cellulose-Based Biomimetics and Their Applications," *Advanced Materials*, vol. 30, no. 19, p. 1703655, May 2018, doi: 10.1002/ADMA.201703655.

[30] S. Tadepalli, J. M. Slocik, M. K. Gupta, R. R. Naik, and S. Singamaneni, "Bio-Optics and Bio-Inspired Optical Materials," *Chemical Reviews*, vol. 117, no. 20, pp. 12705–12763, Oct. 2017, doi: 10.1021/ACS.CHEMREV.7B00153.

[31] Y. Geng, P. L. Almeida, S. N. Fernandes, C. Cheng, P. Palffy-Muhoray, and M. H. Godinho, "A cellulose liquid crystal motor: a steam engine of the second kind," *Scientific Reports 2013 3:1*, vol. 3, no. 1, pp. 1–5, Jan. 2013, doi: 10.1038/srep01028.

[32] O. W. Guirguis, M. T. H. Moselhey, O. W. Guirguis, and M. T. H. Moselhey, "Thermal and structural studies of poly (vinyl alcohol) and hydroxypropyl cellulose blends," *Natural Science*, vol. 4, no. 1, pp. 57–67, Dec. 2011, doi: 10.4236/NS.2012.41009.

[33] J. F. Beecher, "Organic materials: wood, trees and nanotechnology," *Nat Nanotechnol*, vol. 2, no. 8, pp. 466–467, 2007, doi: 10.1038/NNANO.2007.239.

[34] E. Lam, K. B. Male, J. H. Chong, A. C. W. Leung, and J. H. T. Luong, "Applications of functionalized and nanoparticle-modified nanocrystalline cellulose," *Trends Biotechnol*, vol. 30, no. 5, pp. 283–290, May 2012, doi: 10.1016/J.TIBTECH.2012.02.001.

[35] R. J. Moon, A. Martini, J. Nairn, J. Simonsen, and J. Youngblood, "Cellulose nanomaterials review: structure, properties and nanocomposites," *Chemical Society Reviews*, vol. 40, no. 7, pp. 3941–3994, Jun. 2011, doi: 10.1039/C0CS00108B.

[36] X. Song, L. Zhou, B. Ding, X. Cui, Y. Duan, and J. Zhang, "Simultaneous improvement of thermal stability and redispersibility of cellulose nanocrystals by using ionic liquids," *Carbohydr Polym*, vol. 186, pp. 252–259, Apr. 2018, doi: 10.1016/J.CARBPOL.2018.01.055.

[37] M. Nogi, S. Iwamoto, A. N. Nakagaito, and H. Yano, "Optically Transparent Nanofiber Paper," *Advanced Materials*, vol. 21, no. 16, pp. 1595–1598, Apr. 2009, doi: 10.1002/ADMA.200803174.

[38] M. Nogi and H. Yano, "Transparent Nanocomposites Based on Cellulose Produced by Bacteria Offer Potential Innovation in the Electronics Device Industry," *Advanced Materials*, vol. 20, no. 10, pp. 1849–1852, May 2008, doi: 10.1002/ADMA.200702559.

[39] W. K. Czaja, D. J. Young, M. Kawecki, and R. M. Brown, "The future prospects of microbial cellulose in biomedical applications," *Biomacromolecules*, vol. 8, no. 1, pp. 1–12, Jan. 2007, doi: 10.1021/BM060620D.

[40] J. H. Kim, S. Mun, H. U. Ko, G. Y. Yun, and J. Kim, "Disposable chemical sensors and biosensors made on cellulose paper," *Nanotechnology*, vol. 25, no. 9, p. 092001, Feb. 2014, doi: 10.1088/0957-4484/25/9/092001.

[41] J. George and S. N. Sabapathi, “Cellulose nanocrystals: synthesis, functional properties, and applications,” *Nanotechnology, Science and Applications*, vol. 8, p. 45, Nov. 2015, doi: 10.2147/NSA.S64386.

[42] M. Mitov, “Cholesteric liquid crystals in living matter,” *Soft Matter*, vol. 13, no. 23, pp. 4176–4209, Jun. 2017, doi: 10.1039/C7SM00384F.

[43] S. Beck-Candanedo, M. Roman, and D. G. Gray, “Effect of reaction conditions on the properties and behavior of wood cellulose nanocrystal suspensions,” *Biomacromolecules*, vol. 6, no. 2, pp. 1048–1054, Mar. 2005, doi: 10.1021/BM049300P.

[44] S. Elazzouzi-Hafraoui, Y. Nishiyama, J. L. Putaux, L. Heux, F. Dubreuil, and C. Rochas, “The shape and size distribution of crystalline nanoparticles prepared by acid hydrolysis of native cellulose,” *Biomacromolecules*, vol. 9, no. 1, pp. 57–65, Jan. 2008, doi: 10.1021/BM700769P.

[45] F. Bettaieb *et al.*, “Preparation and characterization of new cellulose nanocrystals from marine biomass Posidonia oceanica,” *Industrial Crops and Products*, vol. 72, pp. 175–182, Oct. 2015, doi: 10.1016/J.INDCROP.2014.12.038.

[46] D. v. Saraiva *et al.*, “Flexible and Structural Coloured Composite Films from Cellulose Nanocrystals/Hydroxypropyl Cellulose Lyotropic Suspensions,” *Crystals 2020, Vol. 10, Page 122*, vol. 10, no. 2, p. 122, Feb. 2020, doi: 10.3390/CRYST10020122.

[47] J. Wohlert, M. Bergenstråhle-Wohlert, and L. A. Berglund, “Deformation of cellulose nanocrystals: Entropy, internal energy and temperature dependence,” *Cellulose*, vol. 19, no. 6, pp. 1821–1836, Dec. 2012, doi: 10.1007/S10570-012-9774-5.

[48] M. Mariano, N. el Kissi, and A. Dufresne, “Cellulose nanocrystals and related nanocomposites: Review of some properties and challenges,” *Journal of Polymer Science Part B: Polymer Physics*, vol. 52, no. 12, pp. 791–806, Jun. 2014, doi: 10.1002/POLB.23490.

[49] S. Park, J. O. Baker, M. E. Himmel, P. A. Parilla, and D. K. Johnson, “Cellulose crystallinity index: Measurement techniques and their impact on interpreting cellulase performance,” *Biotechnology for Biofuels*, vol. 3, no. 1, pp. 1–10, May 2010, doi: 10.1186/1754-6834-3-10/TABLES/2.

[50] W. Yang *et al.*, “Effect of cellulose and lignin on disintegration, antimicrobial and antioxidant properties of PLA active films,” *International Journal of Biological Macromolecules*, vol. 89, pp. 360–368, Aug. 2016, doi: 10.1016/J.IJBIOMAC.2016.04.068.

[51] L. Brinchi, F. Cotana, E. Fortunati, and J. M. Kenny, “Production of nanocrystalline cellulose from lignocellulosic biomass: technology and applications,” *Carbohydr Polym*, vol. 94, no. 1, pp. 154–169, Apr. 2013, doi: 10.1016/J.CARBPOL.2013.01.033.

[52] B. L. Peng, N. Dhar, H. L. Liu, and K. C. Tam, “Chemistry and applications of nanocrystalline cellulose and its derivatives: A nanotechnology perspective,” *The Canadian Journal of Chemical Engineering*, vol. 89, no. 5, pp. 1191–1206, Oct. 2011, doi: 10.1002/CJCE.20554.

[53] W. P. Flauzino Neto *et al.*, “Comprehensive morphological and structural investigation of cellulose i and II nanocrystals prepared by sulphuric acid hydrolysis,” *RSC Advances*, vol. 6, no. 79, pp. 76017–76027, 2016, doi: 10.1039/C6RA16295A.

[54] W. P. Flauzino Neto, H. A. Silvério, N. O. Dantas, and D. Pasquini, “Extraction and characterization of cellulose nanocrystals from agro-industrial residue - Soy hulls,” *Industrial Crops and Products*, vol. 42, no. 1, pp. 480–488, Mar. 2013, doi: 10.1016/J.INDCROP.2012.06.041.

[55] G. Sèbe, F. Ham-Pichavant, E. Ibarboure, A. L. C. Koffi, and P. Tingaut, “Supramolecular structure characterization of cellulose II nanowhiskers produced by acid hydrolysis of cellulose I substrates,” *Biomacromolecules*, vol. 13, no. 2, pp. 570–578, Feb. 2012, doi: 10.1021/BM201777J.

[56] N. Lin and A. Dufresne, “Surface chemistry, morphological analysis and properties of cellulose nanocrystals with gradiented sulfation degrees,” *Nanoscale*, vol. 6, no. 10, pp. 5384–5393, May 2014, doi: 10.1039/C3NR06761K.

[57] Silva, Deusanilde & D' Almeida, Maria ,“Cellulose whiskers”, *Revista O Papel*, 70. 34, 2009.

[58] W. Y. Hamad and T. Q. Hu, “Structure–process–yield interrelations in nanocrystalline cellulose extraction,” *The Canadian Journal of Chemical Engineering*, vol. 88, no. 3, pp. 392–402, Jun. 2010, doi: 10.1002/CJCE.20298.

[59] S. N. Fernandes *et al.*, “Mind the Microgap in Iridescent Cellulose Nanocrystal Films,” *Advanced Materials*, vol. 29, no. 2, p. 1603560, Jan. 2017, doi: 10.1002/ADMA.201603560.

[60] O. A. Battista, S. Coppick, J. A. Howsmon, F. F. Morehead, and W. A. Sisson, “Level-Off Degree of Polymerization,” *Industrial & Engineering Chemistry*, vol. 48, no. 2, pp. 333–335, Feb. 2002, doi: 10.1021/IE50554A046.

[61] J. P. F. Lagerwall *et al.*, “Cellulose nanocrystal-based materials: from liquid crystal self-assembly and glass formation to multifunctional thin films,” *NPG Asia Materials 2014 6:1*, vol. 6, no. 1, pp. e80–e80, Jan. 2014, doi: 10.1038/am.2013.69.

[62] X. Liu, M. Li, X. Zheng, E. Retulainen, and S. Fu, “Dual light- and pH-responsive composite of polyazo-derivative grafted cellulose nanocrystals,” *Materials*, vol. 11, no. 9, Sep. 2018, doi: 10.3390/MA11091725.

[63] D. Liu, S. Wang, Z. Ma, D. Tian, M. Gu, and F. Lin, “Structure–color mechanism of iridescent cellulose nanocrystal films,” *RSC Advances*, vol. 4, no. 74, pp. 39322–39331, Aug. 2014, doi: 10.1039/C4RA06268J.

[64] A. Tran, W. Y. Hamad, and M. J. MacLachlan, “Fabrication of cellulose nanocrystal films through differential evaporation for patterned coatings,” *ACS Applied Nano Materials*, vol. 1, no. 7, pp. 3098–3104, Jul. 2018, doi: 10.1021/ACSANM.8B00947/SUPPL_FILE/AN8B00947_SI_001.PDF.

[65] B. Frka-Petesic, G. Guidetti, G. Kamita, and S. Vignolini, “Controlling the Photonic Properties of Cholesteric Cellulose Nanocrystal Films with Magnets,” *Adv Mater*, vol. 29, no. 32, Aug. 2017, doi: 10.1002/ADMA.201701469.

[66] B. Frka-Petesic, H. Radavidson, B. Jean, and L. Heux, “Dynamically Controlled Iridescence of Cholesteric Cellulose Nanocrystal Suspensions Using Electric Fields,” *Advanced Materials*, vol. 29, no. 11, p. 1606208, Mar. 2017, doi: 10.1002/ADMA.201606208.

[67] X. M. Dong, J. F. Revol, and D. G. Gray, “Effect of microcrystallite preparation conditions on the formation of colloid crystals of cellulose,” *Cellulose 1998 5:1*, vol. 5, no. 1, pp. 19–32, 1998, doi: 10.1023/A:1009260511939.

[68] S. Beck, J. Bouchard, and R. Berry, “Controlling the Reflection Wavelength of Iridescent Solid Films of Nanocrystalline Cellulose,” *Biomacromolecules*, vol. 12, no. 1, pp. 167–172, Jan. 2010, doi: 10.1021/BM1010905.

[69] D. Liu, S. Wang, Z. Ma, D. Tian, M. Gu, and F. Lin, “Structure–color mechanism of iridescent cellulose nanocrystal films,” *RSC Advances*, vol. 4, no. 74, pp. 39322–39331, Aug. 2014, doi: 10.1039/C4RA06268J.

[70] T. D. Nguyen, W. Y. Hamad, and M. J. MacLachlan, “Tuning the iridescence of chiral nematic cellulose nanocrystals and mesoporous silica films by substrate variation,” *Chemical Communications*, vol. 49, no. 96, pp. 11296–11298, Nov. 2013, doi: 10.1039/C3CC47337F.

[71] R. H. Marchessault, F. F. Morehead, and N. M. Walter, “Liquid Crystal Systems from Fibrillar Polysaccharides,” *Nature 1959 184:4686*, vol. 184, no. 4686, pp. 632–633, 1959, doi: 10.1038/184632a0.

[72] H. Chanzy, A. Peguy, S. Chaunis, and P. Monzie, “Oriented cellulose films and fibers from a mesophase system,” *Journal of Polymer Science: Polymer Physics Edition*, vol. 18, no. 5, pp. 1137–1144, May 1980, doi: 10.1002/POL.1980.180180517.

[73] P. Navard and J. M. Haudin, “Rheololgy of Mesomorphic Solutions of Cellulose,” *British Polymer Journal*, vol. 12, no. 4, pp. 174–178, Dec. 1980, doi: 10.1002/PI.4980120408.

[74] D. L. Patel and R. D. Gilbert, “Lyotropic mesomorphic formation of cellulose in trifluoroacetic acid-chlorinated-alkane solvent mixtures at room temperature,” *Journal of Polymer Science: Polymer Physics Edition*, vol. 19, no. 8, pp. 1231–1236, Aug. 1981, doi: 10.1002/POL.1981.180190806.

[75] R. S. Werbowyj and D. G. Gray, “Liquid Crystalline Structure In Aqueous Hydroxypropyl Cellulose Solutions,” *http://dx.doi.org/10.1080/15421407608083894*, vol. 34, no. 4, pp. 97–103, 2007, doi: 10.1080/15421407608083894.

[76] R. S. Werbowyj and D. G. Gray, “Ordered Phase Formation in Concentrated Hydroxpropylcellulose Solutions,” *Macromolecules*, vol. 13, no. 1, pp. 69–73, 2002, doi: 10.1021/MA60073A014.

[77] C. Echeverria, P. L. Almeida, G. Feio, J. L. Figueirinhas, and M. H. Godinho, “A cellulosic liquid crystal pool for cellulose nanocrystals: Structure and molecular dynamics at high shear rates,” *European Polymer Journal*, vol. 72, pp. 72–81, Nov. 2015, doi: 10.1016/J.EURPOLYMJ.2015.09.006.

[78] D. G. Gray and X. Mu, “Chiral Nematic Structure of Cellulose Nanocrystal Suspensions and Films; Polarized Light and Atomic Force Microscopy,” *Materials 2015, Vol. 8, Pages 7873-7888*, vol. 8, no. 11, pp. 7873–7888, Nov. 2015, doi: 10.3390/MA8115427.

[79] J. F. Revol, H. Bradford, J. Giasson, R. H. Marchessault, and D. G. Gray, “Helicoidal self-ordering of cellulose microfibrils in aqueous suspension,” *Int J Biol Macromol*, vol. 14, no. 3, pp. 170–172, 1992, doi: 10.1016/S0141-8130(05)80008-X.

[80] L. Onsager, “The effects of shape on the interaction of colloidal particles,” *Ann N Y Acad Sci*, vol. 51, no. 4, pp. 627–659, May 1949, doi: 10.1111/J.1749-6632.1949.TB27296.X.

[81] D. G. Gray, “Chiral nematic ordering of polysaccharides,” *Carbohydrate Polymers*, vol. 25, no. 4, pp. 277–284, Jan. 1994, doi: 10.1016/0144-8617(94)90053-1.

[82] A. Stroobants, H. N. W. Lekkerkerker, and T. Odijk, “Effect of electrostatic interaction on the liquid crystal phase transition in solutions of rodlike polyelectrolytes,” *Macromolecules*, vol. 19, no. 8, pp. 2232–2238, 2002, doi: 10.1021/MA00162A020.

[83] D. G. Gray, “Recent Advances in Chiral Nematic Structure and Iridescent Color of Cellulose Nanocrystal Films,” *Nanomaterials (Basel)*, vol. 6, no. 11, Nov. 2016, doi: 10.3390/NANO6110213.

[84] Y. Zhang, Q. Cheng, C. Chang, and L. Zhang, “Phase transition identification of cellulose nanocrystal suspensions derived from various raw materials,” *Journal of Applied Polymer Science*, vol. 135, no. 24, p. 45702, Jun. 2018, doi: 10.1002/APP.45702.

[85] B. Tjipto-Margo and G. T. Evans, “The Onsager theory of the isotropic–nematic liquid–crystal transition: Biaxial particles in uniaxial phases,” *The Journal of Chemical Physics*, vol. 94, no. 6, p. 4546, Aug. 1998, doi: 10.1063/1.460609.

[86] X. Wei, T. Lin, M. Duan, H. Du, and X. Yin, “Cellulose Nanocrystal-based Liquid Crystal Structures and the Unique Optical Characteristics of Cellulose Nanocrystal Films,” *BioResources*, vol. 16, no. 1, pp. 2116–2137, Jan. 2021.

[87] J. Sun, B. Bhushan, and J. Tong, “Structural coloration in nature,” *RSC Advances*, vol. 3, no. 35, pp. 14862–14889, Sep. 2013, doi: 10.1039/C3RA41096J.

[88] A. R. Parker, “Colour in Burgess Shale animals and the effect of light on evolution in the Cambrian,” *Proceedings of the Royal Society B: Biological Sciences*, vol. 265, no. 1400, p. 967, Jun. 1998, doi: 10.1098/RSPB.1998.0385.

[89] S. Kinoshita, S. Yoshioka, and J. Miyazaki, “Physics of structural colors,” *Reports on Progress in Physics*, vol. 71, no. 7, p. 076401, Jun. 2008, doi: 10.1088/0034-4885/71/7/076401.

[90] Y. Zhao, Z. Xie, H. Gu, C. Zhu, and Z. Gu, “Bio-inspired variable structural color materials,” *Chemical Society Reviews*, vol. 41, no. 8, pp. 3297–3317, Mar. 2012, doi: 10.1039/C2CS15267C.

[91] H. S. Lee, T. S. Shim, H. Hwang, S. M. Yang, and S. H. Kim, “Colloidal photonic crystals toward structural color palettes for security materials,” *Chemistry of Materials*, vol. 25, no. 13, pp. 2684–2690, Jul. 2013, doi: 10.1021/CM4012603/SUPPL_FILE/CM4012603_SI_001.PDF.

[92] M. Kaczmarek and Y. Tomita, “Optics of nanocomposite materials,” *Journal of Optics A: Pure and Applied Optics*, vol. 11, no. 2, p. 020201, Feb. 2009, doi: 10.1088/1464-4258/11/2/020201.

[93] “US5629055A - Solidified liquid crystals of cellulose with optically variable properties - Google Patents.” https://patents.google.com/patent/US5629055A/en.

[94] K. Buhl, Z. Roth, P. Srinivasan, R. Rumpf, and E. Johnson, “Biologically inspired optics: analog semiconductor model of the beetle exoskeleton,” *The Nature of Light: Light in Nature II*, vol. 7057, p. 705707, Aug. 2008, doi: 10.1117/12.794313.

[95] C. D. Edgar and D. G. Gray, “Induced Circular Dichroism of Chiral Nematic Cellulose Films,” *Cellulose 2001 8:1*, vol. 8, no. 1, pp. 5–12, 2001, doi: 10.1023/A:1016624330458.

[96] H. Golmohammadi, E. Morales-Narváez, T. Naghdi, and A. Merkoçi, “Nanocellulose in Sensing and Biosensing,” *Chemistry of Materials*, vol. 29, no. 13, pp. 5426–5446, Jul. 2017, doi: 10.1021/ACS.CHEMMATER.7B01170.

[97] A. Saha, Y. Tanaka, Y. Han, C. M. W. Bastiaansen, D. J. Broer, and R. P. Sijbesma, “Irreversible visual sensing of humidity using a cholesteric liquid crystal,” *Chemical Communications*, vol. 48, no. 38, pp. 4579–4581, Apr. 2012, doi: 10.1039/C2CC16934G.

[98] R. M. A. Domingues, M. E. Gomes, and R. L. Reis, “The potential of cellulose nanocrystals in tissue engineering strategies,” *Biomacromolecules*, vol. 15, no. 7, pp. 2327–2346, Jul. 2014, doi: 10.1021/BM500524S.

[99] G. Mondragon *et al.*, “Nanocomposites of Waterborne Polyurethane Reinforced with Cellulose Nanocrystals from Sisal Fibres,” *J Polym Environ*, vol. 26, pp. 1869–1880, 2018, doi: 10.1007/s10924-017-1089-z.

[100] T. Hiratani, W. Y. Hamad, and M. J. MacLachlan, “Transparent Depolarizing Organic and Inorganic Films for Optics and Sensors,” *Adv Mater*, vol. 29, no. 13, Apr. 2017, doi: 10.1002/ADMA.201606083.

[101] M. Giese, L. K. Blusch, M. K. Khan, W. Y. Hamad, and M. J. Maclachlan, “Responsive mesoporous photonic cellulose films by supramolecular cotemplating,” *Angew Chem Int Ed Engl*, vol. 53, no. 34, pp. 8880–8884, Aug. 2014, doi: 10.1002/ANIE.201402214.

[102] M. Giese, L. K. Blusch, M. K. Khan, and M. J. MacLachlan, “Functional materials from cellulose-derived liquid-crystal templates,” *Angew Chem Int Ed Engl*, vol. 54, no. 10, pp. 2888–2910, Mar. 2015, doi: 10.1002/ANIE.201407141.

[103] M. M. de Souza Lima and R. Borsali, “Rodlike Cellulose Microcrystals: Structure, Properties, and Applications,” *Macromolecular Rapid Communications*, vol. 25, no. 7, pp. 771–787, Apr. 2004, doi: 10.1002/MARC.200300268.

[104] J. Pan, W. Hamad, and S. K. Straus, “Parameters affecting the chiral nematic phase of nanocrystalline cellulose films,” *Macromolecules*, vol. 43, no. 8, pp. 3851–3858, Apr. 2010.

[105] Y. Cao, W. Y. Hamad, and M. J. MacLachlan, “Broadband Circular Polarizing Film Based on Chiral Nematic Liquid Crystals,” *Advanced Optical Materials*, vol. 6, no. 17, p. 1800412, Sep. 2018, doi: 10.1002/ADOM.201800412.

[106] T. H. Zhao *et al.*, “Printing of Responsive Photonic Cellulose Nanocrystal Microfilm Arrays,” *Advanced Functional Materials*, vol. 29, no. 21, p. 1804531, May 2019, doi: 10.1002/ADFM.201804531.

[107] T. Wu, J. Li, J. Li, S. Ye, J. Wei, and J. Guo, “A bio-inspired cellulose nanocrystal-based nanocomposite photonic film with hyper-reflection and humidity-responsive actuator properties,” *Journal of Materials Chemistry C*, vol. 4, no. 41, pp. 9687–9696, Oct. 2016, doi: 10.1039/C6TC02629J.

[108] P. Grey *et al.*, “Field-Effect Transistors on Photonic Cellulose Nanocrystal Solid Electrolyte for Circular Polarized Light Sensing,” *Advanced Functional Materials*, vol. 29, no. 21, p. 1805279, May 2019, doi: 10.1002/ADFM.201805279.

[109] K. Yao, Q. Meng, V. Bulone, and Q. Zhou, “Flexible and Responsive Chiral Nematic Cellulose Nanocrystal/Poly(ethylene glycol) Composite Films with Uniform and Tunable Structural Color,” *Advanced Materials*, vol. 29, no. 28, p. 1701323, Jul. 2017, doi: 10.1002/ADMA.201701323.

[110] L. Wang, A. M. Urbas, and Q. Li, “Nature-Inspired Emerging Chiral Liquid Crystal Nanostructures: From Molecular Self-Assembly to DNA Mesophase and Nanocolloids.,” *Advanced Materials*, vol. 32, no. 41, Oct. 2018, doi: 10.1002/ADMA.201801335.

[111] J. Chen *et al.*, “Self-healing responsive chiral photonic films for sensing and encoding,” *Journal of Materials Chemistry C*, vol. 6, no. 29, pp. 7767–7775, Jul. 2018, doi: 10.1039/C8TC02666A.

[112] Y. P. Zhang, “Nanocrystalline cellulose for covert optical encryption,” *Journal of Nanophotonics*, vol. 6, no. 1, p. 063516, Jul. 2012, doi: 10.1117/1.JNP.6.063516.

[113] L. Gan, N. Feng, S. Liu, S. Zheng, Z. Li, and J. Huang, “Assembly-Induced Emission of Cellulose Nanocrystals for Hiding Information,” *Particle & Particle Systems Characterization*, vol. 36, no. 3, p. 1800412, Mar. 2019, doi: 10.1002/PPSC.201800412.

[114] E. Rusen, A. Mocanu, A. Diacon, and B. Marculescu, “Fluorescence Enhancement of Rhodamine B in the Presence of Photonic Crystal Heterostructures,” *Journal of Physical Chemistry C*, vol. 115, no. 30, pp. 14947–14953, Aug. 2011, doi: 10.1021/JP2041422.

[115] P. Doutora Maria Helena Godinho and P. Associada com Agre-gação, “Elementos oticamente variáveis para sistemas de anti falsificação originários de celulose nanocristalina,” Jun. 2018, Accessed: Jan. 09, 2022. [Online]. Available: https://run.unl.pt/handle/10362/41283

[116] X. M. Dong and D. G. Gray, “Effect of Counterions on Ordered Phase Formation in Suspensions of Charged Rodlike Cellulose Crystallites,” *Langmuir*, vol. 13, no. 8, pp. 2404–2409, Apr. 1997, doi: 10.1021/LA960724H.

[117] J. L. Huang, C. J. Li, and D. G. Gray, “Functionalization of cellulose nanocrystal films via ‘thiol–ene’ click reaction,” *RSC Advances*, vol. 4, no. 14, pp. 6965–6969, Jan. 2014, doi: 10.1039/C3RA47041E.

[118] V. Hospodarova, E. Singovszka, N. Stevulova, V. Hospodarova, E. Singovszka, and N. Stevulova, “Characterization of Cellulosic Fibers by FTIR Spectroscopy for Their Further Implementation to Building Materials,” *American Journal of Analytical Chemistry*, vol. 9, no. 6, pp. 303–310, Jun. 2018, doi: 10.4236/AJAC.2018.96023.

[119] D. Ciolacu, F. Ciolacu, and V. I. Popa, “Amorphous cellulose-structure and characterization,” *Cellulose Chem. Technol*, vol. 45, no. 2, pp. 13–21, 2011.

[120] D. Gaspar *et al.*, “Nanocrystalline cellulose applied simultaneously as the gate dielectric and the substrate in flexible field effect transistors,” *Nanotechnology*, vol. 25, no. 9, Mar. 2014, doi: 10.1088/0957-4484/25/9/094008.

[121] J. L. Huang, C. J. Li, and D. G. Gray, “Cellulose nanocrystals incorporating fluorescent methylcoumarin groups,” *ACS Sustainable Chemistry and Engineering*, vol. 1, no. 9, pp. 1160–1164, Sep. 2013.

[122] C. Honorato-Rios *et al.*, “Fractionation of cellulose nanocrystals: enhancing liquid crystal ordering without promoting gelation,” *NPG Asia Materials 2018 10:5*, vol. 10, no. 5, pp. 455–465, May 2018, doi: 10.1038/s41427-018-0046-1.

[123] C. M. Walters, C. E. Boott, T. D. Nguyen, W. Y. Hamad, and M. J. Maclachlan, “Iridescent cellulose nanocrystal films modified with hydroxypropyl cellulose,” *Biomacromolecules*, vol. 21, no. 3, pp. 1295–1302, Mar. 2020.

[124] M. Bercea, P. Navard, and " Petru, “Viscosity of hydroxypropylcellulose solutions in non-entangled and entangled states,” *Cellulose Chem. Technol*, vol. 52, no. 8, pp. 603–608, 2018.

[125] C. Echeverria, P. L. Almeida, G. Feio, J. L. Figueirinhas, and M. H. Godinho, “A cellulosic liquid crystal pool for cellulose nanocrystals: structure and molecular dynamics at high shear rates,” *European Polymer Journal*, vol. 72, pp. 72–81, Nov. 2015, doi: 10.1016/J.EURPOLYMJ.2015.09.006.

[126] T. Huq *et al.*, “Nanocrystalline cellulose (NCC) reinforced alginate based biodegradable nanocomposite film,” *Carbohydrate Polymers*, vol. 90, no. 4, pp. 1757–1763, Nov. 2012, doi: 10.1016/J.CARBPOL.2012.07.065.

[127] N. F. Vasconcelos *et al.*, “Bacterial cellulose nanocrystals produced under different hydrolysis conditions: Properties and morphological features,” *Carbohydrate Polymers*, vol. 155, pp. 425–431, Jan. 2017, doi: 10.1016/J.CARBPOL.2016.08.090.

[128] R. J. Samuels, “Solid-state characterization of the structure and deformation behavior of water-soluble hydroxypropylcellulose,” *J. Polym. Sci. A-2 Polym. Phys*, vol. 7, no. 7, pp. 1197–1258, Jul. 1969, doi: 10.1002/POL.1969.160070705.

[129] P. L. Smart and I. M. S. Laidlaw, “An evaluation of some fluorescent dyes for water tracing,” *Water Resources Research*, vol. 13, no. 1, pp. 15–33, Feb. 1977, doi: 10.1029/WR013I001P00015.

[130] S. Eyley and W. Thielemans, “Surface modification of cellulose nanocrystals,” *Nanoscale*, vol. 6, no. 14, pp. 7764–7779, Jun. 2014, doi: 10.1039/C4NR01756K.

[131] Z. Cheng, L. Zheng, H. Xu, L. Pang, and H. He, “A rhodamine-based fluorescent probe for Fe3+: synthesis, theoretical calculation and bioimaging application,” *Analytical Methods*, vol. 11, no. 19, pp. 2565–2570, May 2019, doi: 10.1039/C9AY00499H.

[132] X. Ye, Y. Kang, and J. Zhou, “Rhodamine labeled cellulose nanocrystals as selective ‘naked-eye’ colorimetric and fluorescence sensor for Hg2+ in aqueous solutions,” *Cellulose 2020 27:9*, vol. 27, no. 9, pp. 5197–5210, Apr. 2020, doi: 10.1007/S10570-020-03126-5.

[133] J. He, K. Bian, N. Li, and G. Piao, “Generation of full-color and switchable circularly polarized luminescence from nonchiral dyes assembled in cholesteric cellulose films,” *Journal of Materials Chemistry C*, vol. 7, no. 30, pp. 9278–9283, Aug. 2019, doi: 10.1039/C9TC01956A.

[134] J. He, N. Li, K. Bian, and G. Piao, “Optically active polyaniline film based on cellulose nanocrystals,” *Carbohydrate Polymers*, vol. 208, pp. 398–403, Mar. 2019, doi: 10.1016/J.CARBPOL.2018.12.091.

3. Chapter 3: Soft matter based PUF keys using electrospinning

The use of fluorescent materials incorporated in microscopic fibers has been exploited to create anti-counterfeiting labels due to their low cost, good concealment and easy preparation[1]. Several luminescent dyes such as fluorene, rhodamine and azo fluorescent dyes have been developed as dyes for fluorescent fibers[2].

Electrospinning is one of the most used techniques to create fibers from a broad range of polymers [3]. Through this method, it is possible to tune the properties of polymeric nanofibers such as strength, stiffness, fiber porosity and diameter.

Small fluorescent dye molecules can be placed in a solution with a dry polymer and a solvent and, then, be electrospun into fibers. Figure 3.1 shows a confocal microscopy image of electrospun polymeric fibers with an incorporated fluorescent tetramethylrhodamine (TRITC) dye [4] .

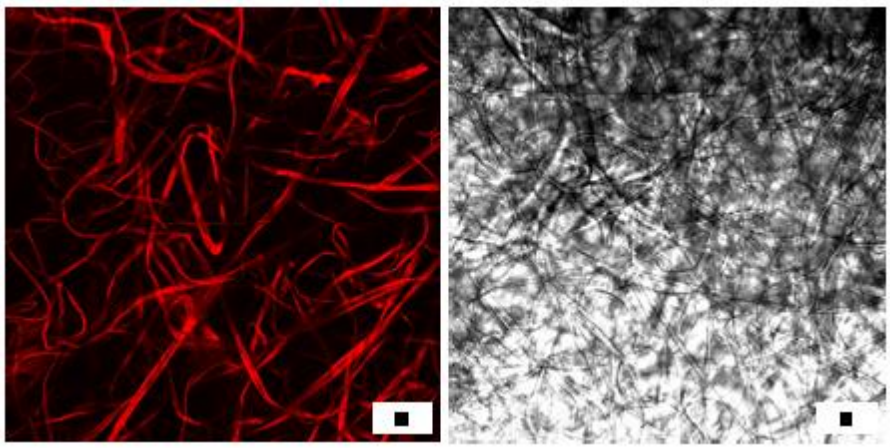

Figure 3. 1 Fluorescence (left) and light microscope (right) images of electrospun polymeric fabric with tetramethylrhodamine (TRITC) dye incorporated, scale bar 10µm.[4]

Unfortunately, several dyes are not environmentally friendly, and this can be a problem if they leak from fibers, or they may undergo photobleaching when exposed to certain wavelengths. For these reasons, a lot of efforts have been done to create dyes with improved characteristics.

As an example, Hendrick et al. in 2010 [4] have developed nanoparticles composed of a dye-rich core surrounded by a silica shell, which exhibit fluorescent emission when excited by an external light source. Silica nanoparticles are 20-30 times brighter than single fluorescent dye molecules, do not have leakage problems, are resistant to quenching, and exhibit greater resistance to photobleaching. The silica shell allows the particles to maintain brightness for longer than a fluorescent dye solution. The authors used several types of nanoparticles with different emission wavelengths to be embedded in electrospun fibers. Since fibers are arranged in an intricate pattern, a unique fluorescent motif can be created.

A similar anti-counterfeit method has been patented using quantum dots as fluorescent taggants in security inks, papers and explosives [5].

Composite fibers made of polymer/liquid crystal have been extensively studied[6]–[8] showing that the liquid crystal optical properties may be transferred to the fiber-containing liquid crystal. In figure 3.2 are shown fibers with a cholesteric liquid crystal core [9]. The periodicity of the helix is in the range of the optical wavelengths and this leads to Bragg's reflection of a specific wavelength. For this reason, fibers appear green on a black background.

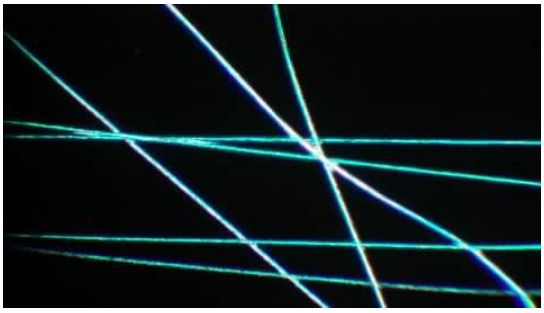

Figure 3. 2 PVP fibers containing a short-pitch cholesteric liquid crystal shine bright green when observed using a polarized light optical microscope. The selectively reflected color depends on the structure of the liquid crystal and it is very sensitive to external influences [9]

The composite fibers, depending on the liquid crystal used, have potential different applications in optics.

Here we propose to electrospun a fluorescent emulsion of a dye-doped liquid crystal inside a polymeric matrix to obtain fibers with peculiar optical properties. The goal is to produce an anticounterfeiting label containing a random fluorescent pattern incorporated inside a free-standing fibers mat. The liquid crystal is doped with materials that are intended to mechanically strengthen the area containing the fluorophore to prevent leakage problems.

Cellulose Nanocrystals are one of the materials used as reinforcement[10] due to their nano-dimensions, high aspect ratio, high crystallinity, low density, high mechanical strength and unique morphology. Studies have been reported on using CNCs as reinforcing material for polymer fibers fabricated by the electrospinning technique [10], [11]. A CNC-functionalized polymer composite shows in addition to the potential as reinforcement also a good promise for chemical crosslinking (due to the -OH groups on both the PVA, in addition to the esterification of the vinyl group, and CNC).

The first part of this chapter is devoted to a description of the preparation of electrospun fibers mats starting from emulsions of dye doped liquid crystal microspheres inside an immiscible fluid matrix of PVA using the electrospinning technique with different deposition parameters.
In the second part, known that the polymer matrices can be reinforced by the addition of cellulose nanocrystals, the preparation of different fibers mats from a mixture of PVA and CNCs will be described.
Finally, the preparation of a CNC reinforced free-standing film containing a random fluorescent pattern of fluorescent liquid crystal microspheres to be used as an anticounterfeiting label will be described. The morphological properties of the fibers mats were analyzed by atomic force microscopy (AFM) and polarized light optical microscopy (POM), while the optical fluorescence properties were analyzed by confocal laser scanning microscopy (CLSM).

3.1.Electrospinning technique

Electrospinning is a fascinating technique that allows to obtain continuous and very thin filaments from a variety of polymers that can be collected in the form of thin self-supported membranes and it also ~~even~~ allows the incorporation of non-polymeric materials in the fibers cores.
The process consists in placing a polymer solution or a melted polymer into a syringe with a metallic needle and applying a strong electric field between the needle (the injector) and a conductive surface (the collector) which is located a few tens of centimetres from the needle while forcing the polymer outside the syringe. Figure 3.3 shows a simplified scheme of the instrument.
When the solution is injected into the system, a drop appears at the end of the needle which is kept stable by the surface tension γ. By applying an electric field, the surface of the drop becomes charged. As the electric field gradually increases, the charge in the fluid also increases, this leads to increasingly strong repulsive interactions that cause the drop to deform. This deformation is influenced by two forces that compete with each other: the surface tension of the fluid which favors the maintenance of the spherical shape by minimizing the surface area and the Coulomb repulsive forces which, instead, favours the increase of the surface area. When the repulsive forces become greater than the surface tension of the drop, the drop deforms into a conical profile called a "*Taylor cone*". Once the applied potential exceeds a threshold value V, assuming that the liquid is so viscous that it does not break, a charged jet is emitted from the Taylor cone shown in the red rectangle in figure 3.3 and is pushed towards the collecting surface. The formation of the Taylor cone is observed when the electrostatic pressure p_e exceeds the capillary pressure p_c. p_e on the surface of the liquid is defined as:

$$p_e = \frac{1}{2}\varepsilon E^2 \tag{3. 1}$$

where ε is the relative permittivity of the surrounding gas and E is the intensity of the electric field. Instead, p_c is defined by the Young-Laplace equation:

$$p_c = \frac{2\gamma}{r} \tag{3. 2}$$

where γ is the surface tension and r is the curvature of the drop surface, equal to the internal radius of the needle. The condition for the formation of the Taylor cone occurs for values $p_e \geq p_c$.

Once the highly charged jet is obtained, the charge density continuously increases due to the evaporation of the solvent before it reaches the surface of the collector, where it is deposited in the form of solid fibers. When the jet begins to solidify, the electrical charges migrate to the surface of the fiber. When this happens, the charges present on the surface cause the jet to fold back on itself, drawing circumferences with an ever-smaller radius. The whirling spiral movement of the jet extends its effective path concerning the small distance between the injector and the collector. It is the lengthening of the path that causes the thinning of the fiber and this is the reason for the thin diameters of the fibers of sub-micrometric dimensions.

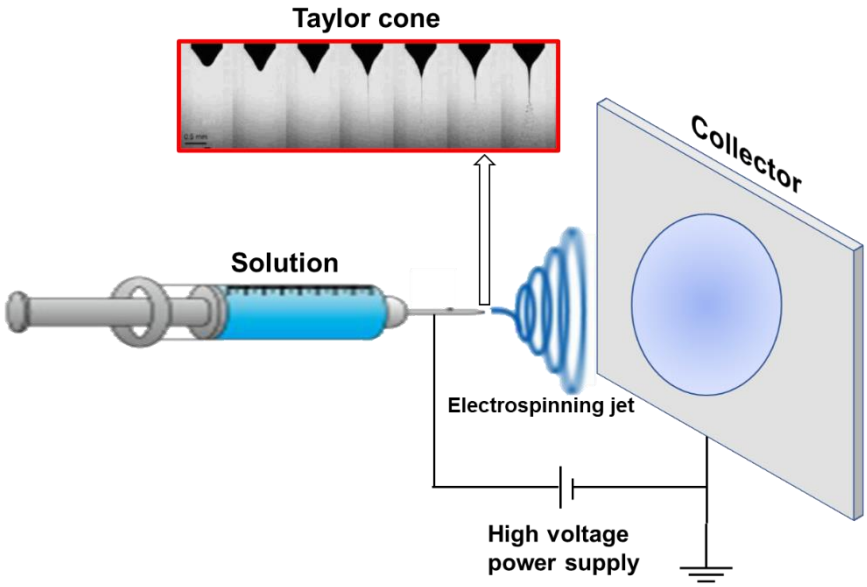

Figure 3. 3 Schematic representation of an electrospinning apparatus. In the red rectangle, the evolution of the profile of a drop at the end of the needle as the applied voltage increases. The rounded profile becomes more and more pointed until the pressure p_e in the drop exceeds the value of p_c, at this point a jet protrudes from the apex.

The electrospinning apparatus used for this work is shown in figure 3.4.

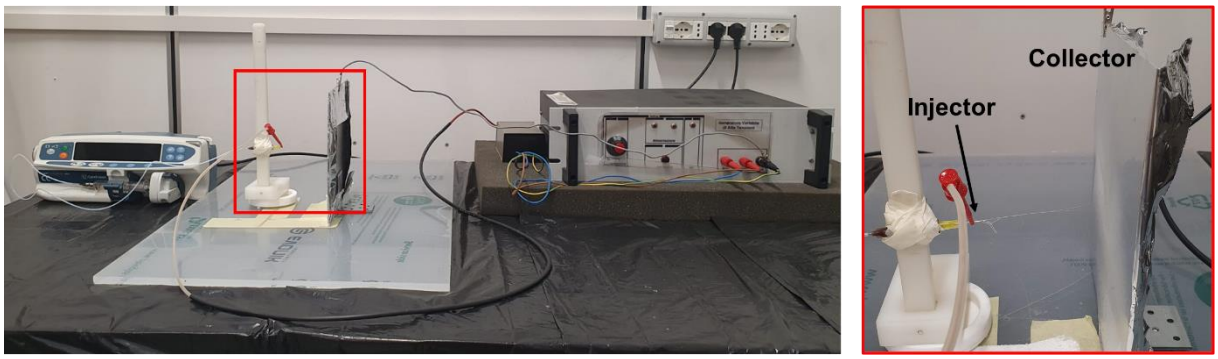

Figure 3. 4Electrospinning setup. On the left a zoom of the injector and the collector part where the electrospun fiber is visible

From a technical point of view, the quality and characteristics of the electrospun fibers depend on many parameters such as the properties of the solution as polymer concentration, viscosity, conductivity, surface tension and type of solvent and on the electrospinning set-up ones such as the applied voltage, the flow rate, the distance of the syringe needle from the collector, the geometry of the collector, the size of the needle and, finally, they depend also from environmental conditions such as temperature and humidity.

3.1.1. Solution parameters

One of the crucial parameters for the electrospinning process is the concentration of the polymer solution that is fundamental for the homogeneity of the fibers, in fact, during the formation of the fiber some domains in the jet itself could try to minimize the surface free energy by forming spherical objects distributed along the fibers themselves, called *beads* (figure 3.5). For low concentrations, a not good quality fiber is obtained with an uneven texture composed of mixed fibers in which the beads are present. As the concentration increases, the beads change shape and take on an elongated form until they disappear completely at high concentrations. In this case, more uniform fibers with larger diameters are obtained.

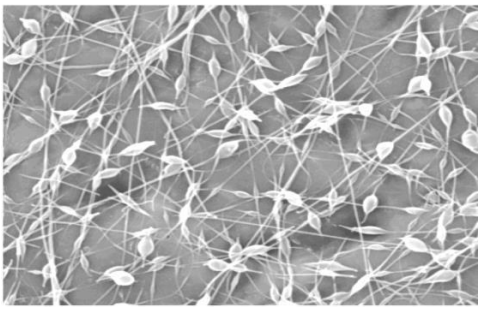

Figure 3. 5 Beads defects created during the electrospinning process.

Also important is the molecular weight of the polymer, which affects the morphology of the fibers. Generally, high molecular weight polymers are preferred because they guarantee the right viscosity for the creation of the fibers. Furthermore, low molecular weight polymers form beads while high molecular weight ones produce fibers with large diameters and a decreased presence of beads.
The viscosity of the solution also plays a fundamental role. A solution viscosity too low causes a non-continuous jet, while a high viscosity causes difficulties in injecting the solution.
The surface tension is related to the solvent properties of the polymer solution. A high surface tension inhibits the electrospinning process, causing instability in the jet and the generation of a spray. Low surface voltage values favour the electrospinning process for lower electric fields.
Finally, by increasing the electrical conductivity of the solution, a decrease in the diameter of the fibers is obtained, while by lowering it, fibers with irregular morphology are produced. The radius of the jet varies inversely to the cube root of the electrical conductivity of the solution. On the other hand, highly conductive solutions are very unstable in the presence of strong electric fields.

3.1.2. Electrospinning parameters

The most important parameter that influences the electrospinning process is the applied voltage: high voltage causes an elongation of the jet during the spinning process, due to the greater Coulomb force that leads to a reduction in the diameter of the fibers, rapid evaporation of the solvent from the fibers and beads formation. Also important is the flow rate of the polymer solution: a low rate is preferred so that the solvent or solvent mixture used can evaporate completely.
Further, the diameter of the fibers is related to the injector-collector distance that must be adequate to allow the evaporation of the solvent present in the polymer solution before the nanofibers are deposited on the collector. Increasing this distance, the diameter of the fibers decreases.
Finally, feed-rate is an important process parameter to manage the dimension of the fibers. For example, some studies on the electrospinning of pure polymers have shown that increasing the feed rate usually leads to a large fiber size [5].

3.1.3. Environmental parameters

Temperature affects the viscosity of the polymer solution, an increase in temperature can contribute to a decrease in the viscosity of the solution and, therefore, to a decrease in the diameter of the fibers.
Another important parameter is humidity. With an increase in humidity, the appearance of small circular pores on the surface of the fibers is noted, and a further increase leads to an increase in the diameter of the pores. Low humidity values cause fast evaporation of the solvent from the electrospun polymer solution, this could lead to an obstruction of the needle.

3.2.Materials and Methods

Polyvinyl alcohol (PVA), is a low-cost, water-soluble and biocompatible polymer. PVA is a polymer obtained by hydrolysis of polyvinyl esters and it was purchased from Sigma Aldrich (M_w 85.000-124.000). Polymers are high molecular weight macromolecules made up of repetitive units, called monomers, identical or different from one other, which bind to form long chains. The repetitive unit of this polymer is shown in figure 3.6.

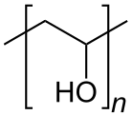

Figure 3. 6 Molecular structure of PVA monomer

PVA was chosen since it is a transparent polymer and it is immiscible in liquid crystals.

As nematic liquid crystal BL-036 (Merck) was used, with birefringence equal to 0.2670 and transition temperature from nematic to isotropic around 95 °C.

As fluorescent dye Coumarin 6 (C6), 3-(2-Benzothiazolyl)-N, N-diethyl-umbelliferyl amine,3-(2-Benzothiazolyl)-7-(diethylamino) coumarin, was used (Radiant Dyes Chemie). C6 has an absorption maximum at 444 nm and a fluorescence emission maximum at 505 nm in ethanol. Its structure is shown in figure 3.7 a.

To photopolymerize the liquid crystalline material a combination of a photoinitiator and a monomer was used. Darocur 1173 (BASF) was used as a photoinitiator and RM 257 (Merck) as a monomer, whose molecular structures are shown in figure 3.7 b and 3.7 c respectively:

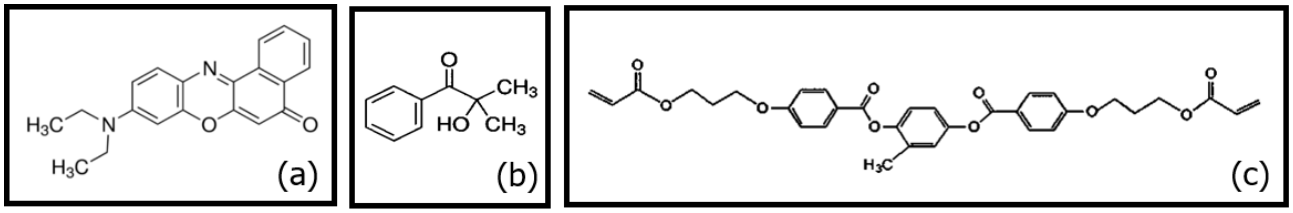

Figure 3. 7 Molecular structures: (a)Coumarin 6, (b) Darocur 1173 and (c) RM 257

The absorption spectrum of Darocur 1173, shown in figure 3.8, has two peaks, with the maximum peak at about 250 nm, in the ultraviolet spectrum.

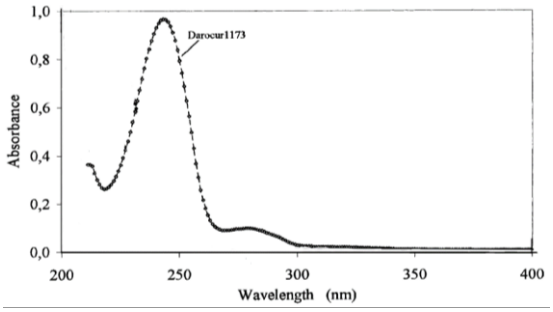

Figure 3. 8 Absorption spectrum of Darocur 1173

A mercury-vapor lamp was used as a light-curing source. The mercury lamp used (Jelosil, HE100AS) has a power of 125 W and is equipped with a UVA filter. Figure 3.9 on the left shows the lamp used and, on the right, its emission spectrum.

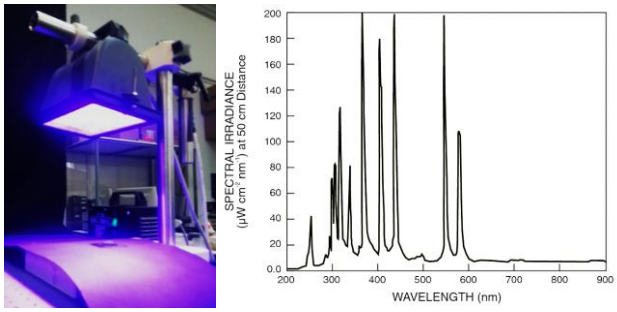

Figure 3. 9 Mercury vapor lamp (left) and its emission spectrum (right).

Commercially available Cellulose Nanocrystals (Sodium form Cellulose Nanocrystals Freeze-dried Width: 5-20 nm and Length: 100-250 nm purchased by CelluloseLab) were used as a reinforcing agent for the polymeric matrix.

Electrospun filaments were characterized using an optical microscope (DMRX, Leica), Atomic Force Microscope (AFM, Multimode 8 equipped with a Nanoscope V controller, Bruker), Confocal Laser Scanning Microscope (CLSM, TCS SP8, Leica).

3.3.Experimental results

In this paragraph, the preparation of anticounterfeiting labels containing a random distribution of liquid crystalline fluorescent microspheres using the electrospinning technique will be described. The characterization of the morphological, optical and fluorescence properties of the electrospun filaments are also reported.

3.3.1. PVA and LC Electrospun fibers mat

The fluid to be used in the electrospinning setup is a PVA matrix containing dye-doped liquid crystal microspheres. The procedure to create this fluid starts with the preparation of the matrix that was made using the PVA polymer dissolved in bidistilled water in the following percentages in weight:

$$\textbf{(a)}\ 92.0\%\ H_2O + 8.0\%\ PVA$$

The mixture was heated to a temperature of about $90°C$ to allow the complete dissolution of the polymer into the water and mixed using a magnetic stirrer.

Subsequently, two mixtures were prepared: one composed of a dye doped liquid crystal (DD-LC) in the following percentages by weight:

$$\textbf{(b)}\ 99.6\%\ BL036 + 0.4\%\ Coumarin\ 6$$

and a second one adding a photoinitiator and the monomer to mixture (b) in the following percentages by weight:

$$\textbf{(c)}\ 90.0\%\ wt.\ (99.6\%\ wt.\ (BL036) + 0.4\%\ wt.\ (\text{Coumarin6})) + 10\%\ wt.\ (f)$$

where $f = 96.0\%$ wt. (RM 257) $+ 4.0\%\ wt.\ (darocur\ 1173)$

Photoinitiator and monomer are essential to mechanically strengthen the liquid crystal microspheres that may undergo through rupture processes when a strong electric field is applied.

Emulsions were obtained by adding a small amount (about 1%) of each mixture (b) and (c) to the PVA/water matrix (a). In the text we will call “mixture A” the sample containing PVA and water only, “mixture B” the emulsion made from (b) plus (a) and “mixture C” the emulsion made from (c) and (a).

The use of PVA as an immiscible matrix has a double motivation. First of all, the PVA provides a planar anchoring of the liquid crystal molecules at the interface, and the liquid crystal molecules orient themselves parallel to the interface allowing the formation of a bipolar configuration. Second, the use of PVA helps to prevent the coalescence of liquid crystal microspheres. The acetate groups give an amphipathic character to the PVA, on a hydrophobic surface (such as that of the liquid crystal) the polymer is absorbed by attacking the acetate groups on the surface, while the vinyl alcohol chains, which are hydrophilic, face the aqueous-medium. Steric interactions stabilize the emulsion.

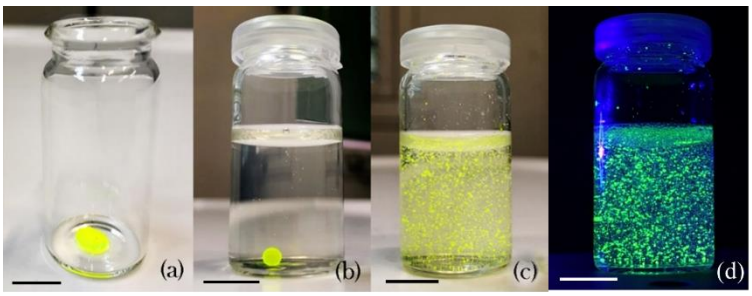

Figure 3. 10 Emulsion preparation: a) drop of DDLC deposited at the bottom of a glass vial, b) addition of the polymer matrix, c) microdroplets formed after mechanical stirring under visible light and d) UV light. Scale bar 1 cm.

A drop of the mixture was deposited at the bottom of a small glass bottle (Fig.3.10 a). A PVA/water solution was, then, added. Due to the immiscibility of the liquid crystal, the drop acquires a spherical shape (Fig. 3.10 b). The glass vial containing the mixture is, then, subjected to a mechanical stirring process to obtain an emulsion, several liquid crystal droplets were formed with diameters ranging from few to tens μm (Fig. 3.10 c). In figure 3.10 d it is shown the emulsion under UV light.

Emulsions were left to stabilize for an hour to remove the trapped air bubbles. After, approximately 4 ml of emulsion were withdrawn into a borosilicate glass syringe and placed in the electrospinning set-up. The syringe was connected via a Teflon tube to the injector of the electrospinning. Teflon was used because of its non-stick properties and good resistance to bending. The injection pressure was set at approximately 53 $mmHg$ and the current was set to approximately 5 mA.

A series of trial-and-error tests were carried out to determine the best parameters to use. Electrospinning was carried out using an applied voltage between the injector and the metal thin film of 15 KV and 22 KV, spinning speeds of 1ml/h and 5ml/h, the distance between injector and collector in a range from 10 cm to 15 cm and spinning time from 1hour to 4hours.

The best set-up parameters for the electrospinning were the following: the distance was 15cm, in most of the tests the electrospinning potential was 15kV and the spinning time was set at 2 hours. The electrospun fibers were collected on a thin aluminium foil, an example is shown in figure 3.11 a, the fibers can be detached from the aluminium foil in a sort of freestanding film as demonstrated in figure 3.11 b.

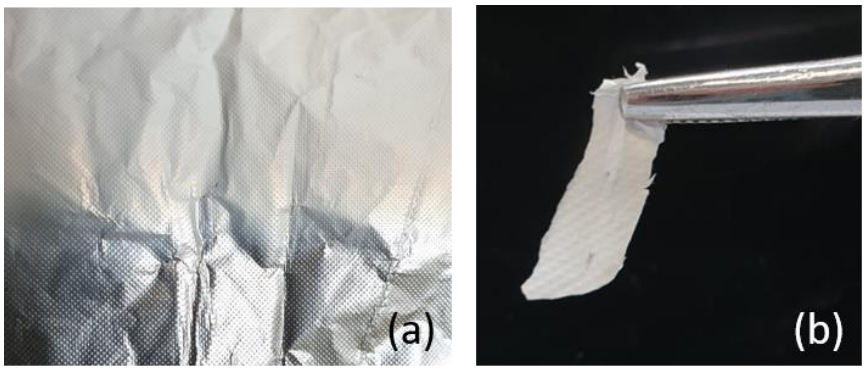

Figure 3. 11 (a) Electrospun fibers mat of pure PVA/water solution on aluminum foil; (b) A small piece of the material detached from the aluminum foil.

3.3.1.1. Morphological Characterization

Small pieces of materials were removed from each sample and observed under a polarized light optical microscope. It was possible to distinguish the single filaments that appear with different brightness when observed between crossed polarizers, this is because the PVA in the form of filament is no longer to be considered an isotropic medium but assumes a privileged direction which presents

an anisotropy and therefore a birefringence. In all cases, the presence of filaments was observed (fig. 3.12) and, from an optical point of view, there seems to be no difference between the different mats. The addition of the liquid crystal in the emulsion produces a brighter yarn with respect to the previous case when observed between crossed polarizers. Furthermore, it is noted that the presence of Mixture C inside the fluid does not modify or affect the optical properties of the samples (Fig. 3.12, b c d). Increasing the applied voltage to 22.5kV (Fig. 3.12, d) and the spinning speed to $5ml/h$ (Fig. 3.12, c) does not cause modification in the optical properties of the fibers mats.

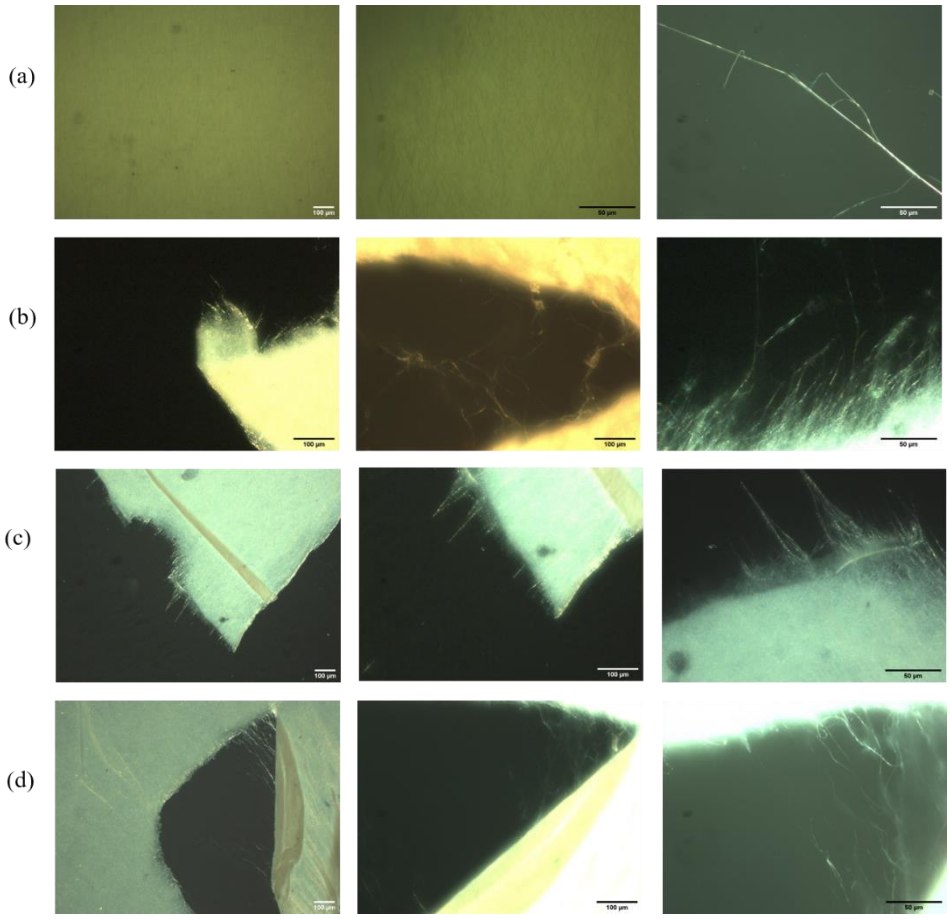

Figure 3. 12 POM images: a) Mixture A, b) Mixture C 1ml/h 18kV , c) Mixture C 5ml/h 18kV, d) Mixture C 1ml/h 22.5kV.

Samples were also analyzed by AFM. The fibers mat obtained from mixture A is homogeneous, the filaments' diameter remains constant along the fiber length (Fig. 3.13). Previous studies have shown that electrospun fibers have a diameter ranging from ten to hundreds of nanometers [10], data confirmed by the graph shown in figure 3.13, a.

While optical microscopy does not reveal any particular difference between the different samples, AFM shows that the presence of the dye-doped liquid crystalline material causes the formation of

beads (Fig.3.13, b). Since the spinning parameters have remained constant, the presence of beads is probably due to the varying viscosity of the solution which now has the properties of a colloidal dispersion.

The addition of the monomer, the photoinitiator and the photopolymerization of the microspheres significantly inhibits or reduces the presence of beads (Fig. 3.13, c). This could be due to the fact that the microspheres, now more rigid, are more resistant to the forces exerted by the electric field and this prevents them from breaking.

The increase in the injection speed to 5ml/h again causes the presence of beads (Fig. 3.13, d), despite the polymerization of the microspheres. This is a phenomenon that can be linked to the difficult evaporation of the solvent contained in the PVA mixture at these electrospinning rates.

If the injection speed returns to 1 ml/h, even if the applied electric field is high (22.5kV), the same type of fibers obtained at 18.5 kV is observed, which shows the almost total absence of beads (Fig. 3.13, e). This confirms the fact that in presence of polymerized microspheres, the appearance of beads can be attributed to the process of evaporation of the solvent during the electrospinning.

AFM data were analyzed through the Diameter J plugin of the Image J program (National Institute of Health) to obtain information on the radii of the fibers created in the different experimental conditions. The data obtained were then processed with Origin lab to draw the histograms shown in figure 3.13 on the right side.

Mixture A shows a dense distribution of filaments, the histogram is interpolated using a Gaussian curve, we obtain a peak with an average value of about 242 nm and a standard deviation of about 152 nm (graph in figure 3.13, a). While, as can be seen from the graph in figure 3.13 b, the presence of liquid crystals in mixture B causes a broadening of the histogram. This is due to the presence of the beads since they have a bigger radius than the filaments, which causes data dispersion. The fitting curve can be created overlapping several Gaussians, the highest peak is centered around 227 nm. If, finally, mixture C is evaluated, as shown in AFM images (Fig. 3.13, c), the histogram confirms that this mixture produces a sample with homogeneous filaments. The peak is narrow with a maximum around 234 nm and the dispersion is smaller than in the previous two cases. The deposition of mixture C at high speed causes an inhomogeneity in the radius of the filaments which affects the width of the histogram (Fig. 3.13, d). The reduction in speed and the increase of the electric field applied to mixture C (Fig. 3.13, e) causes a decrease in the fibres' diameter that becomes narrower with respect to the previous cases, the peak is now centred on the average radius of about 190 nm.

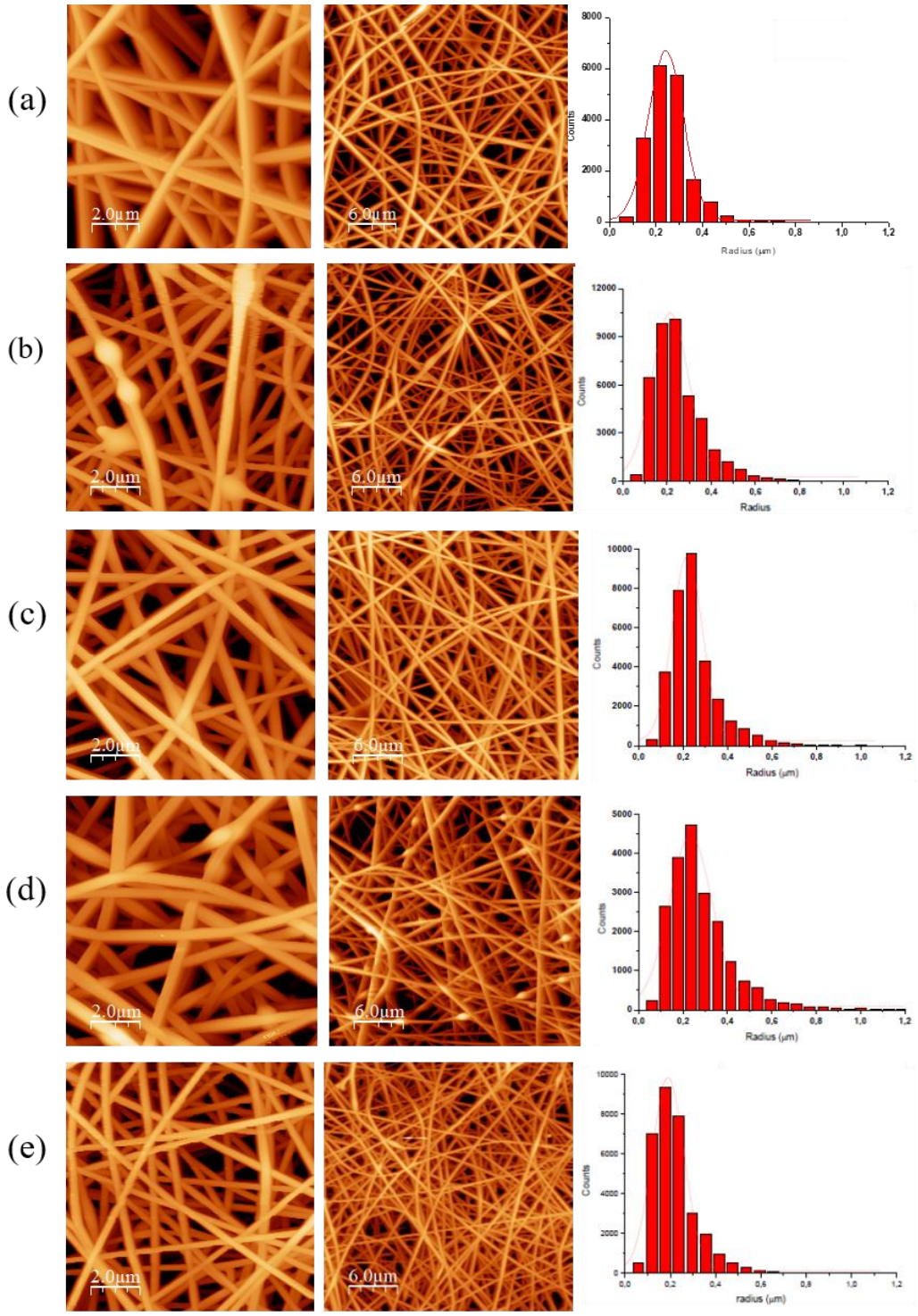

Figure 3. 13 AFM images (right) and fibres' radius histogram (left) of: a) Mixture A, b) Mixture B c) Mixture C at 1ml/h and 18kV , d) Mixture C at 5ml/h and 18kV, e) Mixture C at 1ml/h and 22.5kV.

3.3.1.2. Fluorescence properties

In mats obtained from mixture B confocal microscope analysis was performed showing a sample with an inhomogeneous fluorescence. During the preparation of the fluid to be spun the fluorescent dye

was contained only in the microspheres. It is observed, instead, that the fluorescence comes from all over the fibers mat, this confirms the hypothesis made previously, that most of the microspheres have broken due to the intense applied electric field, releasing their contents inside and on the surface of the fibers mat (Fig. 3.14, a). However, the presence of spherical objects with a diameter of tens of microns can still be recorded.

As already pointed out for AFM images, polymerization in mixture C affects the nature of the fibers mat. Although diffuse fluorescence is still visible, the number of visible microspheres has increased (Fig. 3.14, b) this is further evidence that the photopolymerization process can improve the mechanical properties of the microspheres.

Given the inhomogeneity of the fibers mat obtained at a speed of $5ml/h$, highlighted by the AFM analysis, the yarn obtained was analyzed by reducing the speed at 1ml/h and applying a voltage of 22.5 kV. Confocal microscope images show a reduced fluorescence of the whole sample and a significant presence of fluorescent microspheres inside it (Fig. 3.14, c).

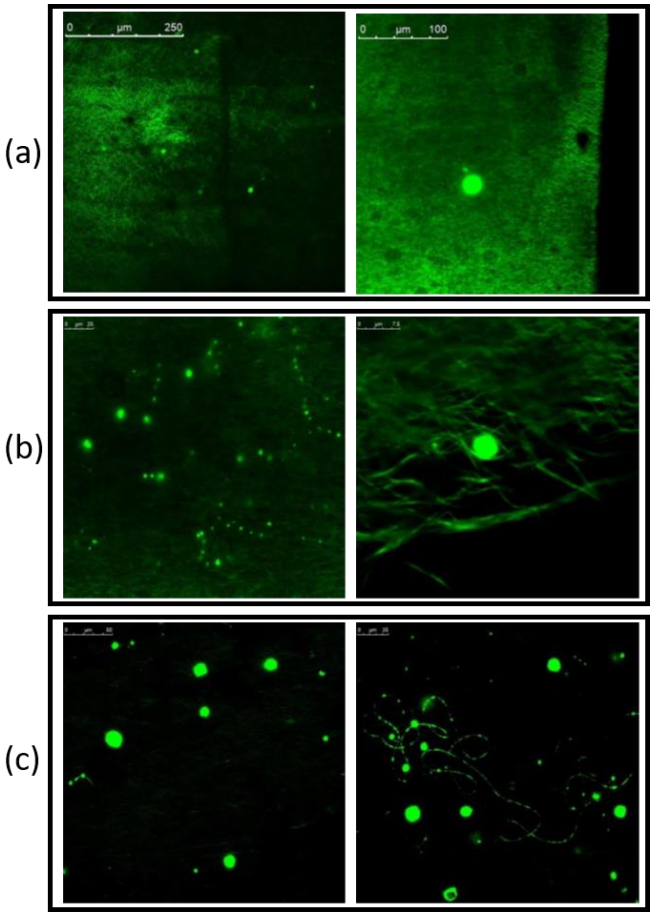

Figure 3. 14 Confocal images from: a) Mixture B, b) Mixture C 1ml/h 18.5kV, c) Mixture C 1ml/h 22.5kV

The electrospinning of mixture B led to a uniform dispersion of the dye on the membrane and the absence of microspheres on the surface, due to the rupture of the microspheres themselves during the deposition phase. This problem was overcome using mixture C. The obtained results are promising because they show that, although there is still a small fluorescence coming from the sample, the fluorescent microspheres are well distinguishable (Fig. 3.14 b, c).

In some points of the sample, fluorescence came only from the DD-LC spheres (Fig. 3.15 a, b) or we note the presence of filaments that appear to contain fluorescent beads, as shown in figure 3.15, c.

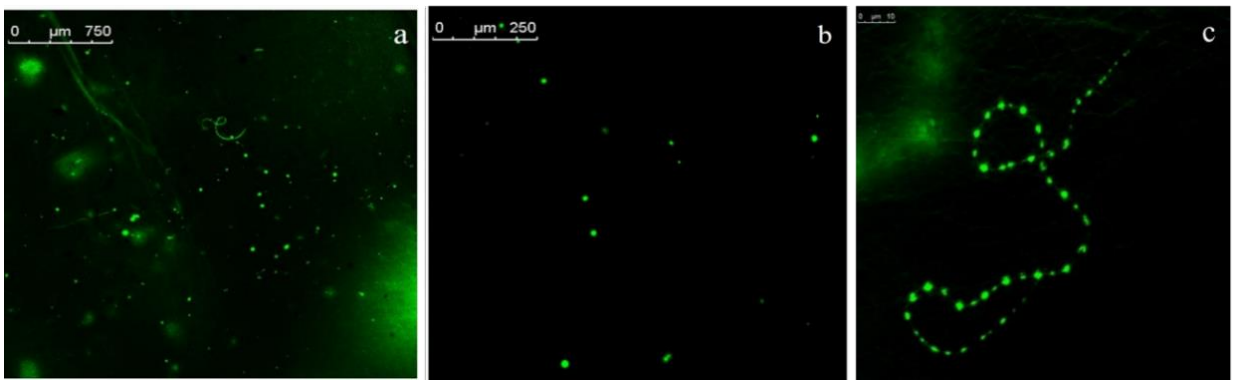

Figure 3. 15 Fluorescence images from different parts of the yarn, DDLC microspheres are present and in c) DDLC into a filament.

The random position of the particles, visible if the sample is illuminated with light at a specific wavelength, can be used to create a PUF key. Our aim is to create anti-counterfeiting tags based on the map of the random positions of the micro-droplets embedded inside the flexible fibers mat. Due to the characteristics of the preparation process the map is irreproducible even to its manufacturer. The presence of one or different fluorescent dyes increases the encoding capabilities of the tags and its safety level.

Fluorescence images are acquired using a CLSM, but confocal would be difficult to use for a quick and practical application. Figure 3.16 was acquired using an optical microscope with a UV lamp (right images) and white light (left images).

Good imaging can also be obtained using a low-resolution microscope, for example a smartphone's camera, illuminating with LEDs at 410nm a unique optical pattern can be easily seen in each area of the surface as shown in figure 3.17.

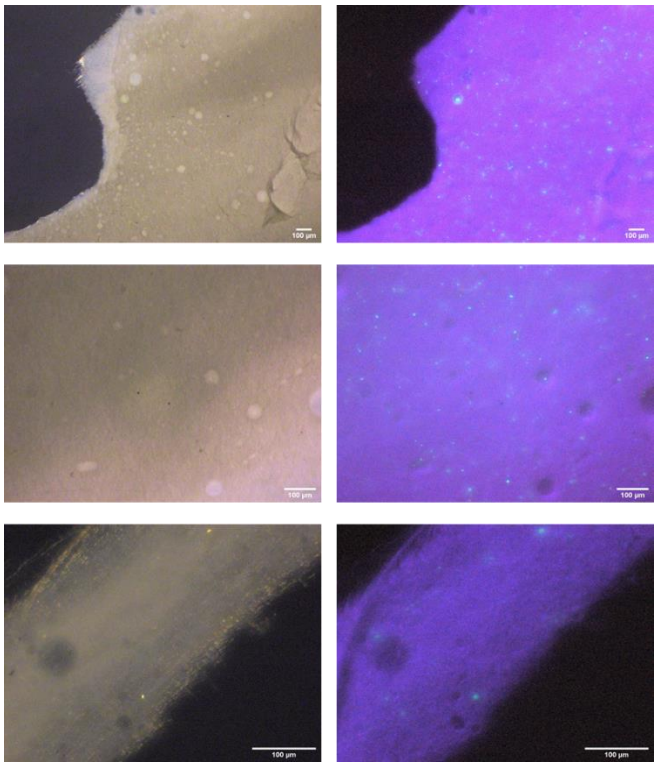

Figure 3. 16 POM images of different part of the electrospun mat from mixture C under white light(left) and under UV light (right)

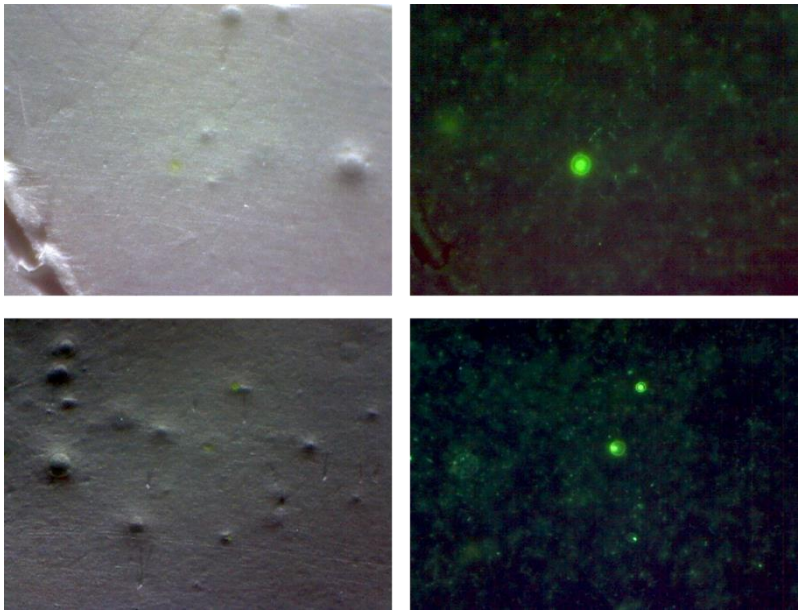

Figure 3. 17 Images of an electrospun mat from mixture C under white light(left) and under UV light (right) acquired using a low-resolution microscope (magnification 60X).

In figures 3.16 and 3.17 images on the left acquired under white light and the images on the right acquired under UV light can represent the ON and OFF state of an anti-counterfeiting tags.

3.3.2. PVA and CNCs Electrospun fibers mat

The second part of this work was devoted to investigate the possibility to use CNCs as reinforcement into PVA-based fibers [12] [13][14]. Processing based on nanocomposites nanofiber solutions requires a good dispersion of both components in the same solvent, CNCs are good candidates to be dispersed in PVA as both are soluble in water. A mixture containing commercial CNCs was prepared with the following weight percentages:

$$98\%\ H_2O + 2\%\ CNCs$$

CNCs were mixed in water using a Vortex mixer and sonicated for 60 minutes until they were well dispersed (Fig. 3.18, a). A certain amount of this mixture was added to mixture (a) containing only PVA and water (Fig. 3.18, b), they were mixed and sonicated as in the previous case until a homogenous solution was obtained (Fig. 3.18, c).

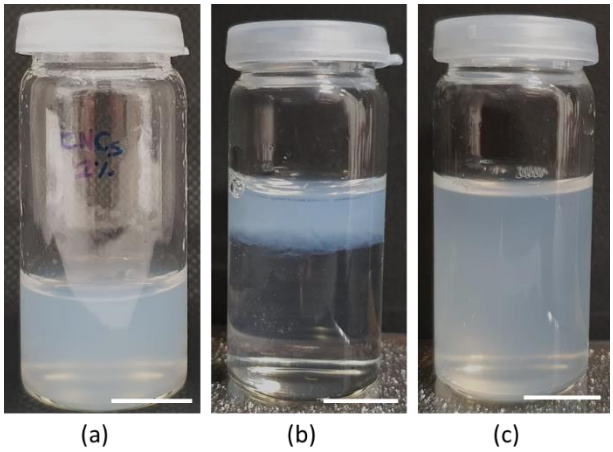

Figure 3. 18 PVA/CNCs emulsion: a) Mixture containing 2% CNCs in water, b) CNCs mixture added to PVA, c) PVA/CNCs emulsion after mixing and sonication processes. Scale bar 1 cm.

Following this procedure, different blends with different CNCs quantities were prepared, CNCs/PVA ratio in the blends was 0, 0.8%, 1.6% and 4.2 %.

Also, in this case, emulsions were prepared and they were left to stabilize for an hour to remove the trapped air bubbles before being transferred into a syringe and connected to the electrospinning apparatus.

We will identify as mixture D, mixture E, mixture F and mixture G the emulsion made from (a) plus the mixture CNCs/H_2O corresponding to CNCs/PVA ratio of 0, 0.8%, 1.6% and 4.2%(a), respectively. The electrospun deposition was performed for all the mixtures.

The physical and mechanical properties of PVA/CNCs mats were investigated with varying CNCs concentrations related to PVA to investigate the effect of the CNCs content.

3.3.2.1. Morphological Characterization

Analyzed through polarized light optical microscopy, the texture of the yarns, obtained electrospinning mixtures E and F, seems to be homogeneous and not very different from the ones observed in absence of CNCs. Images in Figure 3.18 a, b show that fibers appear bright between crossed polarizers and are similar to the ones shown in figure 3.12. On the contrary, the mat obtained electrospinning mixture G, the one with the maximum amount of CNCs, is optically different from the others. As observed in figure 3.18 c, no fibers appear at the borders and the surface shows several pore-like structures. In general, the impression is the one of a more compact yarn with a paper-like appearance.

Also in this case as the previous tests electrospinning' parameters were: the distance 15cm, the electrospinning potential was 15kV, the spinning speed 1ml/h and the spinning time was set at 2 hours.

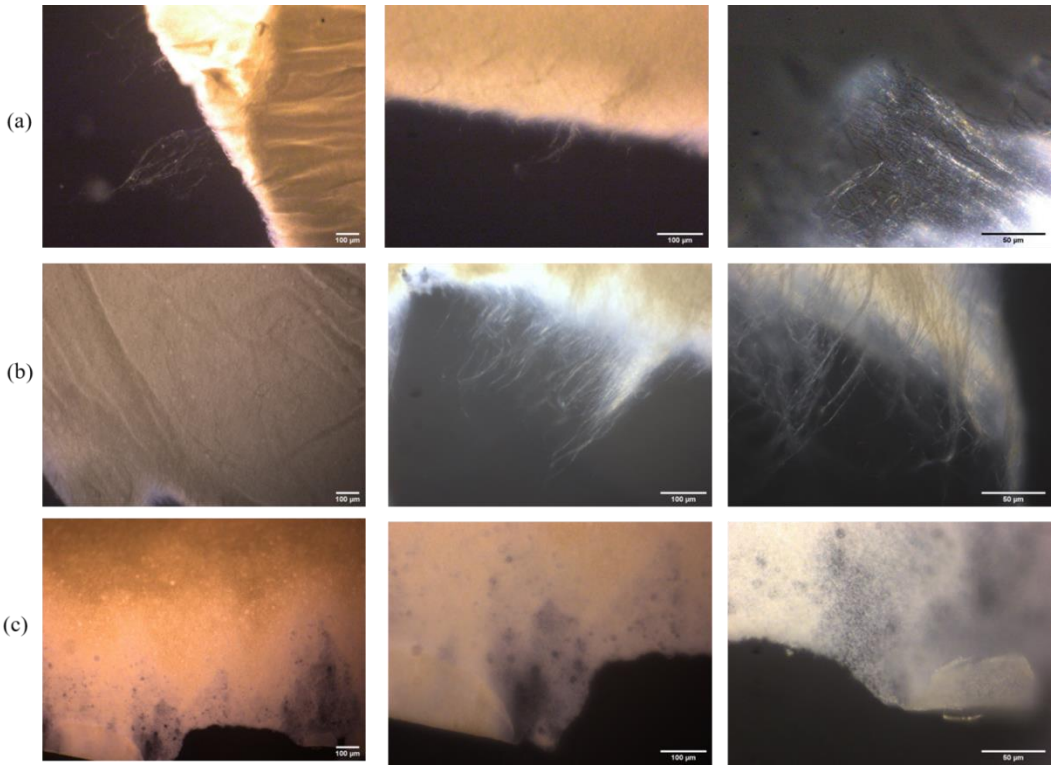

Figure 3. 19 POM images: a) Mixture E, b) Mixture F, c) Mixture G.

The yarns were, then, characterized, as previously described, using atomic force microscopy to measure the fibers diameter and collecting data using histograms.

With respect to the yarns obtained electrospinning mixtures not containing CNCs, the radii of the fibers are bigger. If histograms are interpolated using a Gaussian, the highest peaks for the yarns obtained using mixtures E, F and G are found at about 346nm, 357nm and 306nm respectively. Then,

increasing the percentage of CNCs causes a shift of the measured diameter towards lower values. The histograms are broader for yarns obtained from mixtures F and G with respect to the one obtained from mixture E. This may be due to the presence of bifurcations and veils in the yarn obtained electrospinning mixture F and to the presence of beads in the yarn obtained electrospinning mixture G.

The reduction of the radius of the filament in the mixture G, containing the major quantity of CNCs, could be ascribed to the quantity of CNCs present in the mixture which varies its density.

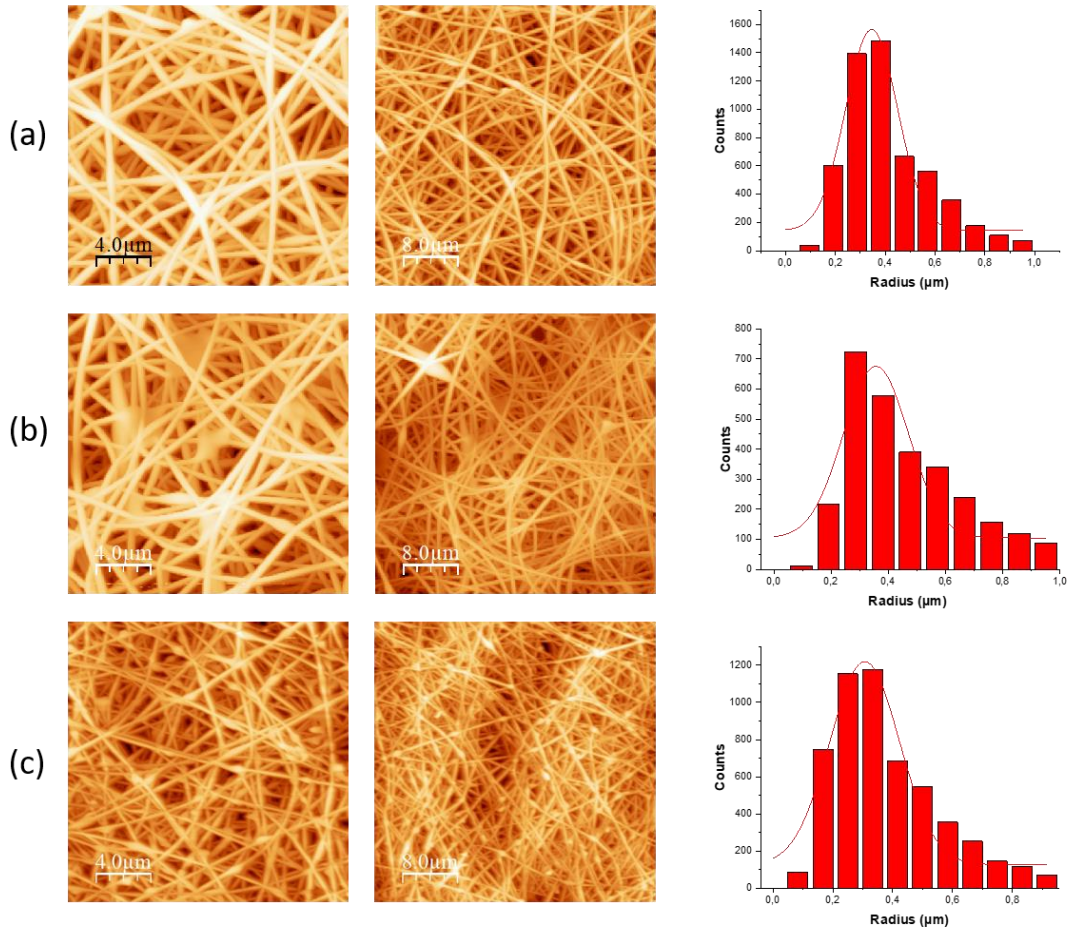

Figure 3. 20 AFM images of yarns obtained electrospinning (a) Mixture E, (b) Mixture F, (c) Mixture G.

Comparing the histograms with the ones obtained electrospinning mixtures not containing CNCs, the major difference is in their widths, being the ones shown in figure 3.20 broader than the ones shown in figure 3.13. This is due to the many “imperfections” (heterogeneity) shown by the surface of the yarns containing CNCs in terms of the presence of beads and “veils” visible from AFM images, probably due to viscosity related instabilities occurring during the electrospinning process. Finally, from a qualitative point of view, the yarns obtained electrospinning mixtures containing CNCs seem to contain more fibers in the imaged areas giving the impression of a more compact surface.

3.3.3. PVA, LC and CNCs Electrospun fibers mat

Following the previous experimental results and in the perspective of creating a tag that can be used as an anti-counterfeiting device, two final mixtures were created: one containing a liquid crystal and CNCs/PVA in a ratio of 4.2% and the second similar to the first one but containing a fluorescent dye inside the liquid crystal.

3.3.3.1. Morphological Characterization

From an optical investigation, figure 3.21 a, b, the textures of the yarns look similar always showing the presence of structures similar to pores on the surface. In the second yarn (Fig. 3.21, b) the presence of LC microdroplets is highlighted due to the fluorescent dye, also, focusing the image it is noted that the micro-droplets are incorporated into the mats.

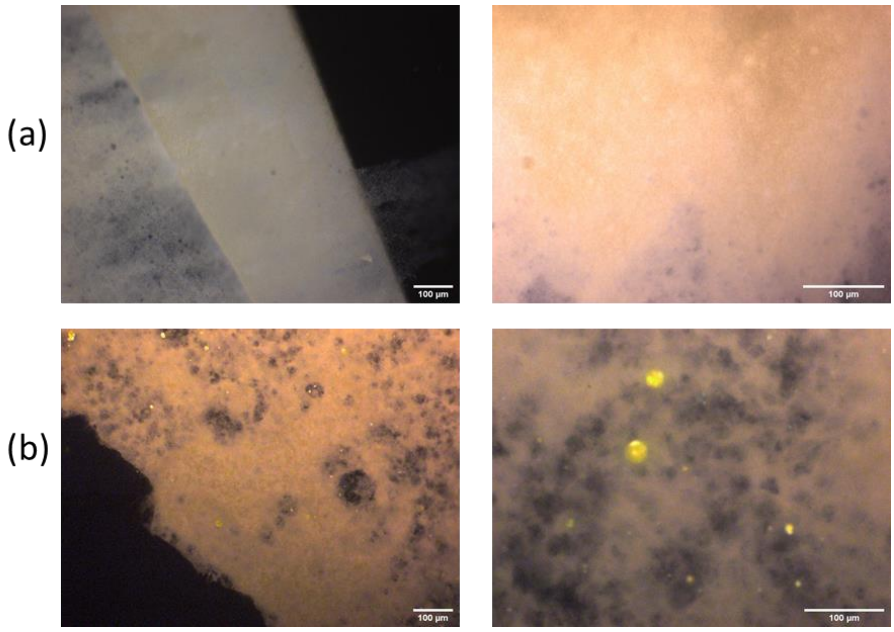

Figure 3. 21 POM images from an electrospun emulsion of (a) Liquid Crystal and CNCs/PVA ratio of 4.2%, (b) Dye Doped Liquid Crystal and CNCs/PVA ratio of 4.2%.

AFM analysis confirms the previous observations for the yarn obtained electrospinning the mixture with the highest concentration of CNCs, while the presence of the dye does not affect the diameter of the fibers. The peak is at about 277nm and 300nm for the fibers obtained from mixtures not containing and containing the fluorescent dye, respectively. Also the width of the histograms is similar.

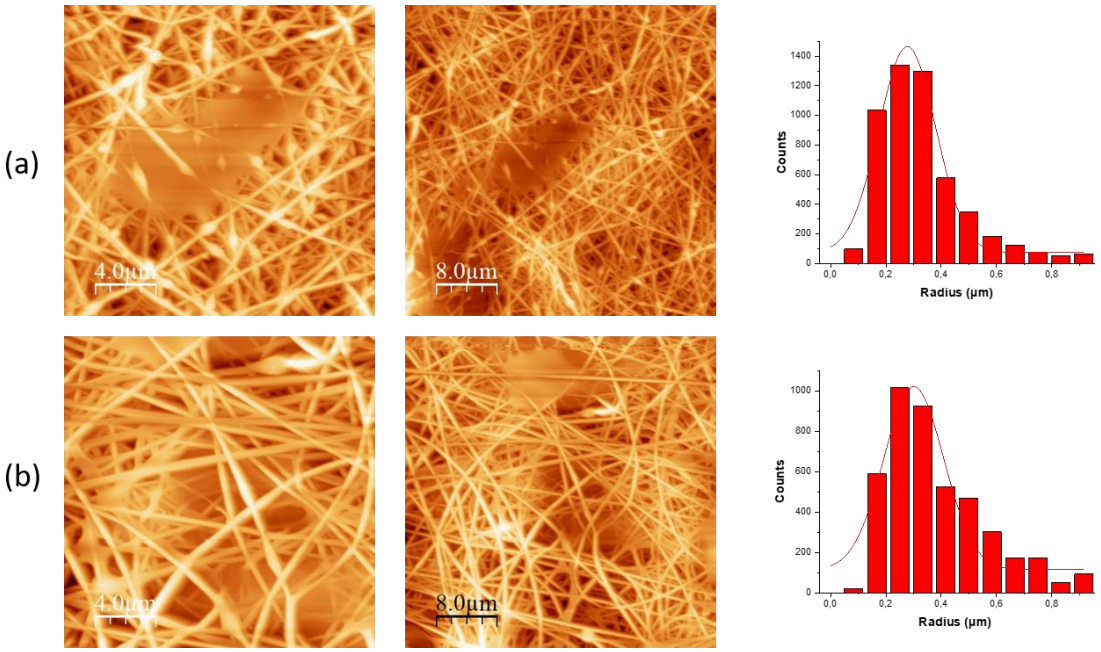

Figure 3. 22 AFM images (a) ~~PVA,~~ yarns obtained electrospinning a mixture of Liquid Crystal and CNCs/PVA ratio of 4.2%, (b) and a mixture of Dye Doped Liquid Crystal and CNCs/PVA ratio of 4.2%.

3.3.3.2. Fluorescent properties

Confocal images of the yarn obtained electrospinning the mixture ~~that~~ containing the dye show well distinguishable fluorescent microspheres as in the case of mixture C electrospun mats. Also, no diffuse fluorescence is visible and this is extremely interesting because it means that microspheres are not broken due the intense electric field. Then, CNCs may have a role in strengthening the microspheres allowing to avoid the use of monomer and photonitiator to prevent dye leakage.

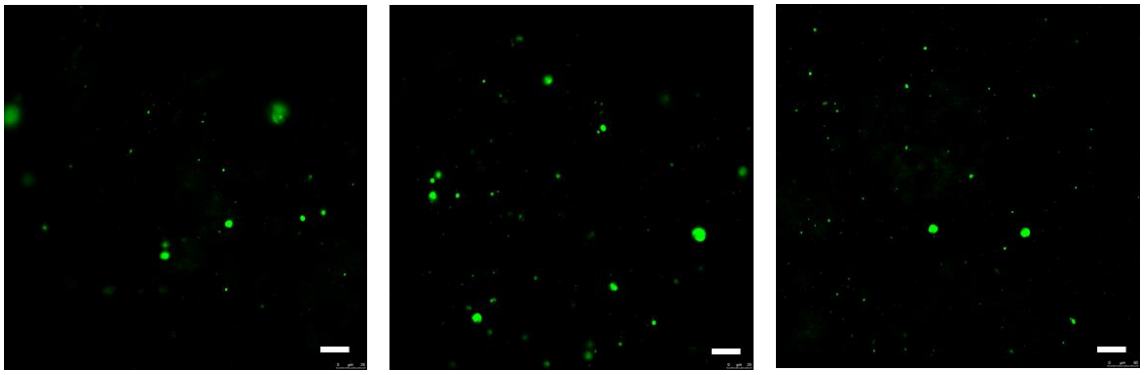

Figure 3. 23 Confocal images of yarns obtained electrospinning a mixture of Dye Doped Liquid Crystal and CNCs/PVA ratio of 4.2%. Scale bar 25um

Figure 3.24 shows POM images acquired using white light (left) and UV light (right) of the same mats.

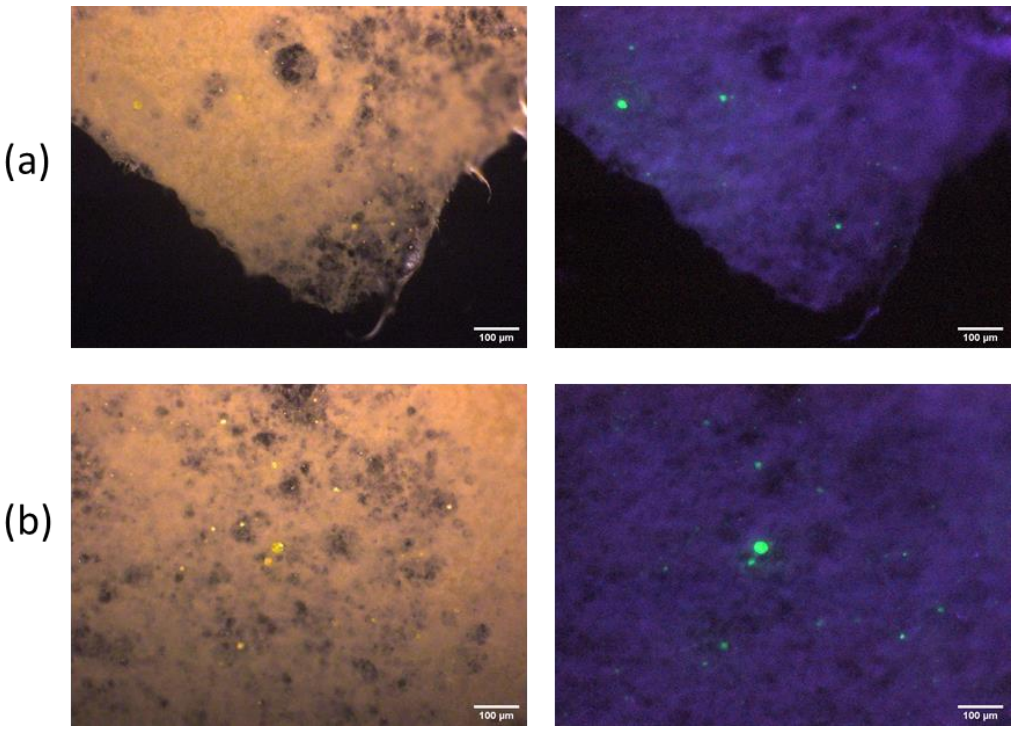

Figure 3. 24 Polarized light optical microscopy images of different mats' areas electrospun from PVA, DD-LC and CNCs/PVA ratio of 4.2%. under white light(left) and under UV light (right)

As visible from previous images a random pattern of fluorescent microspheres embedded in a free-standing film can be obtained. The microspheres positions map, sizes and colour represent a PUF key impossible to reproduce. Further, the level of randomness can be increased electrospinning an emulsion containing microspheres with different dyes and/or using dyes that are invisible in white light, for example absorbing in the UV. In the perspective to create an anti-counterfeiting device, further characterizations are needed to check the stability of the yarn as a function of temperature and humidity.

3.4. Results

The possibility to create an anti-counterfeiting device that uses a positional map of fluorescent microspheres as PUF key has been proposed by our research group. A thin flexible polymeric film containing a casual dispersion of microspheres can be obtained dispersing two or several liquid crystal mixtures doped with different fluorescent materials in a polymeric fluid matrix. The solution is

deposited on a glass slide and, following the evaporation of the solvent contained in the polymeric matrix, a thin free-standing film is obtained (fig. 3.25). [16]

Figure 3. 25 Images of a polymeric film containing fluorescent DDLC microspheres.

The randomness of the microspheres position is granted by the film preparation procedure. Further, the doping of the nematic liquid crystal with fluorescent dyes increases the coding capability of the film. In fact, in addition to a correspondence of the positions of the objects with respect to each other, there must also be a correspondence of the detected fluorescent wavelength that provide a hidden identity for authentication. A piece of the polymeric film can be cut in a circular form and embedded in a tag (fig. 3.26). A software for authenticating this type of tags has already been developed in collaboration with the CNR-ICAR at University of Calabria. For the authentication process a 10x lens and a UV light source, both engineered in a compact object that can be attached to a mobile phone, are used. The customer has the possibility of verifying the authenticity of the product using his own device, exploiting an application that identifies the random position of the microspheres.

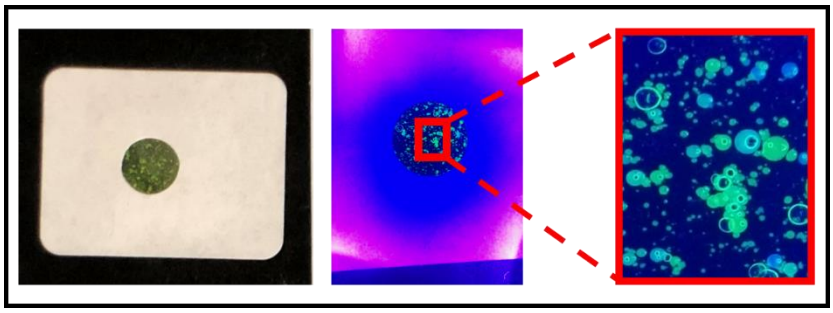

Figure 3. 26 From left to right: Circular tag on a support, example of an image acquired using a mobile phone, a detail of the image.

The information of each tag is recorded and stored on a server and it can be easily recalled during the authentication phase.

Once a picture is acquired using a smartphone, an application identifies the position of all the microspheres and creates a points map (figure 3.2a) that relates each microsphere to the others by their respective distance. Once the microspheres have been identified, the application compares the acquired image with those stored on the server. Figure 3.26b shows an almost final step in the

authentication process. The application has identified the correct image in the server and has drawn yellow lines that go from the characteristic points on a microsphere (red points) to the corresponding characteristic points on the other microsphere (green points). In a successful authentication a large amount of lines is drawn (Figure 3.26b, left), for an unsuccessful match very few lines are drawn (Figure 3.26b, right).

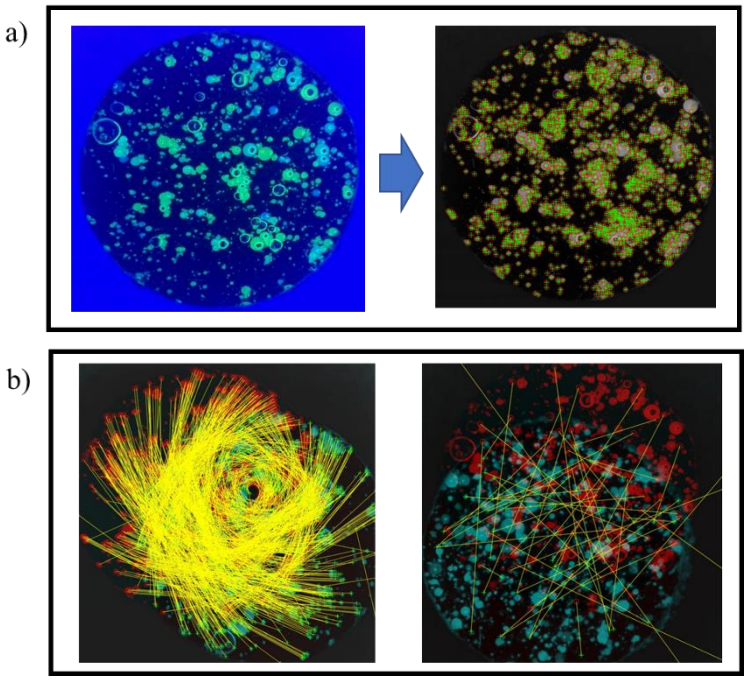

Figure 3. 27 a) Identification of the characteristic points of the specific image; b) Common characteristics in two photos of the same TAG (left), of different TAGs (right)

This tag is going to be used in a small-scale preliminary test to evaluate its robustness as anti-counterfeiting device in collaboration with Poste Italiane.

The tag proposed in this chapter contains similar features to the one shown above and it could be further improved in order to increase its robustness and coding capabilities. The main advantage with respect to the polymeric film containing microspheres is the easiness of production directly related to the electrospinning technique that allows to produce bigger sample in less time with respect to a fluid film slowly evaporating. Further, compared to the polymeric tag, the electrospun films are more flexible and resistant to bending and can be used in the clothing supply chain, even incorporating them inside the garment itself. Apart from the clothing sector, in any field in which fabrics are present (packaging, ...) the proposed tag can be easily hidden making them very difficult to detect. Further, as authentication software the one described previously can be used also for this tag.

Finally, the tag created using biocompatible materials as PVA and CNCs is very attractive in terms of environmental sustainability and recycling.

3.5. References

[1] J. Molina-González, A. Arellano-Morales, O. Meza, G. Ramírez-García, and H. Desirena, "An anti-counterfeiting strategy based on thermochromic pigment activated by highly Yb3+ doped photothermal particles," *Journal of Alloys and Compounds*, vol. 850, p. 156709, Jan. 2021, doi: 10.1016/J.JALLCOM.2020.156709.

[2] S. Rouhani and F. Nahavandifard, "Molecular imprinting-based fluorescent optosensor using a polymerizable 1,8-naphthalimide dye as a florescence functional monomer," *Sensors and Actuators B: Chemical*, vol. 197, pp. 185–192, Jul. 2014, doi: 10.1016/J.SNB.2014.02.082.

[3] T. WE and R. S, "A review on electrospinning design and nanofibre assemblies," *Nanotechnology*, vol. 17, no. 14, Jul. 2006, doi: 10.1088/0957-4484/17/14/R01.

[4] E. Hendrick, M. Frey, E. Herz, and U. Wiesner, "Cellulose Acetate Fibers with Fluorescing Nanoparticles for Anti-counterfeiting and pH-sensing Applications." *Journal of Engineered Fibers and Fabrics*, vol. 5, no. 1, pp. 21–30, Mar. 2010, March 2010, doi: 10.1177/155892501000500103.

[5] Stephen P. McGrew , "Quantum dot security device and method," Sep. 2001, Patent Application US6692031B2.

[6] E. A. Buyuktanir, M. W. Frey, and J. L. West, "Self-assembled, optically responsive nematic liquid crystal/polymer core-shell fibers: Formation and characterization," *Polymer*, vol. 51, no. 21, pp. 4823–4830, 2010, doi: 10.1016/j.polymer.2010.08.011.

[7] S. P. Rwei and C. C. Huang, "Electrospinning PVA solution-rheology and morphology analyses," *Fibers and Polymers*, vol. 13, no. 1, pp. 44–50, Jan. 2012, doi: 10.1007/s12221-012-0044-9.

[8] W. E. Teo and S. Ramakrishna, "A review on electrospinning design and nanofibre assemblies," *Nanotechnology*, vol. 17, no. 14, Jul. 2006, doi: 10.1088/0957-4484/17/14/R01.

[9] J. P. F. Lagerwall, J. T. McCann, E. Formo, G. Scalia, and Y. Xia, "Coaxial electrospinning of microfibres with liquid crystal in the core," *Chemical Communications*, no. 42, pp. 5420–5422, Nov. 2008, doi: 10.1039/B810450F.

[10] M. C. Popescu, B. I. Dogaru, M. Goanta, and D. Timpu, "Structural and morphological evaluation of CNC reinforced PVA/Starch biodegradable films," *International Journal of Biological Macromolecules*, vol. 116, pp. 385–393, Sep. 2018, doi: 10.1016/j.ijbiomac.2018.05.036.

[11] J. E. Sanders, Y. Han, T. S. Rushing, and D. J. Gardner, "Electrospinning of cellulose nanocrystal-filled poly (Vinyl alcohol) solutions: Material property assessment," *Nanomaterials*, vol. 9, no. 5, May 2019, doi: 10.3390/nano9050805.

[12] H. Dong, K. E. Strawhecker, J. F. Snyder, J. A. Orlicki, R. S. Reiner, A. W. Rudie, "Cellulose nanocrystals as a reinforcing material for electrospun poly(methyl methacrylate) fibers: Formation, properties and nanomechanical characterization", Carbohydrate Polymers, Volume 87, Issue 4, 2012, Pages 2488-2495, ISSN 0144-8617, https://doi.org/10.1016/j.carbpol.2011.11.015.

[13] W. Wang, T. Liang, B. Zhang, H. Bai, P. Ma, W. Dong, “Green functionalization of cellulose nanocrystals for application in reinforced poly(methyl methacrylate) nanocomposites”, Carbohydrate Polymers, Volume 202, 2018, Pages 591-599, ISSN 0144-8617, https://doi.org/10.1016/j.carbpol.2018.09.019.

[14] Rochardjo, H.S., Fatkhurrohman, Kusumaatmaja, A., Yudhanto, F., 2021. Fabrication of Nanofiltration Membrane based on Polyvinyl Alcohol Nanofibers Reinforced with Cellulose Nanocrystal using Electrospinning Techniques. International Journal of Technology. Volume 12(2), pp. 329-338.

[15] T. D. Brown, P. D. Dalton, D. W. Hutmacher, “Melt electrospinning today: An opportune time for an emerging polymer process”, Progress in Polymer Science, Volume 56, 2016, Pages 116-166, ISSN 0079-6700, https://doi.org/10.1016/j.progpolymsci.2016.01.001.

[16] Unclonable Patterns by Soft Matter Textures, Bruno M.D.L, Doctoral Thesis 2022 (submission).

4. Conclusions

Nowadays, Physical Unclonable Functions are emerging as a new type of cryptographic primitives, impossible to duplicate and suitable for creating anti-counterfeiting devices.

Novel smart solutions exploiting advanced nano and micro technologies, in particular based on soft materials, offer new possibilities for PUFs creation. Very high definition optical and photonic effects are obtainable by using, for instance, self-assembling materials such as LCs and cellulose-based materials combined with polymeric matrices and organic and inorganic nanoparticles. Novel soft composite materials can be easily prepared using processes that confer them an intrinsic randomness allowing to create very intricate and impossible to reproduce structures. Further, their photonic and optical properties like lasing, interferential selective reflection, scattering, light modulation can be easily combined with the structural properties. This makes them ideal candidates for creating PUF keys and for anti-counterfeiting devices with high coding levels.

The present research work has been carried out in this context. We have presented the results obtained in the effort to create novel smart materials that can be implemented in anti-counterfeiting tags.

In particular, a combination of a chiral nematic liquid crystal and metallic nanoparticles has been confined inside microspheres preparing an emulsion. Applying an intense electric field to the emulsion, a reorientation of the director field is induced that produces, when microspheres are observed between crossed polarizers, fingerprint-like optical textures. Due to the presence of nanoparticles, the shape of the droplets also changes considerably, some of them resembling the one of a human finger. The process of fingerprint-like pattern creation is completely random and can be successfully used to create simultaneously several different textures. This system can be used as a physical fingerprints generator. Fingerprints, then, can be imaged using advanced microscopy technique and used to create labels that can be exploited as anti-counterfeiting devices. A prototype of a label has been manufactured using a fingerprint-like texture and a first test has been carried out using a specially modified software to evaluate the easiness of the authentication process. Further improvements can be done, as an example, the dimension of the label can be reduced as well as using different materials and deposition techniques that can be optimized to reduce the voltage necessary to switch on the label.

In the last years, the attention of researchers has been focused on developing new materials which are biocompatible and eco-friendly in the perspective of using them in anti-counterfeiting devices intended to track, for example, foods and drugs.

For this reason, we have focused our attention on cellulose-based materials as cellulose nanocrystals and hydroxypropyl cellulose. These materials are interesting because they possess as chiral nematic

liquid crystals the propriety to self-assemble into helical structures. As a first step, a procedure to obtain free-standing films of cellulose nanocrystals from microcrystalline cellulose PH-101 doped with different quantities of hydroxypropyl cellulose was developed. Cellulose nanocrystals and CNCs functionalised with RhB were synthesized in the laboratory of Dr Susete Fernandes at NOVA University Lisbon, Portugal. These films have the characteristic to be able to reflect circularly left-handed polarized light and appears black (transmit) when circularly right-handed polarized light is used. Also, the wavelength of the reflected light changes (red-shift wavelenght) based on the percentage of hydroxypropyl cellulose used. As a second step a procedure to synthesize rhodamine functionalized cellulose nanocrystals has been developed. A free-standing film containing both pristine and functionalized nanocrystals has been created. This film exhibits two different optical properties, from one side it shows the structural colours and the selective circularly polarized light reflection of the previous films and it also shows fluorescent properties. Even if in both cases the developed procedure and the optical effects are not intrinsically randomic, nevertheless, the manufacturing procedure is difficult to reproduce, and the optical effect is very effective. Since the film is completely biocompatible it can be used in an anti-counterfeiting tag in direct contact with food. In this perspective, further work has to be done in the attempt to mechanically strengthen the film using a procedure that do not affect its optical properties. The combination of the two composite systems allow to obtain a smart material with tuneable optical features (either overt, structural coloration, or covert, selective light circular reflection, and fluorescence) which can be flexible (depending on the content of HPC use).

Finally, the knowledge acquired using both liquid crystals and cellulose nanocrystals has been used to create a PUF keys that relies on the electrospinning of an emulsion of a fluorescent dye doped liquid crystal immersed in a polymeric matrix containing cellulose nanocrystals. The procedure allows to create a free-standing polymeric yarn, mechanically strengthened by the presence of nanocrystals, that contains a map of randomly distributed fluorescent microdroplets. The positional map of microspheres can be used as a PUF key and the electrospun yarn can be easily included in an anti-counterfeiting tag. For the authentication procedure, in this case, we are going to exploit a technique already used for a pilot project in collaboration with Poste Italiane that uses a polymeric thin film containing several fluorescent nematic droplets. The authentication is performed through the use of a smartphone and a specially developed software. A small miniaturized device, containing a lamp and a lens to be attached to the smartphone, is used to take a picture of the tag and the image is compared immediately with the ones stored in a database providing information about the authentication in real time. With respect to the polymeric film, the electrospun one is easy to be implemented in a device since it is much thinner and bendable. Further, also the random position of

the filaments in the different parts of the film can be used as PUF keys on a different level but a more sophisticated authentication procedure is needed. Finally, to improve the coding capability of the tag we plan to use in the future the fluorescent cellulose nanocrystals to enrich its optical properties.

This research has been carried out in collaboration with Dr Susete Fernandes of the Soft and Biofunctional Materials group at NOVA University Lisbon, Portugal, Ing. Stefano Sinopoli at BIOAGE - BIOelectronics and Advanced Genomic Engineering, Ing. Giuseppe Papuzzo and Ing. Agostino Forestiero at CNR-ICAR, Institute for High Performance and Networking, Dr. Giovanni Golemme at the Department of Environmental Engineering of University of Calabria and Dr. Giovanni Desiderio at CNR-Nanotec, Institute of Nanotechnology.

The work developed in collaboration with the Dr Susete Fernandes is co-financed by FEDER, European funds, through the COMPETE 2020 POCI and PORL, National Funds through FCT—Portuguese Foundation for Science and Technology and POR Lisboa2020, under the projects PIDDAC (POCI-01-0145-FEDER- 007688, reference UIDB/50025/2020-2023) and PTDC/CTM-REF/30529/2017 (Nano- Cell2SEC).

La borsa di dottorato è stata cofinanziata con risorse del
Programma Operativo Nazionale Ricerca e Innovazione 2014-202 (CCI 2014IT16M2OP005)
Fondo Sociale Europeo, Azione I.1 “Dottorati Innovativi con caratterizzazione Industriale”